

# **THE EXPERIMENTAL FLOWFIELD AND THERMAL MEASUREMENTS IN AN EXPERIMENTAL CAN-TYPE GAS TURBINE COMBUSTOR**

by

Bronwyn Clara Meyers

Submitted in partial fulfilment of the requirements for the degree  
Master of Engineering (Mechanical Engineering)  
in the Faculty of Engineering, Built Environment and Information Technology  
University of Pretoria  
Pretoria

November 2009



## ABSTRACT

The experimental flowfield and thermal measurements in an experimental can-type gas turbine combustor

Author: B.C. Meyers

Supervisor: Prof J.P. Meyer

Co-supervisors: Dr G.I. Mahmood

Mr G.C. Snedden

Department: Mechanical and Aeronautical Engineering

Degree: Master of Engineering (Mechanical Engineering)

**Summary:** In this study, experimental data was collected in order to create a test case that can be used to validate computational fluid dynamics (CFD) simulations and the individual models used therein for gas turbine combustor applications. In many cases, the CFD results of gas turbine combustors do not correlate well with experimental results. For this reason, there is a requirement to test the simulation method used before CFD can successfully be used for combustor design. This test case encompasses all the features of a gas turbine combustor such as a swirler, primary, secondary and dilution holes as well as cooling rings.

Experiments were performed on the same combustor geometry for both non-reacting and reacting flows. The non-reacting flow experiments consisted of stereoscopic particle image velocimetry (PIV) measurements performed at various planes in the three zones of the combustor. Data was collected on planes, both in line with the holes and in between the holes of each zone.

For the reacting experiments, the temperatures on the outlet plane were measured using a thermocouple rake, thus a temperature contour plot on the outlet plane was produced. Further, the combustor can was modified with passive inserts, which were tested to determine their influence on the outlet temperature distribution during reacting runs. In this set-up, the outlet velocity profiles were also measured using a Pitot tube during both non-reacting and reacting flows. In addition to the outlet temperature distribution and velocity profiles, images of the flame patterns were captured, which showed the positions of flame tongues, fluctuating flames and steady flames. Carbon burn patterns on the walls of the combustor liner were also captured. From the data collected during the reacting runs, the pattern factor, profile factor, overall pressure loss and pressure loss factor were calculated.

The non-reacting experiments performed using the PIV, produced three-dimensional velocity vector fields throughout the combustor. These experiments were performed at various flow rates, which gave an indication of which features of the combustor flow were affected by the flow rate. When comparing the individual PIV images alongside one another, the temporal nature of the combustor flow was also evident.

The reacting experiments revealed a hot region of exhaust gas around the outer edge of the exhaust while there was a cooler region in the centre of the outlet flow. The PIV flowfield results revealed the reason for the hot outer ring-like region was due to the path the hot gasses would take. The hot combustor gas from the primary zone diverges outwards in the secondary zone then is further forced to the outside by the dilution recirculation zone. The hot flow then leaves the combustor along the wall while the cooler air from the jets leaves the combustor in the centre.

The experiments performed produced a large variety of data that can be used to validate a number of aspects of combustor simulation using CFD. The non-reacting experimental data can be used to validate the turbulence models used and to evaluate how well the flow features were modelled or captured during the non-reacting stage of the combustor simulation process. The typical flow features such as jet penetration depths and the position and size of the recirculation regions are provided for effective comparison. The thermal results presented on the outlet plane of the combustor can be used for comparison with CFD results once combustion is modelled.

**Keywords:** gas turbine combustor, particle image velocimetry, temperature, three-dimensional velocity field.



## ACKNOWLEDGEMENTS

This work is the result of a research effort funded by the Defence Research and Development Board, in terms of Armscor Order KT471006.

A special thanks goes to Glen Snedden at the CSIR for his continued support and influence on this project.



## TABLE OF CONTENTS

Abstract.....	ii
Acknowledgements .....	iii
Table of contents .....	iv
Figures.....	vi
Tables .....	xiii
Nomenclature .....	xiv
Abbreviations .....	xvi
<b>1 Introduction .....</b>	<b>1</b>
1.1 Background.....	1
1.2 Problem statement.....	1
1.3 A brief review of existing knowledge.....	2
1.4 Research objectives.....	3
1.5 Scope of the study .....	3
<b>2 Literature study .....</b>	<b>4</b>
2.1 Previous work.....	4
2.2 Relevance .....	31
2.3 Methodology.....	31
2.3.1 Combustor pressure characteristics .....	31
2.3.2 Combustor thermal characteristics .....	32
2.3.3 Swirl number .....	33
2.3.4 Particle image velocimetry .....	35
2.4 Summary.....	44
<b>3 Experimental process.....</b>	<b>46</b>
3.1 Introduction .....	46
3.2 Experimental set-up .....	47
3.2.1 Reacting experiment.....	47
3.2.2 Non-reacting experiment.....	53
3.2.3 Wedge rings.....	55
3.3 Experimental method .....	57
3.3.1 Reacting experiment.....	57
3.3.1.1 Base case settings.....	57
3.3.1.2 Outlet temperature profile .....	58
3.3.1.3 Qualitative data .....	58
3.3.1.4 Outlet velocity profile.....	59
3.3.2 Non-reacting experiment.....	59
3.3.2.1 Particle image velocimetry .....	59
3.3.3 Wedge rings.....	63



---

3.3.3.1	Outlet temperature profile .....	63
3.3.3.2	Outlet velocity profile.....	63
3.4	Verification .....	64
3.4.1	PIV evaluation .....	64
3.4.2	PIV-Pitot comparison .....	75
3.4.3	Calibration and Instrument Uncertainty .....	76
<b>4</b>	<b>Results .....</b>	<b>79</b>
4.1	Reacting experiment .....	79
4.1.1	Outlet temperature profile .....	79
4.1.2	Qualitative data .....	80
4.1.3	Outlet velocity profile.....	83
4.2	Non-reacting experiment.....	84
4.2.1	Base case flowfield .....	84
4.2.2	Change in flow rate .....	105
4.2.3	Temporal indication.....	120
4.3	Wedge ring tests .....	124
4.3.1	Outlet temperature profile .....	124
4.3.2	Outlet velocity profile.....	129
<b>5</b>	<b>Conclusions.....</b>	<b>130</b>
5.1	Summary.....	130
5.2	Results .....	130
5.2.1	Reacting experiment .....	130
5.2.2	Non-reacting experiment.....	131
5.2.3	Wedge rings .....	132
5.3	Recommendations for future work .....	133
<b>6</b>	<b>References.....</b>	<b>134</b>
<b>Appendix A: Special Nomenclature .....</b>		<b>A-1</b>
<b>Appendix B: Air mass flow rate.....</b>		<b>B-1</b>
Orifice plate theory .....		B-2
<b>Appendix C: Manufacturing drawings .....</b>		<b>C-1</b>
Gas turbine combustor test case .....		C-2
Non-reacting experiment.....		C-2
Wedge ring tests .....		C-14
Reacting experiment .....		C-14
<b>Appendix D: Uncertainty analysis.....</b>		<b>D-1</b>
Theory .....		D-2
<b>Appendix E: Extended results .....</b>		<b>E-1</b>
Non-reacting experiment.....		E-1

---

## FIGURES

Figure 1: The wall jet can combustor used by Cameron <i>et al.</i> [14].....	4
Figure 2: The isothermal mean axial velocity field .....	5
Figure 3: The mean axial velocity field for a nozzle air/fuel ratio = 1.5 (Swirler, Pz, Dz = 25, 35, 40).....	5
Figure 4: The mean axial velocity field for a nozzle air/fuel ratio = 1.5 (Swirler, Pz, Dz = 45, 30, 25).....	5
Figure 5: The RMS axial velocity field for a nozzle air/fuel ratio = 1.5 (Swirler, Pz, Dz = 45, 30, 25).....	5
Figure 6: The mean azimuthal velocity field for a nozzle air/fuel ratio = 1.5 (Swirler, Pz, Dz = 45, 30, 25).....	5
Figure 7: The RMS azimuthal velocity field for a nozzle air/fuel ratio = 1.5 (Swirler, Pz, Dz = 45, 30, 25).....	5
Figure 8: The mean temperature field for a nozzle air/fuel ratio = 1.5 .....	6
Figure 9: The mean axial velocity field for a nozzle air/fuel ratio = 3.0 (Swirler, Pz, Dz = 45, 30, 25).....	6
Figure 10: The mean temperature field for a nozzle air/fuel ratio = 3.0 .....	6
Figure 11: A schematic representation of the hardware used by Eggels and Brown [6] .....	7
Figure 12: A photograph of the combustor used by Eggels and Brown [6].....	8
Figure 13: Axial measurement plane positions of velocity (LDA) and temperature measurements [6] .....	8
Figure 14: Comparison of experimental data and CFD results at a distance of 287 mm above the central injector [6] .....	9
Figure 15: A schematic view of the test plant by Carl <i>et al.</i> [8] .....	10
Figure 16: A cross-section of the combustor and pressure vessel [8] .....	10
Figure 17: CFD grid showing the combustor liner geometry [8].....	11
Figure 18: Gas velocity in the primary zone (a) AFR = 90 (b) AFR = 40 [8] .....	11
Figure 19: Side view of the combustor effusion cooling configuration (configuration 1) in Diers <i>et al.</i> [12].....	12
Figure 20: The position of the measurement planes in the effusion cooling set-up [12].....	13
Figure 21: Side view of the combustor impingement cooling configuration (configuration 2) in Diers <i>et al.</i> [12].....	13
Figure 22: Interpolated vector plot of measured velocities in the nozzle centre area of the effusion set-up [12].....	14
Figure 23: The position of the measurement planes in the impingement cooling set-up [12].....	14
Figure 24: Interpolated velocity vectors, axial velocity in colour scale and histograms with axial velocities in nozzle area (upper: positioned over primary zone cooling air orifice, lower: positioned over secondary air inlet hole) for the impingement set-up [12] .....	15
Figure 25: Experimental set-up including stereoscopic PIV arrangement used by Li and Gutmark [10].....	16
Figure 26: Velocity vectors and contours of axial velocity of the co- (304545) and counter- (3045C45) swirler set-ups [10] .....	17



Figure 27: Contours of $\frac{V_z}{V_0}$ , $\frac{V_\theta}{V_0}$ , and $\frac{k}{V_0^2}$ at $T_{inlet} = 23\text{ }^\circ\text{C}$ with mixing tube length at 0 mm and contraction ratio of 1 [11].....	18
Figure 28: Velocity profiles at $\frac{z}{R} = 0.5$ for $T_{inlet} = 23$ to $300\text{ }^\circ\text{C}$ a) $\frac{V_z}{V_0}$ b) $\frac{V_\theta}{V_0}$ [11] .....	18
Figure 29: A comparison of the temperature distribution for a mixing tube length of 0 and 0.5 mm [11] .....	19
Figure 30: Mandai and Nishida's combustor configuration and conditions for the diffusion flame combustor[7].....	20
Figure 31: Mandai and Nishida's combustor configuration and conditions for the premixed flame combustor [7].....	20
Figure 32: Longitudinal and cross-section of combustion chamber with coordinate system orientation used by Janus <i>et al.</i> [9].....	21
Figure 33: Radial profiles for $u$ , $v$ , $w$ and turbulent kinetic energy at $x = 1\text{ mm}$ for isothermal flow [9].....	22
Figure 34: A half-section streamline plot for isothermal flow [9].....	22
Figure 35: The superposition of the three OH layers with a 2D vector plot of the reacting flowfield [9] .....	23
Figure 36: A schematic diagram of the top view and the side view of the combustion chamber used by Archer and Gupta [5] .....	24
Figure 37: Illustration of the wind tunnel facility used for the combustor simulator experiments by Vakil and Thole [4].....	25
Figure 38: Layout and measurement planes for Vakil and Thole's combustor simulator (dimensions in cm) [4].....	25
Figure 39: Comparison of two- and three-component LDV profiles measured independently in an overlap location downstream of the first row of dilution holes [4].....	26
Figure 40: Flowfield vectors for Plane 2s, downstream of the second row of dilution jets [4].....	26
Figure 41: Thermal field contours for Plane 2s showing Lefebvre's jet penetration correlation [4] .....	27
Figure 42: A schematic diagram of the injector with combustion chamber and a photograph of the flame in Weigand <i>et al.</i> experiments [13] .....	27
Figure 43: Pressure oscillation compared with a pure sine function [13].....	28
Figure 44: A vector plot of the mean $uv$ -velocities. Zones with negative and positive $u$ velocities are marked red and blue, respectively (values mirrored for better visualisation) [13].....	28
Figure 45: Radial profiles of axial velocity (top) and circumferential velocity (bottom) for different phase angles at an axial position of 5 mm [13] .....	29
Figure 46: Contours of $u = 0\text{ m/s}$ for different phase angles indicating the changes of the inner recirculation zone during a pressure cycle (values mirrored for better visualisation) [13] .....	29
Figure 47: 2D temperature distribution from interpolation of single-point Raman measurements indicated by stars in ph1 image [13].....	30
Figure 48: An example calculation of $T_{4max}$ and $T_{4mr}$ .....	33
Figure 49: Scheimflüg stereoscopic arrangement (adapted from [19]).....	36
Figure 50: A backward-scatter camera location [19].....	36
Figure 51: A forward-scatter camera location [19] .....	37
Figure 52: A side-scatter camera location [19].....	37



---

Figure 53: A black and white calibration target [21] .....	38
Figure 54: A diagram showing the grid distortion due to camera perspective [19] .....	38
Figure 55: PIV software, Insight3G, showing the image correction using the calibration algorithm [22] .....	38
Figure 56: A timing diagram to show synchronisation of various events [23] .....	39
Figure 57: A timing diagram showing frame straddling [19] .....	40
Figure 58: Figure showing the cross-correlation method .....	41
Figure 59: A basic vector calculation procedure for particle tracking.....	42
Figure 60: Diagram showing the calculation of the velocity vector [19] .....	43
Figure 61: A particle image for PIV analysis in the primary zone of the can-type combustor.....	43
Figure 62: A cross-correlation diagram with one dominant peak set [19] .....	44
Figure 63: Diagram showing the resolving of the out-of-plane vector [24].....	44
Figure 64: The combustor test rig .....	47
Figure 65: A schematic diagram of the combustor test rig .....	48
Figure 66: A close-up of the fuel system .....	49
Figure 67: A close-up of the combustor liner.....	49
Figure 68: A dimensional drawing of the annular swirler (dimensions are in mm).....	50
Figure 69: A dimensional drawing of the metal combustor liner (dimensions are in mm) .....	51
Figure 70: The five K-type thermocouples in a rake at the combustor outlet.....	51
Figure 71: The data acquisition system and computer used for thermocouple measurements .....	52
Figure 72: A magnetic clamp holds the Pitot tube onto the test rig in the correct position .....	52
Figure 73: The transparent combustor parts - casing, liner and outlet pipe.....	53
Figure 74: The transparent test section assembly .....	54
Figure 75: The transparent test section attached to the combustor test rig in the PIV laboratory .....	55
Figure 76: The 30% (left) and 10% (right) primary and secondary zone wedge rings.....	56
Figure 77: An assembly drawing with cut-out section showing the 30% wedge rings inside the combustor .....	56
Figure 78: The 30% wedge rings installed into the combustor liner .....	57
Figure 79: A schematic diagram of the PIV equipment set-up.....	60
Figure 80: The top and bottom camera images of the calibration target .....	60
Figure 81: Frame A and Frame B taken with the top camera .....	61
Figure 82: A two-dimensional vector plot calculated using the cross-correlation .....	61
Figure 83: The angles showing the positions of the planes in between the holes .....	62
Figure 84: A sparsely populated vector field viewed from the side superimposed on an image of the primary zone.....	64

---



---

Figure 85: Photographs of the corresponding constructions on the combustor that caused the lack of relevant vectors in Figure 86 .....	65
Figure 86: The three-dimensional vectors in the primary zone viewed from the side .....	65
Figure 87: The three-dimensional vectors in the primary zone viewed from the side with the main combustor flow features outlined.....	66
Figure 88: The three-dimensional vectors in the primary zone viewed from the side with the more subtle flow features outlined.....	67
Figure 89: The axial velocity profiles at selected slices along the primary zone length.....	68
Figure 90: The three-dimensional vectors viewed from the left (upstream) .....	69
Figure 91: The three-dimensional vectors viewed from the left (upstream) with the vectors below $Y = 3 \text{ mm}$ removed .....	70
Figure 92: The azimuthal velocity (z-component) profiles at selected slices along the primary zone length.....	71
Figure 93: Contour map of the velocity magnitude in the primary zone.....	72
Figure 94: Contour map of the CHC number for each interrogation region .....	73
Figure 95: A typical primary zone configuration [15].....	74
Figure 96: Lucas primary zone air flow pattern [15].....	74
Figure 97: Recirculation region in a swirling flowfield [15] .....	74
Figure 98: Typical profiles of axial and swirl velocity components in a strongly swirling flow [15].....	74
Figure 99: Typical combustion chamber flow schematic diagram and values [27].....	75
Figure 100: Comparison of the velocity profiles after the outlet of the test rig .....	76
Figure 101: A comparison between the experimental and simulated outlet temperature profile .....	80
Figure 102: The flame photos viewed from straight downstream and from angles of 0, 90, 180 and 270° .....	81
Figure 103: Carbon deposits on the liner walls viewed from straight downstream and from angles of 0, 90, 180 and 270° .....	82
Figure 104: The outlet velocity profile comparison for the base case set-up.....	83
Figure 105: Isometric view of the combustor liner showing the velocity magnitude contours and streamlines in line with the holes.....	87
Figure 106: Normal view of the combustor liner showing the velocity magnitude contours and streamlines in line with the holes.....	88
Figure 107: Normal view of the combustor liner showing the sparse velocity vectors in line with the holes .....	89
Figure 108: Normal view of the combustor liner showing the velocity vectors in line with the holes .....	90
Figure 109: The axial velocity profiles at various positions in the plane in line with the holes.....	91
Figure 110: The radial velocity profiles at various positions in the plane in line with the holes .....	92
Figure 111: The azimuthal velocity profiles at various positions in the plane in line with the holes.....	93
Figure 112: Normal view of the combustor liner showing the CHC contours in line with the holes .....	94

---



Figure 113: Isometric view of the combustor liner showing the velocity magnitude contours and streamlines in between the holes .....	96
Figure 114: Normal view of the combustor liner showing the velocity magnitude contours and streamlines in between the holes .....	97
Figure 115: Normal view of the combustor liner showing the velocity vectors in between the holes .....	98
Figure 116: Normal view of the combustor liner showing the velocity vectors in between the holes .....	99
Figure 117: The axial velocity profiles at various positions in the plane in between the holes of the respective zones.....	100
Figure 118: The radial velocity profiles at various positions in the plane in between the holes of the respective zones.....	101
Figure 119: The azimuthal velocity profiles at various positions in the plane in between the holes of the respective zones.....	102
Figure 120: Normal view of the combustor liner showing the CHC contours in between the holes .....	103
Figure 121: A comparison of the flow in line with the holes and in between the holes of all the zones .....	105
Figure 122: A comparison of the velocity magnitude and streamlines in line with the holes at a) $\dot{m}_A = 0.056$ kg/s, b) $\dot{m}_A = 0.070$ kg/s and c) $\dot{m}_A = 0.091$ kg/s.....	112
Figure 123: A comparison of the sparse velocity vectors in line with the holes at a) $\dot{m}_A = 0.056$ kg/s, b) $\dot{m}_A = 0.070$ kg/s and c) $\dot{m}_A = 0.091$ kg/s.....	113
Figure 124: A comparison of the velocity vectors in line with the holes at a) $\dot{m}_A = 0.056$ kg/s, b) $\dot{m}_A = 0.070$ kg/s and c) $\dot{m}_A = 0.091$ kg/s.....	114
Figure 125: A comparison of the axial velocity profiles in line with the holes at a) $\dot{m}_A = 0.056$ kg/s, b) $\dot{m}_A = 0.070$ kg/s and c) $\dot{m}_A = 0.091$ kg/s.....	115
Figure 126: A comparison of the radial velocity profiles in line with the holes but excluding the jets at a) $\dot{m}_A = 0.056$ kg/s, b) $\dot{m}_A = 0.070$ kg/s and c) $\dot{m}_A = 0.091$ kg/s .....	116
Figure 127: A comparison of the radial velocity profiles in line with the holes at the jets at a) $\dot{m}_A = 0.056$ kg/s, b) $\dot{m}_A = 0.070$ kg/s and c) $\dot{m}_A = 0.091$ kg/s .....	117
Figure 128: A comparison of the azimuthal velocity profiles in line with the holes at a) $\dot{m}_A = 0.056$ kg/s, b) $\dot{m}_A = 0.070$ kg/s and c) $\dot{m}_A = 0.091$ kg/s .....	118
Figure 129: A comparison of the velocity vectors in line with the holes at a) $\dot{m}_A = 0.056$ kg/s, b) $\dot{m}_A = 0.070$ kg/s and c) $\dot{m}_A = 0.091$ kg/s.....	119
Figure 130: The average maximum and minimum temperatures for each experimental set-up .....	126
Figure 131: The average overall pressure loss for each experimental set-up .....	127
Figure 132: The average pressure loss factor for each experimental set-up.....	127
Figure 133: The average pattern factor for each experimental set-up.....	128
Figure 134: The average profile factor for each experimental set-up .....	128
Figure 135: The outlet velocity profile comparison for each experimental set-up.....	129
Figure B.1: A generalised Bernoulli obstruction meter [B.1] .....	B-3
Figure C.1: The machining drawing of the casing .....	C-2
Figure C.2: The machining drawing of the upstream casing flange .....	C-3



---

Figure C.3: The machining drawing of the downstream casing .....	C-3
Figure C.4: The machining drawing of the combustor liner dome.....	C-4
Figure C.5: The machining drawing of the combustor liner primary zone.....	C-4
Figure C.6: The machining drawing of the combustor liner secondary zone .....	C-5
Figure C.7: The machining drawing of the combustor liner dilution zone .....	C-5
Figure C.8: The machining drawing of the outlet section flange .....	C-6
Figure C.9: The machining drawing of the outlet pipe.....	C-6
Figure C.10: The casing assembly drawing .....	C-7
Figure C.11: The final casing tube after parting off .....	C-8
Figure C.12: The assembly drawing of the perspex combustor liner .....	C-8
Figure C.13: The final combustor liner dome after parting off.....	C-9
Figure C.14: The final combustor liner primary zone after parting off.....	C-9
Figure C.15: The final combustor liner secondary zone after parting off .....	C-10
Figure C.16: The final combustor liner dilution zone after parting off .....	C-10
Figure C.17: The assembly drawing of the outlet section .....	C-11
Figure C.18: The final outlet pipe after parting off.....	C-11
Figure C.19: The assembly drawing of the target and mirror holder.....	C-12
Figure C.20: Manufacturing drawing of the calibration target .....	C-13
Figure C.21: Manufacturing drawing of the mirror holder.....	C-13
Figure C.22: Assembly drawing of the metal combustor liner.....	C-14
Figure C.23: The 30% primary wedge ring.....	C-15
Figure C.24: The 30% secondary wedge ring .....	C-15
Figure C.25: The 10% primary wedge ring.....	C-16
Figure C.26: The 10% secondary wedge ring .....	C-16
Figure D.1: The propagation of errors into an experimental result (adapted from [D.3]) .....	D-4
Figure E.1: The top primary zone vector field at $t = 1\ 188\ 625\ 000\ \mu\text{s}$ .....	E-1
Figure E.2: The top primary zone vector field at $t = 1\ 190\ 125\ 000\ \mu\text{s}$ (+ $1\ 500\ 000\ \mu\text{s}$ from Figure E.1).....	E-2
Figure E.3: The top primary zone vector field at $t = 1\ 191\ 625\ 000\ \mu\text{s}$ (+ $1\ 500\ 000\ \mu\text{s}$ from Figure E.2).....	E-3
Figure E.4: The top primary zone vector field at $t = 1\ 193\ 328\ 125\ \mu\text{s}$ (+ $1\ 703\ 125\ \mu\text{s}$ from Figure E.3).....	E-4
Figure E.5: The top primary zone vector field at $t = 1\ 195\ 031\ 250\ \mu\text{s}$ (+ $1\ 703\ 125\ \mu\text{s}$ from Figure E.4).....	E-5
Figure E.6: The top primary zone vector field at $t = 1\ 196\ 531\ 250\ \mu\text{s}$ (+ $1\ 500\ 000\ \mu\text{s}$ from Figure E.5).....	E-6
Figure E.7: The bottom secondary zone vector field at $t = 1\ 088\ 437\ 500\ \mu\text{s}$ .....	E-7
Figure E.8: The bottom secondary zone vector field at $t = 1\ 089\ 937\ 500\ \mu\text{s}$ (+ $1\ 500\ 000\ \mu\text{s}$ from Figure E.7) .....	E-8

---



---

Figure E.9: The bottom secondary zone vector field at $t = 1\,091\,437\,500\ \mu\text{s}$ (+ $1\,500\,000\ \mu\text{s}$ from Figure E.8) .....	E-9
Figure E.10: The bottom secondary zone vector field at $t = 1\,092\,937\,500\ \mu\text{s}$ (+ $1\,500\,000\ \mu\text{s}$ from Figure E.9) .....	E-10
Figure E.11: The bottom secondary zone vector field at $t = 1\,094\,640\,625\ \mu\text{s}$ (+ $1\,703\,125\ \mu\text{s}$ from Figure E.10) .....	E-11
Figure E.12: The bottom secondary zone vector field at $t = 1\,096\,046\,875\ \mu\text{s}$ (+ $1\,406\,250\ \mu\text{s}$ from Figure E.11) .....	E-12
Figure E.13: The bottom dilution zone vector field at $t = 1\,105\,406\,250\ \mu\text{s}$ .....	E-13
Figure E.14: The bottom dilution zone vector field at $t = 1\,106\,703\,125\ \mu\text{s}$ (+ $1\,296\,875\ \mu\text{s}$ from Figure E.13) .....	E-14
Figure E.15: The bottom dilution zone vector field at $t = 1\,108\,203\,125\ \mu\text{s}$ (+ $1\,500\,000\ \mu\text{s}$ from Figure E.14) .....	E-15
Figure E.16: The bottom dilution zone vector field at $t = 1\,109\,906\,250\ \mu\text{s}$ (+ $1\,703\,125\ \mu\text{s}$ from Figure E.15) .....	E-16
Figure E.17: The bottom dilution zone vector field at $t = 1\,111\,406\,250\ \mu\text{s}$ (+ $1\,500\,000\ \mu\text{s}$ from Figure E.16) .....	E-17
Figure E.18: The bottom dilution zone vector field at $t = 1\,112\,906\,250\ \mu\text{s}$ (+ $1\,500\,000\ \mu\text{s}$ from Figure E.17) .....	E-18



## TABLES

Table 1: The comparison of results from Cameron <i>et al.</i> [14] .....	5
Table 2: The experimental test matrix for the reacting experiments .....	46
Table 3: The experimental test matrix for the PIV experiments .....	46
Table 4: Pressure drop over orifice plate and corresponding air mass flow rate .....	63
Table 5: The uncertainties of the various pieces of equipment used .....	77
Table 6: The experimental test matrix for the reacting experiments .....	79
Table 7: The normalised temperature results for the base case .....	80
Table 8: The experimental test matrix for the PIV experiments .....	84
Table 9: Comparison of velocity magnitude contours and stream lines in the primary zone as the air mass flow rate is increased from 0.056 to 0.091 kg/s .....	107
Table 10: Comparison of sparse velocity vectors in the primary zone as the air mass flow rate is increased from 0.056 to 0.091 kg/s .....	108
Table 11: Comparison of velocity vectors in the primary zone as the air mass flow rate is increased from 0.056 to 0.091 kg/s .....	109
Table 12: Comparison of CHC values in the primary zone as the air mass flow rate is increased from 0.056 to 0.091 kg/s .....	110
Table 13: The primary zone vectors at the top recirculation zone at times starting at $t = 1\ 188\ 625\ 000\ \mu\text{s}$ to $t = 1\ 196\ 531\ 250\ \mu\text{s}$ .....	121
Table 14: The primary zone vectors at the bottom jet region at times starting at $t = 1\ 188\ 625\ 000\ \mu\text{s}$ to $t = 1\ 196\ 531\ 250\ \mu\text{s}$ .....	122
Table 15: The primary zone vectors at the reverse flow region at times starting at $t = 1\ 188\ 625\ 000\ \mu\text{s}$ to $t = 1\ 196\ 531\ 250\ \mu\text{s}$ .....	123
Table 16: The experimental test matrix for the reacting experiments .....	124
Table 17: The normalised temperature results for the no wedge ring case .....	124
Table 18: A comparison of the normalised outlet temperature profiles for the seven configurations .....	125



## NOMENCLATURE

The nomenclature and abbreviations for Section 2.1 are given in Appendix A.

Technical characters:

$\dot{m}$	Mass flow rate
$\bar{T}$	Mean temperature
$\infty$	Infinite

Greek characters:

$\alpha$	The angle measured from the right horizontal on the outlet plane
$\Delta$	Change in a value
$\phi$	Diameter or equivalence ratio
$\eta$	Effectiveness
$\rho$	Density

Latin characters:

A	Frame A vector
a	Length of Vector A
B	Frame B vector
b	Length of Vector B
D	Diameter
f	Motor controller frequency
G	The elements of the cross-correlation result
Gm	Axial flux of angular momentum
Gt	Axial thrust
M	Magnification factor
m	Mass
n	The number of divisions in the diameter
P	Total pressure
p	Static pressure
q	Dynamic pressure
R	Radius
r	Radius
R <sub>AB</sub>	Cross-correlation vector
Sn	Swirl number
s	The number of elements a particle moved
T	Temperature
t	Time
U	Axial velocity or in plane velocity
u	Velocity



---

V	Radial Velocity
W	Tangential velocity or through-plane velocity
X	Axial distance or perceived distance in the $x$ -direction
x	Radial distance or actual distance in the $x$ -direction
Y	Radial distance or perceived distance in the $y$ -direction
y	Axial distance or actual distance in the $y$ -direction
Z	Radial/tangential distance
z	Radial/tangential distance
Superscripts:	
'	A padded vector for cross-correlation
Subscripts:	
0	The position of the original bright pixel in Frame A
1	Referring to upstream of the orifice plate or time in Frame A
3	Referring to combustor inlet
4	Referring to combustor outlet
A	Referring to air
AFT	Adiabatic flame temperature
atm	Referring to atmospheric values
cs	Referring to a cross-section
F	Referring to fuel
i	Indices
j	Indices
k	Indices
L	Referring to the combustor liner
m	momentum
max	Maximum
min	Minimum
mr	Maximum mean value of all points at a common radius
O	Referring to the orifice plate
r	Mean value of all points at a common radius
s	Referring to the new particle position
sw	Swirler
t	Thrust
x	Referring to the horizontal velocity component
y	Referring to the vertical velocity component

---



## ABBREVIATIONS

3D	Three-dimensional
2D	Two-dimensional
AFR	Air/Fuel ratio
Av	Average
B	Referring to the bottom camera
CCD	Charge-coupled device
CFD	Computational fluid dynamics
CFR	Compact folded resonator
CHC	Choice code
CNC	Computer numerical control
Cont.	Continued
CSIR	Council for scientific and industrial research
Dz	Dilution zone
f-ratio	Focal length divided by the effective aperture diameter
ICE	Integrated cooling and electronics
ID	Inner diameter
ISO	A measure of the digital camera sensor light sensitivity
JP-4	Jet propellant 4
LDA	Laser Doppler anemometry
LDV	Laser Doppler velocimetry
LES	Large eddy simulation
MAX	Maximum value
MEAN	Mean value
MIN	Minimum value
NC	No combustion
Nd:YAG	Neodymium (-doped): yttrium aluminium garnet
PIV	Particle image velocimetry
PLIF	Planar laser-induced Fluorescence
Pz	Primary zone
RANS	Reynolds-averaged Navier-Stokes
Sn	Swirl number
Sz	Secondary zone
T	Referring to the top camera
TTL	Transistor-transistor logic
Vel	Velocity
Vel Mag	Velocity magnitude
WR	Wedge rings

# 1 INTRODUCTION

## 1.1 Background

During previous years, a number of different experiments have been performed using the experimental can-type combustor test rig at the University of Pretoria (currently at the CSIR) [1,2,3]. Problems became evident when comparing computational fluid dynamics (CFD) simulations to the actual experimental results obtained. It is a general problem that there are many inconsistencies between experimental work and CFD solutions [4,5]. Combustion CFD solutions often compare poorly with experimental values owing to inaccuracies in both flow modelling as well as combustion modelling. This makes CFD a less reliable tool for combustor design. The solution to this is not a simple one and thus a start to enabling the use of CFD for combustor design would be to create an experimental test case for CFD solution validation.

Further, during the course of the previous experiments in this combustor test rig, which entailed a variety of variables being modified and tested, the outlet temperature profile obtained was undesirable. For all variables modified, the outlet temperature profile consistently had a colder core and hotter perimeter, which is the opposite profile to that which one would expect. For turbine design, the assumed temperature profile is usually flat or parabolic with the hottest temperature in the centre.

## 1.2 Problem statement

CFD modelling is a cheap tool, in comparison with experimentation [6,7], however, there are still problems with using CFD for the design and optimisation of gas turbine combustors and experimentation is still to a great extent needed in the design process [6,7,8,9]. In combustor modelling, the accuracy of the reacting (combusting) runs is heavily dependent on the turbulence model used [4,7,10]. For reasonably accurate results, the large eddy simulation (LES) turbulence model can be used but, due to the required grid size, this takes a large amount of time and computing power [7,11]. In addition, if one wants to optimise a design using CFD, then fast runs are required due to the amount of runs required for the optimisation process. In most cases, a form of Reynolds-averaged Navier-Stokes (RANS) simulations with a turbulence model is used [6]. The problem with these models is that they often can either resolve swirling flow or jets in cross-flow but not both to the required accuracy for good combustion results.

Due to the CFD shortfalls, experimental data on combustors is required for multiple reasons [4,5,6,7,12]:

- to obtain insight into the mechanisms of the flow in order to choose more appropriate models before performing numerical runs;
- to compare results in order to test and validate current, new and modified models, which are introduced to CFD software [5,6,8,13];
- and to see what the actual flaws in the models are and to determine which features are over- or underpredicted or not predicted at all.

This dissertation contains the results of steady-state experiments on an experimental can-type forward flow combustor. The data reported for the non-reacting (non-combusting or isothermal) flow is the three-dimensional flowfield. For the reacting (combusting) flow, the outlet temperature profile, the outlet velocity profile as well as qualitative data are reported.

This data can be used for comparison with CFD runs for this combustor geometry, as well as form a basis of a test case for other combustor work. As a test case, the data can be used by the modeller to adjust various coefficients and variables as well as the weighting of dual turbulence model runs.

In addition to the test case created, passive inserts will be tested to attempt to even out uneven outlet temperature profiles with high gradients, which are specific to this combustor.

### 1.3 A brief review of existing knowledge

In the past, other data sets have been collected for the purpose of CFD validation and improvement. There are, however, various similarities and differences in the experimental set-ups used both in this study and those performed by others.

Various combustor configurations as well as a variety of conditions have been used to create experimental data sets. The data sets have been varied according to the air supply characteristics, the presence of a combustion reaction (reacting flow) or not (non-reacting or isothermal flow), the fuel type and delivery in the reaction, the outlet configuration as well as the physical geometry of the combustor. Various methods were also used to collect the data, which then also determined the type, quality and quantity of experimental results available.

For flowfield measurements the two main methods used for data collection in combustors are laser Doppler velocimetry (LDV) and particle image velocimetry (PIV). LDV is a point-wise technique and thus many measurements are required to plot the velocity field or the velocities along a line. PIV, on the other hand, is a planar technique and thus the velocity field can be obtained for a larger area more easily than, but not as accurately as, LDV.

Two-dimensional LDV or LDA was used to plot the two-dimensional velocity fields at various positions in the experiments conducted by Vakil and Thole [4], Eggels and Brown [6], Carl *et al.* [8] and Cameron *et al.* [14]. In the experiments performed by Janus *et al.* [9], a double set of two-dimensional LDA was used to obtain the three-dimensional velocities along a cross-section of a can-type combustor at various axial positions. A two-dimensional velocity field was also obtained in the recirculation zone of the combustor.

Archer and Gupta [5] and Li and Gutmark [11] used a three-dimensional PIV system to plot the axial velocity field over an area in the recirculation zone and the axial and tangential velocities along various cross-sectional diameters. Full three-dimensional velocity fields on a plane in the recirculation zone were measured and plotted by Li and Gutmark [10].

For thermal field measurements, the most common method used is thermocouples. Li and Gutmark [11] and Eggels and Brown [6] used thermocouples to measure the temperature profile along various radii within the combustor. Cameron *et al.* [14] measured the temperature profiles on various diameters along the length of a can-type combustor showing some asymmetry in the profiles. Finally, a planar thermal field was measured using thermocouples and a two-dimensional traverse in work done by Diers *et al.* [12].

Weigand *et al.* [13] used point-wise laser Raman scattering to obtain the thermal field in a combustor in a non-intrusive way. The 48 points taken were interpolated to show a planar thermal field in one half of a can-type combustor.

Various experiments were done with both preheating and pressurised inlet air conditions [8,9,11], while others had been done with only preheating [7,12,14] of the inlet air. Experiments were also done with the inlet air at atmospheric conditions [6,13]. Both premixed [7,8,10,11,13] and diffusion (non-premixed) [5,7,9,14] inlets were used. Some of the inlet set-ups were variable and their effect on the combustor performance was tested such as in the work done by Li and Gutmark [10] and Cameron *et al.* [14].

Some flowfield data was collected in experiments with no reactions taking place. These experiments showed the effect of varying set-ups on the flow conditions [4,10]. A number of the experiments consisted of both non-reacting and reacting data. For some papers, flowfield data was collected in both the reacting and non-reacting set-ups [5,6,8,9,11,14], while for others, the flowfield was only captured in the reacting set-up [7,12,13]. In order to perform the reacting experiments, a variety of fuels have been used, e.g. natural gas [6,7,9,11], methane [13], propane [5], kerosene [8] and JP-4 [14].

Of the combustor experiments that were meant to be used for can-type combustor comparison, some only included the swirler with no primary, secondary, dilution or cooling holes [5,9,10,11,13]. Some of the experiments had a swirler and one set of holes [6,7]. There were experiments that had circular liner shapes [6,7,10], but more of the liners seem to be approximations of a circular liner such as octagonal [11], rectangular or square [5,13] or circular with flat windows inserted [9,14].

Other combustor experiments were done on sectors of annular combustors. Vakil and Thole [4] collected data in a combustor sector that consisted only of cooling and dilution holes (no swirler), while Diers *et al.* [12] tested different cooling hole methods and their experiment included two sets of holes but also had no swirler. Carl *et al.* [8] had an annular combustor sector which consisted of four swirlers, three sets of holes and an

exit contraction thus representing the most complete combustor in terms of including all the factors influencing the flow inside the combustor as well as reacting flow. However, the two-dimensional LDA data was only taken in the recirculation zone. Cameron *et al.* [14] had an almost complete can-type combustor with a swirler and two sets of holes at two axial positions along the length of the combustor. This combustor was, however, not fully round and had some flat windows on the sides. For both the combustors by Carl *et al.* [8] and Cameron *et al.* [14] there was an absence of cooling holes and the data collected was not for the entire combustor. Carl *et al.* [8] acquired mostly velocity data in the primary zone whereas Cameron *et al.* [14] had seven cross-sections on which two velocity components and temperatures were collected.

## 1.4 Research objectives

The purpose of this study was to collect data on a complete can-type combustor that could be used to validate CFD results so that CFD can be used as a reliable design tool for gas turbine combustors. The design of a combustor could entail simulations in order to prove or test a specific combustor set-up or the optimisation of a preliminary design [5,7,9]. The data could also be used as a test case for CFD models.

In most CFD cases, a non-reacting (isothermal) run is done first in order to ensure that the turbulence model is predicting the flowfield and the position of the important flow phenomena correctly [4,7]. This step is important because the combustion characteristics and the correctness of the reacting (combusting) flow results are dependent on the flow characteristics [5,11]. The flowfield within an atmospheric pressure gas turbine combustor was measured using a stereoscopic PIV system in order to validate this step in the modelling process.

Once the non-reacting flow has been modelled satisfactorily, the reacting flow can then be modelled. In order to validate the results of a reacting run, the temperature field was measured. The outlet temperature profile was obtained using a thermocouple rake. The outlet temperature profile also provided a means of testing the influence of the passive inserts.

Similar to Carl *et al.* [8] and Cameron *et al.* [14], attempts had to be made to ensure that as many of the factors that influence the combustor flow were included in the tests. In this case, a full circular cylindrical can-type combustor, with swirler, primary, secondary and dilution holes as well as the cooling holes present in both the metal reacting combustor and the perspex flow visualisation combustor, was tested.

## 1.5 Scope of the study

For this study, the first aim was to obtain a three-dimensional flowfield inside a fully representative can-type forward flow experimental combustor. The combustor was run at atmospheric conditions with the air flow supplied from a fan and the outlet was straight to atmosphere.

A stereoscopic particle image velocimetry (PIV) system was used to obtain the time-averaged flowfield of the combustor in the non-reacting condition. Three dimensional velocity data was collected on planes in line with the holes and in between the holes of the three zones of the combustor. The PIV data was collected for the purpose of validating numerical simulations on non-reacting combustor flows. In order for these measurements to be taken, an optically accessible combustor, with the same geometry as the reacting combustor, was manufactured.

For reacting flows, the temperature profile at the outlet plane of the combustor was measured using a thermocouple rake consisting of five K-type thermocouples spanning the radius of the combustor outlet. The thermocouple rake was rotated around the outlet to obtain the full outlet temperature profile. Velocity profiles at the exit both with and without combustion were measured with a Pitot tube for comparison with the PIV data. For insight purposes, photographs were taken of the flames during combustion of one of the thermal experiments as well as of carbon deposits on the walls of the combustor after a specialised experiment was performed.

The reacting experiments also included testing the influence of the passive inserts. These inserts were manufactured during the course of this project.

## 2 LITERATURE STUDY

Please note that the nomenclature and abbreviations for Section 2.1 are given in Appendix A. The reason is that a large number of figures were scanned from literature and on these figures, in many cases, are nomenclature that are not directly relevant to this study or are in conflict with other figures.

### 2.1 Previous work

In 1989, Cameron *et al.* [14] performed velocity and temperature measurements of a model gas turbine combustor. The velocities were measured in an isothermal and reacting set-up. This data was a start to a database that was to be used for the study of interactions and influences of certain characteristics of a practical combustor. The combustor was a can-type combustor with four flat optical windows inserted at 90° intervals for optical access. The combustor had an annular swirler in the dome section with an injector for the fuel (JP-4) in the centre of the swirler. All the air entering the combustor was preheated to 100 °C. The liner had two sets of holes along the length, 4 x 7 mm primary holes at one combustor diameter downstream and 4 x 9.5 mm holes at two combustor diameters downstream from the nozzle. A drawing of the combustor is shown in Figure 1. The outlet of the combustor was open to atmosphere.

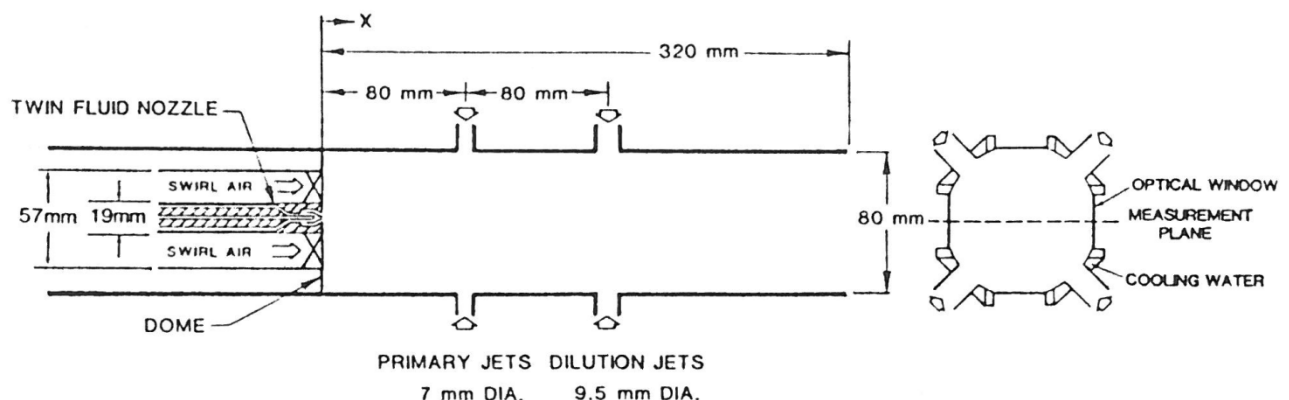


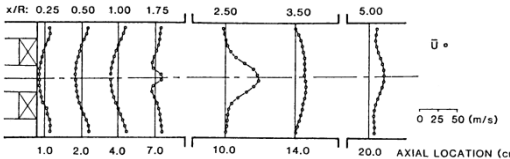
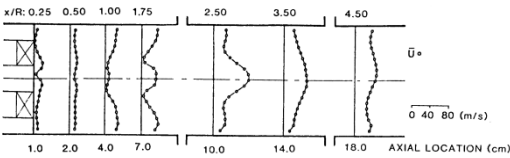
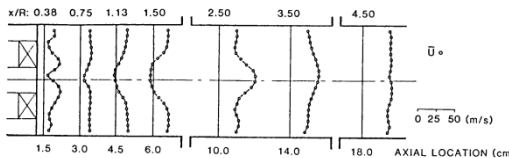
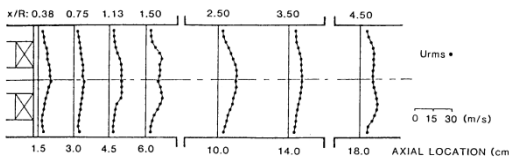
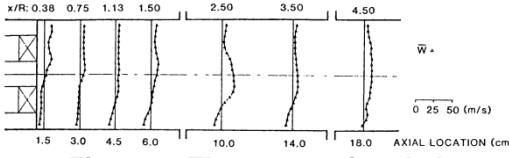
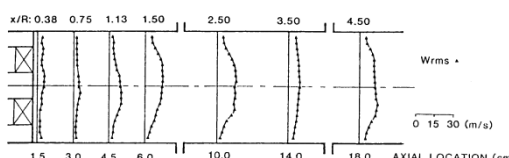
Figure 1: The wall jet can combustor used by Cameron *et al.* [14]

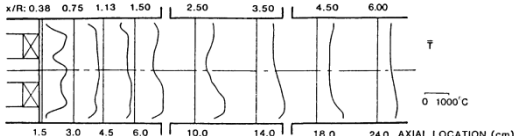
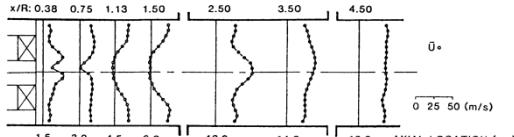
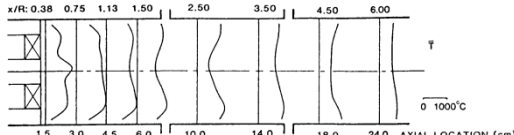
Certain of the parameters were varied to observe trends in the measured fields. The variables were the nozzle air/fuel ratio (AFR) and the flow splits to the various inlets. The nozzle AFR was infinite (no fuel) for the isothermal condition and then set at 1.5 and 3.0 for the reacting condition. The flow splits were initially at 25% to the swirler, 35% to the primary holes and 40% to the dilution holes for the isothermal and first reacting test with AFR = 1.5. The flow splits were then modified to the swirler, primary holes and dilution holes receiving 45%, 30% and 25%, respectively, to restore the on-axis recirculation zone. The measurements were taken across diameters of the combustor at  $\frac{x}{R}$  values (axial positions) of 0.25 (flow splits = 25, 35, 40 only), 0.38 (flow splits = 45, 30, 25 only), 0.50, 1.0, 1.75, 2.50, 3.50, (all tests) 4.50 (reacting tests only), 5.0 (isothermal test only) and 6.0 (temperature measurements only). A two-component (dual-beam) laser anemometer was used to measure the axial and azimuthal velocities at the measurement positions. The flow was seeded using 1  $\mu\text{m}$  alumina powder. The mean and rms velocity values at various test conditions are presented in Table 1. The temperature fields at the measurement positions were measured using a cooled R-type thermocouple (see Table 1).

The results shown in Figure 2 and Figure 3, show that the introduction of combustion without varying the flow splits caused the recirculation zone to move off axis. Due to a slight asymmetry in the fuel injection, the velocity profile was asymmetrical until  $\frac{x}{R} = 0.5$  but became more symmetrical as the flow progressed along the combustor. At  $\frac{x}{R} = 2.5$  to 3.5, the velocity profiles remained the same shape but the velocity magnitude

was higher with combustion (Figure 3). When comparing Figure 3 with Figure 4, the recirculation zone was moved back on axis due to the increase of swirler flow. The weakening of the dilution jets aided in a more uniform velocity profile at the outlet of the combustor. Figure 6 shows the azimuthal velocities of the flow indicating the presence of swirling motion.

**Table 1: The comparison of results from Cameron *et al.* [14]**

<p>Flow splits % (Swirler, Pz, Dz) →</p>	<p>25, 35, 40</p>	<p>45, 30, 25</p>
<p>Nozzle AFR ↓</p>		
<p>∞ (Isothermal)</p>	 <p><b>Figure 2: The isothermal mean axial velocity field</b></p>	
<p>1.5</p>	 <p><b>Figure 3: The mean axial velocity field for a nozzle air/fuel ratio = 1.5 (Swirler, Pz, Dz = 25, 35, 40)</b></p>	 <p><b>Figure 4: The mean axial velocity field for a nozzle air/fuel ratio = 1.5 (Swirler, Pz, Dz = 45, 30, 25)</b></p>  <p><b>Figure 5: The RMS axial velocity field for a nozzle air/fuel ratio = 1.5 (Swirler, Pz, Dz = 45, 30, 25)</b></p>  <p><b>Figure 6: The mean azimuthal velocity field for a nozzle air/fuel ratio = 1.5 (Swirler, Pz, Dz = 45, 30, 25)</b></p>  <p><b>Figure 7: The RMS azimuthal velocity field for a nozzle air/fuel ratio = 1.5 (Swirler, Pz, Dz = 45, 30, 25)</b></p>

Flow splits % (Swirler, Pz, Dz) (Continued) →	25, 35, 40 (Continued)	45, 30, 25 (Continued)
Nozzle AFR (Continued) ↓		
1.5		 <p><b>Figure 8: The mean temperature field for a nozzle air/fuel ratio = 1.5</b></p>
3.0		 <p><b>Figure 9: The mean axial velocity field for a nozzle air/fuel ratio = 3.0 (Swirler, Pz, Dz = 45, 30, 25)</b></p>  <p><b>Figure 10: The mean temperature field for a nozzle air/fuel ratio = 3.0</b></p>

The temperature profiles measured for a nozzle AFR = 1.5 are shown in Figure 8. At  $\frac{x}{R} = 0.38$ , the asymmetrical temperature profile shows that there is asymmetry in the fuel spray. The temperature distribution then becomes relatively uniform until  $\frac{x}{R} = 1.50$  where new asymmetry shows evidence of a hot streak below the centreline. At  $\frac{x}{R} = 6.00$ , the temperature profile has become more uniform and there is little evidence of the hot streak.

Increasing the nozzle AFR gave an increase in the velocity magnitudes (see Figure 9) in the primary zone with an improvement in the flame composition (removal of yellow streaks). The temperature profile in Figure 10 shows that the asymmetry is still present near the nozzle but the hot streak effect was diminished and the temperature profile was relatively uniform through the last half of the combustor.

The conclusions determined by Cameron *et al.* [14] showed that the recirculation zone was formed only by the swirling flow and that primary jets only provided closure to the recirculation zone. It was also concluded that the introduction of the combustion affected the position of the recirculation zone. In this case, increasing the nozzle AFR helped to create a more symmetrical temperature profile especially after the primary jets.

In 2001, Eggels and Brown [6] obtained flowfield data for non-reacting and reacting flow as well as thermal measurements for reacting flow in an industrial combustor. This data was then compared with computational fluid dynamics (CFD) simulations of the same combustor. The combustor liner was made of two quartz glass tubes joined by a metal cone with square inlet ports for the inlet of secondary air (see Figure 11 and Figure 12). The fuel/air flow entering at the primary zone entered through a counter-swirl inlet. This liner was inside an air plenum that had quartz windows for optical access to the transparent liner. The combustor outlet was open to the atmosphere so the tests were not pressurised.

The velocity measurements were performed using two-component laser Doppler anemometry (LDA) on both reacting and non-reacting flows. The flow was seeded with 1  $\mu\text{m}$  alumina particles using a high volume

seeder. Measurements were taken on certain cross-sections as shown in Figure 13. The axial and radial velocity components were measured and reported alongside the CFD results. Thermal measurements were taken for the reacting flow using an unexposed K-type thermocouple surrounded by a water jacket.

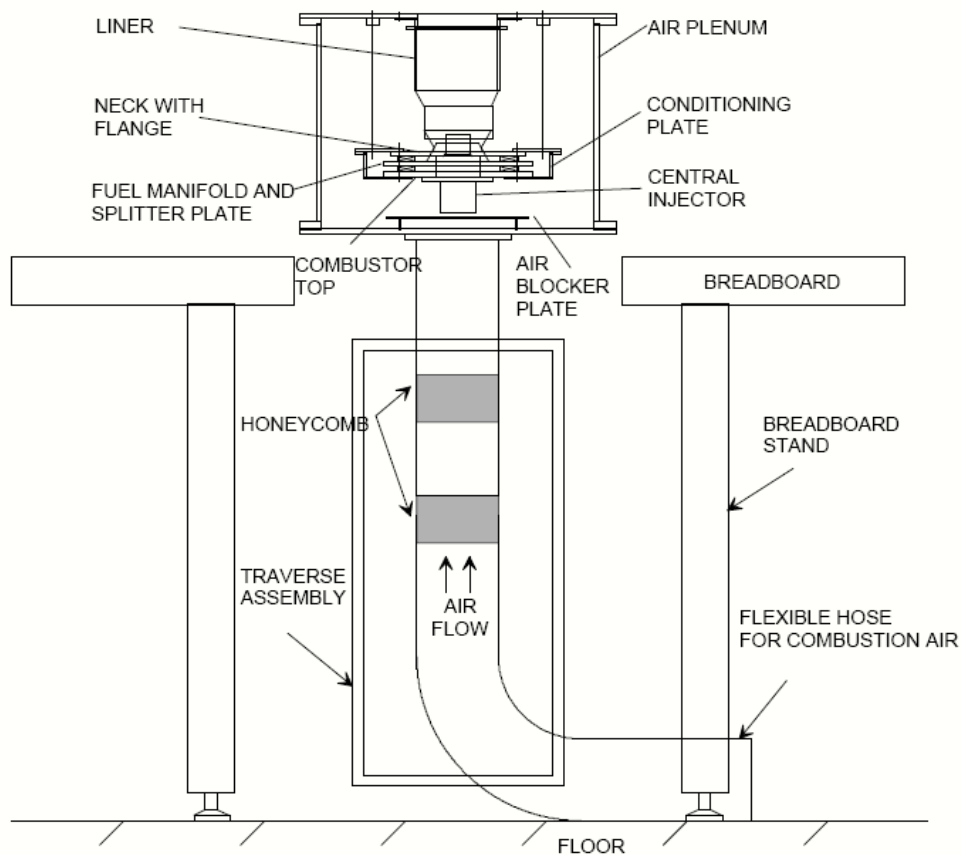
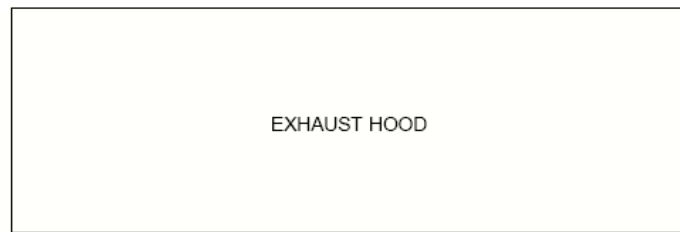


**Figure 11: A schematic representation of the hardware used by Eggels and Brown [6]**

Both isothermal (non-reacting) and combustion CFD runs of the experimental combustor were performed. The turbulence was modelled using a standard  $k-\epsilon$  turbulence model with wall functions to resolve the near-wall flow. Two combustion runs were performed, one using the flame generated manifold (FGM) reduced reaction mechanism and one using the global reaction mechanism (GRM) to simulate the combustion.

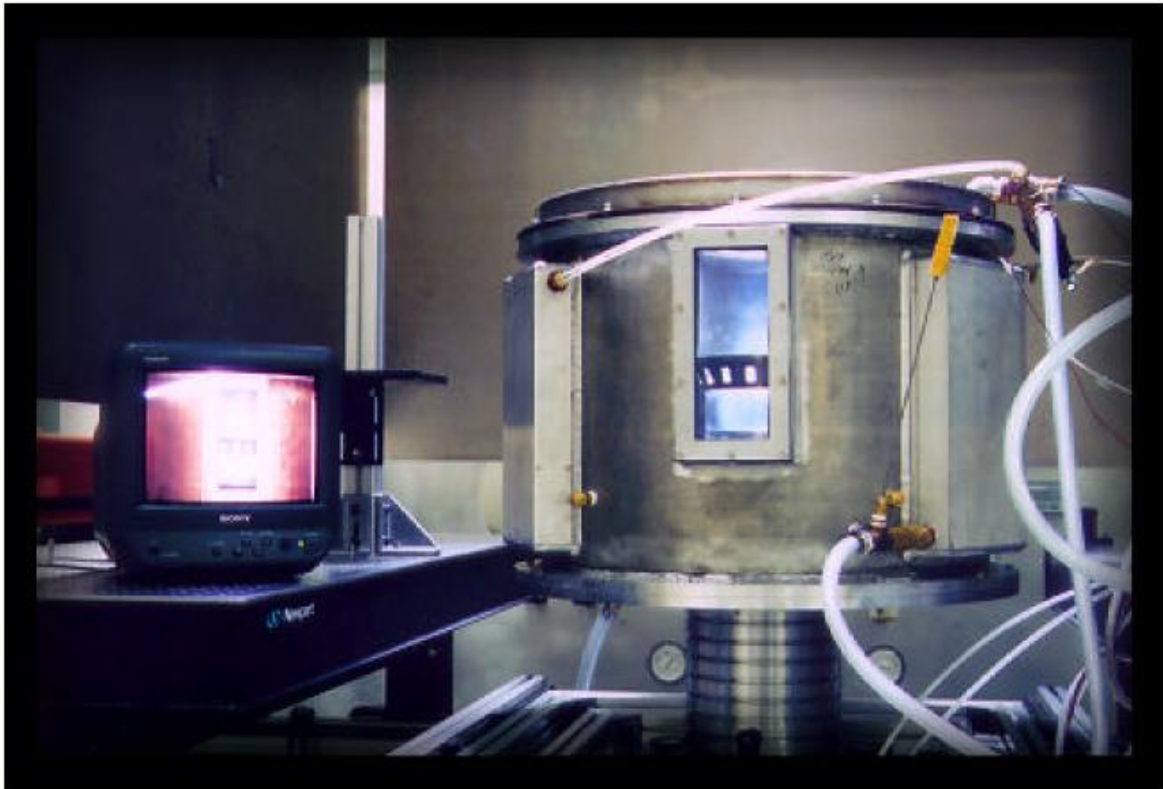


Figure 12: A photograph of the combustor used by Eggels and Brown [6]

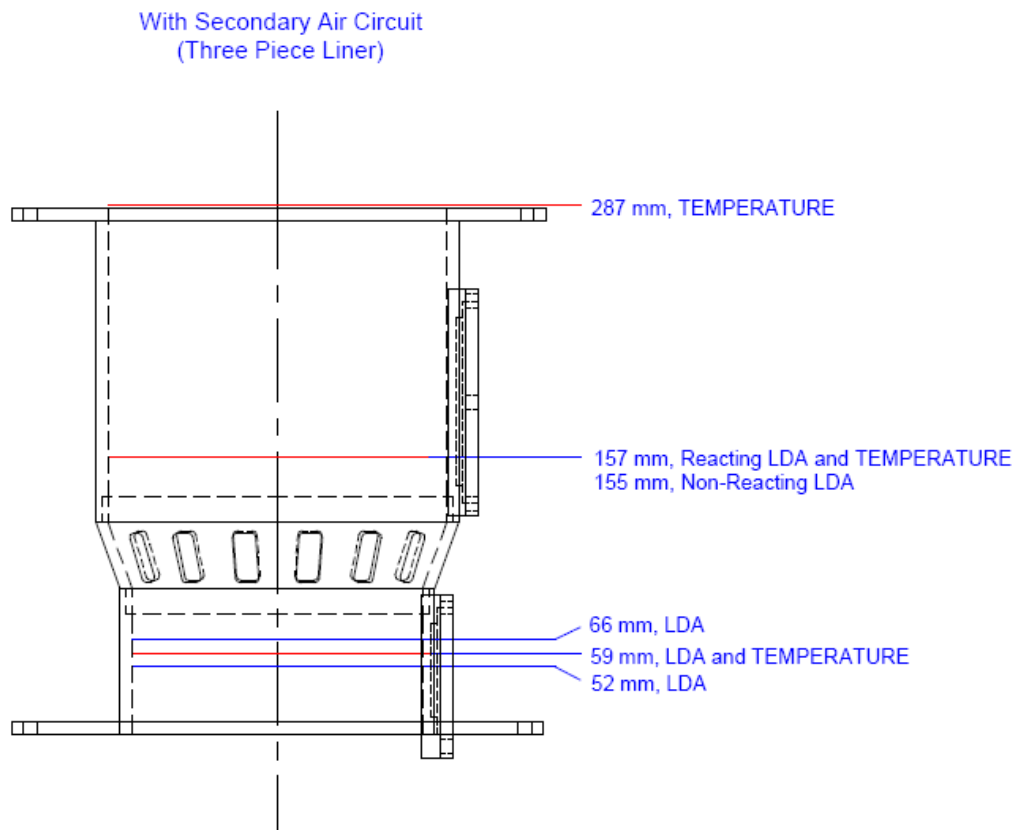
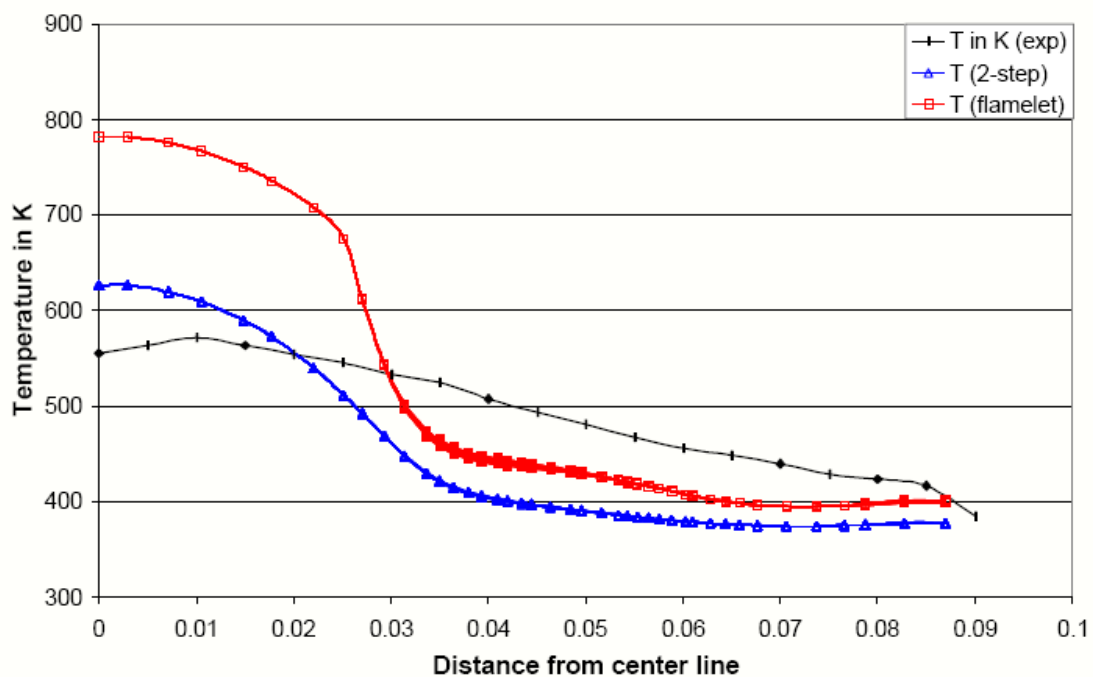


Figure 13: Axial measurement plane positions of velocity (LDA) and temperature measurements [6]

For both methods, a polynomial probability density function model was used to couple the chemistry and turbulence. For the non-reacting flow, the CFD predicted the global structures quite well but showed an overprediction of the length of the recirculation zone. There were also large differences in the swirl velocities, possibly due to the swirl velocities being estimated from the angle of the swirl vanes, which were upstream from the CFD inlet boundary. For the reacting flow, the flowfield was similar to the non-reacting simulated flowfield. In the primary zone, the experiment and CFD velocity profiles compared well. In the secondary zone, the velocities did not agree well because this was at the end of the recirculation zone and the recirculation zone length was not predicted well. For the reacting flow, the temperatures were overpredicted in the primary zone. It was concluded that the FGM method predicts the temperature quite well at the end of the recirculation zone while the GRM underpredicts the temperatures at the centreline. At the outlet plane, the FGM (flamelet) method did not predict the temperatures well especially at the centreline and the GRM (2-step) shows better results, shown in Figure 14. These results show that one method of combustion modelling was not better than the other and that they both have their faults.



**Figure 14: Comparison of experimental data and CFD results at a distance of 287 mm above the central injector [6]**

Carl *et al.* [8] showed the mixing field of a sector of an annular combustor that was measured in non-reacting and reacting flow and compared with the CFD modelling of the same combustor sector. For combustor flow, the velocities, the fuel spray concentrations and the combustion regions (i.e. regions of high Hydroxide radical ( $\text{OH}^*$ ) concentration) were mapped. Part of the aim of this study was to verify the CFD models with experimental data. The test rig consisted of a rectangular section of an annular combustor, which covered four nozzles along the circumference as seen in Figure 16. The burner was inside a casing that had glass windows for optical accessibility to the combustor liner. The whole casing was inside a pressure vessel with its own pressure windows to give optical accessibility to the rig inside (see Figure 15 and Figure 16).

The combustor nozzle supplies swirling flow and there are three rows of dilution holes further downstream. The liner constricts slightly towards the outlet. Figure 17 is of the CFD grid used to show the geometry of the liner.

Tests were done and results were given for rich and lean conditions at 6 bar. The inlet temperature was 700 K. For the non-reacting investigation, the mixing was measured using Mie scattering, which measured the dilution of one flow by a second. This was done by seeding one of the flows and using a laser sheet and a CCD camera to capture the local concentrations of particles. The CFD simulation of the isothermal flow was performed using three-dimensional Navier-Stokes equations. The turbulence model used was the  $k-\epsilon$  model. The reacting flow was evaluated using many different techniques. Laser Doppler anemometry (LDA)

was used to measure the velocity of the gas. Figure 18 shows the velocity field measured at two different air/fuel ratios. The velocity and diameter of the fuel droplets were measured using phase Doppler anemometry. The qualitative distribution of the kerosene fuel near the nozzle was measured using Mie scattering. OH\* Chemiluminescence was used to indicate the position of the flame reaction zone. The radiation of the electronically excited OH radicals within the flame front was used. Laser-induced fluorescence (LIF) of OH was performed to detect the OH radicals inside the regions of high temperatures.

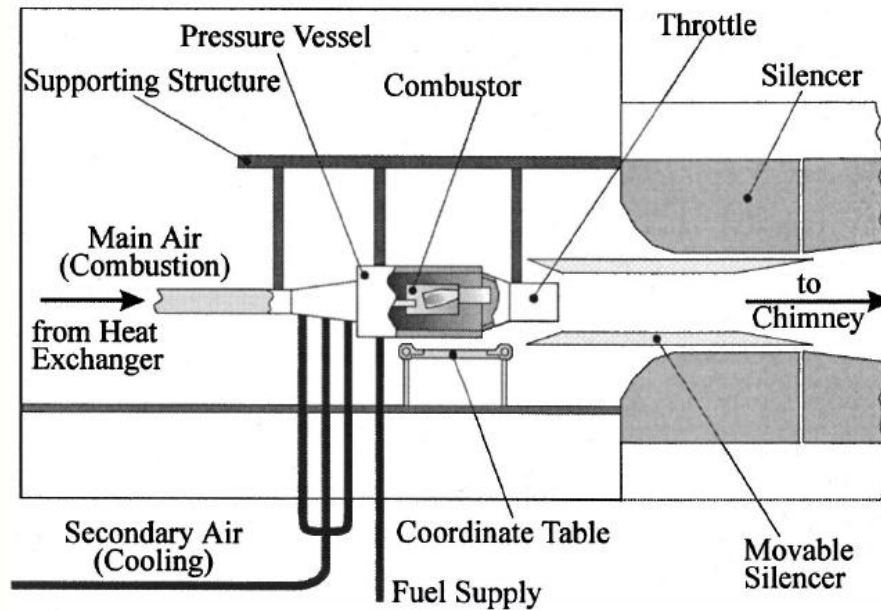


Figure 15: A schematic view of the test plant by Carl *et al.* [8]

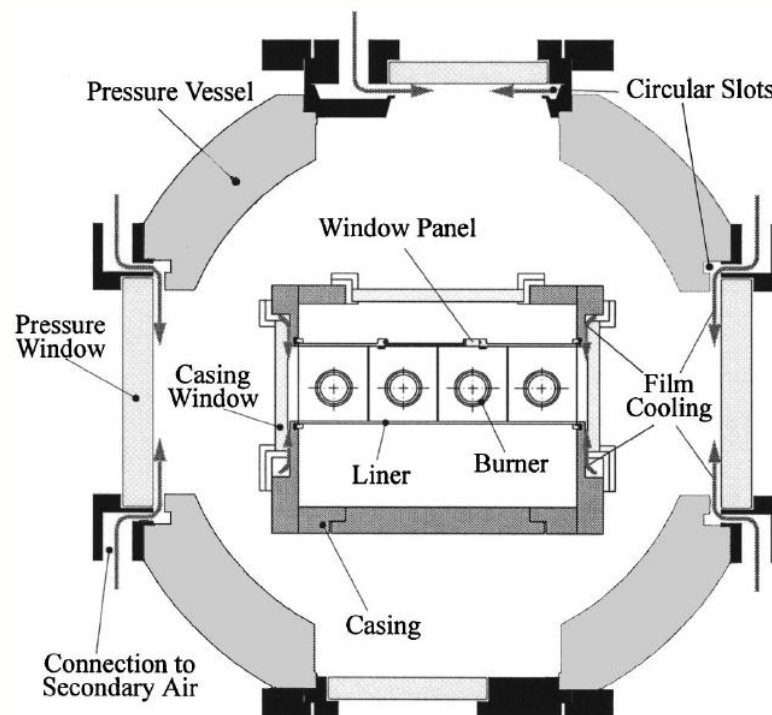


Figure 16: A cross-section of the combustor and pressure vessel [8]

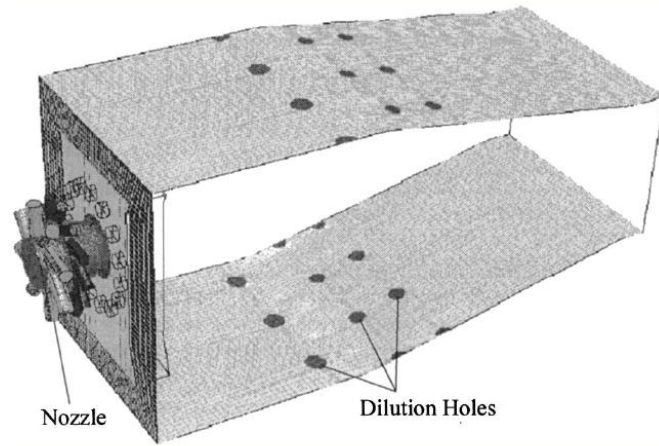


Figure 17: CFD grid showing the combustor liner geometry [8]

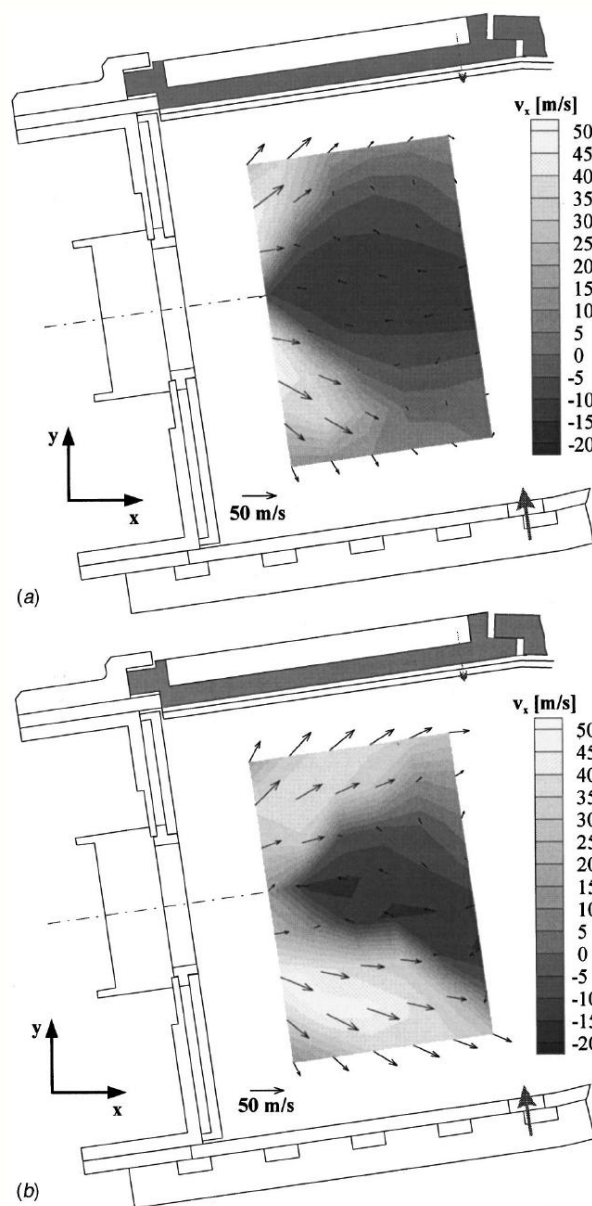


Figure 18: Gas velocity in the primary zone (a) AFR = 90 (b) AFR = 40 [8]

The modelled mixing field on the plane through the centre of the nozzle showed good correlation with the measured mixing field on the same plane. The dilution jet flow was seeded while the swirling flow was not, thus no conclusion could be drawn about the swirling flow region. For combustion tests, the results were given for the primary zone and then the mixing zone. In the primary zone, an asymmetrical recirculation zone was found. This is due to the asymmetrical horizontal position of the nozzles in the combustor head. For richer conditions, the expansion angle was smaller and the recirculation region narrower due to the hot expanding gasses in the corner squeezing the swirling flow. The stabilisation zone had the same axial extension for both rich and lean combustion but the flame reached up to the end of the primary zone for the lean combustion. In the mixing zone, it was found that the first jet on the lower side was quickly turned around by the primary flow but the second jet on the upper wall penetrated right through the measuring domain towards the lower wall. After the mixing zone, the OH-LIF showed low OH levels indicating that the flow was well mixed. It was suggested that the data gives the potential to advance CFD combustor design by supplying local and global information, which could then give insight into the degree of complexity or refinement that is needed in the physical models that are important to the goals of industrial CFD.

In 2002, Diers *et al.* [12] investigated the effect of two different liner cooling methods for a rich quench lean combustor. These two methods were effusion cooling and impingement cooling. The investigation was done by measuring the emissions with a suction probe attached to several analysers for  $\text{CO}_2$ ,  $\text{CO}$ ,  $\text{O}_2$ ,  $\text{H}_2$ , UHC, and  $\text{NO}$  ( $\text{NO}_x$ ), measuring the velocities using LDA and measuring the temperatures using a thermocouple and coherent anti-Stokes Raman scattering (CARS). Numerical simulations of the effusion cooling were done. The rig consisted of a rectangular section of a combustor with two rectangular windows mounted in the sidewalls of the combustor. The rig ran under atmospheric conditions with the air supply preheated to 650 K. Most measurements were taken on a plane in the centre of the central nozzle of a set of five nozzles where sidewall effects are minimal. For the effusion set-up, the three airflows were separated and supplied to the combustor through separate supply channels. The primary air came from the primary air channel and into the combustor through air blast nozzles. The secondary air entered the combustor through two rows of staggered secondary holes from the secondary air channel and the effusion cooling air was supplied from the effusion air pipe and entered the combustor through the effusion cooling holes all over the combustor wall. The effusion cooling set-up is shown in Figure 19 while the measurement planes are shown in Figure 20.

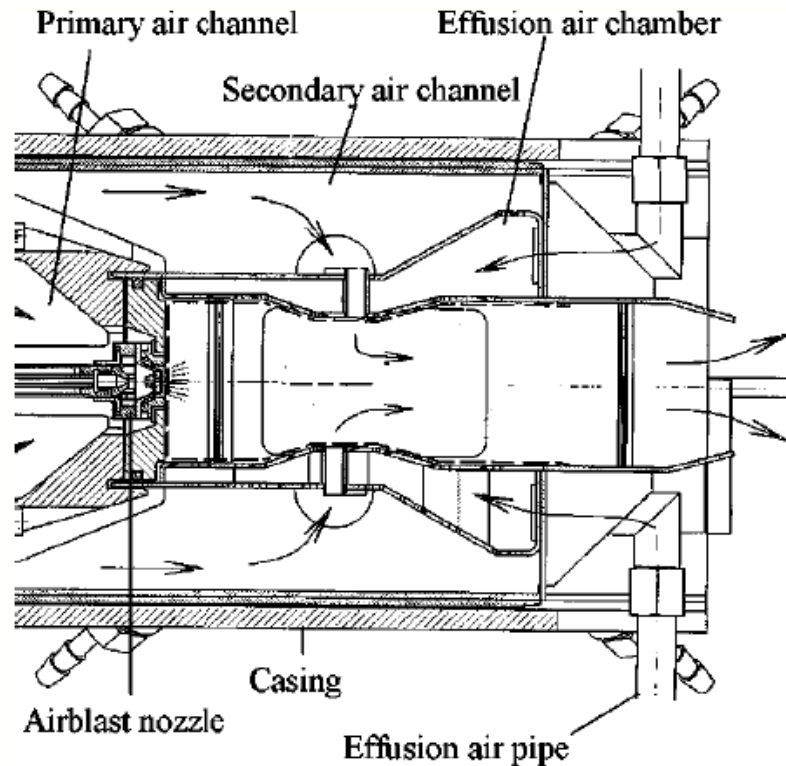


Figure 19: Side view of the combustor effusion cooling configuration (configuration 1) in Diers *et al.* [12]

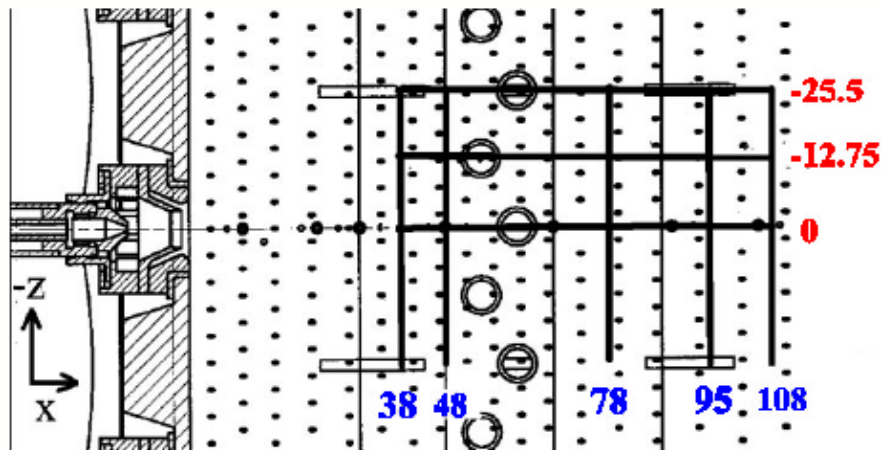


Figure 20: The position of the measurement planes in the effusion cooling set-up [12]

For the impingement set-up, the primary air was split away and entered the combustor through the air blast nozzles. The secondary air entered the combustor from the casing axially through the primary holes at the dome. The secondary air also entered the combustor radially at the primary zone cooling holes, the single row of secondary holes and secondary zone cooling holes. Figure 21 shows the impingement cooling set-up.

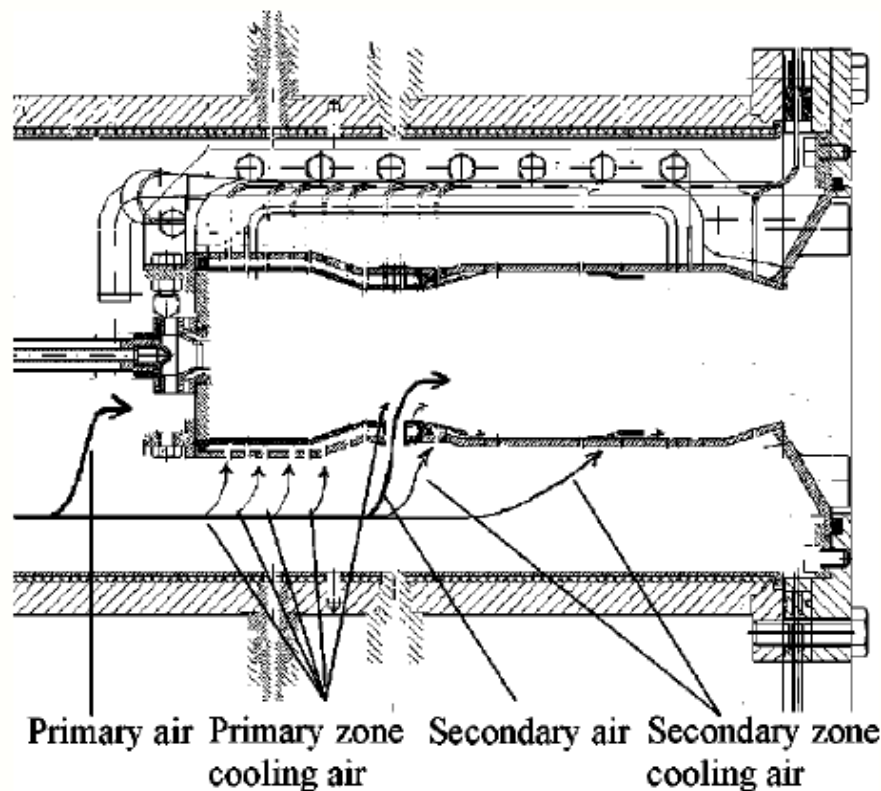


Figure 21: Side view of the combustor impingement cooling configuration (configuration 2) in Diers *et al.* [12]

In the effusion set-up, the total fixed nitrogen, rest total fixed nitrogen and NO were measured at planes  $x = 38, 48, 78, 95$  and  $108$  mm shown in blue in Figure 20. The LDA revealed the velocity components within the combustor on the nozzle centre plane (shown in red in Figure 20 at  $x = 0$  mm), which also intersects a secondary jet. The interpolated velocities measured on this plane are shown in Figure 22.

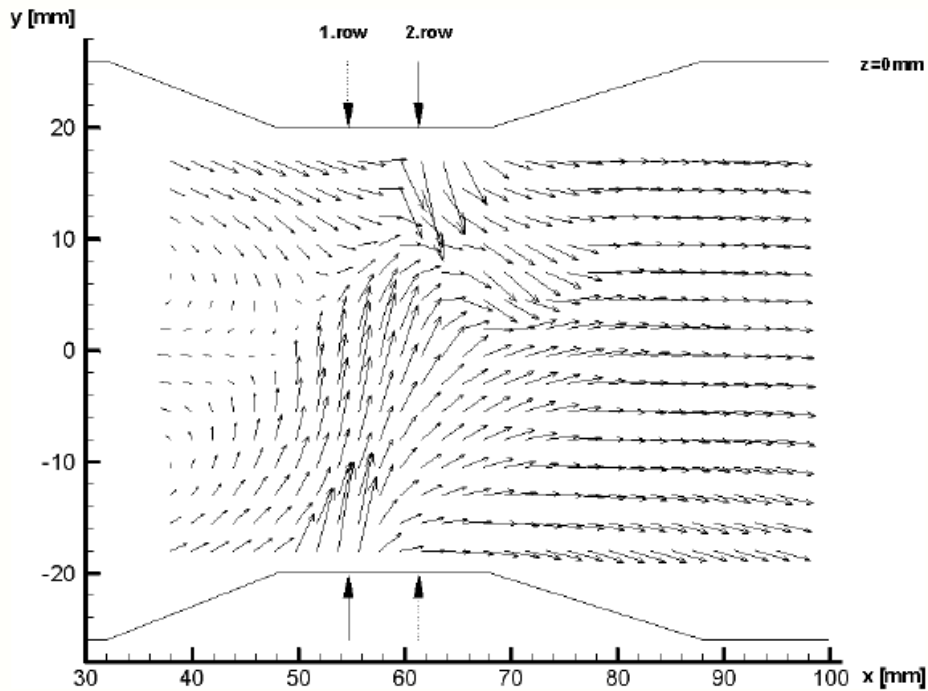


Figure 22: Interpolated vector plot of measured velocities in the nozzle centre area of the effusion set-up [12]

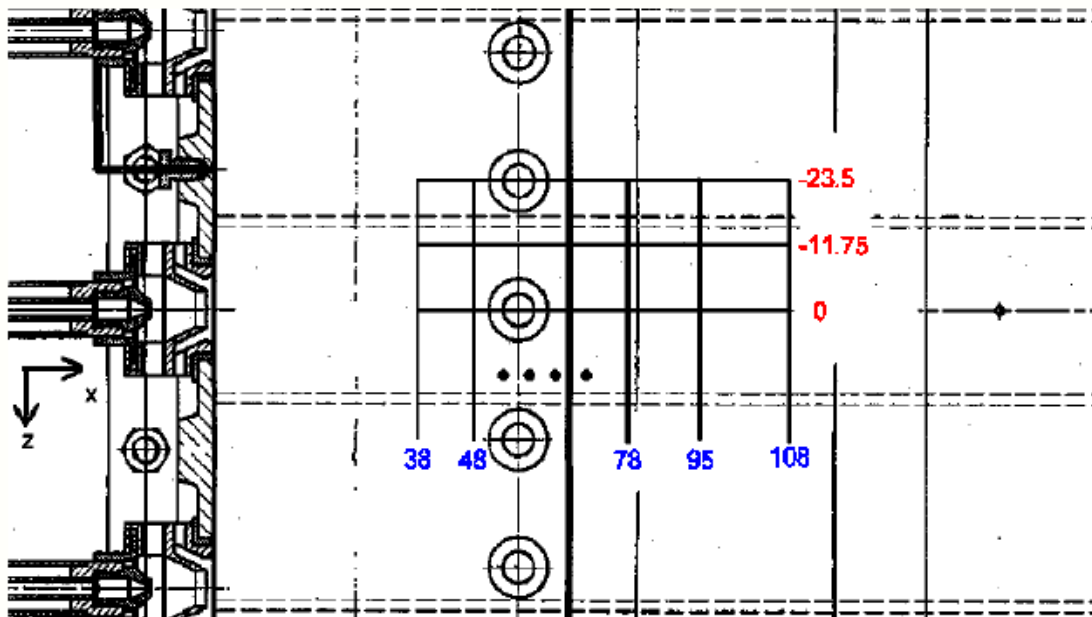
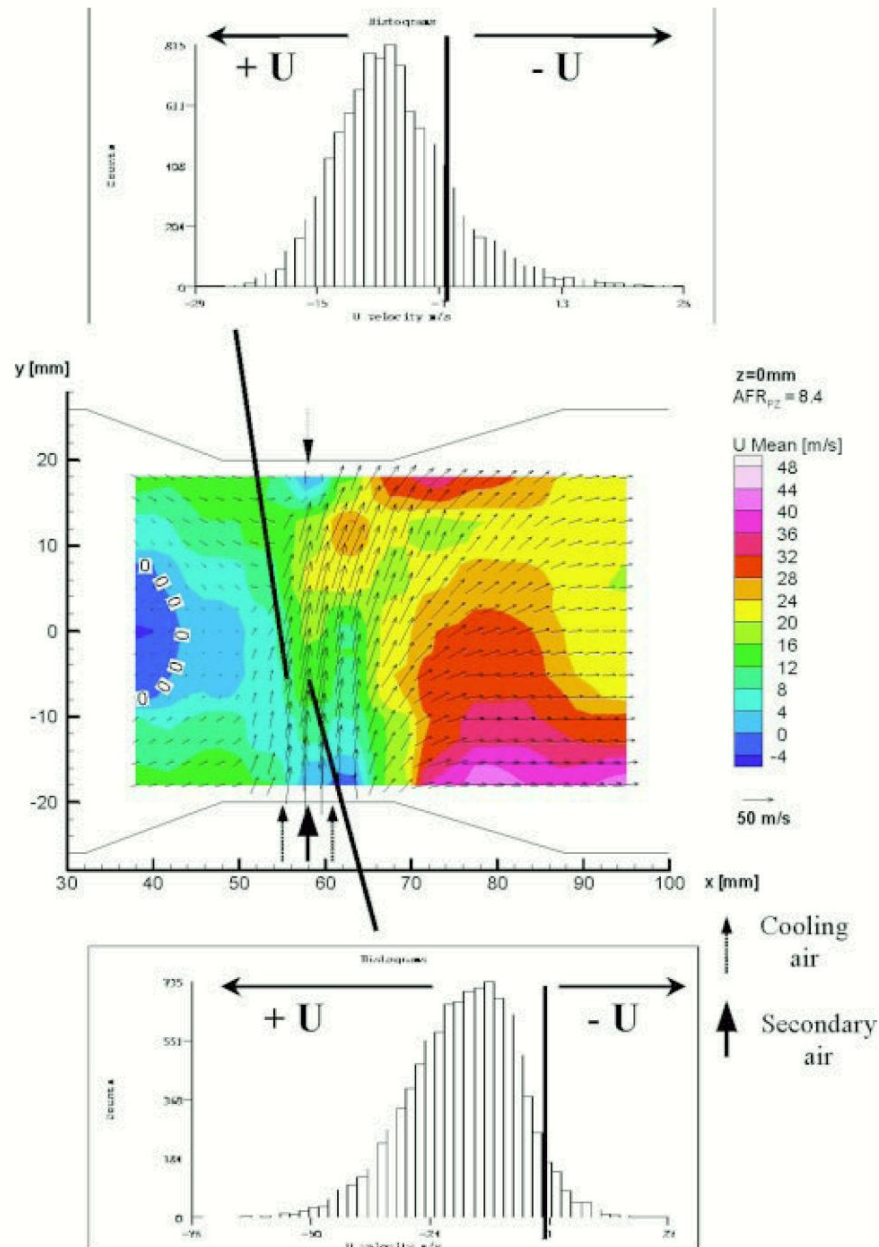


Figure 23: The position of the measurement planes in the impingement cooling set-up [12]

This plot shows that the recirculation zone of the air blast nozzle extended up to the end of the reduction of the liner height where the secondary holes were. The CARS temperature measurements show that no reaction between the primary zone air and the effusion air occurred. The experiment also demonstrated that higher preheat temperature increasing evaporation and higher pressure accelerating the reaction both contributed to decreasing the amount of unreacted fuel. The CFD results show that the highest temperatures occurred in the effusion zone, which contradicts the temperature measurements taken.

The positions of measurement for the impingement cooling set-up are shown in Figure 23. For impingement cooling, the recirculation zones are isolated and much smaller than for effusion cooling. This set-up also demonstrated faster conversion of fuel in the primary zone. There was overpenetration of the secondary air jet due to the encapsulating primary zone cooling air preventing good mixing of primary and secondary air. This led to incomplete mixing. The velocity result for the impingement cooling experiment is shown in Figure 24.



**Figure 24: Interpolated velocity vectors, axial velocity in colour scale and histograms with axial velocities in nozzle area (upper: positioned over primary zone cooling air orifice, lower: positioned over secondary air inlet hole) for the impingement set-up [12]**

In summary, the effusion cooling demonstrated incomplete combustion in the primary zone but the two-staged secondary holes caused good mixing resulting in acceptable  $\text{NO}_x$  emissions. Impingement cooling had a faster reaction in the primary zone but the desired reaction progress of the primary zone was not fully reached. Increasing the pressure could solve this. There was also not such good mixing in the quench zone due to the encapsulation of the primary air by the first row of secondary jets and the primary zone cooling air.

The suggestion for the impingement set-up is to modify the quench mixing design to obtain decreased  $\text{NO}_x$  emissions.

In 2003, the velocity contours, three-dimensional velocity vectors and fluctuation frequency data was collected for a combustor-type set-up, which used a triple annular research swirler (TARS) by Li and Gutmark [10]. The swirler configurations could be adjusted by changing the swirler vane angles of all three axial swirler sections as well as whether they were co-rotating or counter-rotating. The TARS was at the entrance to a variable length mixing tube, which entered the optically accessible can-type combustion chamber. This chamber terminated in a variable contraction exhaust nozzle. The combustor did not have jets for mixing. The tests were done in non-reacting flow. The experimental set-up is shown in Figure 25.

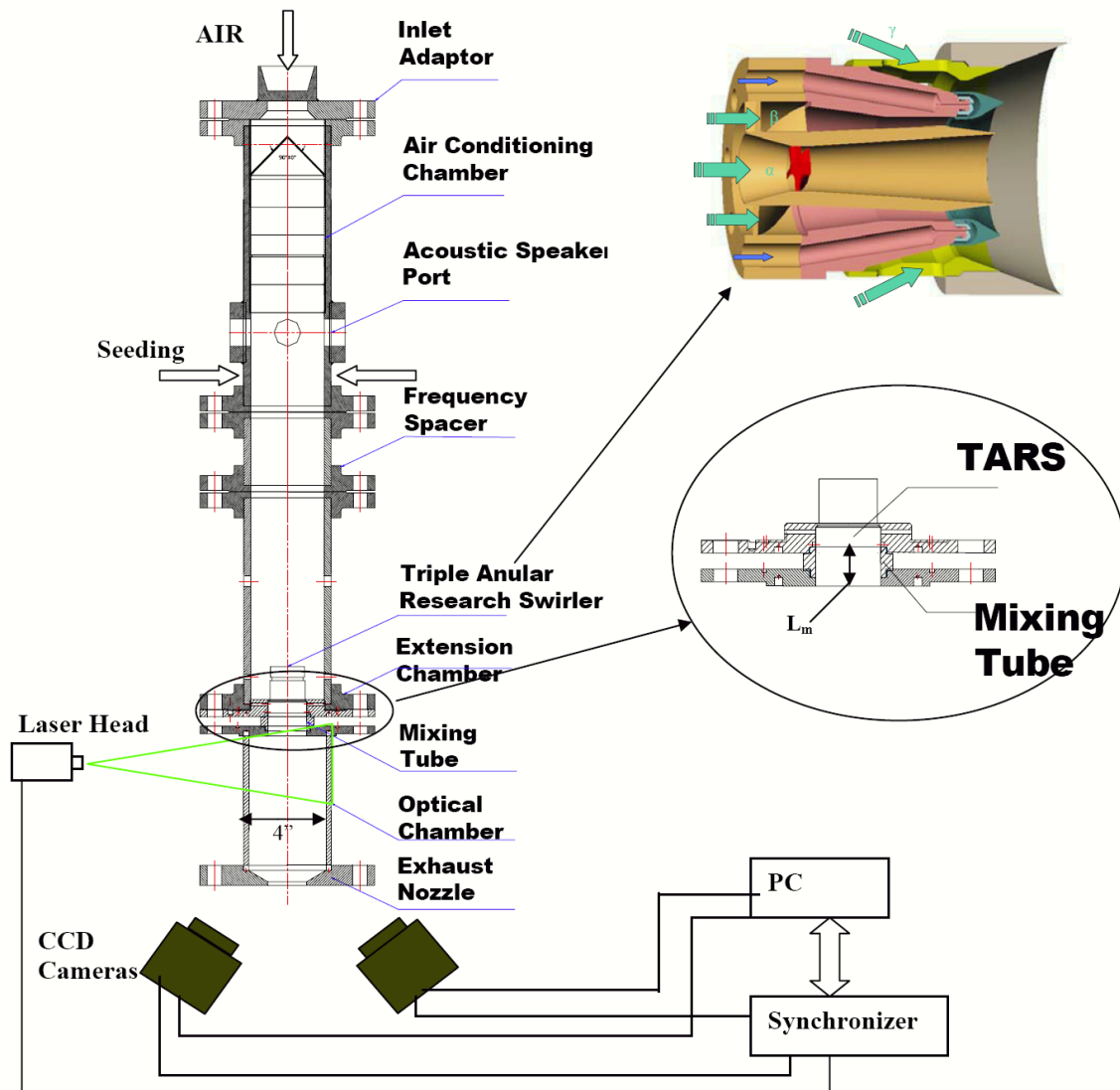
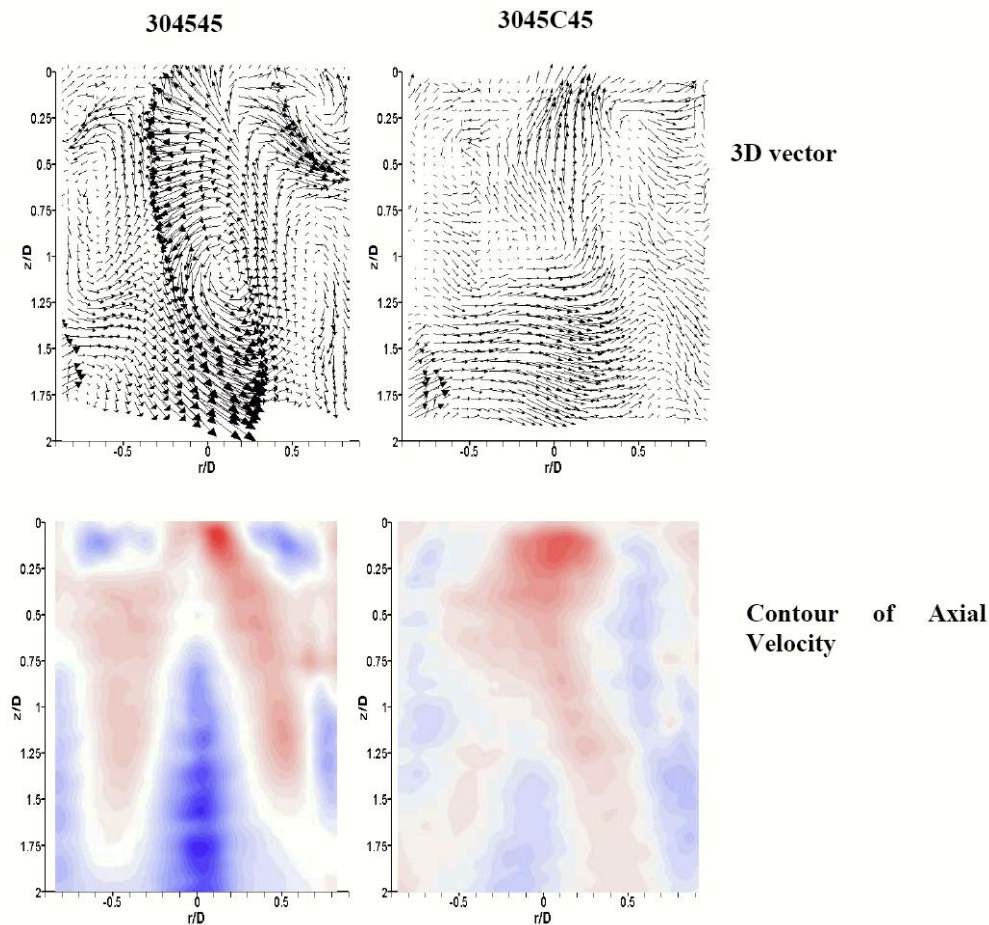


Figure 25: Experimental set-up including stereoscopic PIV arrangement used by Li and Gutmark [10]

Stereoscopic PIV was performed in order to get the 3D velocity vectors as well as the normalised velocity contours in the combustor. This showed the recirculation zone velocities and shapes in the combustor as a function of the different variables. Hotwire/film measurements were performed in order to obtain the spectral data for the flow. The combustor flow demonstrated a central toroidal recirculation zone (CTRZ), which changed from a conical "V"-shape to a bubble shape as the ratio of combustor diameter to exhaust nozzle throat diameter decreased. Thus changing the exhaust nozzle size changed the shape of the CTRZ. Adding a mixing tube caused a substantial change to the structure of the flowfield and it enhanced the characteristics. The mixing tube increased the exit jet axial velocity and formed large vortical structures. Slight changes to the position of the large vortex at the CTRZ and the inner stagnation point occurred.

Stronger flows were also observed in certain positions. Increasing the mixing length did not cause a substantial additional modification to the flow. The previous results were seen with co-rotating swirlers. Reversing the second swirler to be counter-rotating caused the “V”-shaped recirculation zone to change to a “Y”-shape. This result is shown in Figure 26.



**Figure 26: Velocity vectors and contours of axial velocity of the co- (304545) and counter- (3045C45) swirler set-ups [10]**

The spectral analysis revealed that a high frequency fluctuation was present in a very small region near the combustor inlet and dissipated immediately after the jet entered the combustion chamber. The downstream exhaust nozzle and combustor shape had little effect on the high frequency. A mid-range frequency was located near 2.6 diameters downstream and was affected by the inlet conditions (e.g. mixing tube length, Reynolds number, swirler combination) and slightly affected by the exit conditions. A low frequency was situated in the downstream region and was affected by the outlet conditions.

In 2006, Li and Gutmark [11] again presented experimental work performed on the test rig shown in Figure 25. A base case was measured, after which, the effect of varying inlet and outlet boundary conditions (BC) was looked at. The base case had an air mass flow rate of 32 g/s, which was the same flow rate for all of the experiments. The parameters recorded using LabView were: the main airflow rate, air inlet temperature, plenum pressure, pressure inside the combustion chamber, combustion gas temperature, combustion wall temperature and emissions data. The inlet temperature ( $T_{\text{inlet}}$ ) for the base case was 230 °C while it was varied to be 23, 100, 200 and 300 °C for the isothermal tests. Isothermal swirling flow experiment results for velocity,  $\frac{V_z}{V_0}$ , showed a spherical central recirculation zone (CRZ) for all velocity fields in the temperature range  $T_{\text{inlet}} = 23$  to 300 °C. The values for the normalised total turbulent kinetic energy (TKE),  $\frac{k}{V_0^2}$ , showed the distribution of total turbulence, which indicated that the turbulence was strongest at the shear layer between the swirling jet and the CRZ and was lower inside the CRZ. The level of the turbulence intensity in the shear

layer was more than twice the turbulence intensity level in the CRZ. The velocity and turbulent kinetic energy results for the  $T_{\text{inlet}} = 23\text{ °C}$  test are shown in Figure 27.

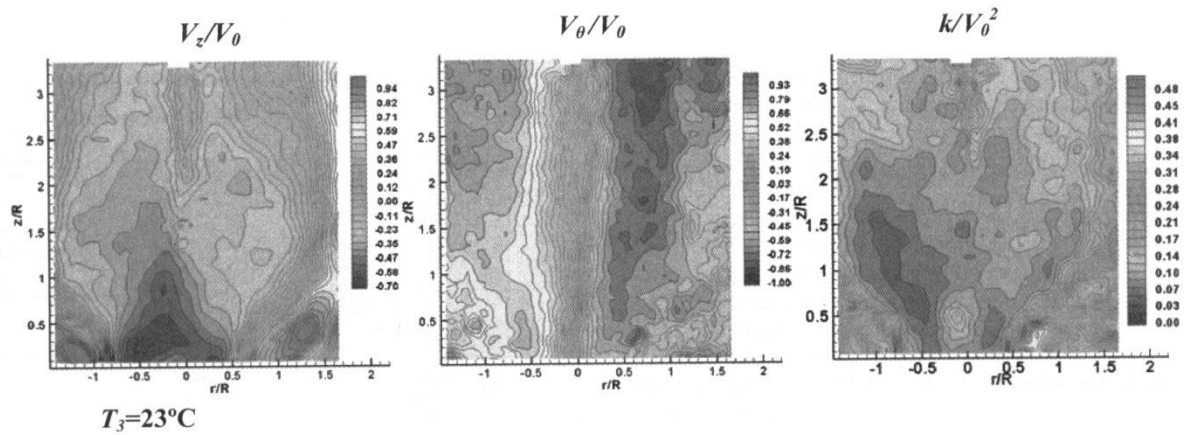


Figure 27: Contours of  $\frac{V_z}{V_0}$ ,  $\frac{V_\theta}{V_0}$ , and  $\frac{k}{V_0^2}$  at  $T_{\text{inlet}} = 23\text{ °C}$  with mixing tube length at 0 mm and contraction ratio of 1 [11]

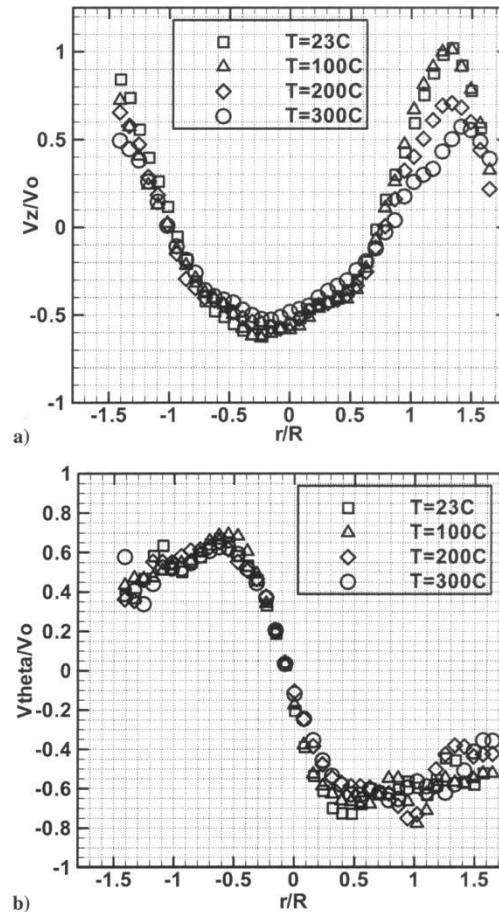
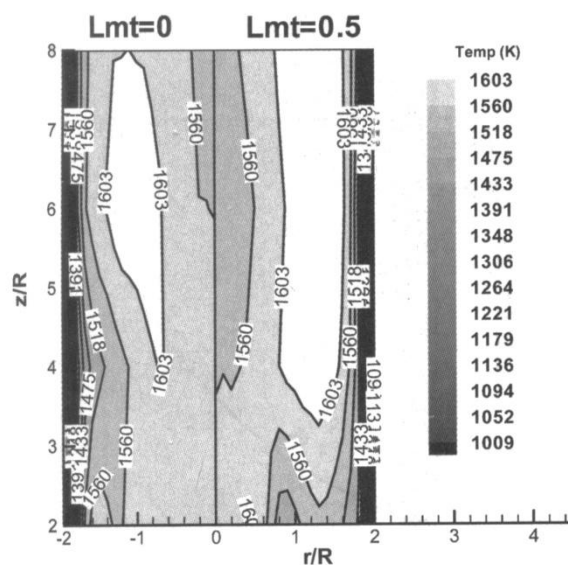


Figure 28: Velocity profiles at  $\frac{z}{R} = 0.5$  for  $T_{\text{inlet}} = 23$  to  $300\text{ °C}$  a)  $\frac{V_z}{V_0}$  b)  $\frac{V_\theta}{V_0}$  [11]

As the inlet temperature increased, the mean velocity field preserved its characteristics (see Figure 28), but magnitudes of the velocity components changed, therefore bulk velocity increased but the mass flow rate was kept constant. The temperature increase also increased the bulk viscosity. These changes in velocity and viscosity significantly changed the inlet Reynolds number, potentially affecting the swirling flow

dynamics. This result shows that the inlet air temperature is a major factor for gas turbine combustion performance and thus knowledge of its effects on the swirling flowfield is necessary for combustor design and combustion performance improvements.

For the reacting swirling flow experiment, the same variables were measured as for the isothermal experiments and then compared. In the reacting experiment, combustion heat was released causing a temperature change to occur compared with the isothermal experiment, thus the velocity field of reacting swirling flow differs from the isothermal flow. An increase in the inlet air temperature enhanced the magnitude of reverse flow in the central region and increased the tangential velocity in the swirling jets. An increase was also shown in the energy of the turbulent velocity fluctuations. These effects can lead to an enhanced reaction and heat release rate as well as an increased residence time (due to enhanced recirculation), which together contribute to the typical  $\text{NO}_x$  increase with higher inlet air temperature. For testing the effect of some other BC, a  $T_{\text{inlet}}$  of  $230^\circ\text{C}$  was used and the following data was collected: velocity field using PIV; spectra of velocity in swirling flow (frequencies) using a constant temperature anemometer; the temperature distribution across the cross-section using B-type thermocouples; the reaction heat release rate using  $\text{OH}^*$  and  $\text{CH}^*$  Chemiluminescence and  $\text{NO}_x$  emission measurements using a gas analyser. The  $\text{NO}_x$  increased as fuel equivalence ratio and flame temperature increased. In order to evaluate the effect of the inlet BC, the length of the mixing tube between the swirler outlet and combustor inlet was changed. The temperature distribution measured with the thermocouple for two of the mixing tube configurations is shown in Figure 29.



**Figure 29: A comparison of the temperature distribution for a mixing tube length of 0 and 0.5 mm [11]**

Li and Gutmark [11] concluded that “[the mixing tube] not only served as additional mixing volume for fuel and air, but also led to aerodynamic changes of the swirling flowfield”. The mixing tube affected the magnitude of  $V_z$  and  $V_\theta$  as well as the formation of the CRZ. The mixing tube addition also substantially reduced the  $\text{NO}_x$  emissions but CO increased. Flame stability was also reduced. To evaluate the effect of the outlet BC, the contraction ratio was varied. As the contraction ratio increased, the recirculation zone changed from spherical to “V”-shaped (conical) and  $V_\theta$  inside the vortex core was increased greatly. The downstream BC is important for liquid sprays. It is important to model the downstream condition in CFD.

In 2004, Mandai and Nishida [7] did a study to list the advantages and disadvantages of CFD and experimentation in combustor design. CFD studies were performed on a premixed flame combustor and a diffusion flame combustor and the results for these were compared with experimental results corresponding to each configuration. The diffusion flame can-type combustor is shown in Figure 30 while the premixed flame can-type combustor is shown in Figure 31.

For lower computing time and cost, it is usually practical to use RANS and the eddy dissipation concept model (EDC model) for combustor development. For the diffusion flame type combustor, the flow vectors, gas temperatures,  $\text{O}_2$  distribution and  $\text{NO}_x$  distribution were modelled, measured and then compared. For the

diffusion flame case, a qualitative agreement in the flow states, gas temperature distribution and oxygen concentration distributions was seen between the CFD and experimental results. The  $\text{NO}_x$  concentration distributions, however, did not agree qualitatively. Quantitatively, the gas temperatures were between 50 - 100 K lower than the experimental results due to radiation errors. The authors, however, stated that if the experimental temperatures were corrected for radiation, there were still a few regions where the temperature predicted by CFD was higher than the experiment results. This indicated that the CFD simulated a heat rate that was too high.



Figure 30: Mandai and Nishida's combustor configuration and conditions for the diffusion flame combustor [7]

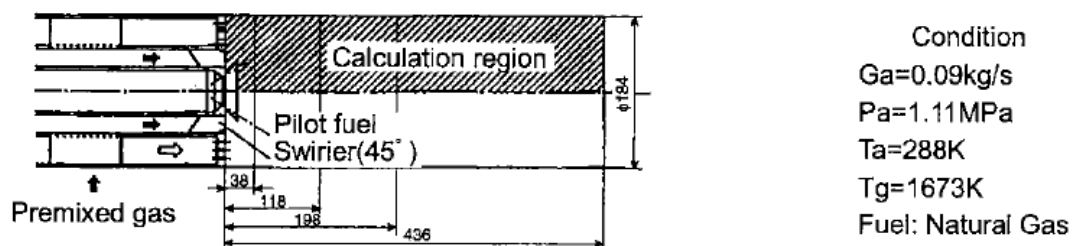


Figure 31: Mandai and Nishida's combustor configuration and conditions for the premixed flame combustor [7]

The authors suggest that the temperature discrepancies might be due to the applicability of the EDC model. The EDC model is applicable to cases where the ratio of the mixing rate to the reaction rate is either zero or infinity (either the mixing rate or the reaction rate is the dominant contributor to the combustion process). In this case the two rates were of a similar order and thus the ratio was equal to one. The  $\text{NO}_x$  concentration values were also underpredicted. For the premixed flame type combustor, a CFD run was conducted, which used the same models (RANS and EDC) as the diffusion combustor and then also a second run, which used a model that was theoretically more applicable to the premixed type of combustor (RANS and MIN model). The MIN model considered both the mixing and reaction rate to contribute to the combustion process. Fuel concentration and gas temperature were reported here. The results of these two runs were compared with experimental results. For the EDC model run, the velocity distribution qualitatively agreed with the experimental results. The fuel concentration, however, was different from the tests at an axial distance of 38 mm already. This is due to the estimate of the fuel stream jet penetration in the CFD to be lower than the actual value. The CFD also predicted gas temperatures indicative of a reaction in certain downstream regions near the wall, whereas in the experiment, the reaction had not yet progressed to that position. The MIN model analysis shows better agreement between the experimental and CFD fuel concentration distribution. The temperatures in the downstream region also show better agreement with the profiles of the experimental results.

In a study of Janus *et al.* [9], data was collected from an optically accessible combustor. The data was collected using non-intrusive laser techniques. The purpose of the data collection was for the validation of numerical simulations. Data was acquired for isothermal and reacting flows. The test rig consisted of a swirler and injector nozzle entering into a can-type combustor. The combustor had three flat glass windows inserted into the sides of the combustor liner. The combustor did not have primary, secondary, dilution or cooling holes. The test rig configuration is shown in Figure 32.

The region investigated was from 1 to 50 mm from the nozzle outlet ( $x$ -axis). The combustor liner was inside a pressurised chamber, which also had three fused silica windows coinciding with the windows of the liner. Cooling air was circulated in this region between the liner and the outer chamber wall. Preheated air (623K) was used for the combustion and was pumped into the combustor through the nozzle. The air was also pressurised to 2 bar. For the isothermal flow, the three components of velocity vectors were measured using

a two-component fibre-optic-coupled LDA. The radial profiles were taken traversing the fibre probes along the  $y$ - and  $z$ - axes recording the axial and radial or tangential velocity components. The measurements were taken along a diameter (cross-section) at axial positions of 1, 10, 15, 20 and 50 mm. The turbulent kinetic energy was also reported for each cross-section. The velocities and turbulent kinetic energy values for the  $x = 1$  mm line are shown in Figure 33.

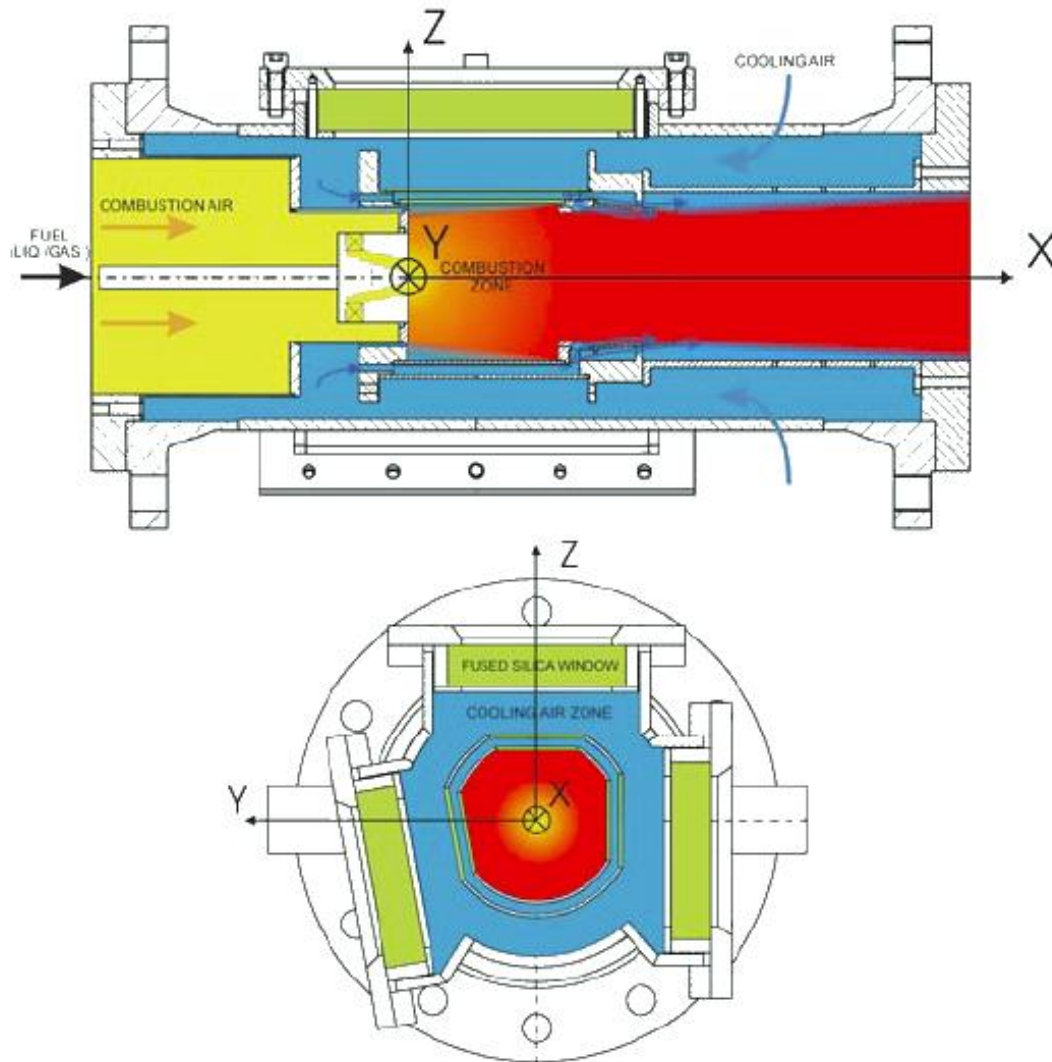


**Figure 32: Longitudinal and cross-section of combustion chamber with coordinate system orientation used by Janus *et al.* [9]**

Two recirculation zones (RZ1 and RZ2) and a stagnation point (SP) were shown in the measured region. This is shown in Figure 34.

Time series measurements were also taken at several axial distances up to 20 mm downstream of the combustor inlet. For the reacting experiment, LDA was also used to collect the same velocity and TKE data at the same positions for comparison with isothermal results (see Figure 33). OH-PLIF was also performed on the reacting flow. These results gave information about the flame structure. From these results, a correlation between the flame position, the velocity and TKE data was shown. The two-dimensional velocity field and some OH-PLIF results are shown in Figure 35.

The flame stabilisation region can be seen to be near the stagnation point and the apex angle of the flame was approximated. The flame brush thickness was also calculated. The comparison of isothermal and reacting LDA results showed that the flowfield was not significantly changed upstream of the average flame stabilisation region. Further downstream the heat release gave rise to a retarded decay of the axial velocity

component. Two recirculation zones were found due to the swirling flow. URANS simulations showed a third recirculation zone, which was not found in the measurement region.

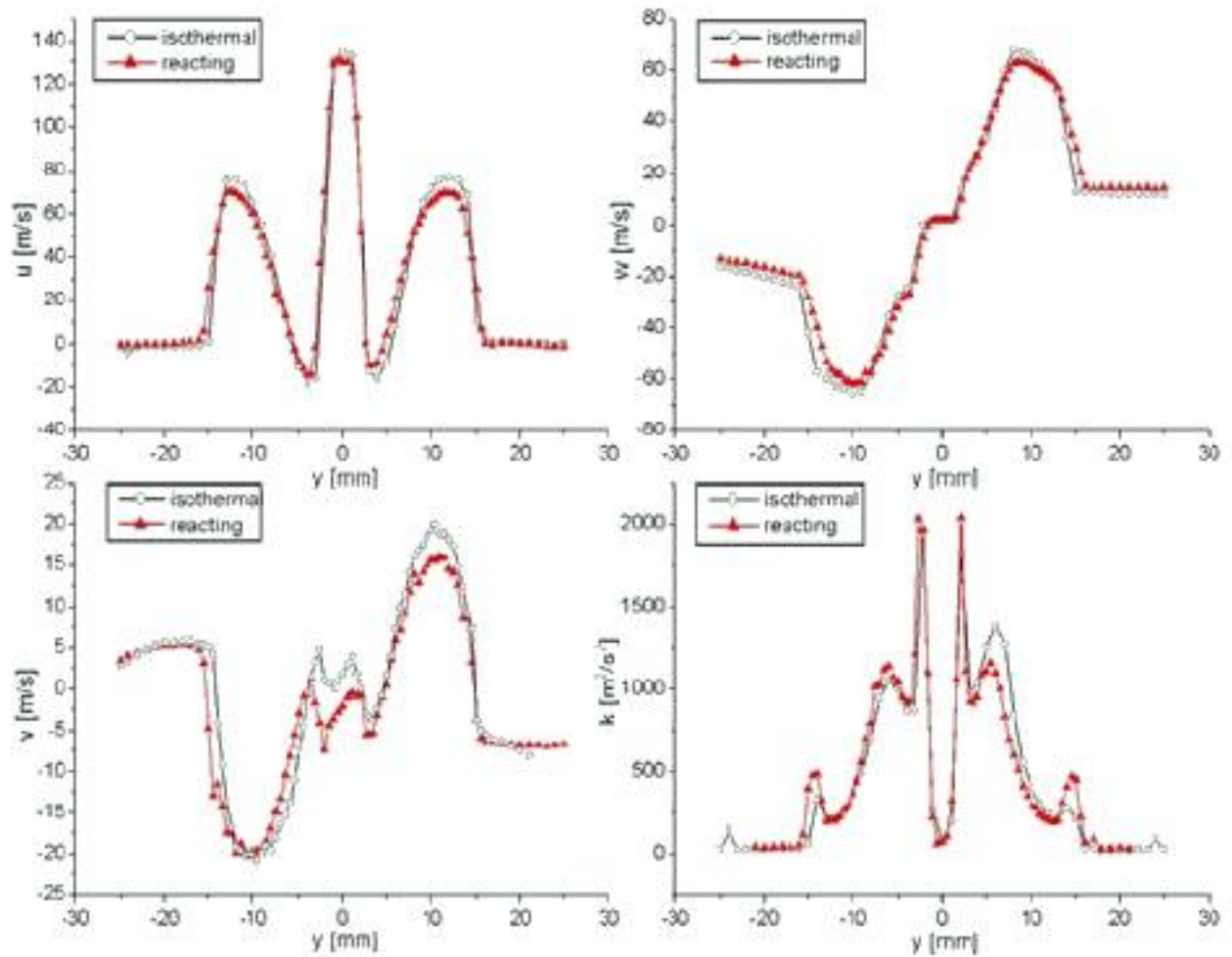


Figure 33: Radial profiles for  $u$ ,  $v$ ,  $w$  and turbulent kinetic energy at  $x = 1$  mm for isothermal flow [9]

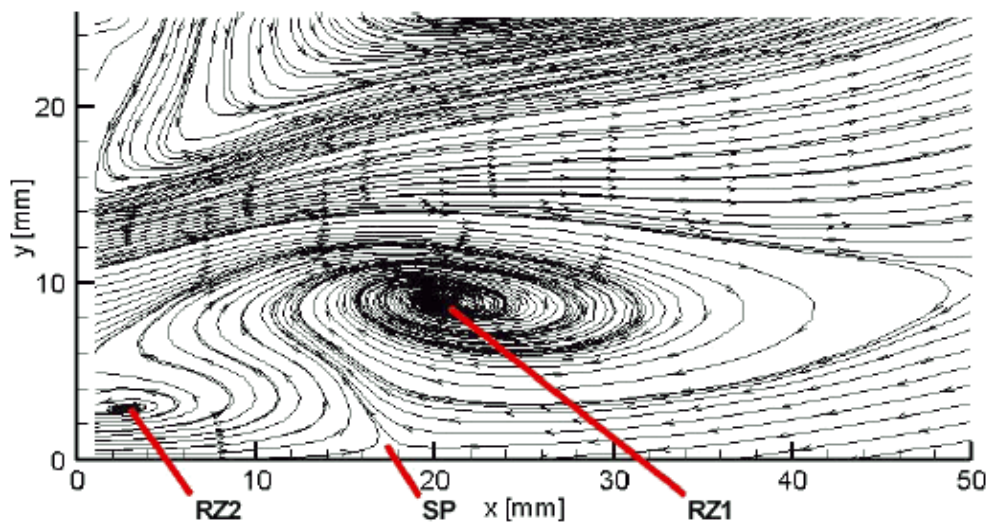
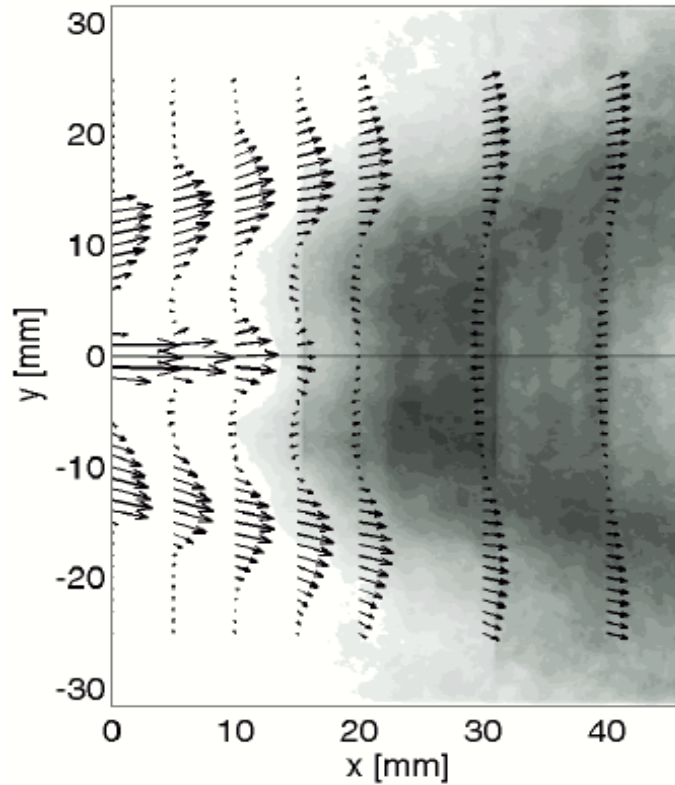


Figure 34: A half-section streamline plot for isothermal flow [9]



**Figure 35: The superposition of the three OH layers with a 2D vector plot of the reacting flowfield [9]**

Archer and Gupta [5] used a PIV system to obtain the three-dimensional flowfield and TKE of a simplified combustor geometry under differing conditions. The test rig consisted of four flat quartz windows arranged into a box format. At the one end, a swirler and injector set-up was placed. The swirler consisted of a double annular swirler with the outer swirler able to be changed to enable both a co- and counter-swirled configuration. The outlet of the combustor can be changed to have no or a 25% contraction. There are no primary, secondary, dilution or cooling holes in the combustor walls. The combustor geometry is shown in Figure 36.

The injection system was non-premixed and falls under the lean direct injection category. The fuel used was propane. The area measured using the PIV system was a 64 mm x 50 mm rectangle just in front of the inlet plane at the swirler outlet. The flow was seeded with submicron-sized titanium oxide particles. With this configuration, the flowfield was measured and direct flame photographs were taken. The flow characteristics were examined both with and without combustion. For each of the isothermal and reacting flows, the effect of co- and counter-swirl as well as confined and unconfined geometry was tested. Firstly, the unconfined isothermal configuration was tested with co- and counter-swirl. The 3D velocity vectors were presented as well as the TKE contours for each swirl configuration. The authors calculated the turbulent kinetic energy, using

$$k = \frac{U_{rms}^2 + V_{rms}^2 + W_{rms}^2}{2} \quad [1]$$

where  $U_{rms}$  = radial root mean square velocity

$V_{rms}$  = axial root mean square velocity

$W_{rms}$  = tangential root mean square velocity

This equation, as shown above, is referred to as the mean kinetic energy in other texts. From the flowfield, the swirl number was also calculated as follows:

$$Sn = \frac{\int w r \rho u 2\pi r dr}{r \int u \rho u 2\pi r dr} \quad [2]$$

where  $w$  = tangential velocity

$r$  = radius

$\rho$  = density

$u$  = axial velocity

There was some confusion with the use of symbols in the previous equations since the letters  $u$ ,  $v$  and  $w$  were described differently for each equation.

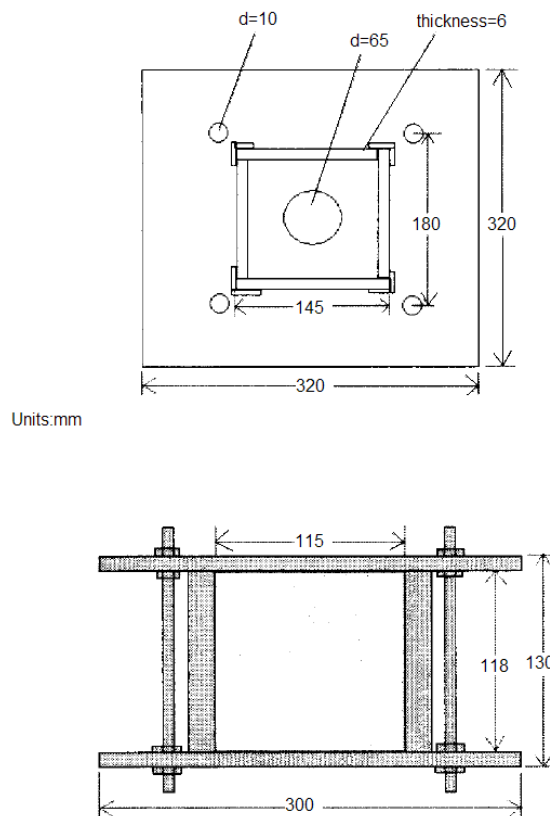


**Figure 36: A schematic diagram of the top view and the side view of the combustion chamber used by Archer and Gupta [5]**

The second configuration tested was the confined isothermal set-up. Here again the flowfield and TKE were obtained through 3D PIV for both the co- and counter-swirl configurations. Lastly, the unconfined reacting case was evaluated also with both co- and counter-swirl configurations. For the reacting case, direct flame photographs were taken for both swirl set-ups. The six configurations tested showed the following conclusions: "1. Co-swirl configuration produced thinner and more elongated internal recirculation zones, possibly leading to longer residence times. 2. Counter-swirl configurations reduce swirl strength in the flowfields. 3. Combustion affects flowfields with increased heat release thus causing thermal expansion. Combustion also affects the formation of vortical structures within the flowfields, by decreasing them in size and number. 4. Confined flowfields have greater velocity magnitudes. Co-swirl confined flowfields have stronger swirl strength. 5. Counter-swirl configurations provide better fluid mixing at the interface of the two flow streams. 6. Counter-swirl configurations increase mixing without increasing swirl strength."

Vakil and Thole [4] measured the flowfield and thermal field surrounding the dilution holes of a sector of an annular combustor rig (see Figure 37). The test rig was a rectangular rig that had the sides of the rig transparent for optical accessibility.

The data acquired was for a non-reacting flow. Flowfield measurements were taken on certain predetermined planes. Three of the planes running perpendicular to the flow covered areas just after the cooling holes and just after each of the two dilution hole sets. Another two planes ran parallel to the flow each through one hole of each of the dilution rows. The planes are shown in Figure 38.

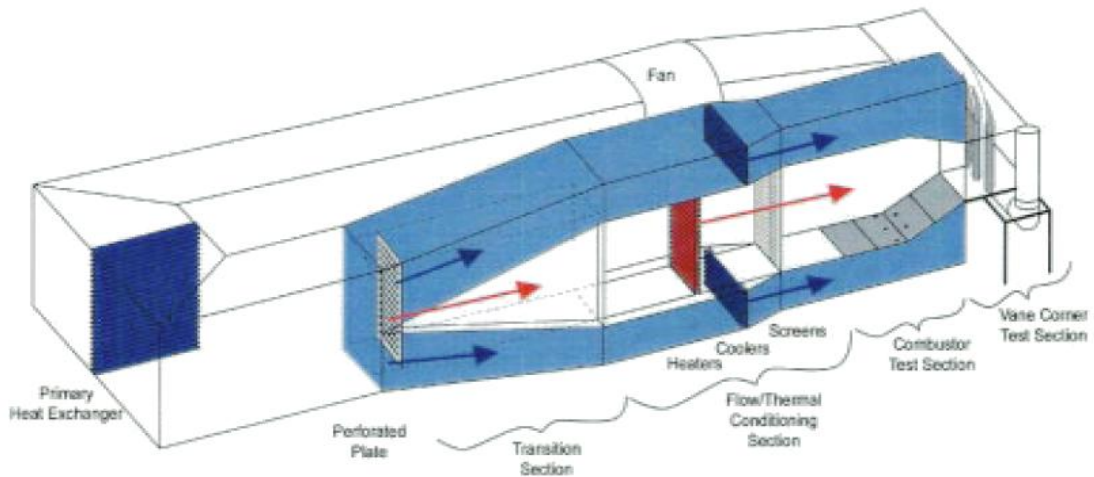


Figure 37: Illustration of the wind tunnel facility used for the combustor simulator experiments by Vakil and Thole [4]

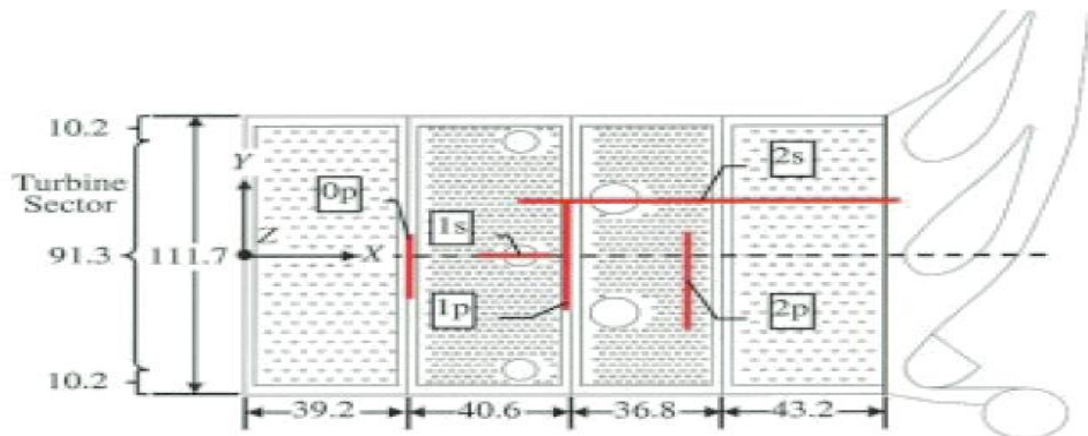
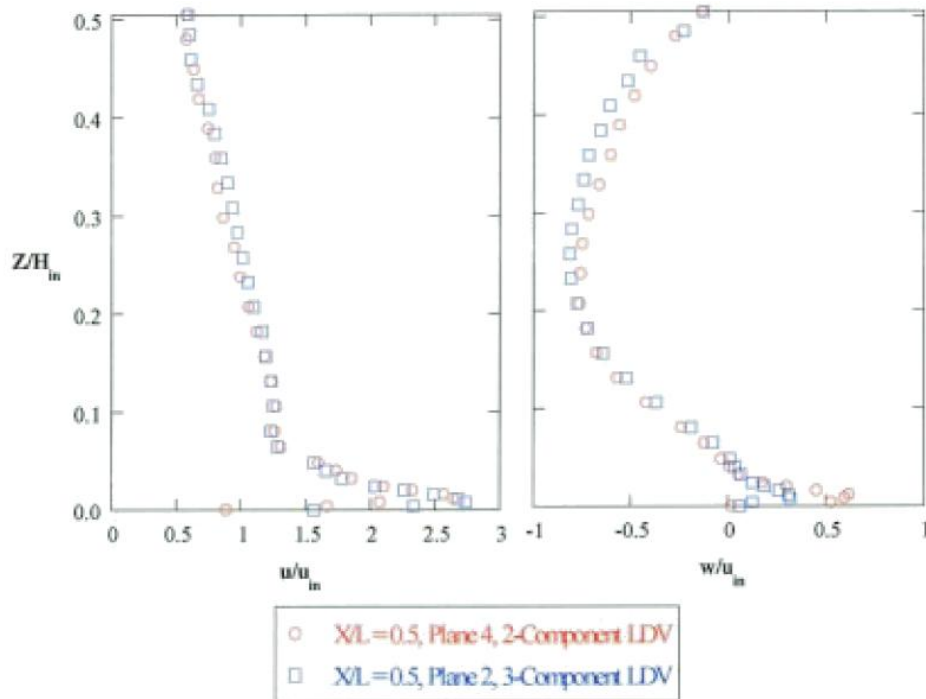


Figure 38: Layout and measurement planes for Vakil and Thole's combustor simulator (dimensions in cm) [4]

The main combustor flow (flow not coming from the annulus through the cooling and dilution holes) was heated using electrically heated bars in the flow. The flowfield was measured on the planes using a two-component or three-component laser Doppler velocimeter (LDV). A comparison between two- and three-dimensional LDV (Plane 4 and Plane 2, respectively) at the intersection of Plane 1p and Plane 2s is shown in Figure 39.

In order to perform these measurements, olive oil was used to seed the flow. The turbulence levels and three-dimensional turbulence fluctuations were measured for the planes after each of the dilution rows. The temperature field was measured using a thermocouple rake on all five planes. The thermocouple rake had 21 E-type thermocouple probes, which covered a distance of 10.2 cm. The thermal fields were shown in non-dimensional form as  $\theta = \frac{T_{\infty} - T}{T_{\infty} - T_c}$  where the measured temperature is normalised with the free-stream (primary flow) condition and the coolant (secondary flow) condition. The experiments conducted showed that the

dilution jets had a dominant role in affecting the flow and thermal fields of the combustor. The kidney-shaped thermal fields after the dilution jets were measured and found to be present as was expected. These phenomena are a result of the interaction of the jets with the mainstream. A recirculation region was found to occur just downstream of the jets, and it was found that this flow transported warm fluid to just behind the jets (see Figure 40 and Figure 41). The flow action just after the jet caused the near-wall cooling flow to become thinner just downstream of the dilution jet. The cooling flow then became thicker once it had passed the recirculation region.



**Figure 39: Comparison of two- and three-component LDV profiles measured independently in an overlap location downstream of the first row of dilution holes [4]**

The measured turbulence levels were found to be high throughout the combustor. The turbulent fluctuations for each of the three components showed an anisotropic characteristic, which is one of the possible reasons for turbulence models in general underpredicting the turbulence levels. The two-equation turbulence model assumes isotropic turbulence.

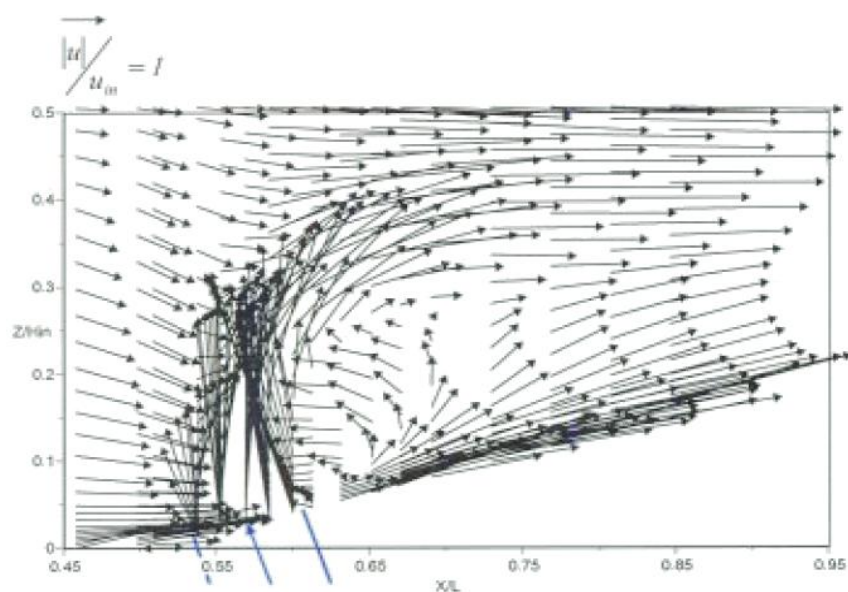


**Figure 40: Flowfield vectors for Plane 2s, downstream of the second row of dilution jets [4]**

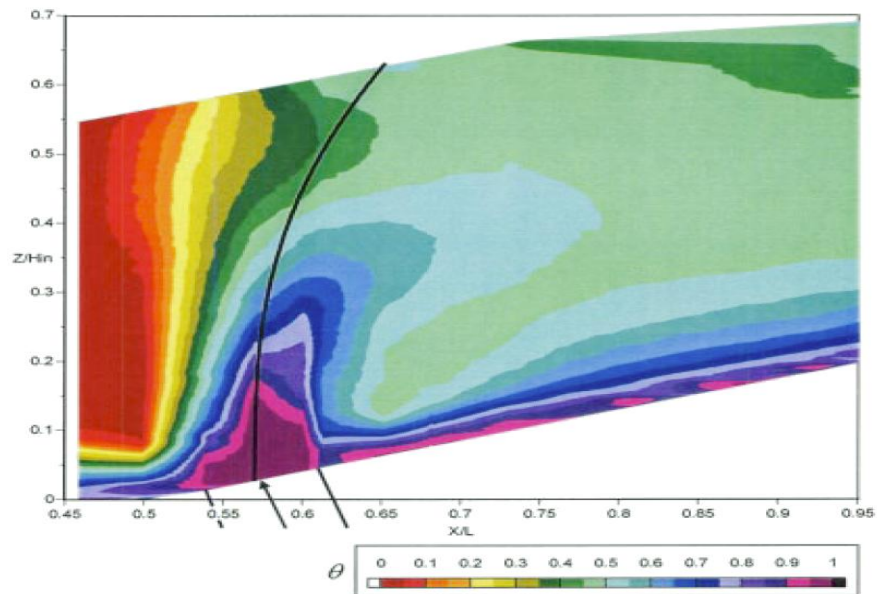


Figure 41: Thermal field contours for Plane 2s showing Lefebvre's jet penetration correlation [4]

Weigand *et al.* [13] measured the characteristics of an oscillating flame using non-intrusive laser-based techniques. The data was presented with respect to the phase position of the pressure fluctuations measured. The test rig consisted of a premixed combustor that was made up of four quartz walls set in a square with 85 mm sides. These walls were 114 mm long ending in a conical contraction at the outlet. The combustor had no primary, secondary, dilution or cooling holes and was mounted vertically. The combustor set-up is shown in Figure 42.

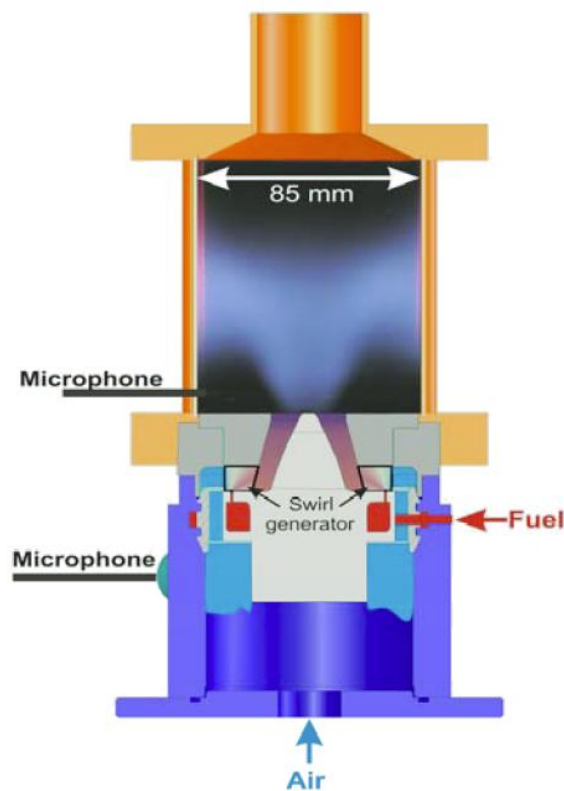
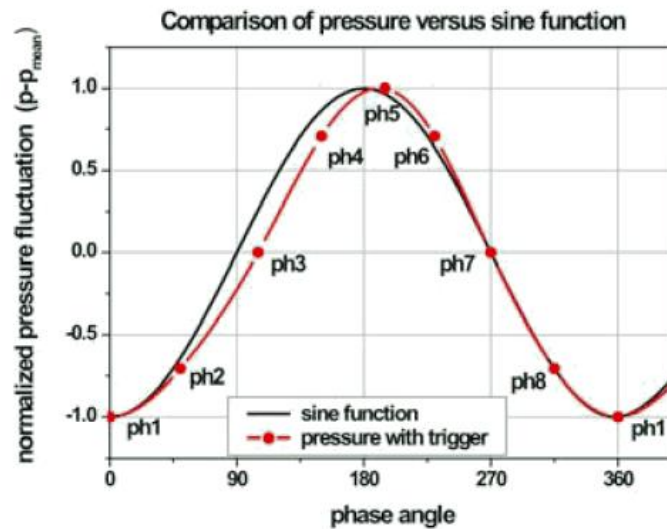


Figure 42: A schematic diagram of the injector with combustion chamber and a photograph of the flame in Weigand *et al.* experiments [13]

The airflow was fed into the premixing region along with the CH<sub>4</sub> (methane) gas, which was fed in radially to the plenum after which the fuel/air mixture passes through the swirler into the combustion chamber. Firstly, the pressure fluctuations in the plenum and combustion chamber were measured using two microphones. The fluctuations were found to be at a frequency of about 300 Hz. It was also found that the combustion chamber fluctuation was ahead of the plenum by about 80°. All the data measured was presented with respect to the plenum pressure fluctuation, which was divided into eight phases with Phase 1 at the minimum pressure, Phase 5 at the maximum pressure and Phase 3 and Phase 7 at zero pressure (see Figure 43). The other phases were spaced evenly in between those.



**Figure 43: Pressure oscillation compared with a pure sine function [13]**

The markers ph1 - ph8 indicate the assigned phase angles at which measurements were performed.

The velocity data was measured using a three-dimensional LDV system along radial profiles at axial distances of 6, 15, 25, 35 and 60 mm. A velocity plot is shown in Figure 44.

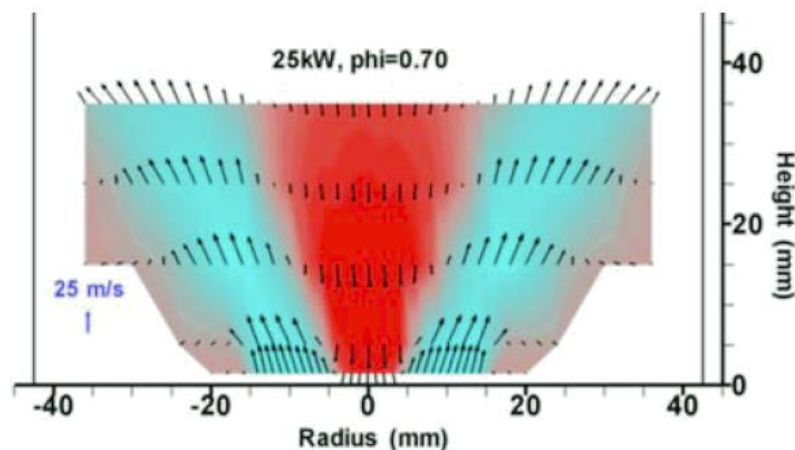


**Figure 44: A vector plot of the mean uv-velocities. Zones with negative and positive u velocities are marked red and blue, respectively (values mirrored for better visualisation) [13]**

These measurements were repeated for each of the eight chosen phases of the pressure fluctuation in the plenum. These results are shown in Figure 45.

An axial pumping motion was observed by plotting the forward and backward motion of the 0 m/s mean axial velocity isoline. Figure 46 shows the fluctuations of the isolines. Intensity changes in the inner recirculation

zone were observed corresponding to the axial velocity changes as well as the circumferential velocity changes.

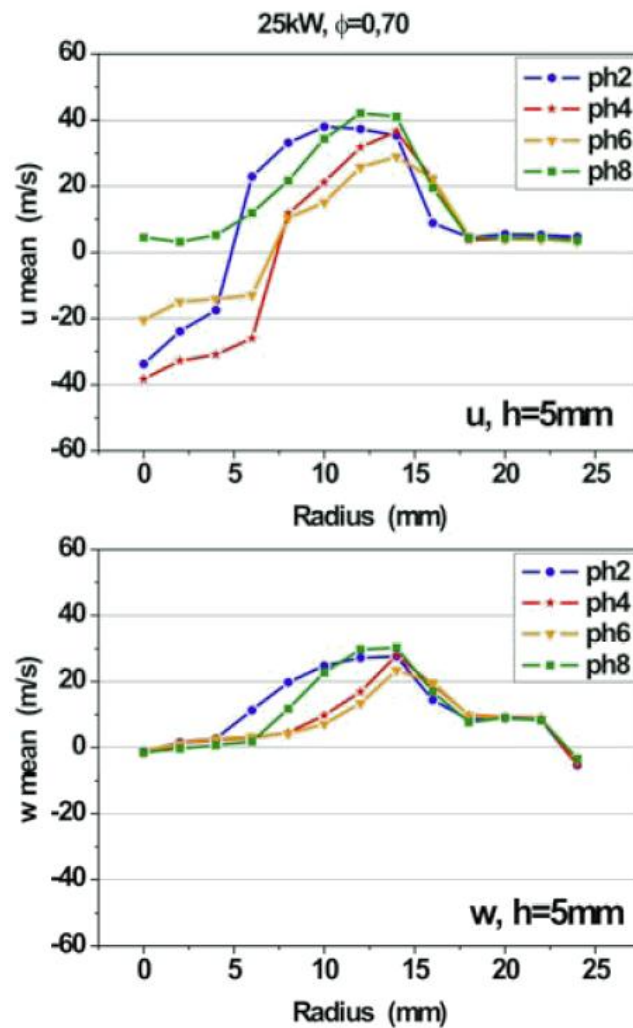


Figure 45: Radial profiles of axial velocity (top) and circumferential velocity (bottom) for different phase angles at an axial position of 5 mm [13]

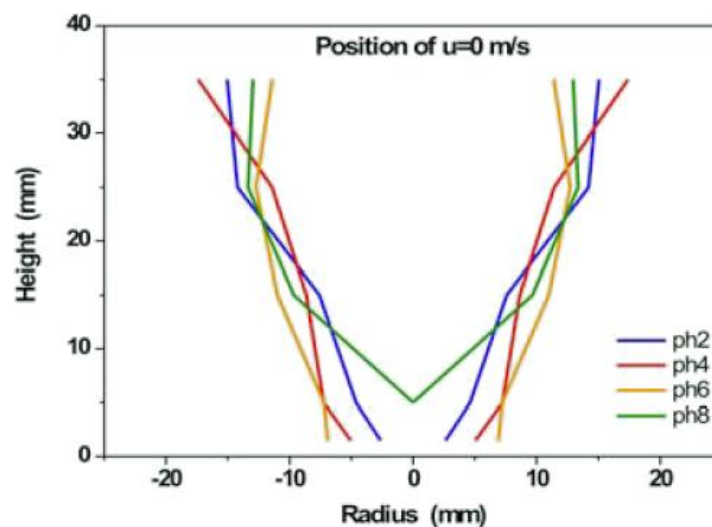


Figure 46: Contours of  $u = 0$  m/s for different phase angles indicating the changes of the inner recirculation zone during a pressure cycle (values mirrored for better visualisation) [13]

OH\* Chemiluminescence was performed to give indications of the heat release intensity, which gives an indication of the flame zone location. OH\* Chemiluminescence showed the position of the high intensity flames changing from near the nozzle in Phase 1 to along the cone to higher up and near the wall in Phase 3. This reaction is due to the changes in AFR coming into the combustor, which in turn is due to the pressure fluctuations experienced in the combustion chamber. Laser Raman spectroscopy was performed in order to measure the species concentration (in this case, CH<sub>4</sub> concentration), temperature and mixture fractions. Point measurements were taken using the laser Raman spectroscope and the region in between was interpolated. The temperature changes were shown over the pressure cycle, which showed a 60 to 90 degree lag to the heat release, i.e. the maximum heat release is at Phase 3 while the maximum temperature is at Phase 5.

The CH<sub>4</sub> volume fraction distribution was shown to correspond well with the temperature plots. Where there was high mass fraction of new, cooler mixture from the plenum, the temperatures were lower (see Figure 47). The mentioned measurements, especially the laser Raman spectroscopy, revealed good insight into the pressure cycle mechanism, which is described as follows: "The pumping behaviour of the flame is mainly due to changes in the equivalence ratio of the fuel air mixture entering the combustion chamber and not primarily due to acoustical effects." The pressure fluctuation is mainly caused by a variation of air/fuel mixture, which itself is caused by the pressure fluctuations. Pressure fluctuations cause the airflow velocity to fluctuate, but not so much the fuel flow velocity, and thus the AFR fluctuates between rich mixture and lean mixture causing the pressure fluctuations in the combustion chamber.

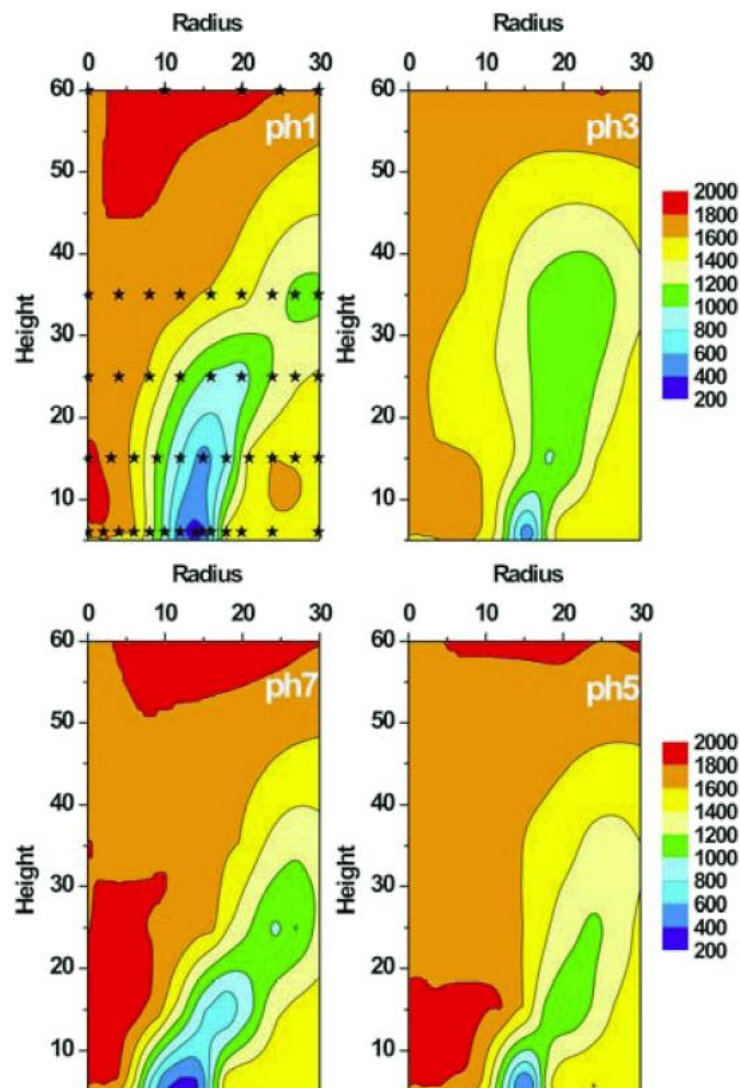


Figure 47: 2D temperature distribution from interpolation of single-point Raman measurements indicated by stars in ph1 image [13]

## 2.2 Relevance

The various experiments from the literature presented in the previous sections have many similarities and differences as well as a combination of advantages and disadvantages. The work presented in this dissertation is intended to perhaps improve on the disadvantages of some of the work but unfortunately also has various disadvantages of its own.

The experimental work, especially the optical experiments, in the combustor test rigs are often performed in approximations of gas turbine combustors with an annular combustor sector being approximated by a rectangular test section and the can-type combustors being approximated by square, rectangular or hexagonal cylinders or circular cylinders with flat sides/windows. The combustor used in this project is fully cylindrical with no flat edges, and the optically accessible combustor is a transparent replica of the metal combusting liner.

The experiments performed for this project, whether in the optically accessible combustor or the metal combustor, are performed on a full generic can-type combustor that includes a swirler, primary, secondary and dilution holes as well as the cooling rings. The data presented in the previous section often was measured on only a part of a combustor such as only a swirler or only the holes.

The experiments performed by Cameron *et al.* [14] are the most complete and most similar to the data sets acquired for this project. The disadvantage of the work by Cameron *et al.* [14] was that the combustor had flat sides for optical accessibility, no cooling rings, non-typical hole sets (only two zones not three) and the data was measured only on certain cross-sections along the full length of the combustor. With the newer measurement equipment (PIV) the data can be collected on whole planes at once thus the data presented here is more complete and has full planes at two orientations throughout the combustor.

There are a few disadvantages of the test rig and data collected for this dissertation. Firstly, the test rig is run under atmospheric conditions as opposed to the higher pressure (from 2 to 42 bar) usually provided by the compressor and the similarly higher back pressure provided by the turbine in practical combustor setups. Secondly, due to the lower pressure and commercial grade kerosene used, the temperatures are lower than expected in a practical combustor ( $T_{max} = 817K$  instead of 1850K in practical combustors [15]). Thirdly, the outlet is rather straight and does not have curves or a contraction at the outlet, which is often the case in a practical combustor. Fourth, the temperature measurements are performed by an intrusive thermocouple rake thus flow interruption occurs. Fifth, the PIV performed is without combustion due to the optically accessible combustor being manufacture out of perspex instead of a high temperature glass due to cost constraints and lastly, the PIV data provided is steady state data due to the PIV acquisition rate being too slow to provide full unsteady data. For these reasons it should be noted that the data set acquired here is to supplement the previous work since the effect of higher pressures and combustion on the flow can be seen in the experiments performed by others.

## 2.3 Methodology

### 2.3.1 Combustor pressure characteristics

A few factors are used to describe the characteristics of a gas turbine combustor [15]. It is desirable for the pressure drop across a combustor to be as small as possible with the loss in pressure contributing as much as possible to efficient combustion. This then implies that the pressure loss should be used for the proper mixing required for efficient and complete combustion. The two factors used to describe the pressure loss over the combustor are the overall pressure loss and the pressure loss factor. The pressure loss factor is an indication of the flow resistance introduced into the air stream between the compressor exit and turbine inlet due to the combustor liner presence. It is a sort of drag coefficient.

The total pressure drop across the combustor liner,  $P_{34}$ , is used in the calculation of the overall pressure loss and the pressure loss factor. The total pressure drop can be calculated using the following equation:

$$P_{34} = (p_3 + q_3) - (p_4 + q_4) \quad [3]$$

Since the test rig is open to atmosphere,  $p_4$  is the same as the atmospheric static pressure that is the atmospheric total pressure because the air in the room was stationary. Thus, the total pressure drop is calculated using

$$P_{34} = \left( P_{\text{atm}} + \Delta p_L + \frac{1}{2} \rho_3 V_3^2 \right) - \left( P_{\text{atm}} + \frac{1}{2} \rho_4 V_4^2 \right) \quad [4]$$

Using the total pressure loss value, the pressure loss factor is calculated using

$$\text{Pressure Loss Factor} = \frac{P_{34}}{q_3} \quad [5]$$

The overall pressure loss is the total pressure loss of the liner as a percentage of the total inlet pressure. The overall pressure loss is usually between 3 - 5%. The overall pressure loss is given by the following equation:

$$\text{Overall Pressure Loss} = \frac{P_{34}}{P_3} \times 100 \quad [6]$$

### 2.3.2 Combustor thermal characteristics

Just as for pressure, there are certain temperature factors that are used to describe the gas turbine combustor characteristics [15], namely the pattern factor and the profile factor. These factors are a guide as to how well the outlet temperature profile of the combustor complies with the requirements for the inlet temperature profile for the turbine. The ideal thermal profile is a flat profile at a temperature below a certain limit prescribed by the turbine requirements. The pattern factor is an indication of the "peakiness" of the outlet temperature profile. A flat profile would have a pattern factor of zero thus a smaller pattern factor indicates a trend towards the ideal profile. The pattern factor is calculated using the following equation:

$$\text{Pattern Factor} = \frac{T_{4\text{max}} - \overline{T_4}}{\overline{T_4} - \overline{T_3}} \quad [7]$$

where  $T_{4\text{max}}$  = Maximum temperature at the outlet

$\overline{T_4}$  = Average temperature at the outlet

$\overline{T_3}$  = Average temperature at the inlet

The profile factor is an indication of the gradient steepness of the outlet profile in the radial direction. The gradients in the radial direction are looked at alone because due to the rotating turbine blades, the gradients in the azimuthal directions are smoothed or smudged and thus the blades tend to only see a radial gradient. The profile factor too is zero for a flat profile and thus the smaller the profile factor, the better the life of the turbine due to a smaller thermal gradient in the radial direction. The profile factor is given below.

$$\text{Profile Factor} = \frac{T_{4\text{mr}} - \overline{T_4}}{\overline{T_4} - \overline{T_3}} \quad [8]$$

where  $T_{4\text{mr}}$  = Maximum mean value of all points at a common radius at the outlet (see Figure 48)

Decreasing trends in these factors can be used to show the effects of various inputs to the combustor system but care should be taken not to rely only on the factors, and the whole picture should be considered. Figure 48 shows an example calculation of  $T_{4max}$  and  $T_{4mr}$ .

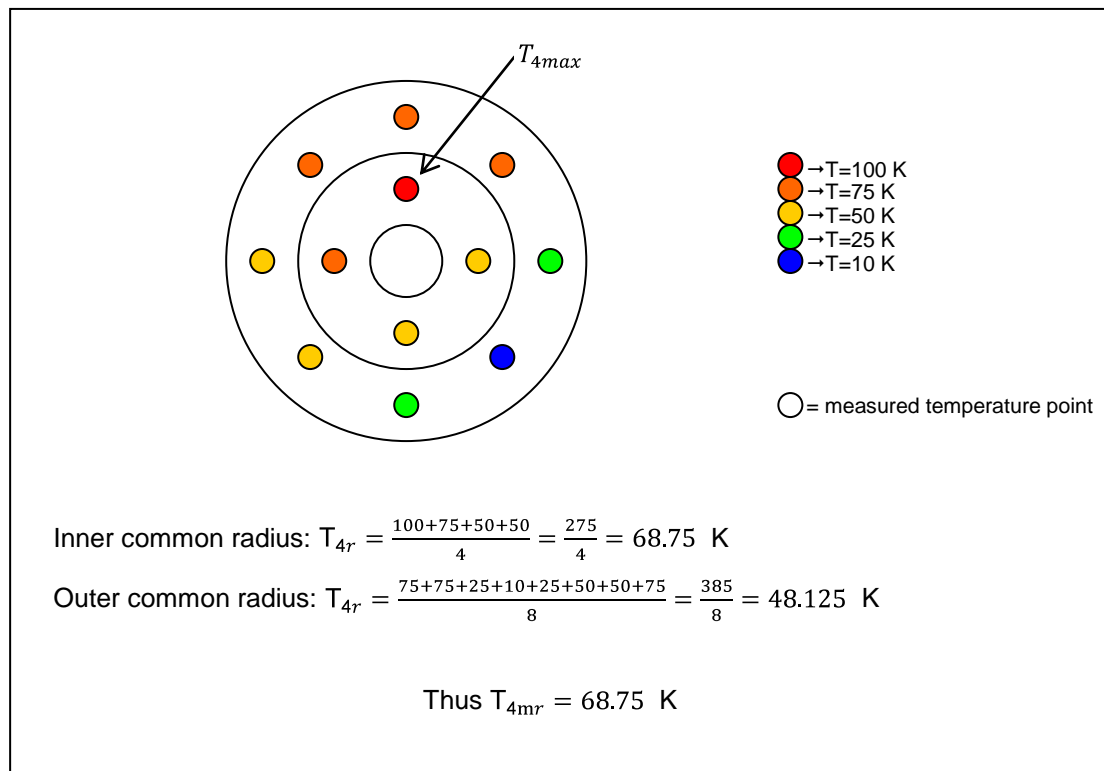


**Figure 48: An example calculation of  $T_{4max}$  and  $T_{4mr}$**

For this project, many batches of fuel were used for experiments that were done on different days with different ambient conditions. For this reason, the temperature values obtained for each point measured at the outlet profile were normalised using the adiabatic flame temperature,  $T_{AFT}$ , and the average combustor inlet temperature,  $\bar{T}_3$ . The normalised temperature at each point,  $i$ , at the outlet was calculated using the following equation:

$$\text{Normalised Temperature} = \frac{T_{4i} - \bar{T}_3}{T_{AFT} - \bar{T}_3} \quad [9]$$

The adiabatic flame temperature for all saturated hydrocarbon fuels with general formula  $C_nH_{2n+2}$  including kerosenes is 1990 K. To calculate the adiabatic flame temperature, the average temperature and average altitude in Pretoria, South Africa from the South African Weather Service [16] and Table A6 from White [17] were used to calculate the average atmospheric pressure for Pretoria, South Africa. This value and the average atmospheric temperature were then used to interpolate between the 30 kPa and 100 kPa  $T_{AFT}$  vs.  $T_{atm}$  graphs [18] to obtain the adiabatic flame temperature.

### 2.3.3 Swirl number

Two of the main flow features in the primary zone of a gas turbine combustor are swirling flow and a recirculation zone. The swirling flow is in the tangential/azimuthal plane of the combustor while the recirculation zone is in the axial plane. Swirling flow sets up the condition for a lower static pressure in the upstream region of the primary zone just after the swirler. This adverse gradient or decrease in upstream static pressure, when low enough, induces a reverse flow and thus a recirculation zone. For this reason, the strength of the swirl determines the presence and intensity of the recirculation zone. The swirl number ( $S_n$ ) is a non-dimensional value used to give an indication of the amount of rotation (called swirl) imparted to the

axial inlet flow by the swirler. The value of the swirl number is used to indicate if recirculation, and thus reverse flow, is present. If the  $Sn < 0.4$ , then the swirl is considered weak and no recirculation is obtained. For  $0.4 < Sn < 0.6$ , the swirl is considered to be of moderate strength. There will still be no recirculation present but the streamlines entering the combustor will be considerably divergent after the swirler inlet. Once the  $Sn > 0.6$ , the static pressure in the central core just downstream of the swirler will have decreased to the extent where reverse flow is induced. This is considered to be a strong swirl situation. In very high swirl cases where  $Sn > \pm 2.5$  (for flat vanes, and  $Sn > \pm 2$  for curved vanes), the reverse flow mass flow rate can exceed the swirler mass flow rate by entraining flow from the jets. Most practical swirlers operate in the strong to very strong swirl regime ( $Sn \gg 0.6$ ). [15]

The swirl number is defined as the ratio of the axial flux of angular momentum ( $G_m$ ) to the axial thrust ( $G_t$ ). The swirl number is defined by Lefebvre [15] as:

$$Sn = \frac{2G_m}{D_{sw}G_t} \quad [10]$$

where  $D_{sw}$  = The swirler diameter

The components of equation [10] are given as follows:

$$G_m = \int_0^{\frac{D_{sw}}{2}} 2\pi r W r \rho U dr \quad [11]$$

$$G_t = \int_0^{\frac{D_{sw}}{2}} 2\pi r \rho U^2 dr + \int_0^{\frac{D_{sw}}{2}} 2\pi r p dr \quad [12]$$

where  $U$  = The axial velocity at the cross-section of interest

$W$  = The tangential velocity at the cross-section of interest

$p$  = The static pressure at the cross-section of interest

$r$  = The radius at the cross-section of interest

$\rho$  = The density at the cross-section of interest

Substituting equations [11] and [12] into equation [10] the swirl number is given by the following equation:

$$Sn = \frac{2 \int_0^{\frac{D_{sw}}{2}} 2\pi \rho U W r^2 dr}{D_{sw} \int_0^{\frac{D_{sw}}{2}} 2\pi \rho U^2 r dr + \int_0^{\frac{D_{sw}}{2}} 2\pi r p dr} \quad [13]$$

In the case of Archer and Gupta [5], the static pressure term was not used and the swirl number is thus given by:

$$Sn = \frac{2 \int_0^{\frac{D_{sw}}{2}} 2\pi \rho U W r^2 dr}{D_{sw} \int_0^{\frac{D_{sw}}{2}} 2\pi \rho U^2 r dr} \quad [14]$$

It is assumed by the author that the pressure term in this case is disregarded by Archer and Gupta [5] due to an assumption that the static pressure is close to constant throughout the combustor liner and thus the contribution to the swirl number would be common throughout the combustor liner and can thus be

disregarded. Further simplification is achieved by assuming that the density along the cross-section is constant and removing the  $2\pi$  constants leading to the following equation:

$$Sn = \frac{2 \int_0^{\frac{D_{sw}}{2}} UW r^2 dr}{D_{sw} \int_0^{\frac{D_{sw}}{2}} U^2 r dr} \quad [15]$$

The same equation can be used to calculate the swirl number at any cross-section if the diameter used is replaced by the diameter at that cross-section [15]. Furthermore, if the absolute value is used, then the data from both sides of the centreline can be used giving the swirl number as follows:

$$Sn = \frac{2 \int_{-\frac{D_{cs}}{2}}^{\frac{D_{cs}}{2}} |UW r^2| dr}{D_{cs} \int_{-\frac{D_{cs}}{2}}^{\frac{D_{cs}}{2}} |U^2 r| dr} \quad [16]$$

In order to calculate the swirl number from discrete data, numerical integration is used thus transforming equation [16] into the following format:

$$Sn = \frac{2 \sum_{i=1}^n |0.5\{U_i W_i r_i^2 \Delta r_i + U_{i+1} W_{i+1} r_{i+1}^2 \Delta r_i\}|}{D_{cs} \sum_{i=1}^n |0.5\{U_i^2 r_i \Delta r_i + U_{i+1}^2 r_{i+1} \Delta r_i\}|} \quad [17]$$

where  $n$  = The number of data points from  $\frac{-D_{cs}}{2}$  to  $\frac{D_{cs}}{2}$

Equation [16] in the format of equation [17] was tested on some of the data published by Archer and Gupta [5]. Archer and Gupta [5] only presented the profiles over the radius of the combustor, so in order to test the calculation of the swirl number over the diameter of the combustor the axial profile was mirrored and the azimuthal profile mirrored and flipped to represent a full profile across the combustor diameter. The absolute values of the numerator and denominator were used so as to prevent the cancelling of the azimuthal velocity influence due to the one side being a flipped version of the other. Thus, using equation [17], the swirl number calculated with Archer and Gupta's [5] full diameter velocity profiles matched that calculated using their half profiles.

### 2.3.4 Particle image velocimetry

The definition of particle image velocimetry (PIV), according to TSI Incorporated [19], is that it is "an optical imaging technique to measure fluid or particulate velocity vectors at many points in a flowfield simultaneously". In order to use this technique, a range of apparatus is required. A shortlist of the equipment is given below:

- A laser sheet (dual laser for short time between pulses)
- An optically accessible test section
- Flow-compatible seeding particles
- Camera (two for three-dimensional velocities)
- A synchroniser
- A calibration target
- Analysis software

The basic method of applying stereoscopic PIV to obtain velocity fields in fluid flow is as follows. Seeding particles are introduced into the fluid and should be chosen such that they follow the fluid flow. The laser sheet is then shone into the fluid flow on the plane of which the velocity vectors are of interest. Two cameras are then placed at an angle to each other looking at the laser sheet. Two laser pulses occur and, synchronised with each laser pulse, a photograph of the particle images is taken simultaneously with the two cameras thus producing four photos: a Frame A and a Frame B for each camera where Frame A corresponds to the first laser pulse and Frame B corresponds to the second laser pulse. For each camera, the Frame A and Frame B are divided into interrogation areas and a cross-correlation is applied to calculate the velocity vectors in each camera view. Two images of two-dimensional flowfields, one for each camera, are then produced. Vector geometry along with a calibration function is then used to calculate the three-dimensional velocity vectors for the region of flow in the laser sheet.

For stereoscopic PIV, the cameras, lenses and laser sheet need to be set up in an arrangement that allows the best focus in the whole image. The configuration that allows the best focus is called the Scheimflüg stereoscopic arrangement [19]. This arrangement is such that the laser sheet plane, the lens principal plane and the image plane should intersect at a common line (see Figure 49). It can be seen that the camera and the lens are at an angle to each other. This enables the lens to focus the light from all sections of the object (which is also at angle to the camera and lens) onto the image plane. If the Scheimflüg stereoscopic arrangement is set up correctly, the whole image will be in focus.

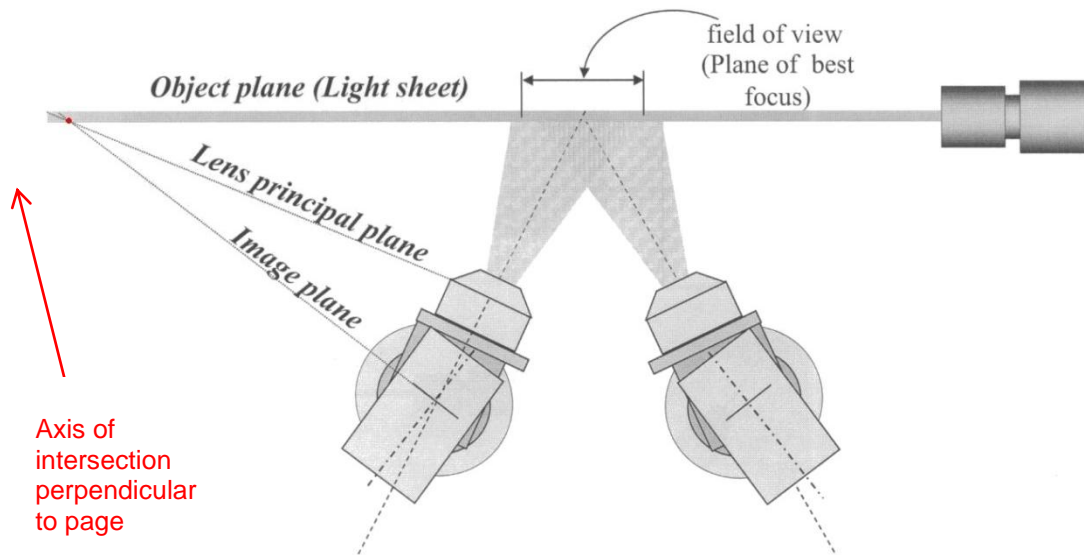


**Figure 49: Scheimflüg stereoscopic arrangement (adapted from [19])**

The camera locations can be in three geometric arrangements. The cameras can be either side of the laser sheet in a backward scatter configuration as in Figure 50. This configuration has a low light intensity, thus low contrast, which makes PIV analysis in this configuration difficult.

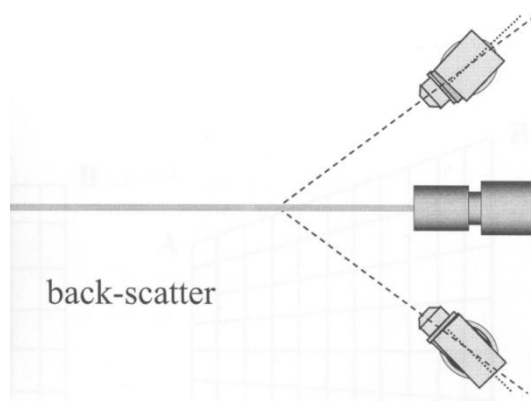


**Figure 50: A backward-scatter camera location [19]**

If the cameras are on either side of the laser sheet but facing the laser aperture, then it is in a forward-scatter configuration as in Figure 51. This configuration has high light intensity and thus could not have enough contrast for PIV analysis depending on the laser settings. If both cameras are on the same side of the laser sheet, then it is in a side-scatter configuration as in Figure 52. In this configuration, the two cameras will have different light intensities and one or both of the images could have analysis problems. There are methods to solve the intensity problems mentioned, e.g. changing the laser power settings or the laser lens that converts the beam into a sheet, thus choosing the camera locations would usually be driven by accessibility.

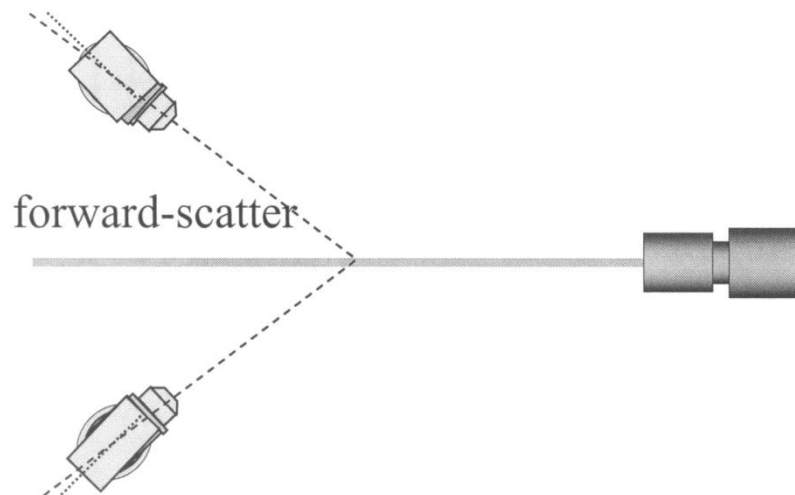


**Figure 51: A forward-scatter camera location [19]**

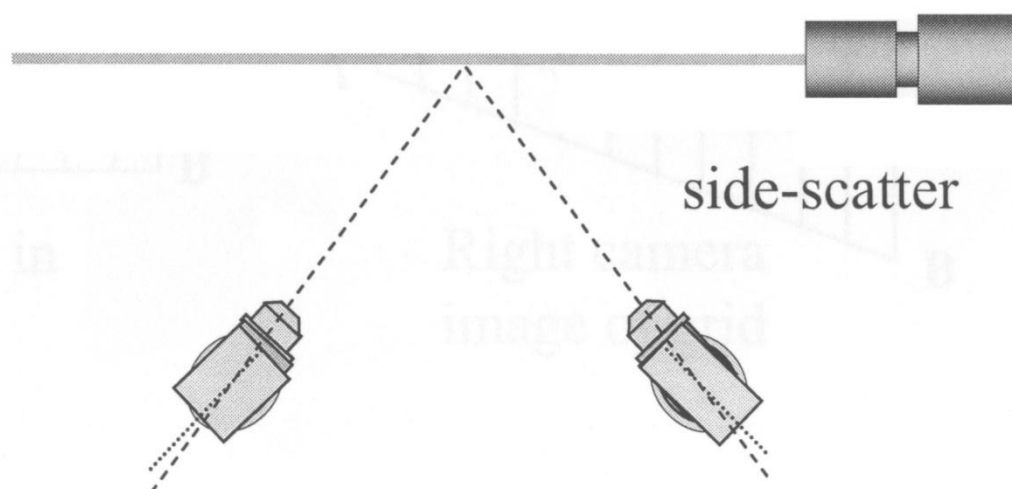


**Figure 52: A side-scatter camera location [19]**

In order to perform the PIV analysis, a calibration with a target with known spatial distances is used (see Figure 53). The target is coloured with black and white to get a maximum contrast in the images to enable more accurate calibration. The target has grooves so that calibration for the velocities perpendicular to the light sheet can also be calculated. The target's uppermost surface should be aligned with the laser sheet to ensure that the calibration algorithm can be calculated for the plane where the laser sheet will shine. The cameras are then adjusted by configuring the cameras according to the Scheimflug stereoscopic arrangement discussed above thus achieving a best focus view. An initial set of photos is then captured with the cameras in their correct positions using the PIV software. Using the two images, a calibration algorithm is calculated. The calibration algorithm will compensate for curvature of test section walls, the magnification of the lenses, the perspectives of the two cameras (see Figure 54) and any other image-distorting factors that may be present. Figure 55 shows the corrections made to each of the images by the PIV software, Insight3G [20].



Figure 53: A black and white calibration target [21]

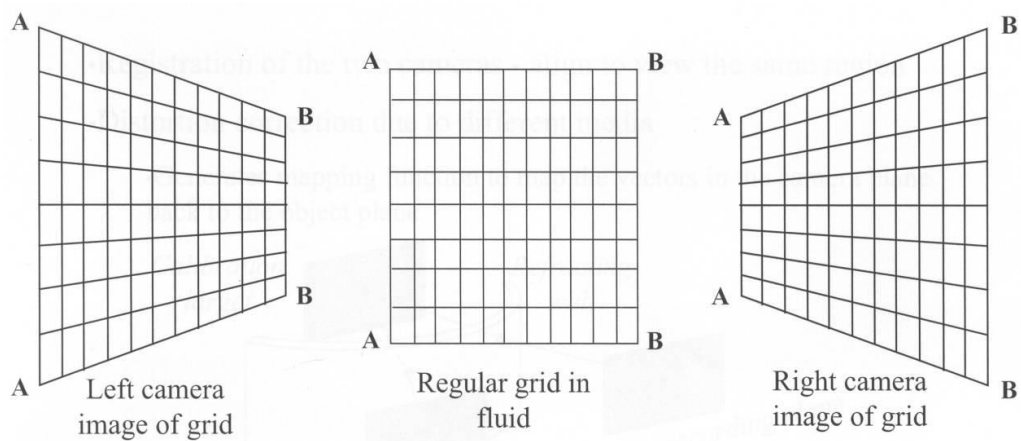


Figure 54: A diagram showing the grid distortion due to camera perspective [19]

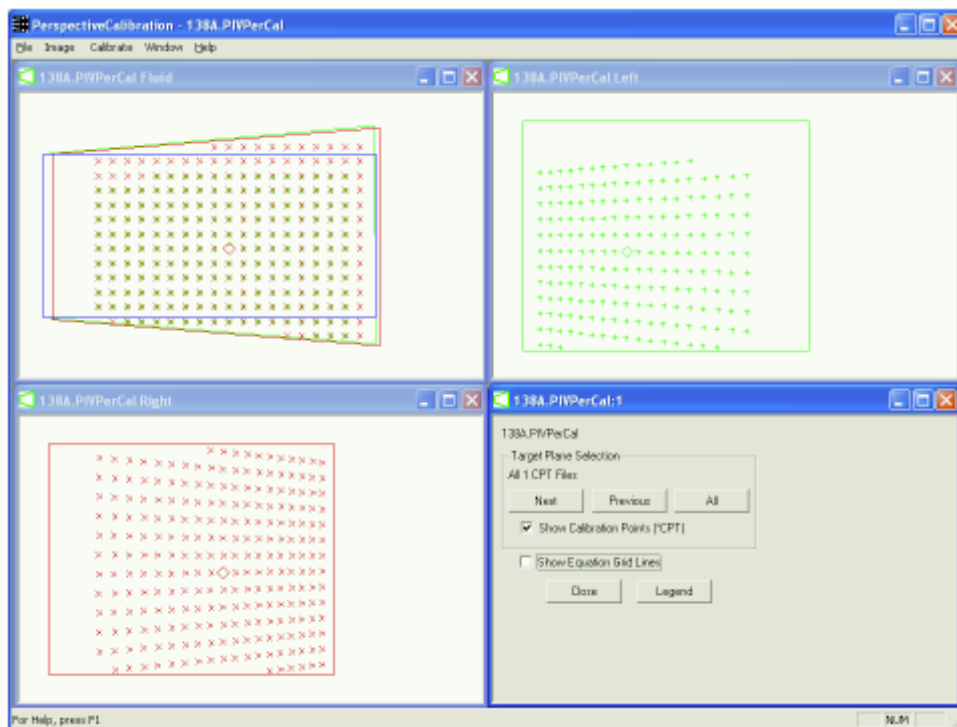


Figure 55: PIV software, Insight3G, showing the image correction using the calibration algorithm [22]

Once the calibration is done, then the actual data collection can begin. The fluid flow is started and the seeding particles added. The choice of seeding particle and insertion is based on the following aspects:

- the type of flow phenomena to be shown;
- the particle's ability to follow the flow;
- the particle's ability to reflect light;
- the distribution required for good analysis.

If the general flowfield is the result one is aiming for, then larger particles are used. In order to pick up turbulence in the flow, then submicron particles in the order of  $0.3 \mu\text{m}$  are used. For the flow characteristics to be found, the particles need to follow the flow correctly. How well they follow is dependent on the particle density and diameter. If the particle is much denser than the fluid flow, it will have a tendency to overshoot flow direction changes and vortices. If it is a lot less dense than the fluid, then buoyancy forces will become significant and the particles will not show true flow phenomena. The particle diameter also is important because if it is too large, then the flow phenomena smaller than it will not be able to affect the particle path. The particle size should be smaller than the size of the phenomena trying to be found. The particle should also be as spherical as possible. Light intensity and contrast play an integral part in the cross-correlation performed by the PIV software and thus the particles should be able to reflect light effectively so that the particles are considerably brighter than the surrounding surfaces. The distribution of the particles should be such that in the area of interest each interrogation region has enough particles for a correlation to be found between the images, but not so dense that the contrast is lost and the cross-correlation cannot find a trend.

In order to ensure that the laser pulses and the camera exposures overlap correctly, a synchroniser is used. The synchroniser ensures that the first laser pulse occurs near the end part of the cameras' Frame A (Frame 1 in Figure 57) exposure and that the second laser pulse occurs near the beginning of the Frame Bs (Frame 2 in Figure 57). This is called frame straddling and can be seen in Figure 56 and Figure 57. As can be seen by the timing diagram in Figure 56, each event needs to occur at the correct time to ensure the success of the PIV image capture. It can also be seen that the transferring of the image back to the computer is the bottleneck and determines the maximum rate at which PIV images can be captured. The synchroniser can also be used to synchronise the PIV image capture with an external trigger as well as to control the start and stop of a seeder so that seeding particles are only inserted when needed.

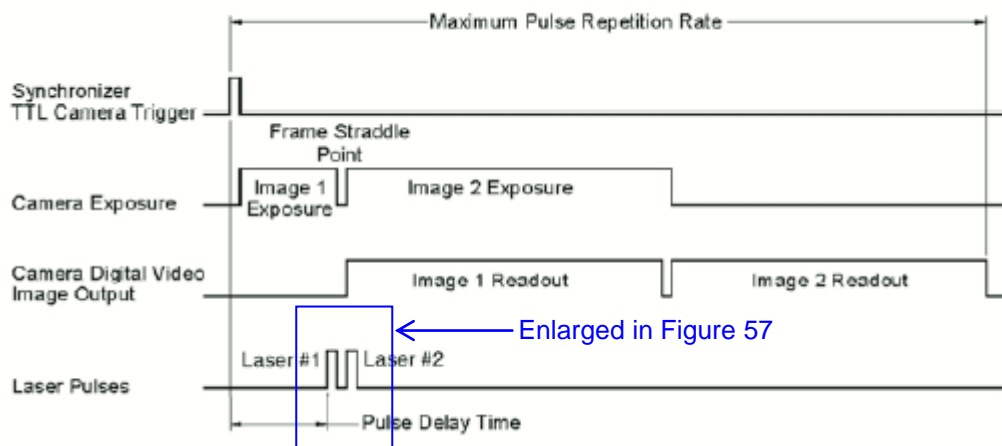


**Figure 56: A timing diagram to show synchronisation of various events [23]**

Once a set of PIV images are captured, a cross-correlation is performed using Frame A and Frame B of each camera to find the representative vector magnitude and direction. The images are in greyscale format and thus each pixel is evaluated and assigned a number from 0 to 255 depending on the pixel brightness. Figure 58 is a simplified diagram to show the basic method of the cross-correlation.

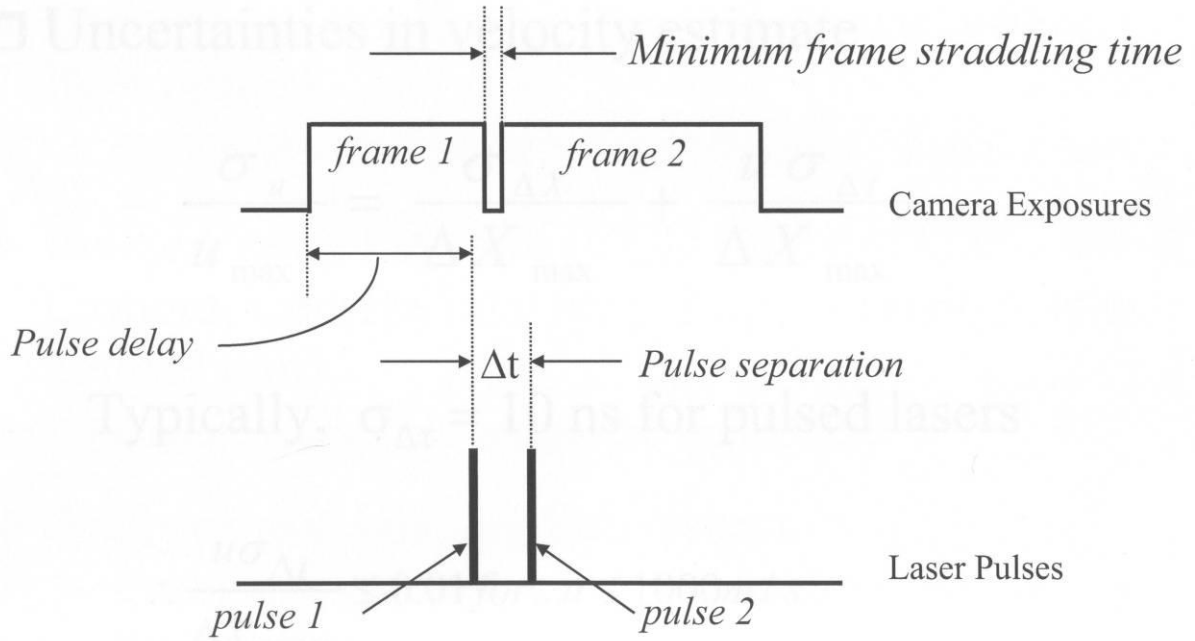


**Figure 57: A timing diagram showing frame straddling [19]**

In Figure 58, Frame A has a bright particle at  $A_5$  and in Frame B, this same particle has moved to  $B_{15}$  thus  $A_5$  and  $B_{15}$  have the value of 255 while the rest of the interrogation region has a value of 0 due to there being no reflection. The two Frames A and B are then divided up into smaller sections called interrogation regions. The two corresponding interrogation regions are then “unfolded” to form two vectors, A and B, of greyscale numbers. A is a  $1 \times a$  vector while B is a  $1 \times b$  vector. In this simple case, a and b are the same value and are equal to 16. Due to the cross-correlation method described below, Vector B needs to be padded with zeros. A new Vector B' is thus created by defining the first  $a - 1$  components to be zero, the next b components to equal the components of B and then the last  $b - 1$  components to be zero. The cross-correlation is then given by

$$G_j = \sum_{j=-(a-1)}^{b-1} \sum_{k=0}^{a-1} A_k B'_{k+j} \quad [18]$$

Each G value is then put into a vector,  $R_{AB}$ , which will show the number of spaces between the particle's initial position in Frame A and its final position in Frame B. Using this spacing and the known interrogation region dimensions, the magnitude and direction of the vector can be drawn. This vector is then drawn initiating from the centre pixel of the interrogation region. The magnitude of Vector  $R_{AB}$ , is given by

$$R_{ABi} = \sum_{i=0}^{a+b-2} G_{[i-(a-1)]} \quad [19]$$

The naming of the elements of Vector  $R_{AB}$  has the following format:

$$R_{AB} = [R_{-(a-1)} R_{-(a-2)} R_{-(a-3)} \cdots R_{-1} R_0 R_1 \cdots R_s \cdots R_{b-1}] \rightarrow 1 \times (a + b - 1) \quad [20]$$

The  $a^{\text{th}}$  element,  $R_0$ , represents the position of the original bright pixel in the Frame A interrogation region and the position of the peak value,  $R_s$ , with respect to the  $R_0$ , will give the number of pixels away, s, that the particle has moved. If  $R_s$  lies to the right of  $R_0$  then the pixels are counted in the rightward direction from the original pixel, wrapping around when the edge of the interrogation region-sized grid is reached. If  $R_s$  lies to the left, then the opposite direction is counted but there is still wrapping at the edges of the grid. The direction and magnitude of the vector are then found and placed at the centre of the interrogation region grid. This procedure is shown in Figure 59.



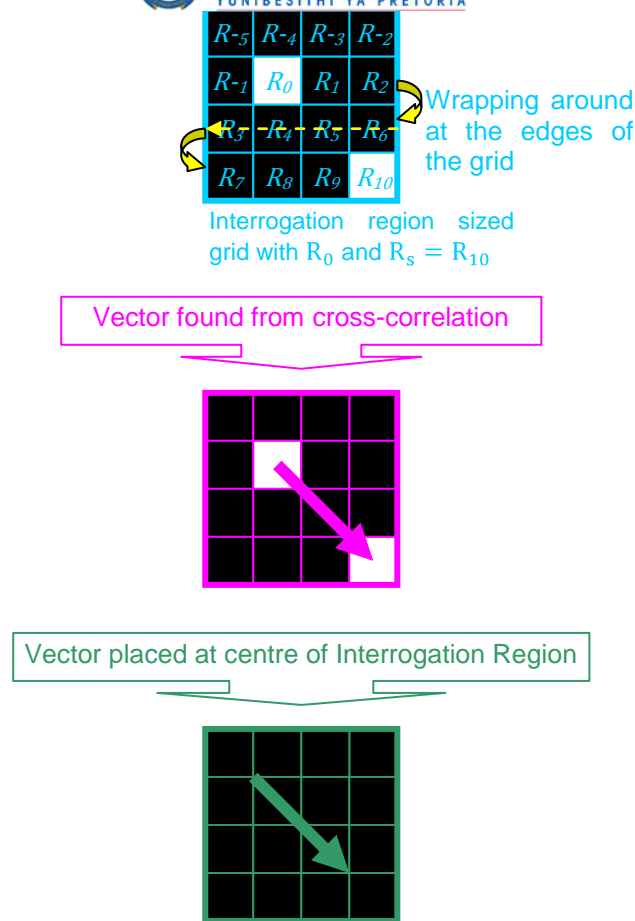


**Figure 59: A basic vector calculation procedure for particle tracking**

This procedure is performed for each interrogation region in the image and a first iteration for the flow vectors is complete. In reality, other information and techniques are combined with this procedure to deal with the edges of the interrogation regions in instances such as if a particle leaves or enters the region between Frame A and Frame B, then this would need to be disregarded.

For the second iteration, the interrogation regions are divided into smaller interrogation regions for further vector calculations. This procedure is performed differently from the first one in that instead of the interrogation regions moving across and wrapping around, they are moved in the direction of the first vector found in the larger interrogation region. This method is to hopefully find more particles that have remained in the interrogation region and thus be able to fine-tune the vector calculated in the first iteration.

These vectors supply two components for the particle movement for each camera. Using the magnification,  $M$ , the vector components  $\Delta X$  and  $\Delta Y$  and the time between frames,  $\Delta t$ , the two component velocity vectors are then calculated for each camera as seen in Figure 60. The magnification is one of the values calculated during calibration.  $\Delta x$  and  $\Delta y$  in Figure 60 are the true  $x$  and  $y$  displacements and  $u_x$  and  $u_y$  are the calculated velocity components in the  $x$ - and  $y$ -direction, respectively.

The two iterations demonstrated above may seem like a trivial procedure since the vector in the example case could have been found by inspection but for an actual set of images, as can be seen in Figure 61, there are often many particles. The particles are the grey grainy mass in the image. There are also many interrogation areas with much larger grid sizes (usually of the order of  $64 \times 64$ ).

When the above procedure is performed on real PIV images, then  $R_{AB}$  looks more like Figure 62. What can also be seen in Figure 62 is that the "peak" representing the new position of the particle actually covers more than one pixel and is made up of a few peaks. The height of the peaks making up the set can be slightly skewed. Each peak is a whole pixel big, which could limit the resolution to that of the camera, which would then limit the accuracy of the procedure to one pixel. To overcome these two aspects, a sub-pixel

interpolation is performed. This is done by fitting a Gaussian curve to the peak set thus estimating the actual position of the highest point of the highest peak within that pixel.

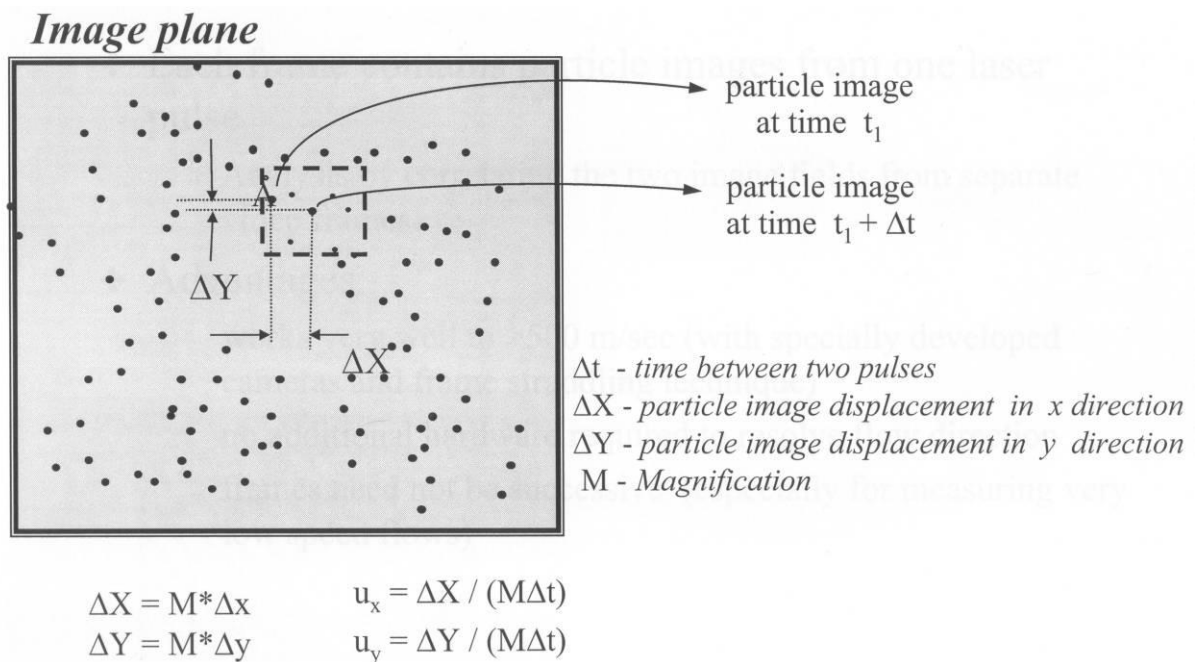


Figure 60: Diagram showing the calculation of the velocity vector [19]

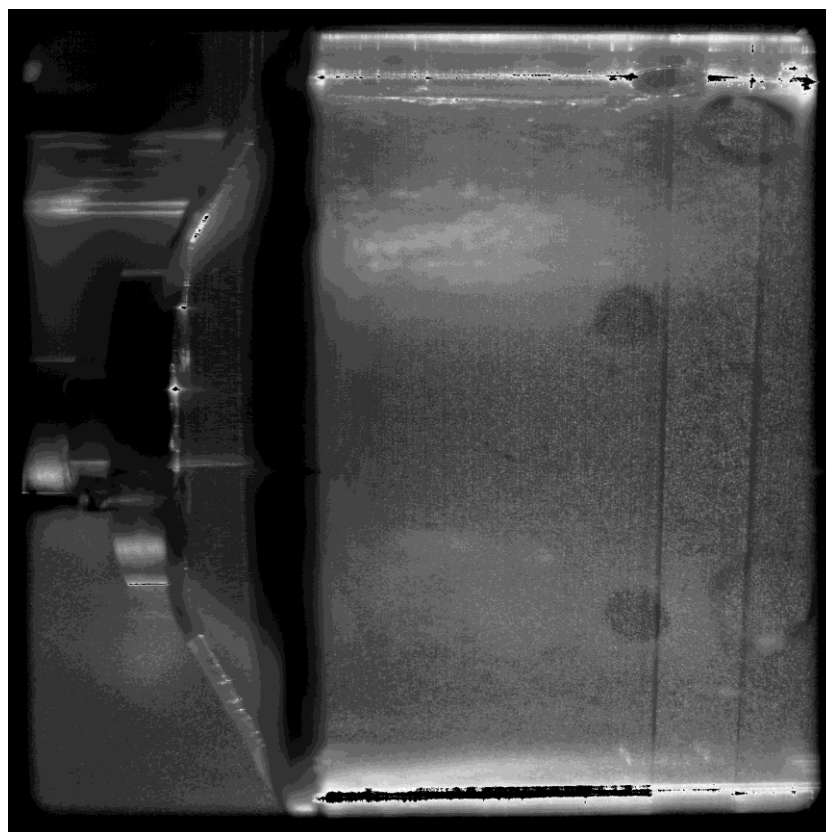
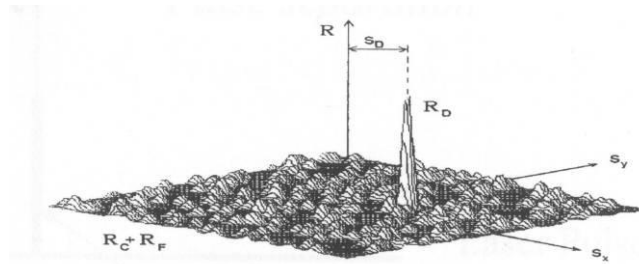


Figure 61: A particle image for PIV analysis in the primary zone of the can-type combustor

The PIV result is two images with two-dimensional vector plots. These two two-dimensional vector plots then need to be combined using vector geometry to show the three-dimensional vectors in that region. The out-of-plane vector is calculated from the two corresponding two-dimensional vectors similarly to the method shown in Figure 63. The camera angles and interpretation of actual distances are found during the calibration stage.



## Crosscorrelation

Figure 62: A cross-correlation diagram with one dominant peak set [19]

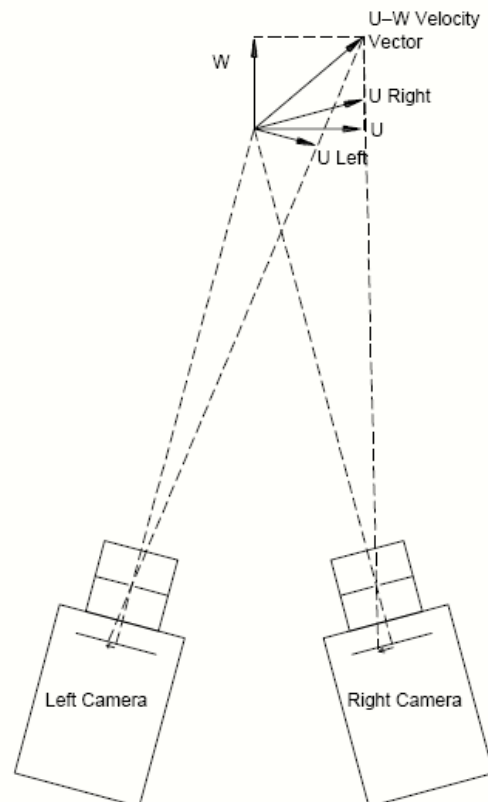


Figure 63: Diagram showing the resolving of the out-of-plane vector [24]

## 2.4 Summary

In this chapter a literature study was presented. The purpose of the literature study was to investigate if there was a general need for experimental test cases for CFD comparison, what data was already available and the experimental methods used to collect the data sets in previous work. Cameron *et al.* [14] had a data set most similar to that measures in this study.

The combustor used by Cameron *et al.* [14] was almost a complete can-type combustor with a swirler and two sets of holes. The velocity and temperature profiles were measured in both reacting and non-reacting flows. Janus *et al.* [9] and Weigand *et al.* [13] also presented detailed velocity data in the primary zone of can-type combustors, however, their set-ups only had a swirler in a can-type combustor configuration.

In the work presented by Cameron *et al.* [14], Janus *et al.* [9], and Weigand *et al.* [13] the primary zone velocity profiles showed a reverse flow region in the centre of the combustor with forward flow at the outer



radius indicating a recirculation zone. In the secondary zone, after the first set of jets, Cameron *et al.* [14] showed the velocity profile no longer had reverse flow at the core and had instead transitioned to a large positive velocity profile at the core of the combustor with the outer radius velocities close to 0 m/s. As the flow advanced downstream the velocity magnitude at the core started to decrease as the second set of jets was approached. Finally at the outlet of the combustor, after the second set of jets, a slightly bell shaped positive profile was measured.

This chapter also presents the factors that are used to represent the flow characteristics of a gas turbine combustor as well as showing a simplification of the calculations performed by the PIV software during analysis.

### 3 EXPERIMENTAL PROCESS

#### 3.1 Introduction

In this chapter the experiments performed to capture the data for the experimental test case for CFD validation are discussed. The test case consists firstly, of a base case reacting experiment in the metal combustor where temperature and velocity profiles are measured; secondly, a non-reacting experiment where the velocity fields on various planes are measured in a transparent combustor and where the effect of flow rate are investigated; and finally, a reacting test where the effect of passive inserts (wedge rings) are evaluated by comparing the temperature and velocity profiles to the base case reacting test.

The experimental test matrices for all the experiments performed are shown in Table 2 and Table 3. The base case reacting experiment consists of the unmodified original combustor liner from the test rig. This liner was designed for a nominal air mass flow rate of 0.1 kg/s and an AFR of 100. For the reacting experiments the test rig was run as close as possible to the design point. The base case for the reacting tests is the no wedge ring setup shown in Table 2 with a green border. The base cases for the non-reacting experiments are shown in Table 3 with the light blue border. These six experiments were done to obtain the planes of flowfield data in line with and in between the holes in each of the three zones. The flow rate for these experiments was 60% of the reacting experiment flow rate. Further non-reacting PIV experiments were performed on the transparent combustor liner with increasing flow rates. These experiments are shown as green shaded cells in Table 3. The experiments with the varying wedge ring configurations are shown in Table 2. These experiments were also performed under reacting conditions. All the reacting experiments have the same flow rate as the PIV experiments performed with the highest flow rate. This is indicated with the red border around Table 2 corresponding to the red border around the Dilution zone (Dz) experiment with  $\dot{m}_A = 0.091$  kg/s in Table 3.

**Table 2: The experimental test matrix for the reacting experiments**

Data types measured	Wedge ring configuration →	Both wedge rings	Pz wedge rings	Sz wedge rings	No wedge rings (base case)
Wedge ring set ↓		<ul style="list-style-type: none"> <li>• Outlet plane temperature contours</li> <li>• Outlet Velocity profile with combustion</li> <li>• Outlet Velocity profile without combustion</li> </ul>			
10%					
30%					

= Reacting flow base case

**Table 3: The experimental test matrix for the PIV experiments**

PIV Test matrix	Air mass flow rate →	$\dot{m}_A = 0.056$ kg/s		$\dot{m}_A = 0.059$ kg/s		$\dot{m}_A = 0.064$ kg/s		$\dot{m}_A = 0.070$ kg/s		$\dot{m}_A = 0.078$ kg/s		$\dot{m}_A = 0.091$ kg/s	
	Laser Position →	In line Holes	In between										
Pz	Section ↓ Camera Angle ↓												
	T = 5° B = 20°	3D: 15 μs	3D: 15 μs	3D: 15 μs									
Sz	T = 0° B = 23°	2D: 15 μs	2D: 15 μs										
	T = 5° B = 20°	3D: 5 μs	3D: 5 μs					3D: 2.5 μs				3D: 2 μs	
Dz	T = 0° B = 23°	2D: 15 μs	2D: 15 μs										
	T = 5° B = 20°	3D: 5 μs	3D: 5 μs					3D: 4 μs				3D: 2 μs	
	T = 0° B = 23°	2D: 5 μs	2D: 5 μs										

= Completed PIV Experiments  
 = Experimental setup for combustion tests (see Table 3)  
 = Not planned for this project  
 = Experimental setup for isothermal base case tests  
 Pz = Primary zone  
 Sz = Secondary zone  
 Dz = Dilution zone  
 $\dot{m}_A$  = Air mass flow rate  
 T = Top camera  
 B = Bottom camera

The CFD test case consists of the reacting experiment base case and all the non-reacting PIV experiments. The PIV experiments include the base case and increasing flow rate data as well as the data that indicates the temporal nature of the combustor. The passive inserts experiments consist of the reacting experiment base case compared to all the wedge ring reacting experiments.

The experimental set-up and method for all these experiments is discussed in the following sections.

## 3.2 Experimental set-up

### 3.2.1 Reacting experiment

The gas turbine combustor test rig (Figure 64) consists of a fan run by an 11 kW motor to supply the air for combustion. The fan is attached to one end of a set of pipes with the combustor liner placed at the other end of the pipes at the outlet. The combustor then exhausts to atmosphere. Figure 65 shows a schematic diagram of the test rig. A photograph of the actual test rig is shown in Figure 64.

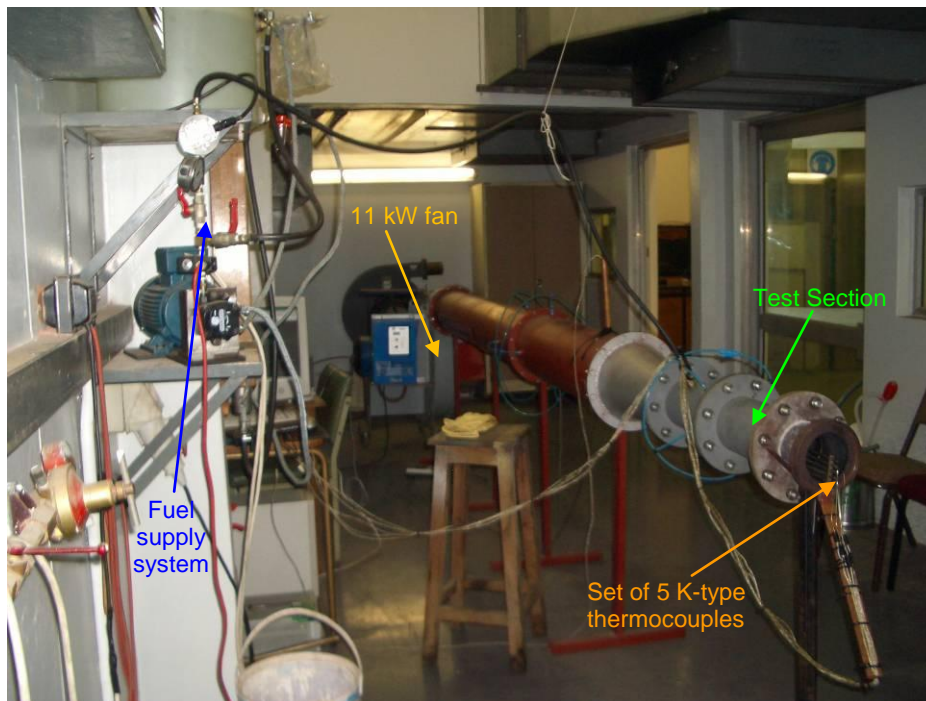


**Figure 64: The combustor test rig**

The fuel supply system consisted of a tank that contained the fuel, in this case kerosene, a fuel pump to ensure a constant pressurised supply of fuel and a variety of pipes and valves connecting the components. The fuel line terminated in the centre of the combustor liner swirler with an injector to inject a cone-shaped fuel spray. One of the fuel paths contained a glass burette used for metering the fuel. This burette had two lines marked on it above and below the top bubble between which the fuel usage could be measured. The burette could also be isolated from the tank so that all the fuel used for combustion only came from the burette. Figure 66 shows the fuel system including the burette.

The combustor liner is a non-premixed can-type combustor. Figure 67 is a close-up of the liner. The combustor has an annular swirler in the dome to allow for mixing and recirculation. The swirler has 10 flat vanes angled at  $50^\circ$  to the inlet plane (see Figure 68). The fuel is injected in the centre of the swirler from an  $80^\circ$  cone injector. The primary zone has six circular holes each 9.5 mm in diameter and evenly spaced around the combustor circumference. There are eight secondary zone holes of 5 mm each also evenly spaced around the circumference. The dilution zone has ten evenly spaced holes of 11.8 mm each.

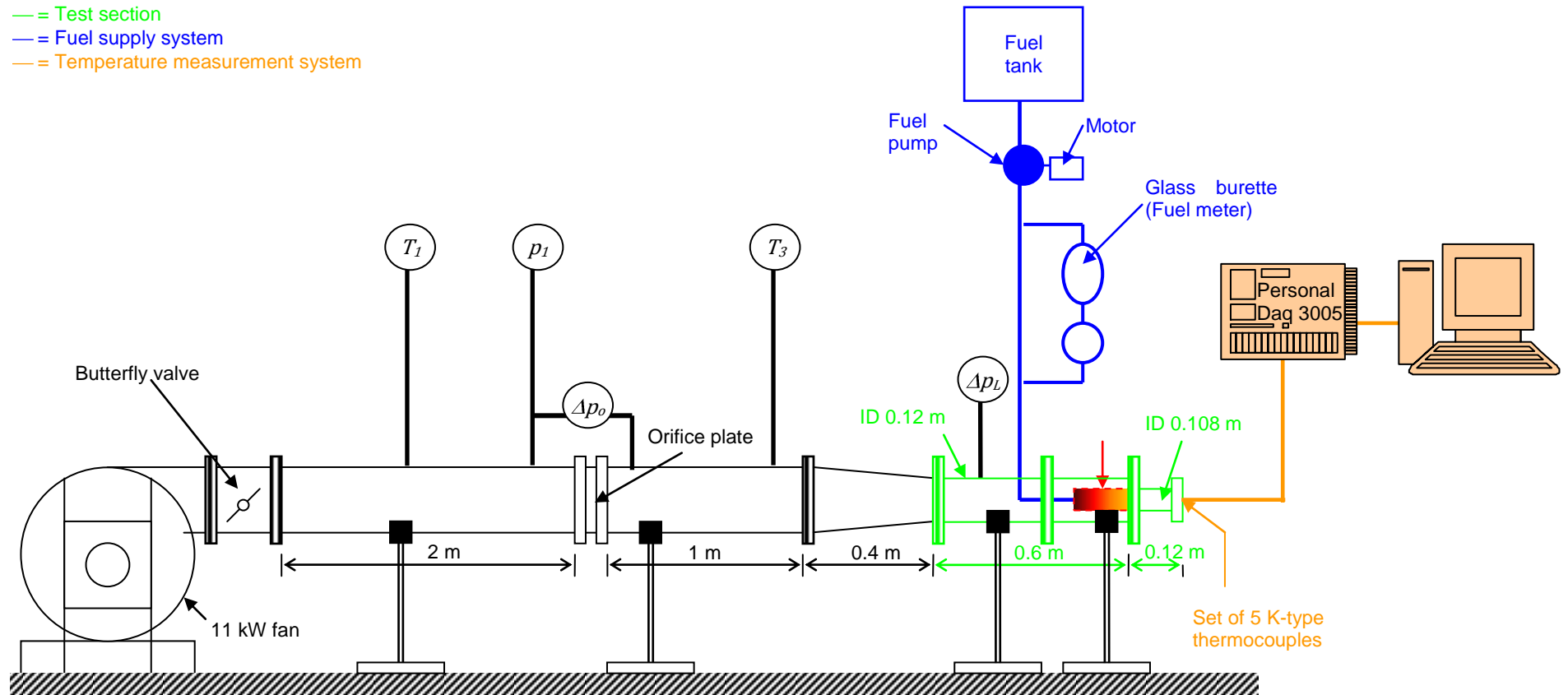


Figure 65: A schematic diagram of the combustor test rig

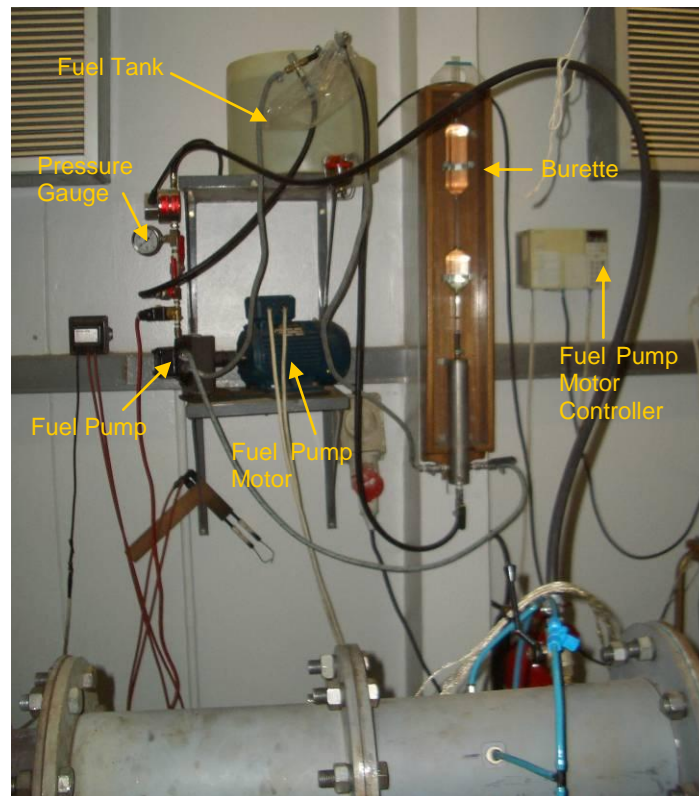


Figure 66: A close-up of the fuel system

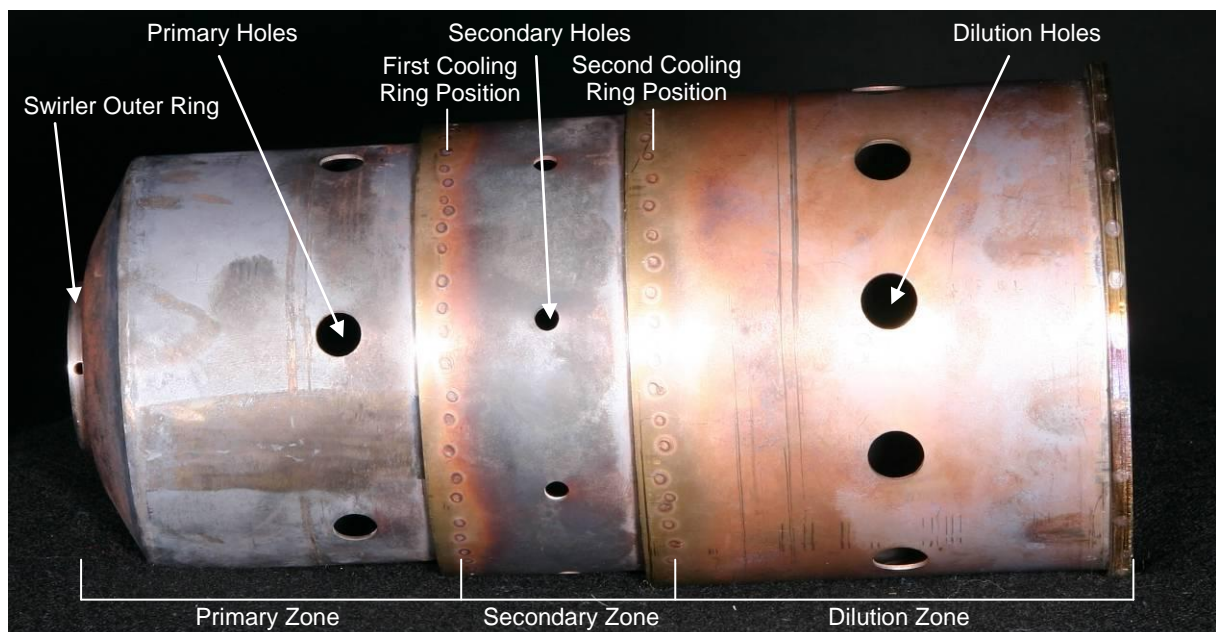


Figure 67: A close-up of the combustor liner

The dilution zone wall and the secondary zone wall have cooling rings with 50 and 30 holes, respectively, with a diameter of 1.2 mm each. A drawing of the combustor with its dimensions is shown in Figure 69.

To keep track of the atmospheric conditions in each experiment, the atmospheric temperature,  $T_{atm}$ , and pressure,  $P_{atm}$ , were measured. The atmospheric temperature was measured using a mercury thermometer with 2 °C increments and the atmospheric pressure was measured using a Fortin barometer.

An orifice plate was used for mass flow rate calculations using the method described in Appendix B and equations [B-17], [B-18] and [B-19]. The upstream orifice plate temperature,  $T_1$ , was measured using a

PT105 probe with a digital display inserted into the pipe between the fan outlet and orifice plate. The pressure drop across the orifice plate,  $\Delta p_o$ , as well as the difference between the atmosphere and upstream pressure was measured using a dpm t-series digital manometer. The inlet combustor temperature,  $T_3$ , was measured using one K-type thermocouple inserted into the pipe upstream of the combustor. The pressure drop across the liner,  $\Delta p_L$ , was measured using the same manometer used to measure the pressure drop across the orifice plate.

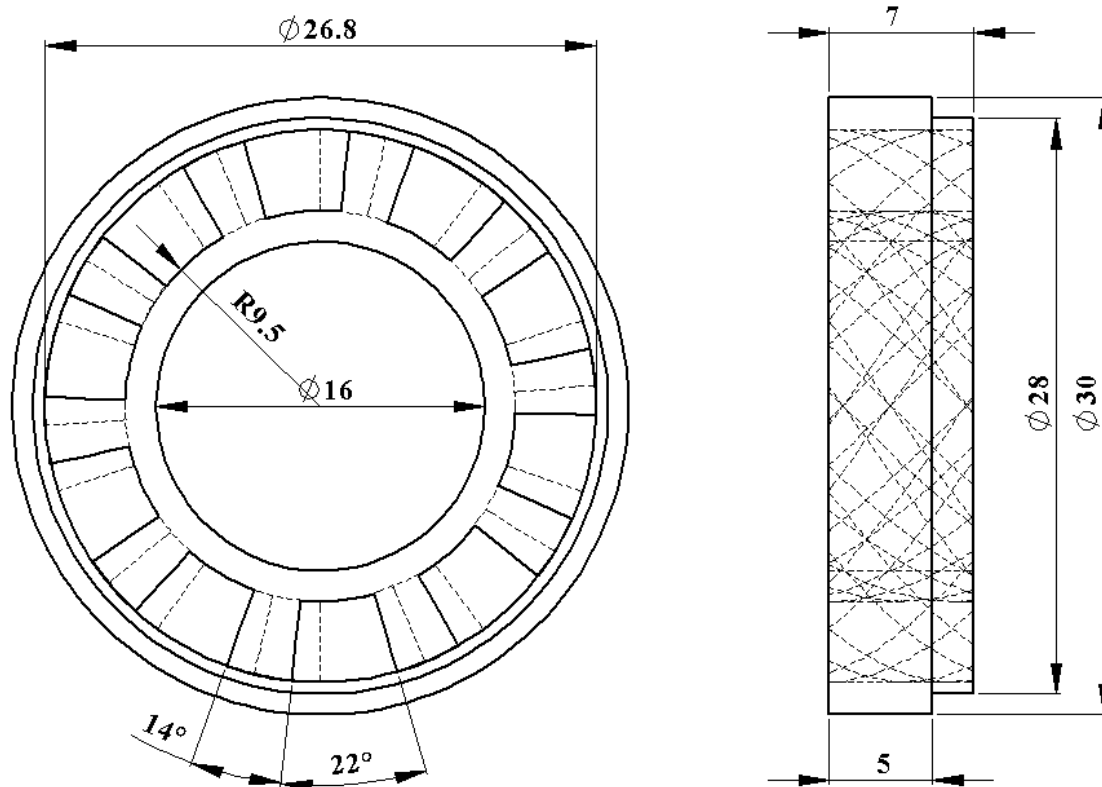


**Figure 68: A dimensional drawing of the annular swirler (dimensions are in mm)**

To monitor the fuel flow in each experiment, the pressure in the fuel line was measured using a pressure gauge. The pressure gauge was an analogue gauge that was modified on manufacture to display 50 kPa increments instead of 100 kPa. The fuel flow was also indirectly monitored by setting the fuel pump motor controller to the same value for all experiments. The fuel flow rate for this motor setting was measured in a separate experiment that ran with all the same conditions as the main experiments but the fuel usage was measured. In order to measure the fuel flow rate,  $\dot{m}_F$ , the mass of fuel used in a certain time needed to be found. To do this, repeated experiments were performed to measure the mass of fuel burned from between the two marker lines on the fuel burette. This was done by weighing the fuel that was used to fill the burette between the two markers using a strain gauge scale. Once the mass of the fuel between the markers was known a separate set of experiments was done to see how long it took for the fuel between the markers to be burned. To do this, the burette and a running stopwatch were filmed using a video camera during multiple combustion runs. The time was taken in this way to remove the undefined human reaction time and error from the timing process. The videos were then analysed afterwards in a frame-by-frame manner to find the fuel usage time. The fuel flow rate was then calculated.

The outlet temperature data was measured using a five-thermocouple rake. The rake consisted of 5 x 6.4 mm diameter tubes with the centres spaced 10 mm apart in a line along a radius of the combustor outlet. The rake could be rotated around the centre axis by moving the outer clamp along a guide that ran around the circumference of the combustor outlet pipe. Each tube, which acted somewhat as a radiation shield, contained one 1.5 mm diameter stainless steel-shielded K-type thermocouple. A photograph of the rake positioned at the outlet of the combustor is shown in Figure 70. The rake was such that the thermocouple shield tips ended on the plane at the outlet of the combustor liner some 150 mm in from the outlet pipe exit.

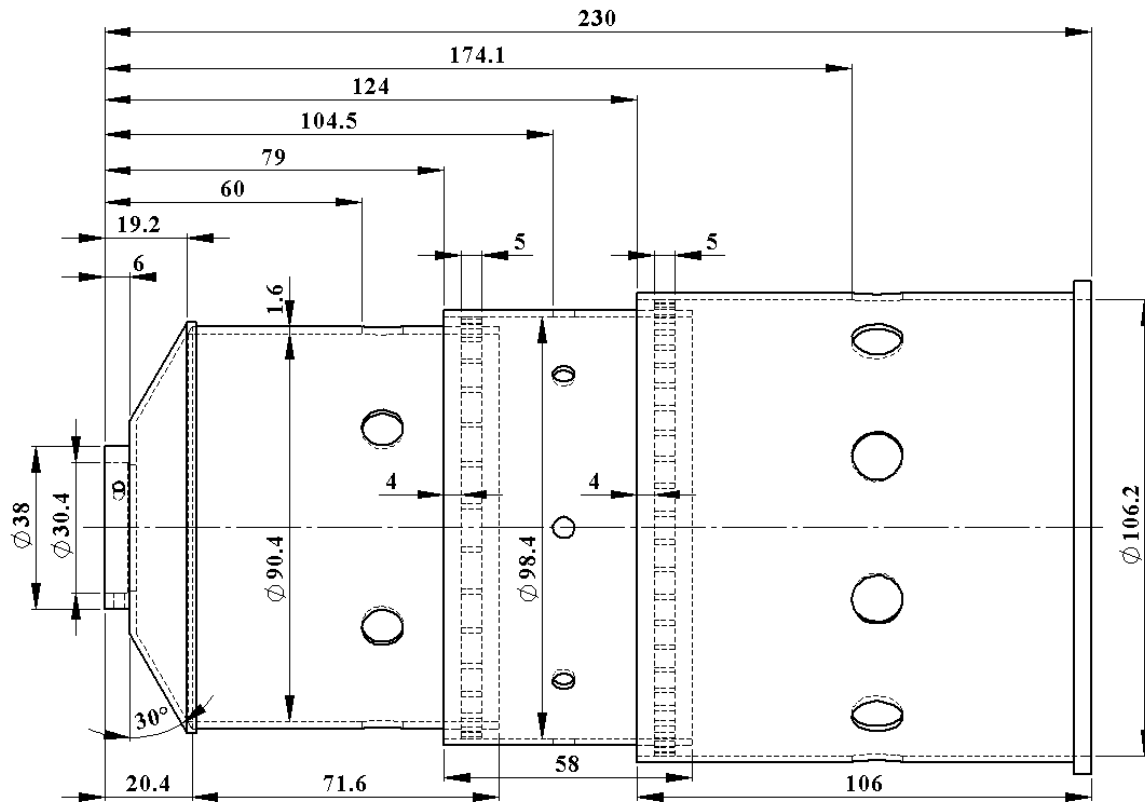


Figure 69: A dimensional drawing of the metal combustor liner (dimensions are in mm)

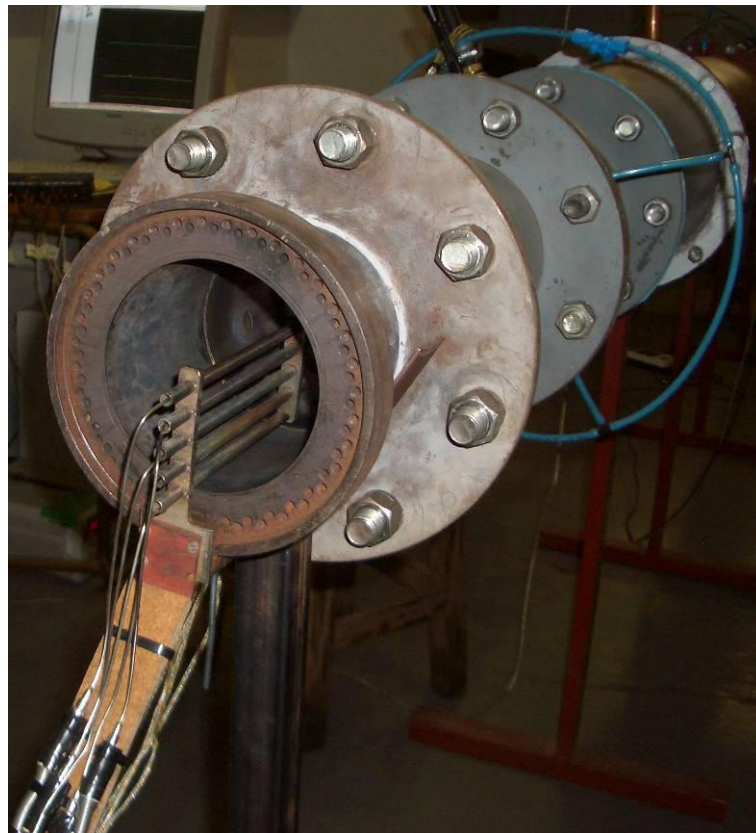


Figure 70: The five K-type thermocouples in a rake at the combustor outlet

These five thermocouples as well as the thermocouple used to measure the inlet temperature terminated into the analogue in channels of an IOTech personal Daq 3000 Series data acquisition system. The data acquisition system was plugged into the universal serial bus of a desktop computer, which then logged the thermocouple readings using the IOTech software. The data acquisition system is shown in Figure 71.



**Figure 71: The data acquisition system and computer used for thermocouple measurements**

The velocity profile at a plane, parallel but about 60 mm downstream of the outlet to the combustor liner, was measured using a Pitot tube. The Pitot tube was mounted onto the test rig using a magnetic clamp. Markings were made 5 mm apart on the plastic Pitot tube sheath. The pressure difference between the total and static pressure ports was measured using the digital manometer. A picture of this set-up is shown in Figure 72.



**Figure 72: A magnetic clamp holds the Pitot tube onto the test rig in the correct position**

### 3.2.2 Non-reacting experiment

The transparent combustor was designed to have a geometry that was almost identical to the metal combustor. The inner diameters of the cylinders were a match to the metal combustor, while the annulus around the transparent combustor has the same hydraulic diameter as the metal combustor. The actual diameters of the metal combustor could not be matched due to the 0.6 mm thicker walls required for the transparent combustor. A photograph of the components of the transparent test section is shown in Figure 73. The transparent test section was designed to fit onto the existing combustor test rig that was usually used for combustion experiments. The transparent test section, shown assembled in Figure 74, for non-reacting experiments, replaced the last two sections on the combustion rig as seen in Figure 75.

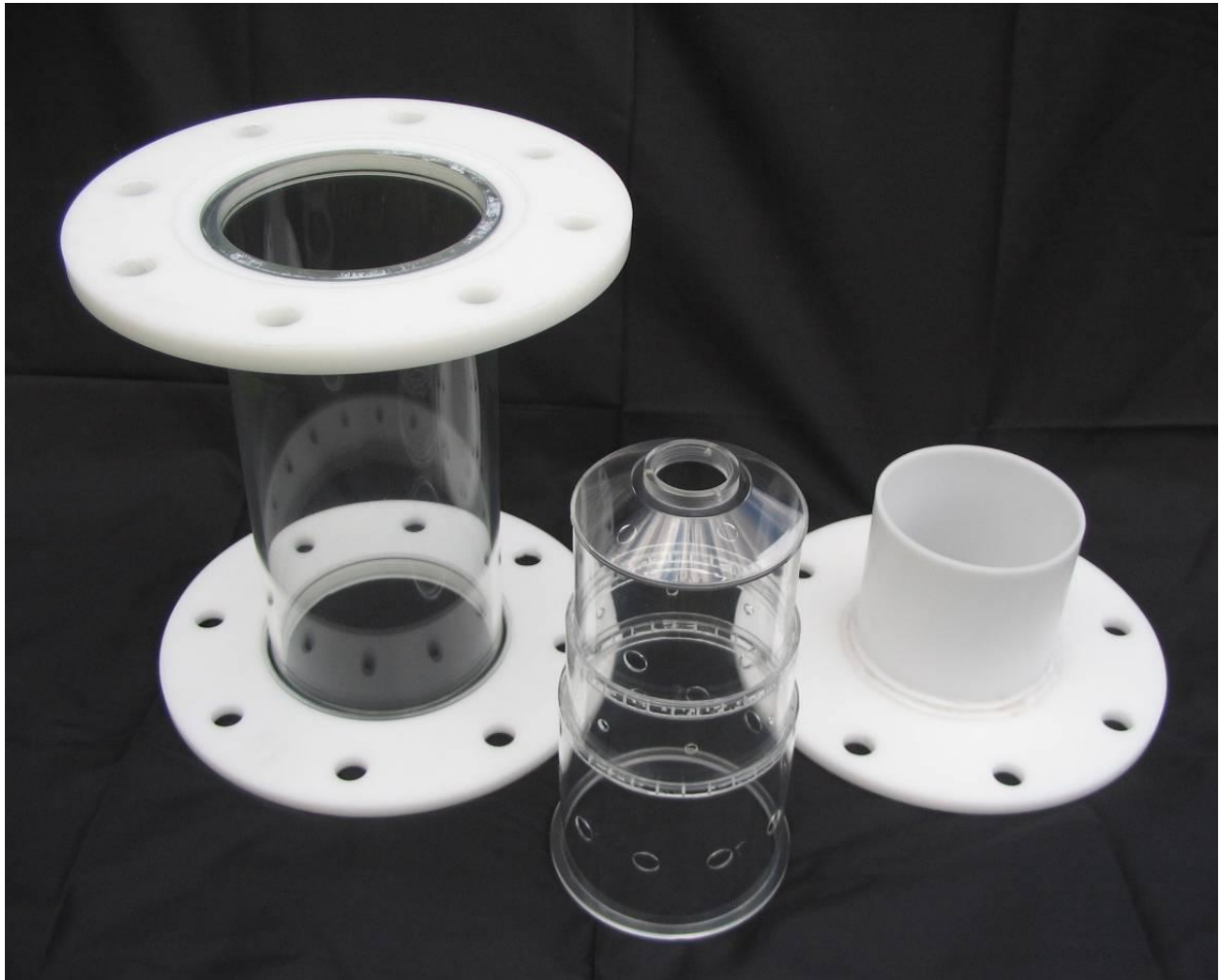


**Figure 73: The transparent combustor parts - casing, liner and outlet pipe**

Before any of the processes were used to manufacture the final combustor, test pieces were manufactured to ensure that the cutting speeds and tools used were correct. These same test pieces were used to test the annealing, polishing, laser cutting and gluing.

The transparent parts of the test section, namely the combustor liner and casing, were manufactured out of perspex. Perspex was chosen mainly because its optical quality was the best out of the available transparent plastics. The combustor liner was made out of four parts, a dilution zone cylinder, a secondary zone cylinder with attached cooling ring, a primary zone cylinder with attached cooling ring and a dome. The transparent combustor casing was one part. The manufacturing drawings are shown in Appendix C. The white parts of the test section were made of Ertacetal C. This material was chosen for the opaque parts because they were not required to be transparent and thus the material could be chosen using other criteria. Ertacetal C is tough, easy to machine and low in cost.

The transparent parts of the test section were manufactured using the following procedure:

- Machining to a rough dimension
- Annealing in an oven at about 80 °C
- Final machining
- Drilling of cooling holes using a dividing head drill press
- Polishing on a lathe using a polishing paste and a longitudinal motion to try have as few lines as possible on the surface
- Laser cutting the large primary, secondary and dilution holes
- Laser cutting off the spare material
- Assembling and gluing the combustor liner together



**Figure 74: The transparent test section assembly**

To manufacture the opaque parts was a lot simpler. The parts were machined to final specifications without annealing. The outlet pipe and flange for the outlet section were plastic-welded together. The two flanges making up the rest of the casing were threaded on the inner diameter and attached to the transparent casing with a screw thread.

Since the combustor was too small for the calibration target supplied with the PIV system, a smaller target had to be manufactured. The target was CNC-machined out of aluminium. The target was then anodised matt black to ensure that it was not too reflective since reflective surfaces are considered a safety hazard in laser areas. The white spots were painted onto the target by hand by filling each drilled hole with white enamel paint. The mirror holder that fits onto the side of the target was also machined using a CNC mill and anodised matt black. The manufacturing drawings for the target and the mirror holder can be found in Appendix C. Legs were made for the target by modifying telescopic radio antennae.

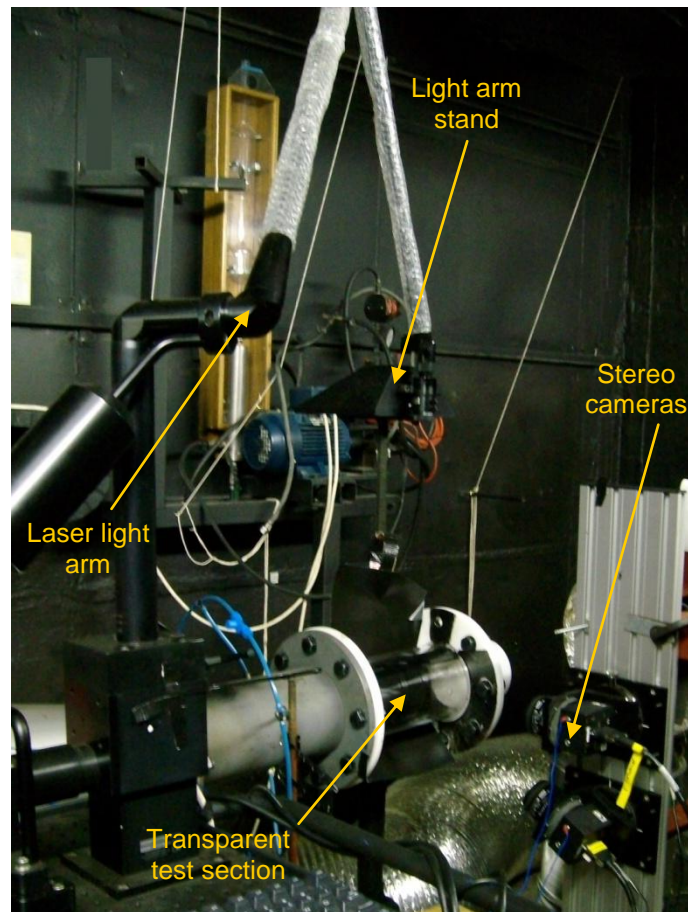


**Figure 75: The transparent test section attached to the combustor test rig in the PIV laboratory**

The PIV system consists of a Big Sky Laser dual head laser system that has two CFR 200 (Class IV Nd:YAG 190 mJ) lasers that can function up to 15 Hz. The dual laser head enable a minimum time between laser pulses of 1  $\mu$ s. The laser light has a wavelength of 532 nm. The laser is shone along a laser arm to a set of lenses that focus and convert the beam into a sheet. A -25 mm focal point cylindrical lens turns the beam into a sheet and a 500 mm focal point spherical lens focuses the sheet to give it a sheet thickness of approximately 1.5 mm in the test section. Each laser head has its own Ultra style integrated cooling and electronics (ICE) unit which is the power supply, cooling unit and control electronics for the laser head. The lasers in the PIV system are controlled either directly from the ICEs or from the TSI software Insight 3G [20]. There is a Model 610035 LASERPULSE™ synchroniser to ensure that the timing of the cameras and laser pulses is conducive to PIV. The two cameras used are Powerview 4M Plus greyscale CCD cameras each with a 2048 x 2048 pixel array. During image capture the images from the cameras are acquired onto the computer via a dual frame grabber that enables both cameras' images to be saved at the same time.

### 3.2.3 Wedge rings

The geometric variation tests were performed on the same test rig with the same experimental set-up as for the reacting experiment base case. The experimental set-up described in Section 3.2.1 applies to the experiments described in this section.

In an attempt to passively control the outlet temperature profile, two sets of wedge rings were manufactured. The wedge rings were manufactured from stainless steel 304 (Figure 76). Each set of wedge rings consisted of one wedge ring for the primary zone and one for the secondary zone. The first set protruded 30% of the radius into the liner flow while the second set only protruded 10% of the radial distance into the flow. Figure 77 shows how the wedge rings would fit into the combustor liner while Figure 78 shows a photograph of the

liner without the wedge rings on the left and of the liner with the 30% wedge rings installed on the right. The dimensional drawings of all four wedge rings are to be found in Appendix C.



Figure 76: The 30% (left) and 10% (right) primary and secondary zone wedge rings

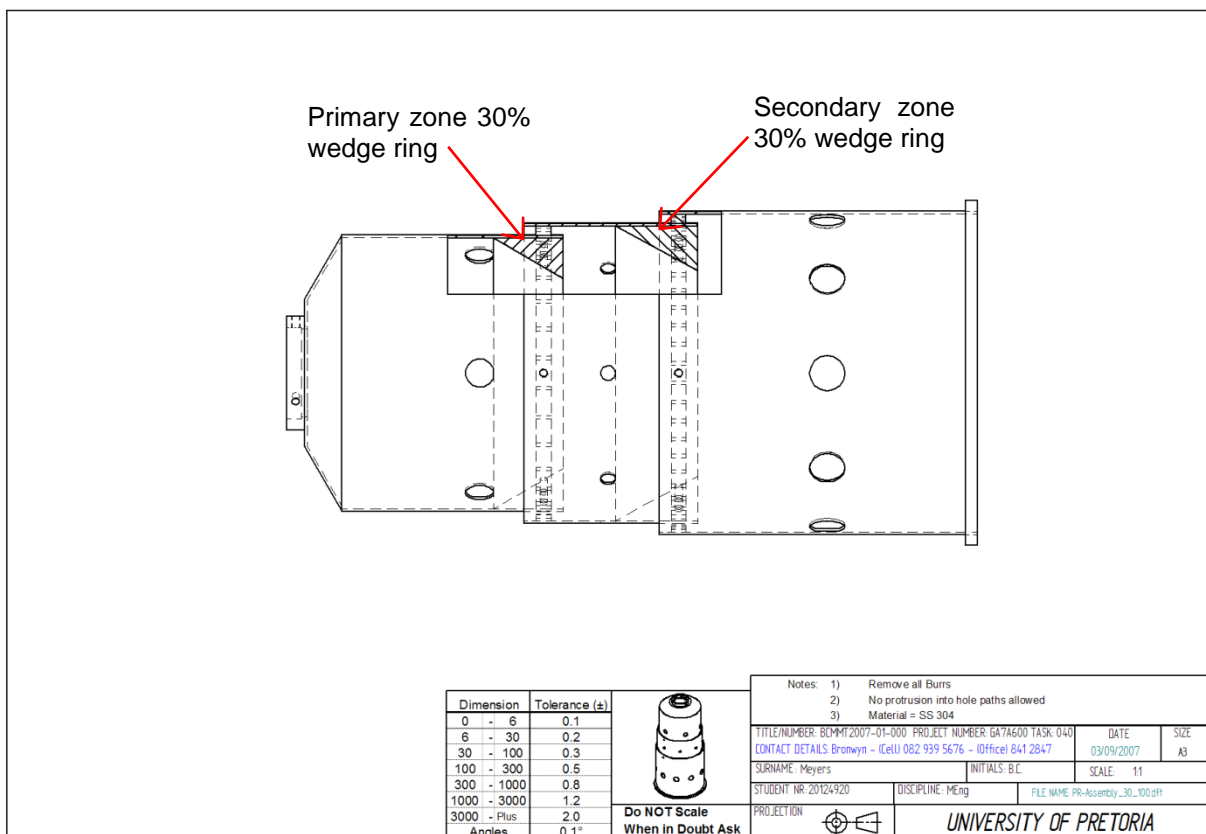


Figure 77: An assembly drawing with cut-out section showing the 30% wedge rings inside the combustor

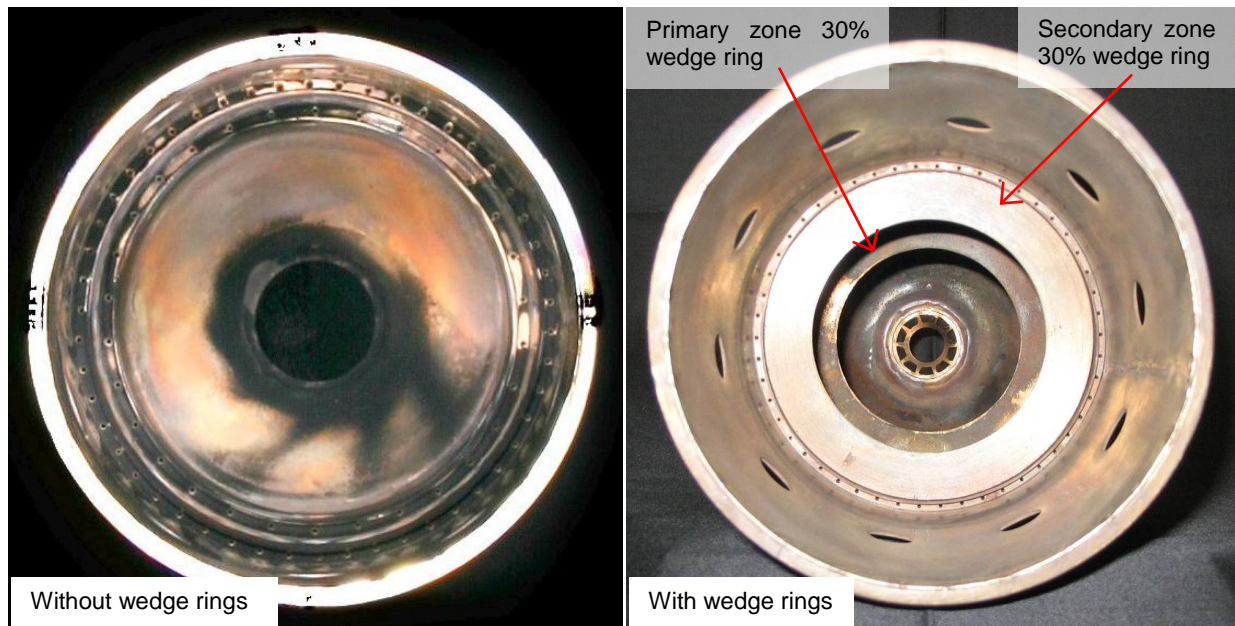


Figure 78: The 30% wedge rings installed into the combustor liner

### 3.3 Experimental method

#### 3.3.1 Reacting experiment

##### 3.3.1.1 Base case settings

To ensure that the experiments performed were comparable, certain of the properties that were controllable were kept constant. The two most important factors are the air flow rate and the fuel flow rate. Also after a few preliminary tests revealed a skewed outlet profile, the orientation of the combustor components was also set. The properties set at start of each run were:

- Pressure drop over orifice plate ( $\Delta p_o$ ) at 2.60 kPa thus giving  $\dot{m}_A \approx 0.091$  kg/s
- Fuel motor controller frequency ( $f_F$ ) at 18.5 Hz thus giving  $\dot{m}_F \approx 0.000784$  kg/s

This results in an air/fuel ratio of  $AFR \approx 116$

- The orientation of the combustor components was set such that a mark made on the swirler lined up with a mark made on the combustor liner, which was positioned at the top of the test rig.

A summarised repeat of the properties calculated and measured are listed below.

Properties measured at start and end of each run:

- Atmospheric temperature [ $T_{atm}$ ]
- Atmospheric pressure [ $P_{atm}$ ]
- Upstream orifice plate temperature [ $T_1$ ]
- Upstream orifice plate pressure [ $p_1$ ]
- Pressure drop over combustor [ $\Delta p_L$ ]

Properties measured during run:

- Pressure drop over orifice plate  $[\Delta p_o]$
- Fuel pressure  $[P_F]$
- Combustor inlet temperature  $[T_3]$
- Combustor outlet temperature at five different radii, and 36 different azimuthal positions  $[T_{4i}]$
- Dynamic pressure across Pitot tube

Properties calculated from measured data:

- Air mass flow rate  $[\dot{m}_A]$
- Outlet temperature profile
- Overall total pressure loss  $[P_{34}]$
- Overall pressure loss [%]
- Pressure loss factor
- Pattern factor
- Profile factor
- Velocity profile along horizontal diameter  $[U]$

### 3.3.1.2 Outlet temperature profile

The base case mentioned above is the set-up used for creating the reacting experimental results.

The outlet temperature profile was measured over the whole plane at the outlet of the combustor liner. This was done by rotating the thermocouple rake around the outlet measuring data at every  $10^\circ$ . The rake started at  $270^\circ$  and was rotated in a clockwise direction. Once the rake reached  $270^\circ$  again ( $-90^\circ$ ), the measurements were repeated for another  $20^\circ$ . Thus 38 data sets were collected for each experiment and a  $20^\circ$  overlap was used for checking purposes. At each azimuthal position, time was taken for the thermocouple readings to stabilise before the data was recorded. The time to stabilization varied at each point but was in the region of 3 minutes.

For the data acquisition of the thermocouple outputs, the data acquisition system software was set with the following settings: the oversample was set to 512 and with the six thermocouple and four cold junction channels and the system acquisition capability of 1 MHz, the scan rate was 195 scans per second. At each position, the thermocouple data was recorded for 4 000 scans, which takes about 20 seconds. The average value for this 20-second run was then used to plot the temperature at each point in the outlet plane.

The outlet temperature profile was plotted using the contour function in Matlab [25]. Scripts and functions to sort the data and plot the data were also programmed in Matlab [25].

### 3.3.1.3 Qualitative data

All photos taken for qualitative data in the combustor liner were taken in a set group of orientations. Each set has a straight-on photograph and photos taken at the four angles  $0$ ,  $90$ ,  $180$  and  $270^\circ$ , so as to show all the inner walls of the liner.

In order to obtain the flame photos in the following section, a photographer was enlisted. The test rig was run at the base case conditions discussed above for comparative purposes. The camera used was a 12.7 megapixel Canon 5D digital camera. The camera settings used were: a shutter speed of 250; an f-ratio of 11 and an ISO of 1600.

To obtain the carbon flow pattern results, two steps were required. First, the test rig was run at a rich air/fuel ratio that deposited a complete layer of carbon on the inner liner walls. The test rig was then switched off and restarted at base case test conditions. The carbon in certain areas burned away and in other areas did not resulting in a wall burn-pattern shown in Section 4.1.2. The orientation of the combustor components for this experiment was not noted.

#### 3.3.1.4 Outlet velocity profile

The velocity profile at a plane, parallel but about 60 mm downstream of the outlet to the combustor liner, was measured using a Pitot tube as described in Section 3.2.1. The velocity profile was measured both with and without combustion. For the experiments with combustion, the standard base case settings were used. The experiments without combustion also had the same settings as the base case except for the fuel being turned off.

The velocity profiles were constructed from 21 points across the horizontal diameter of the test rig outlet. The profiles spanned 100 mm and were made up of points 5 mm apart.

### 3.3.2 Non-reacting experiment

#### 3.3.2.1 Particle image velocimetry

The velocity data was collected on the plane lying lengthwise along the central axis. This plane was chosen because it would encompass a large amount of information and it was one of the ways that would allow the cameras to be positioned in such a way that larger areas could be measured. The flow was seeded using a smoke produced from burning oil (Shell Ondina EL). The cameras were required to be approximately 100 - 200 mm away from the combustor in a side-scatter configuration. This was both to try and fill as much of the camera frame with the region of interest in the combustor and because the smoke particles do not reflect light that well so the light intensity was not enough to place the cameras very far away.

A schematic diagram of the PIV equipment set-up is shown in Figure 79. The stereoscopic camera orientation has been rotated such that the “left” camera discussed in Section 2.3.4 was at the top in Figure 75 and Figure 79 while the “right” camera was at the bottom. The top camera was placed at a 5° angle to the normal of the laser plane pointing downwards while the bottom camera was placed at a 20° angle to the normal pointing upwards. The maximum angle that the top camera could be placed at was 5° due to the top position being in back scatter. If the top camera angle was increased, due to the camera being in back scatter, the light intensity was not sufficient to capture particle positions in the full combustor width.

The calibration images were captured by placing the target inside the combustor. The calibration images for a primary zone experiment are shown in Figure 80. The black arrow shows the direction of the bulk flow during a running experiment.

Once the calibration was done, the test rig was turned on, allowed to warm up and reach equilibrium ( $\pm 45$  minutes) and then the seeding was introduced. A sequence of 720 image sets were captured to increase the chances of obtaining an image that had the correct criteria to perform PIV analysis. An example of one of these images is shown in Figure 81. As can be seen in Figure 81, there can be overexposed regions (coloured pink). Removing these overexposed areas is not necessary for the analysis to be performed, however, there will be no data there. Figure 81 shows the two top camera images (Frame A and Frame B) that were used for the PIV analysis.

The PIV software, Insight3G [20], performs the cross-correlation between the two images in Figure 81 to calculate the vectors that are shown in Figure 82. The image in Figure 82 is the top camera image of the two images that will be combined to obtain the three-dimensional vector plot using Tecplot 10 [26].

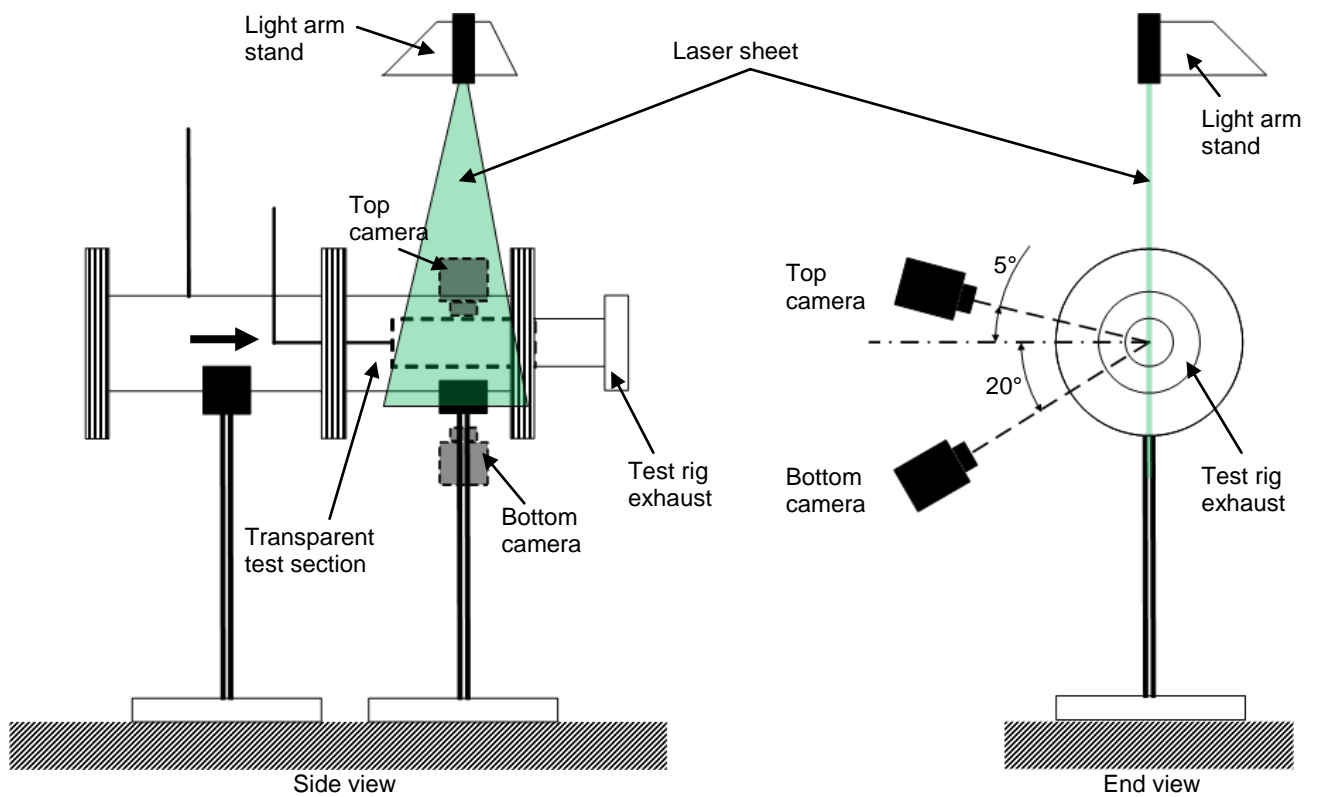


Figure 79: A schematic diagram of the PIV equipment set-up

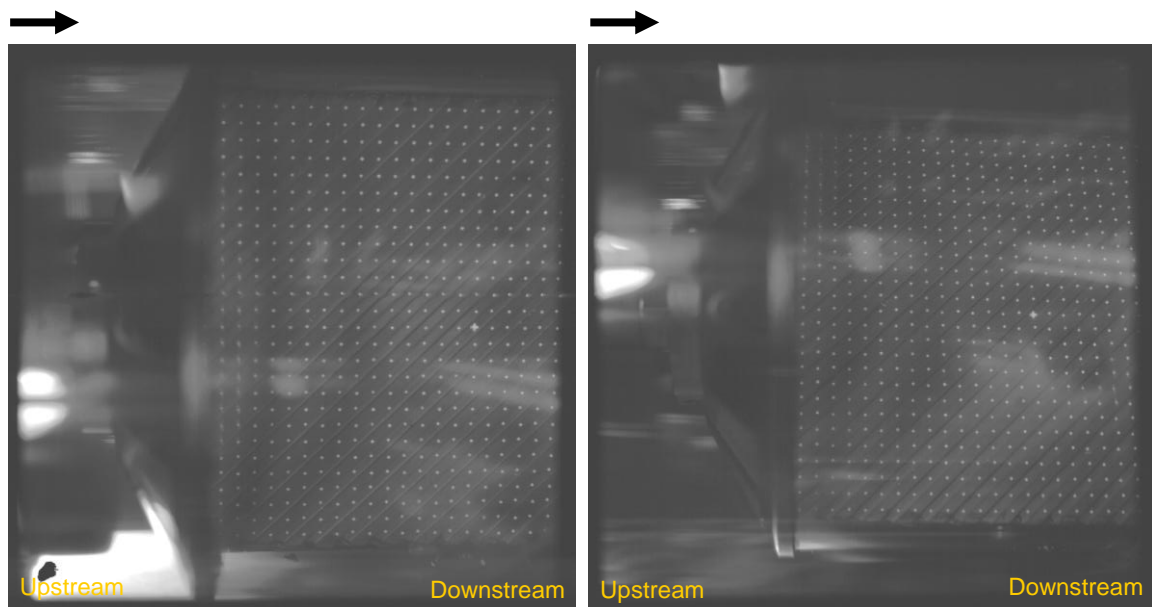


Figure 80: The top and bottom camera images of the calibration target

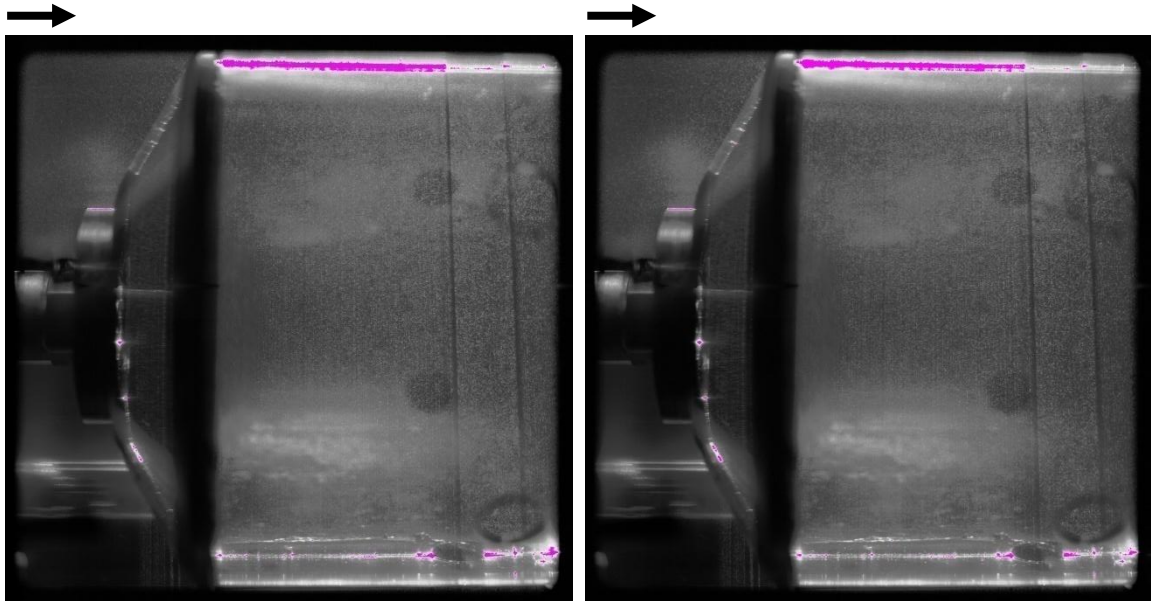


Figure 81: Frame A and Frame B taken with the top camera

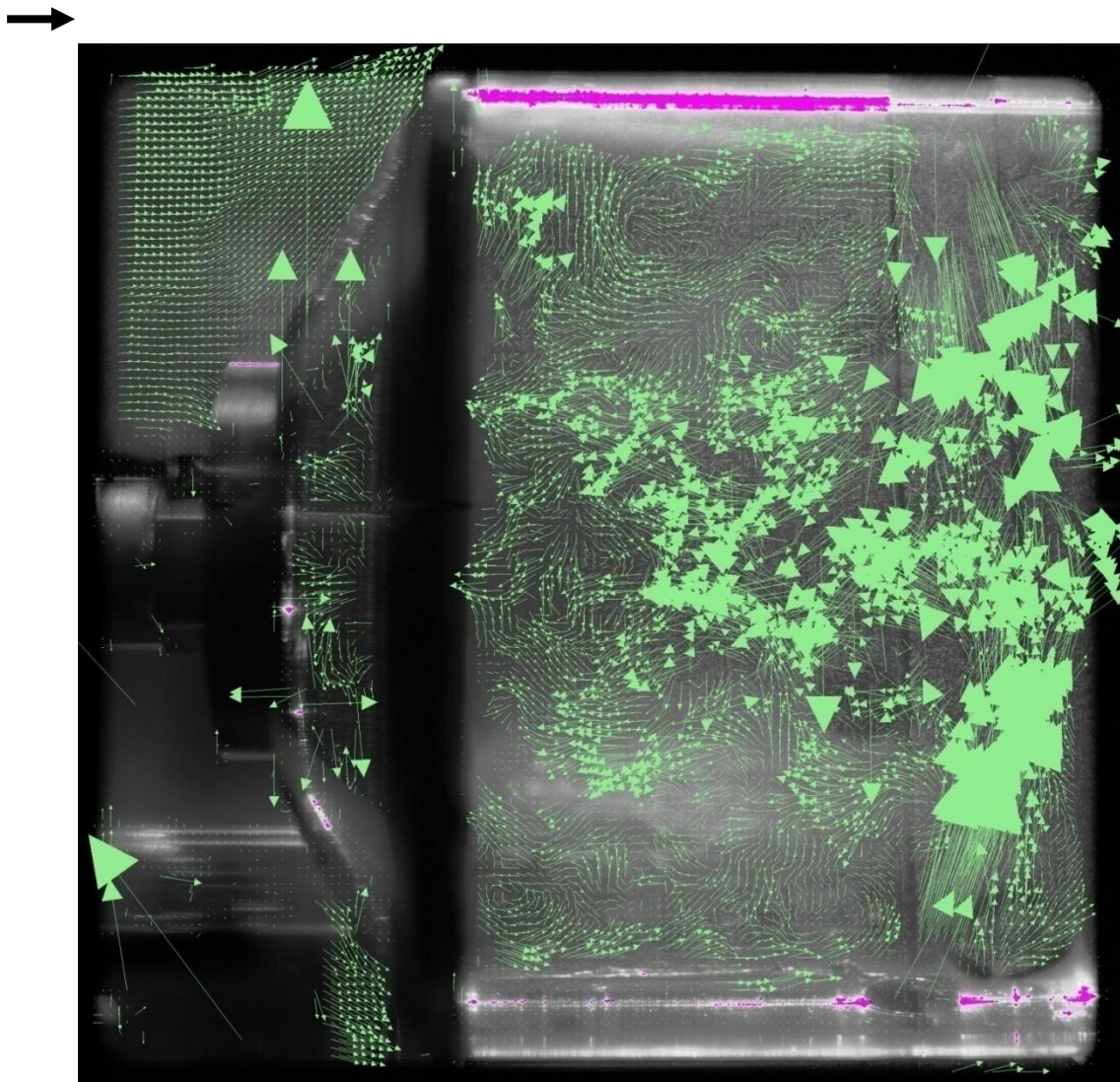
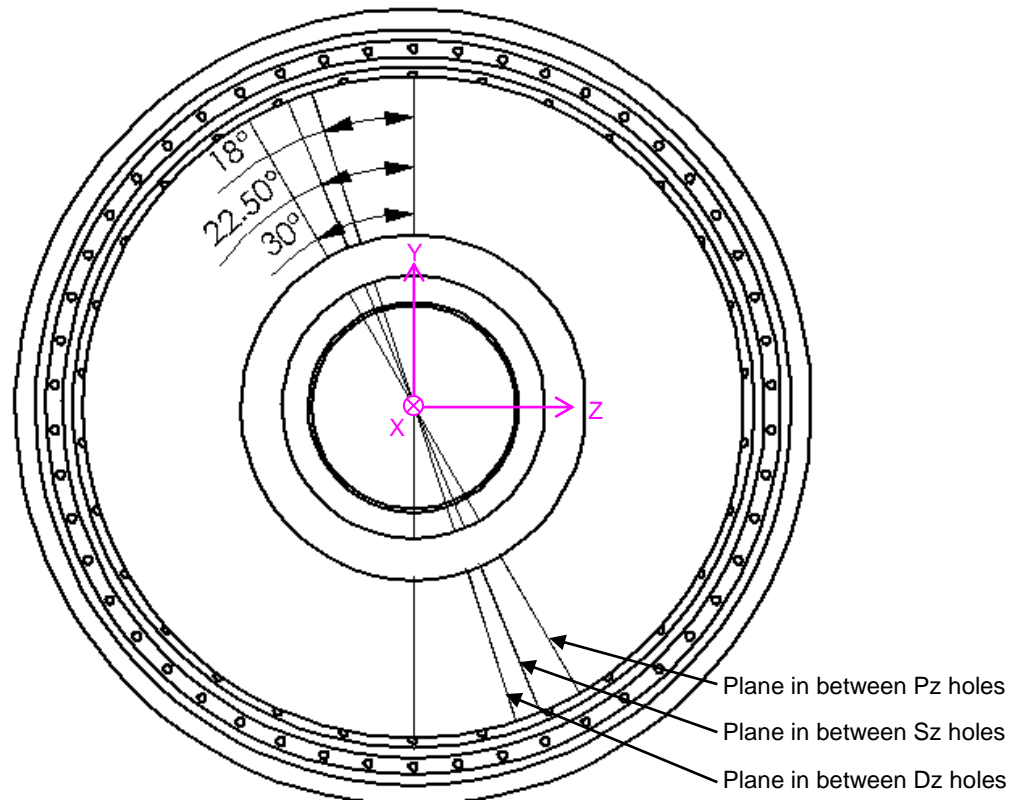


Figure 82: A two-dimensional vector plot calculated using the cross-correlation

The above information has been collected for various different set-ups throughout the combustor. The laser plane was placed in line with the holes in the above experiment and in each of the sections in the combustor (primary, secondary and dilution zones). For each of the zones, the cameras were placed in two configurations, one with the top camera at  $5^\circ$  ( $T = 5^\circ$ ) and the bottom camera at  $20^\circ$  ( $B = 20^\circ$ ), and the second with the top camera at  $0^\circ$  ( $T = 0^\circ$ ) and the bottom camera at  $23^\circ$  ( $B = 23^\circ$ ). The second camera configuration is to get a plain two-dimensional vector field with the top camera and to compare two sets of three-dimensional flowfields with different camera configurations.

For each of the camera configurations, data was taken with the laser plane in line with the holes and in between the holes of each of the combustor zones. The primary zone plane is at  $30^\circ$  to the plane in line with the holes, the secondary zone is at  $22.5^\circ$  and the dilution zone is at  $18^\circ$ . A diagram showing the plane positions for each zone in between the holes is shown in Figure 83.



**Figure 83: The angles showing the positions of the planes in between the holes**

The base case data set for the PIV was taken at a lower flow rate than the reacting tests due to limitations in the experimental set-up. As the flow rate increases, the data set gets sparser due to timing limitations. For this reason, the base case data set was taken at a pressure drop over the orifice plate ( $\Delta p_o$ ) of about 1 kPa, which corresponds to an air mass flow rate ( $\dot{m}_A$ ) of 0.056 kg/s. This is about 60% of the flow rate for the hot tests. For this reason, in the primary zone, data was also collected at  $\Delta p_o = 1.1$  kPa, 1.3 kPa, 1.6 kPa, 2 kPa and 2.6 kPa. The data quality did deteriorate through this range but a trend was visible in the flowfield, which will be discussed later. Table 4 shows the pressure drops over the orifice plates at which the tests were done and the corresponding air mass flow rate for each pressure drop.

For completeness, in the secondary and dilution zones, data was also collected in line with the holes for the  $T = 5^\circ$  and  $B = 20^\circ$  camera configuration at  $\dot{m}_A = 0.070$  kg/s and  $\dot{m}_A = 0.091$  kg/s. The test matrix showing all the PIV experimental configurations is shown in Table 3.

In order to perform the PIV experiments certain of the Insight 3G software capture settings were varied from the default values. For each experiment, as far as possible, the time between laser pulses,  $\Delta t$ , was briefly tested and a  $\Delta t$  that provided the highest quantity of vectors distributed over the largest area was chosen. The time between laser pulses for each experiment is shown in Table 3. For all of the experiments the PIV

application was used with the exposure mode set to synchronized and the capture mode on sequence where 720 captures were taken and saved directly to the hard disk. The laser delay and PIV exposure time were varied to accommodate the chosen time between laser pulses. The lasers' q-switch time was set so as to provide a medium intensity laser pulse thus the laser timing for both Laser A and B were set to values ranging from 145 to 152  $\mu$ s.

The PIV processor settings used were identical for all the experiments performed. No processing mask or validation scheme was used on the vectors calculated. For each experimental setup a set of calibration images were captured and a three-dimensional (3D stereo) calibration file created. The plug-ins used were as follows: The grid engine used was a Recursive Nyquist grid with Spot A set to 64 and Spot B set to 32 pixels. No mask was used for the spot mask engine while the correlation engine used was the Fast Fourier Transform Correlation which uses a Fast Fourier Transform to perform the cross correlation. The Gaussian Peak engine was used for the sub-pixel interpolation. The plug-in setting that was modified was the Peak to No Peak signal to noise ratio which was set to greater than 1.2.

**Table 4: Pressure drop over orifice plate and corresponding air mass flow rate**

Pressure drop over orifice plate ( $\Delta p_o$ )	Corresponding air mass flow rate ( $\dot{m}_A$ )		
	[kPa]	[kg/s]	[kg/h]
1		0.056	201.6
1.1		0.059	212.4
1.3		0.064	230.4
1.6		0.070	252.0
2		0.078	280.8
2.6		0.091	327.6

### 3.3.3 Wedge rings

#### 3.3.3.1 Outlet temperature profile

For all the experiments performed to obtain the outlet temperature profile, whether the wedge rings were in or not, the test rig was set up according to the base case settings discussed in Section 3.3.1.1. The method of data collection and analysis was also identical to the base case.

Tests were done with no wedge rings in, both 10 and 30% wedge rings in, and then with only one ring in at a time, i.e. 10% primary zone ring, 10% secondary zone ring, 30% primary zone ring and 30% secondary zone ring. This makes seven different configurations for testing.

For each of the 10% wedge ring cases, three experiments were done and the repeatability of the results was tested. Three experiments were also performed for the case with both 30% rings installed and with no rings installed. The method proved to be quite repeatable and thus the tests with only the primary 30% wedge ring and secondary 30% wedge ring were performed only once. For those configurations where more than one experiment was performed, the average values of the three experiments were used for the result report.

#### 3.3.3.2 Outlet velocity profile

The velocity profile was measured for all seven wedge ring configurations both with and without combustion. Again as for the outlet temperature profile, the same measurement method was used as for the base case.

### 3.4 Verification

Due to the unique geometry of the combustor and unique test rig involved, absolute verification with other available data sets of the experimental data was not possible. Due to this, three methods were used to check the validity of the results produced. Firstly, a basic PIV result evaluation was performed. The data was investigated for weaknesses and strengths and for possible reasons for bad data and a comparison was made with respect to typical can-type combustor flowfields, Secondly, a comparison was made to a known velocity measurement technique and thirdly, the instruments used were either calibrated or the uncertainty obtained and the uncertainty calculated results was also calculated.

#### 3.4.1 PIV evaluation

The following images (Figure 84 to Figure 94) are the results obtained during one of the data capturing experiments in the primary zone using PIV in the transparent combustor. The experimental configuration has the laser light in line with the primary zone holes, the nominal pressure drop over the orifice plate at 1 kPa (0.056 kg/s) and the top camera angle at 5° above the normal and the bottom camera at 20° below the normal (see Figure 79).

Figure 84 shows the average velocity field of 720 three-dimensional velocity fields. The vectors are shown sparsely populated for better visibility in the swirling and return flow sections.

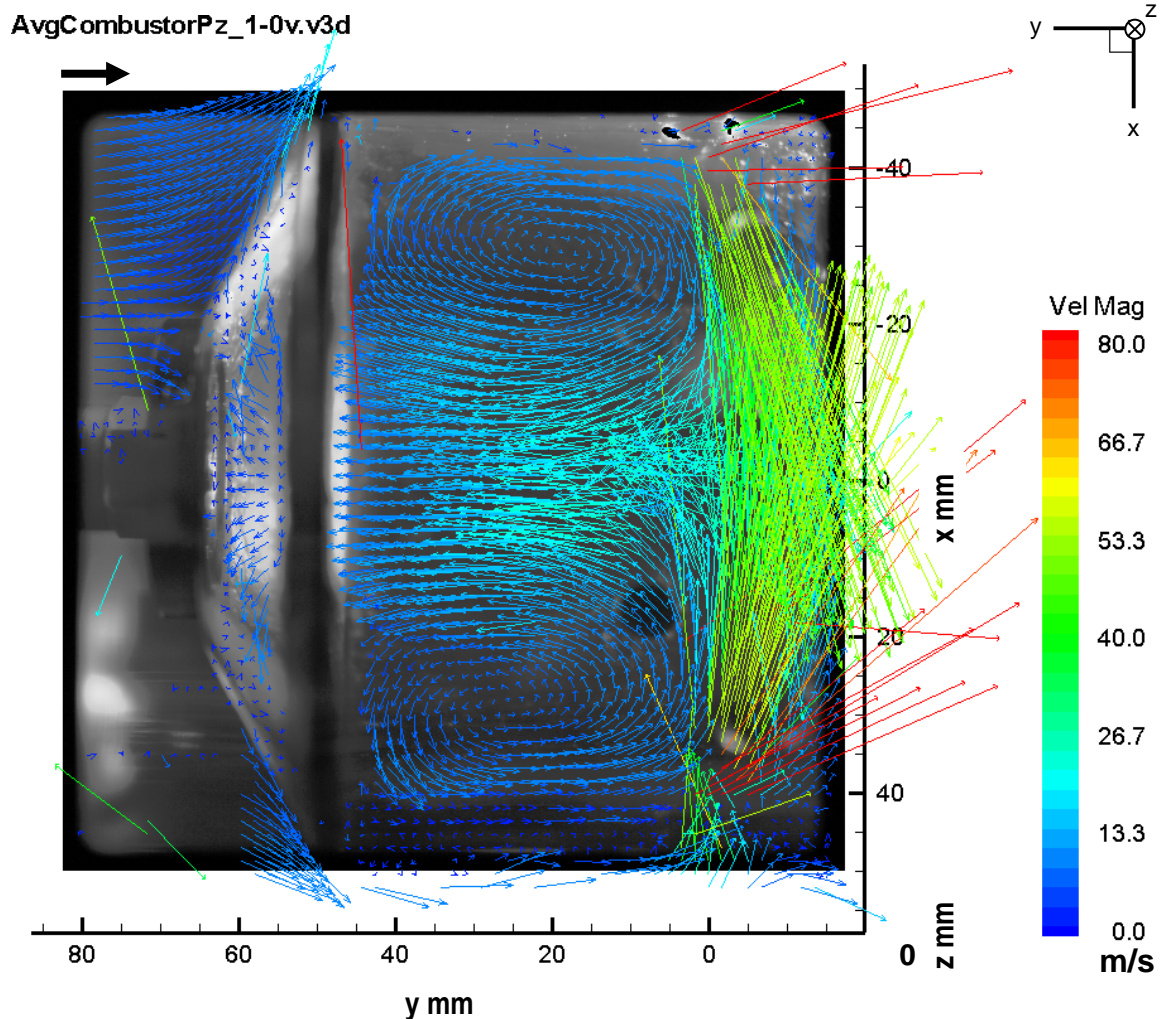


Figure 84: A sparsely populated vector field viewed from the side superimposed on an image of the primary zone

Figure 85 and Figure 86 show the correspondences between the patches of missing vectors in the vector field and the physical features that cause them.

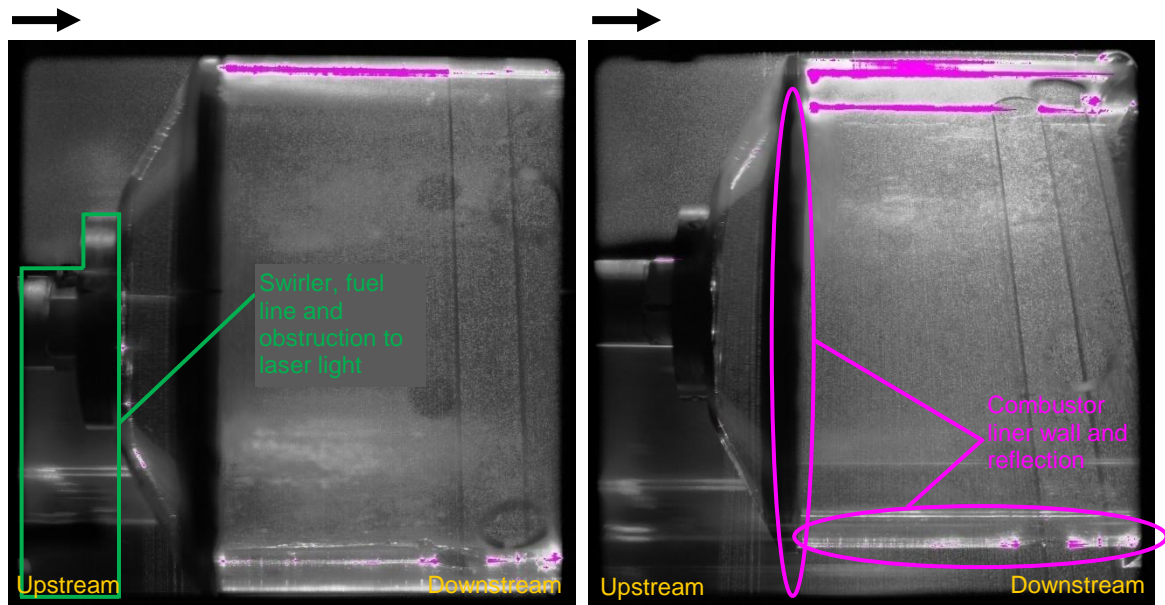


Figure 85: Photographs of the corresponding constructions on the combustor that caused the lack of relevant vectors in Figure 86

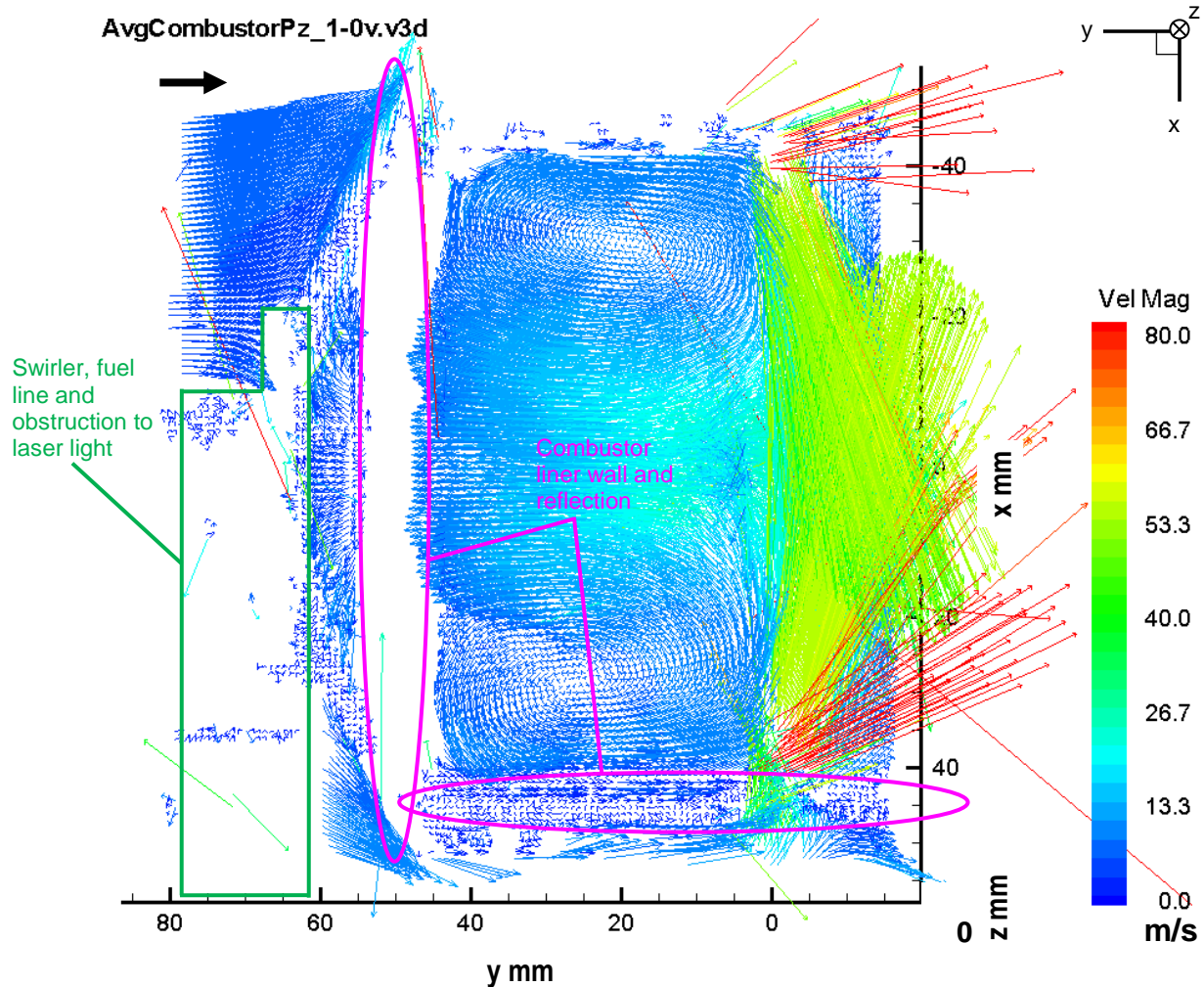
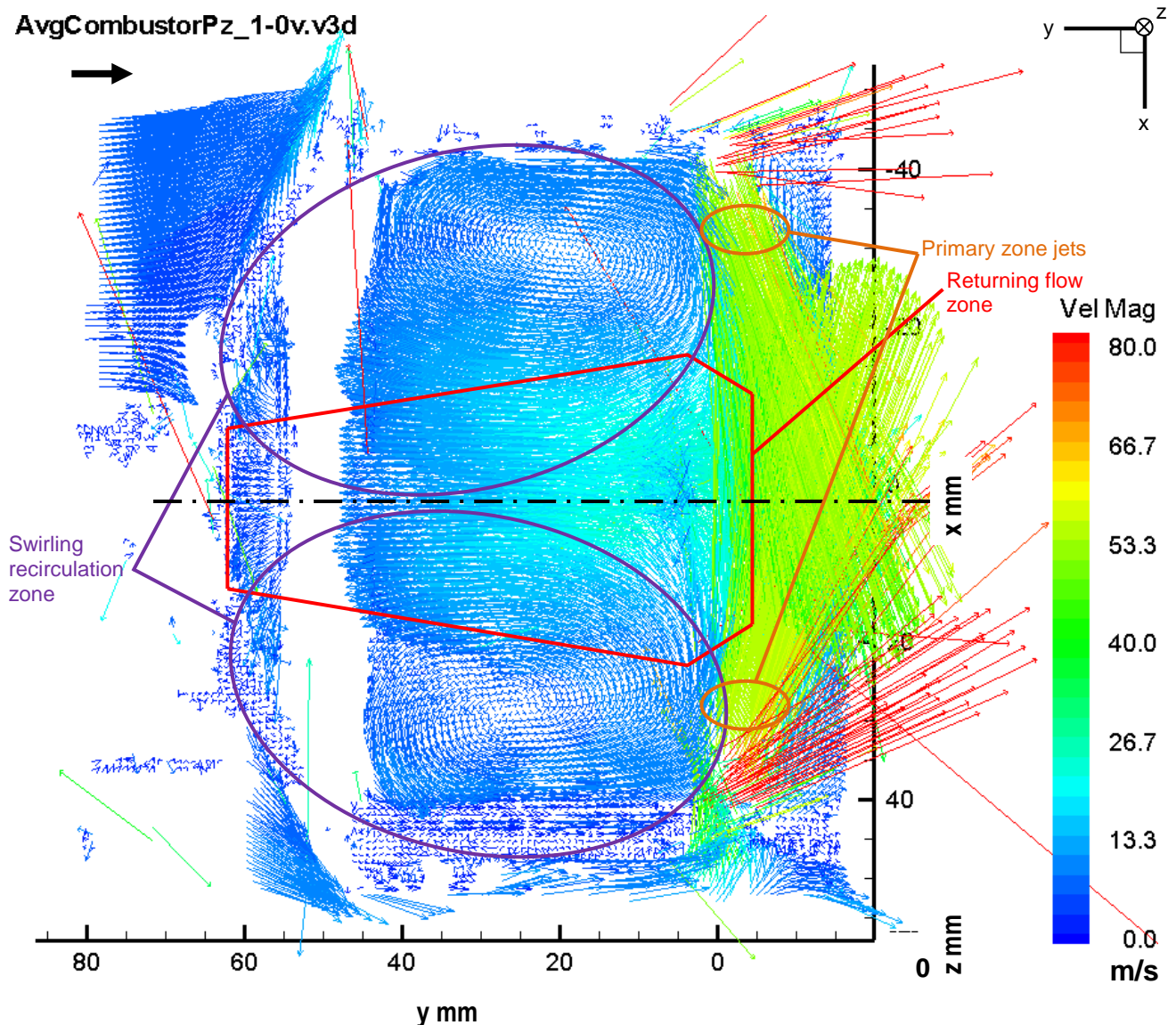


Figure 86: The three-dimensional vectors in the primary zone viewed from the side

Figure 87 shows the three-dimensional vectors calculated using Tecplot 10 [26]. In this figure, the return flow zone can be seen in the red outline (mostly in light blue and cyan). The jets are shown as yellow-green vectors (pointed out in orange). The position of the swirling recirculation zone above and below the centreline ( $X = 0$  mm) is shown in the purple outline.

**AvgCombustorPz\_1-0v.v3d**



**Figure 87: The three-dimensional vectors in the primary zone viewed from the side with the main combustor flow features outlined**

Some of the more subtle features that can be seen in the vector field are shown in Figure 88. The bulk flow splitting off to enter the swirler can be seen as well as the convergence of the bulk flow to enter the annulus around the combustor liner. The flow in the annulus is also evident as well as some annulus flow curving into a primary zone hole to form a jet. The remaining annulus flow can be seen converging into a smaller annulus around the next zone at the bottom right.

The separate components of the velocities can be plotted individually and velocity profiles extracted as slices along the data set. In Figure 89, the axial velocity slices at various positions along the primary zone have been extracted. The velocity profiles are the red or black lines that pass through the series of data points marked with letters (A to H in Figure 89). The magnitude of the velocity component is measured from the straight vertical solid pink or grey line (zero line) associated with each profile marked with a corresponding letter (A to H). This line also marks the position of the slice the velocity profile corresponds to. If the velocity profile lies to the right of the zero line, the velocity is positive and the flow is moving in a downstream direction. Points to the left of the zero line are negative values and indicate reverse flow.

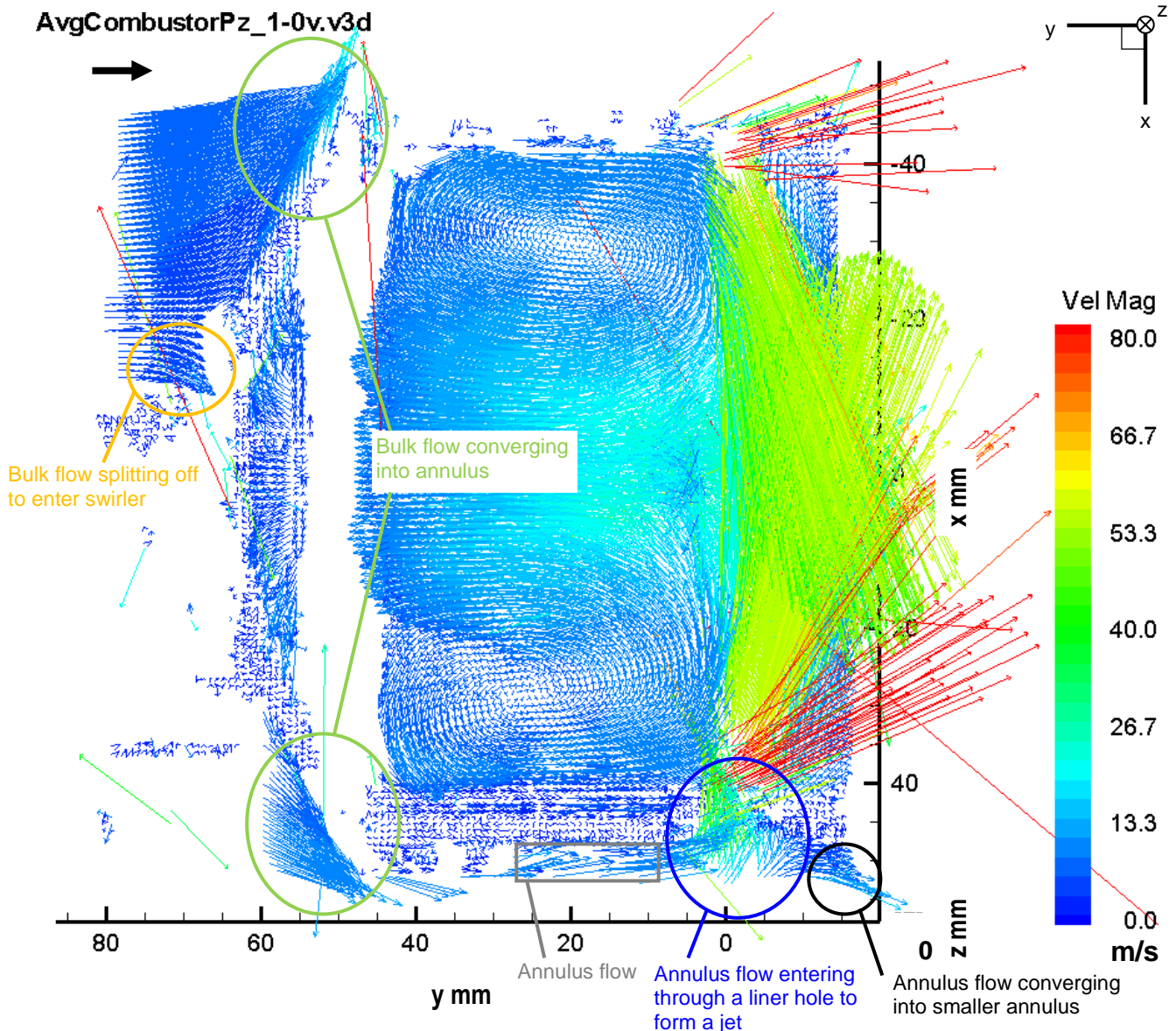


**Figure 88: The three-dimensional vectors in the primary zone viewed from the side with the more subtle flow features outlined**

The first velocity profile on the left (Profile A) is the axial velocity profile of the bulk flow before the flow starts to converge into the annulus around the combustor. This profile shows an almost uniform axial velocity profile in the bulk flow, which is expected. The second velocity profile (Profile B) is positioned just before the swirler entrance. The variations at the bottom 10 points are an indication of the disturbance of the bulk flow due to the flow separating to enter the swirler. Profiles C to G show very similar shapes to the profiles measured by Cameron *et al.* [14] in the primary zone. The profiles shown in Figure 2 at  $\frac{x}{R} = 1.25, 0.50$  and  $1.00$  all have a central region that points in the upstream direction and the outer regions of the profiles point in the downstream direction. These are typical axial profiles in the recirculation zone region and similar profiles can be seen in other measurements in the literature including those done by Janus *et al.* [9] (see Figure 35) and Weigand *et al.* [13] (see Figure 44).

The second-last profile (Profile G) goes through the jets giving a large positive axial flow in a wide outer band along the wall. Profile H is after the jets and is showing the transition from a predominantly reverse flow situation at the core to a forward flow region at the core of the secondary zone (see later discussion in Chapter 4).

Figure 90 is the same plane as in Figure 86 to Figure 88 but viewed from the left (upstream side). The two dotted arcs show the positions of the combustor liner and casing. Here it is clear that the vectors are three-dimensional and that the fluid has a significant out-of-plane flow. This is expected due to the swirler. It can

also be seen that there are some vectors with invalid z-components (mostly the red vectors in the jets). This is due to abnormally small non-real vectors being picked up in the analysis in one of the top or bottom images. This would be due to fluctuating reflections in the images or other phenomenon that could be interpreted as moving particles by the cross-correlation process. In most cases, the x- and y-components of these vectors are most likely correct and fit in with the trends of the surrounding vectors. Most of these vectors occur by the entrance of the jets, although there is some invalid z-components at the convergence of the bulk flow into the annulus.

### AvgCombustorPz\_1-0v.v3d

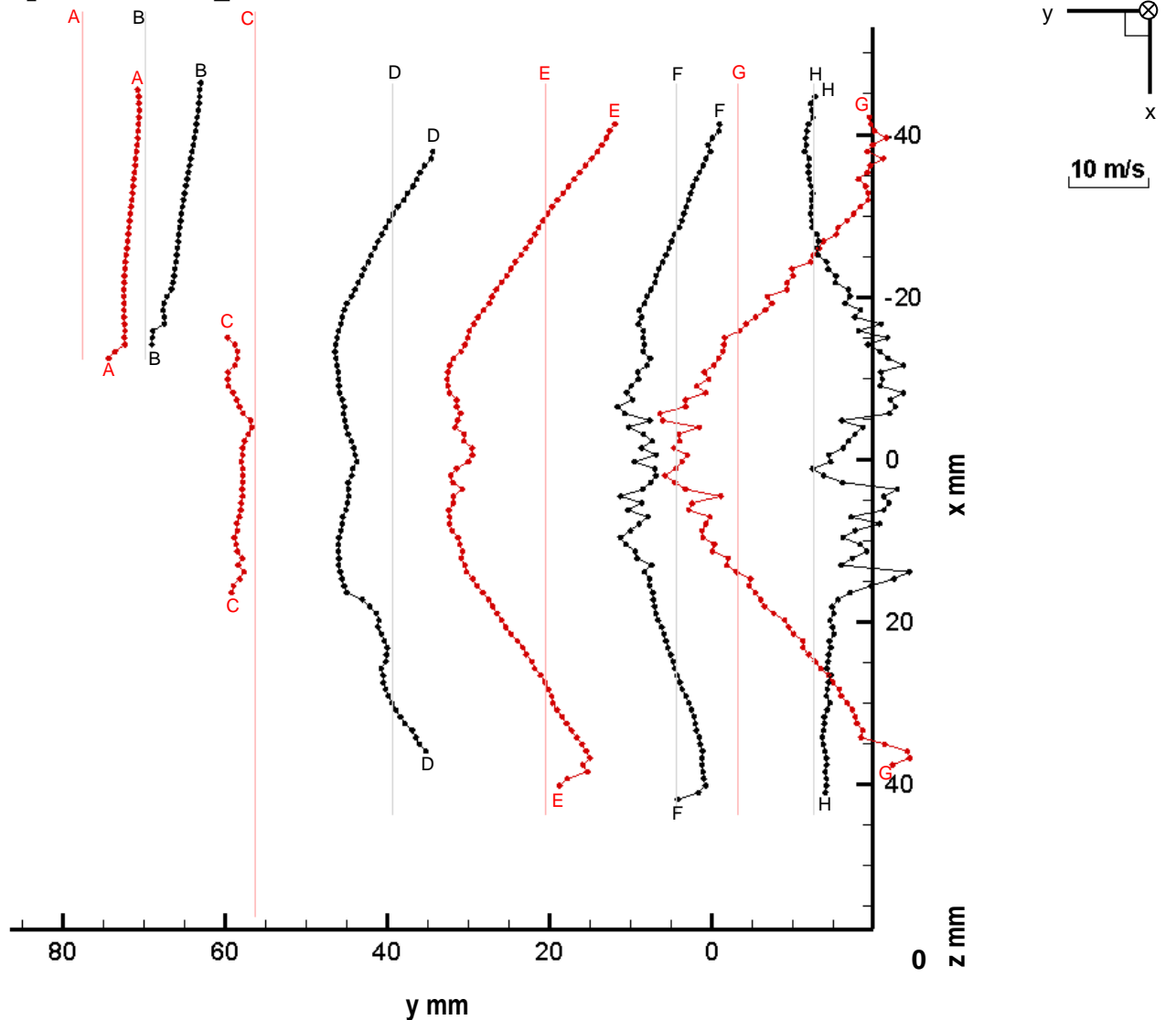


**Figure 89: The axial velocity profiles at selected slices along the primary zone length**

Figure 91 shows the same view as in Figure 90 but the vectors below  $Y = 3$  mm have been removed to isolate the swirling recirculation zone. It can clearly be seen that for  $X > 0$  mm the vectors point in the positive z-direction and for  $X < 0$  mm the vectors point in the negative z-direction. This shows clearly that there is swirling flow due to the swirler. It also shows that the swirl velocity (z-component) decreases as one moves away from the centre towards the liner wall.

Figure 92 shows the azimuthal velocity profiles at the same slice positions as those for the axial velocity profiles in Figure 89. The profile at each position has been rotated by  $90^\circ$  about the zero line to show the profile shape that would be perpendicular to the page. The positive (based on the y-axis direction) profile regions (left of the zero line) would be facing into the page while the negative (based on the y-axis direction) profile regions would be facing out of the page.

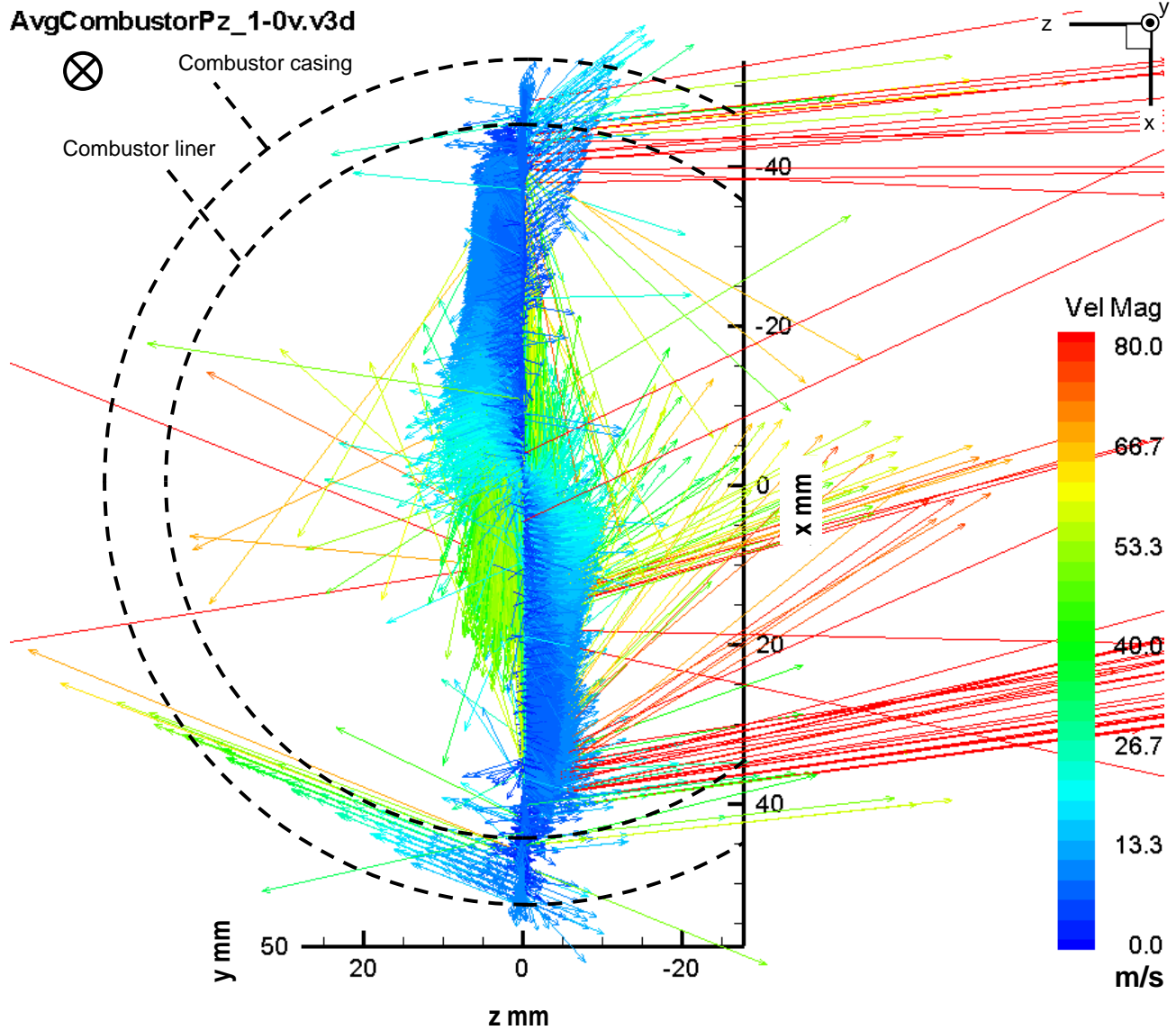


Figure 90: The three-dimensional vectors viewed from the left (upstream)

Profile A and B show zero azimuthal velocity magnitude indicating that the bulk flow being supplied to the combustor has a predominantly axial flow that is fairly uniform with no initial swirl. The fluctuations in Profile B at the bottom 10 points are the position at which the flow is encountering the swirler entrance thus the velocity changes direction. The rest of the slices are inside the combustor. All the slices in the combustor primary zone show negative velocity above the centreline ( $X = 0$  mm) and positive below it. This shows the swirling flow induced by the swirler.

As one steps through Profile C to F in the downstream direction, the azimuthal velocity magnitude and thus swirl intensity increases. As the radial distance increases from the centre of the combustor, the azimuthal velocity decreases showing a decrease in swirl intensity along the walls of the combustor. Similar “S”-shaped azimuthal velocities were measured by Li and Gutmark [11] and Janus *et al.* [9] and some of their results are shown in Figure 28 and Figure 33, respectively.

The last three slices (Profiles F to H) show much higher levels of fluctuation indicating an increase in turbulence in the region where the jets enter the combustor. Swirl is still evident in the last two slices, however, it is not as neatly defined due to the higher fluctuations. Profile G passes through the jets.

Similar profiles can be extracted for the radial velocity components. These are shown and discussed in Chapter 4.

AvgCombustorPz\_1-0v.v3d

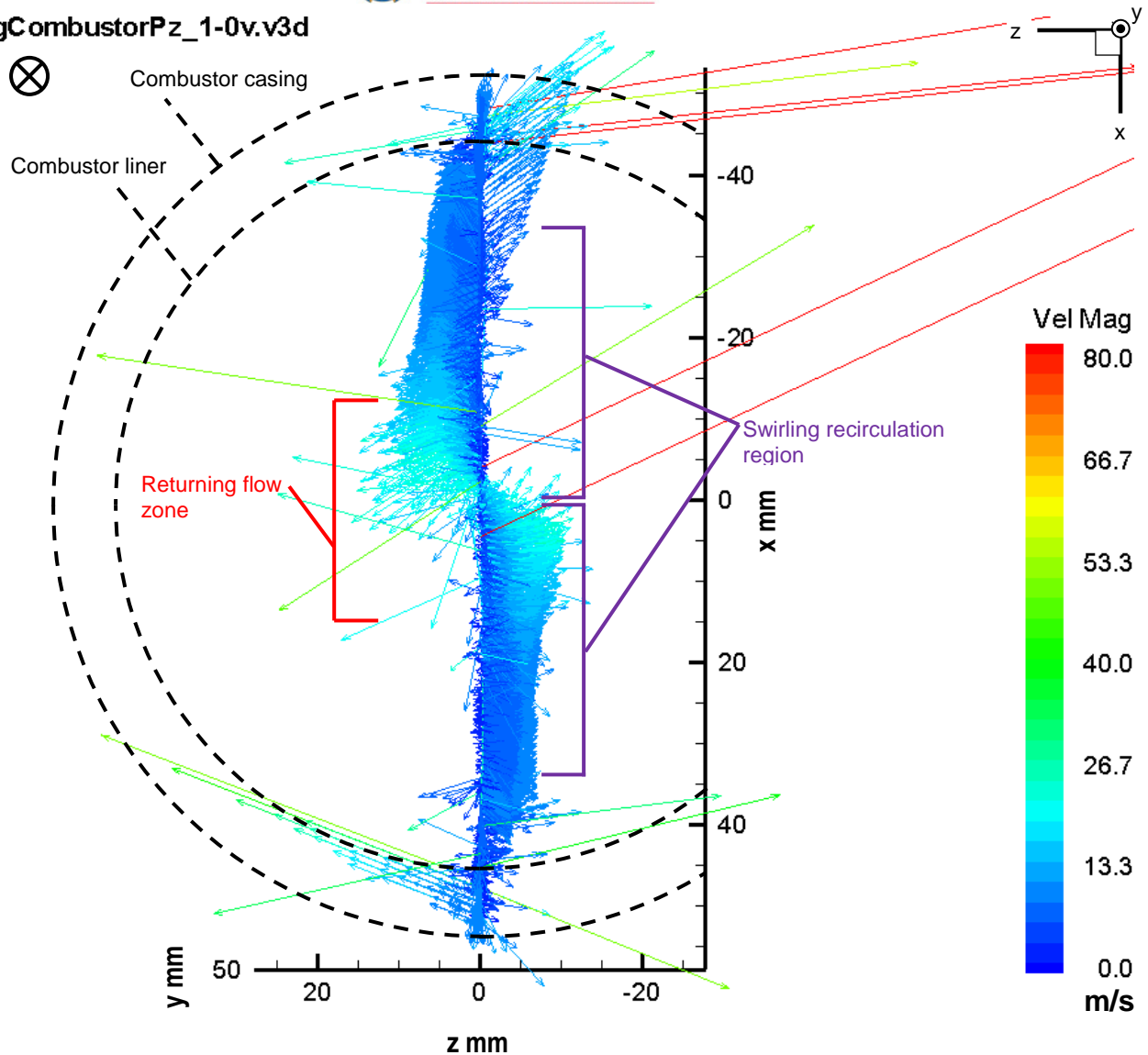


**Figure 91: The three-dimensional vectors viewed from the left (upstream) with the vectors below  $Y = 3$  mm removed**

In Figure 93, the plane in the combustor is coloured by velocity magnitudes. The high velocity regions of the jets stretch up to about 30 mm in from the liner wall and are shown in the yellow-green regions. The vectors in the jets with the non-real z-components (red cells) are close to a region with missing data (white cells) indicating a difficulty in cross-correlation in that region. The reverse flow region shape can also be picked up here and it seems to be more rectangular rather than “V”- or “Y”-shaped which is the more common shapes [10] for a combustor recirculation zone.

An indication of the validity of the vector for each interrogation region (cell) is the choice code (CHC). This is the number of vectors used to calculate the average vector in that interrogation region. In Figure 94, the interrogation regions are coloured by the CHC number in each cell. It can be seen that in the slower flow regions, 200 or more vectors were used for the calculation of the average vector in that cell. In the regions of faster flow, i.e. the jets and lower recirculation region, fewer vectors were used. Although fewer vectors were used in these regions, most of the vectors were calculated with more than 31 vectors thus are still statistically valid.

For further validation, the literature is referred to for typical flow features, which were looked for in the PIV results measured within the combustor itself. Even though the combustor used is unique, it is also generic in that it still has all the typical features of a can-type gas turbine combustor such as a diffuser at the combustor

inlet, an annular swirler, primary, secondary and dilution holes as well as film cooling rings. For this reason, typical flow features are expected and shown to be present (see Results in Chapter 4).

AvgCombustorPz\_1-0v.v3d

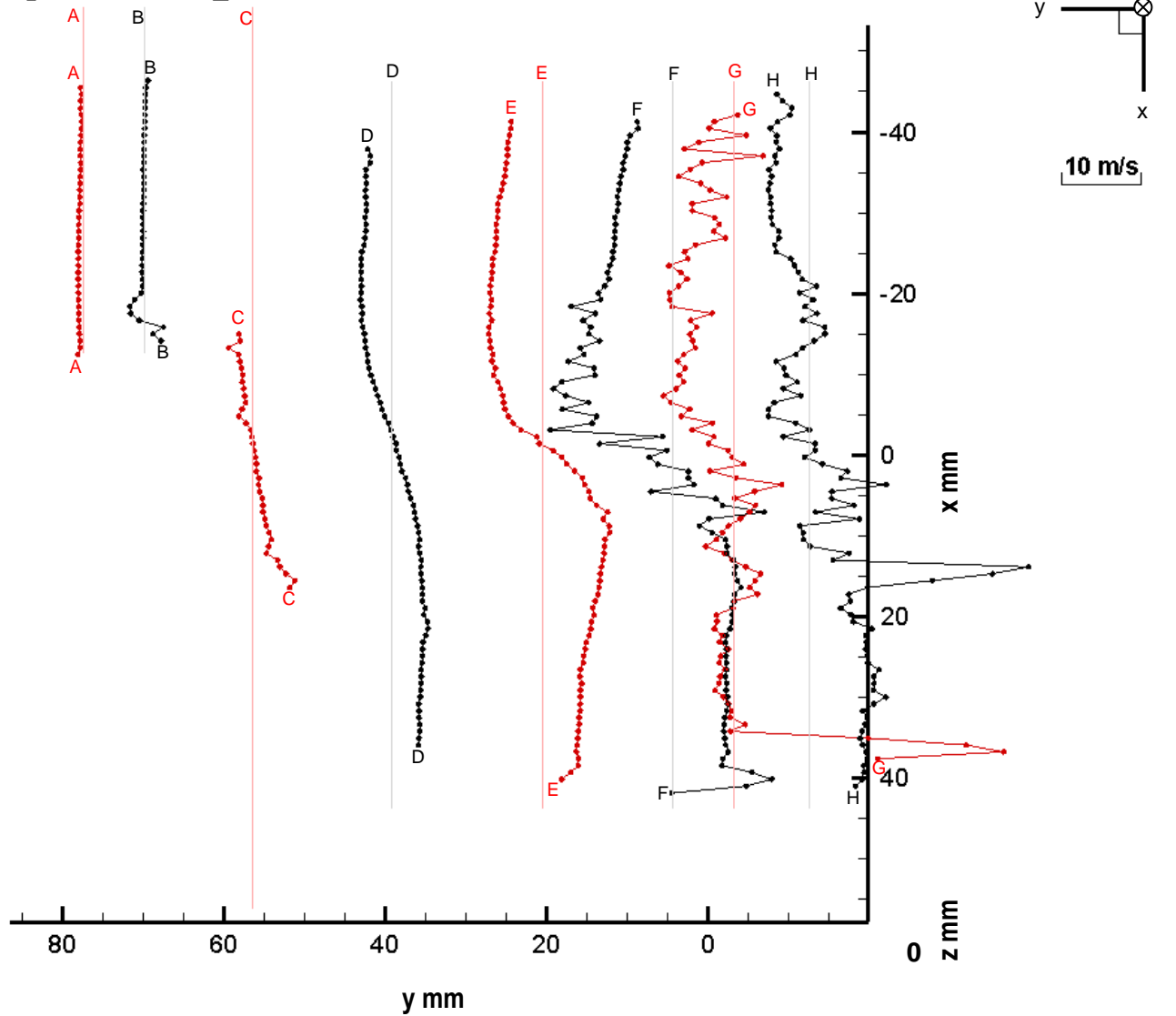


Figure 92: The azimuthal velocity (z-component) profiles at selected slices along the primary zone length



AvgCombustorPz\_1-0v.v3d

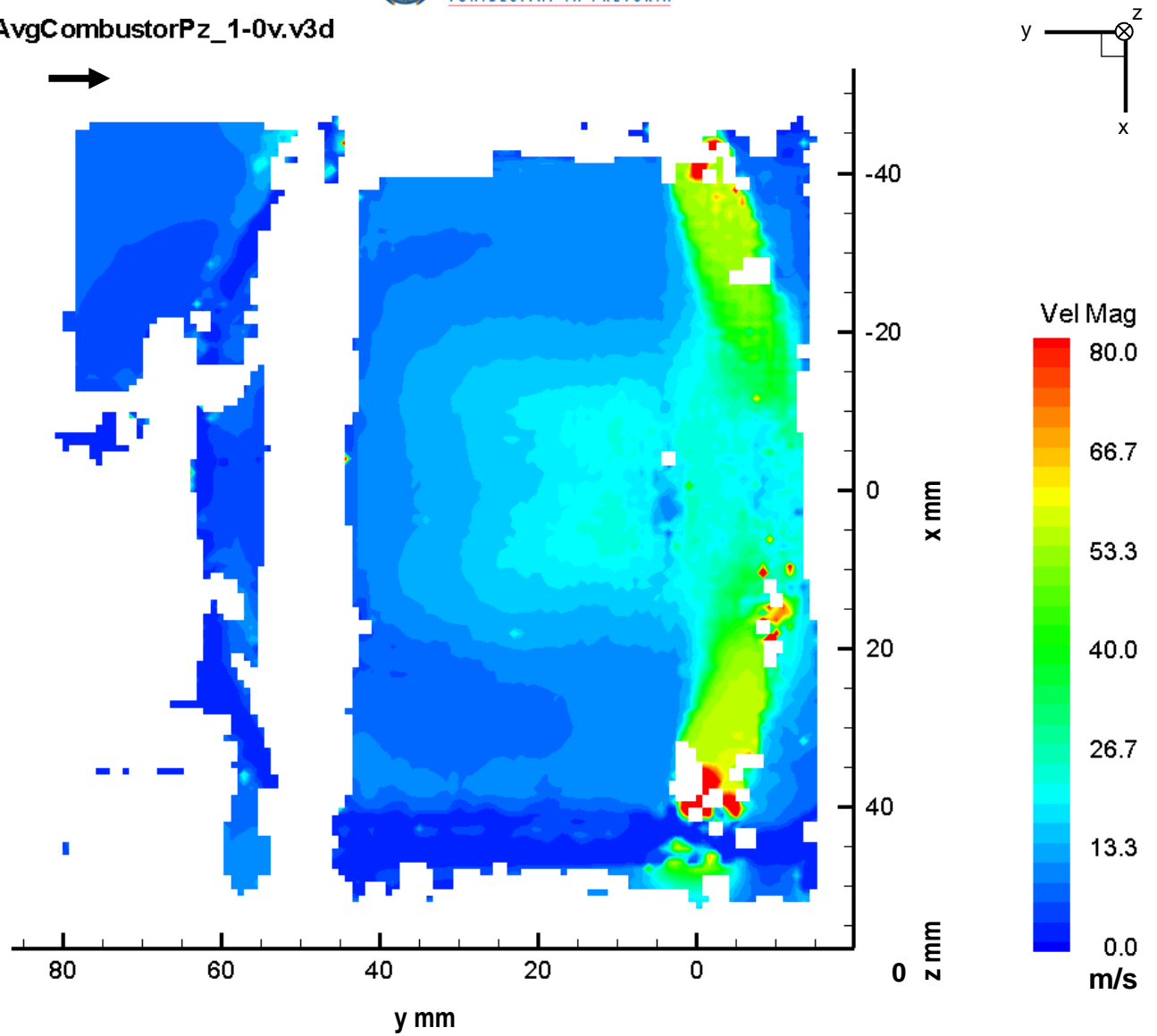
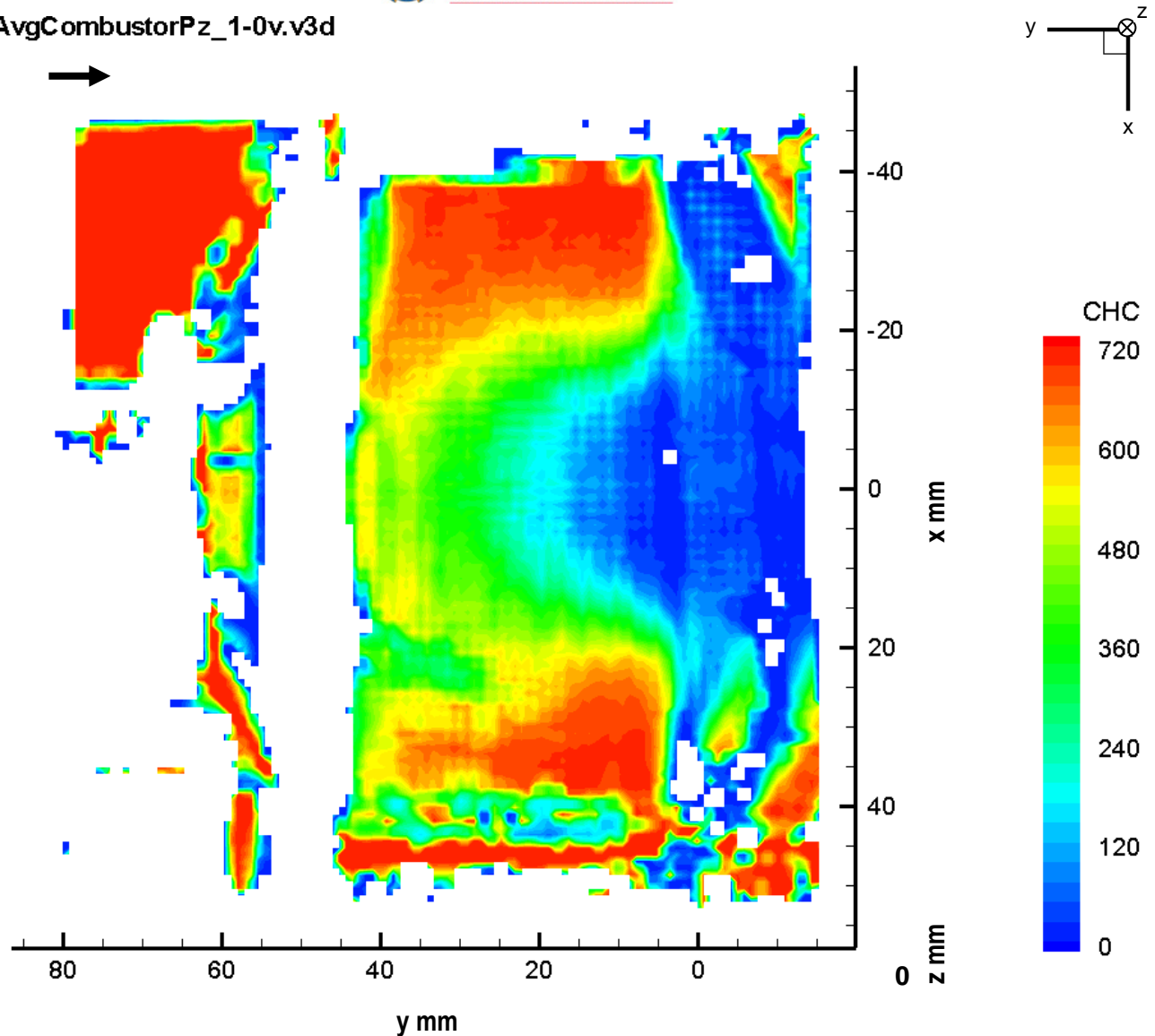


Figure 93: Contour map of the velocity magnitude in the primary zone

AvgCombustorPz\_1-0v.v3d



**Figure 94: Contour map of the CHC number for each interrogation region**

The region where there are the most flow features that can be used for comparison is the primary zone. Figure 95 and Figure 96 show typical primary zone flow patterns that can be expected. Both pictures show a recirculation zone and flow entering through the primary holes, which then either joins the recirculation zone or splits off to join the flow moving downstream. Figure 97 and Figure 98 show typical recirculation zones. In Figure 98, the typical axial and azimuthal (swirl) velocity profiles are shown. Within the recirculation zone, the axial velocity profile has a negative velocity in the core region where the reverse flow occurs. The outer edge of the axial profile has a positive velocity. The profile just after the recirculation zone becomes entirely positive, however, the core flow still has a smaller velocity magnitude than the outer flow region. The azimuthal velocity profile has an “S”-shape along the diameter with a decrease in the swirl velocity as one moves towards the outer edge of the combustor. The intensity of the swirl decreases after the recirculation zone.

Figure 99 shows the typical flow expected through the whole length of a can-type combustor. It also shows the typical zones and holes as well as some typical temperature and equivalence ratio values throughout the combustor length.

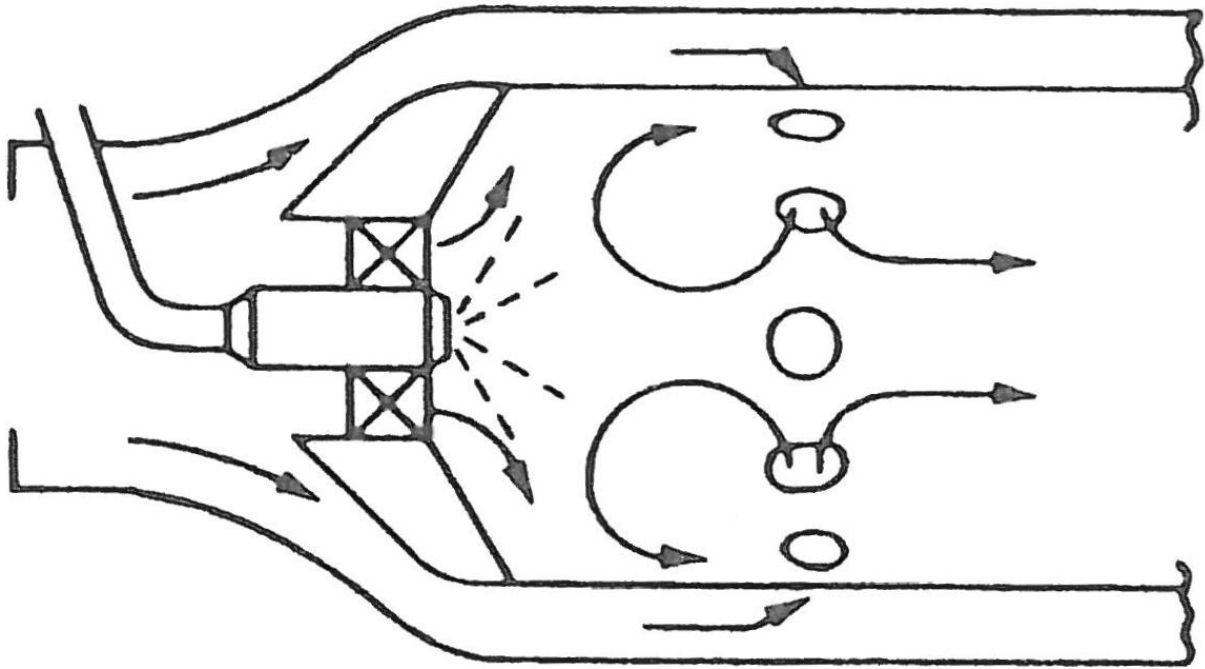


Figure 95: A typical primary zone configuration [15]

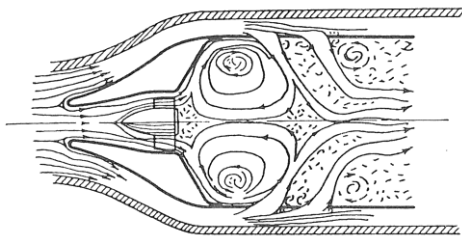


Figure 96: Lucas primary zone air flow pattern [15]

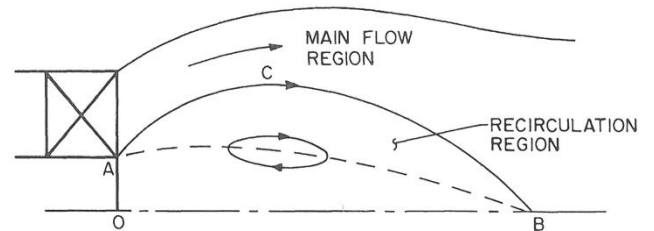


Figure 97: Recirculation region in a swirling flowfield [15]

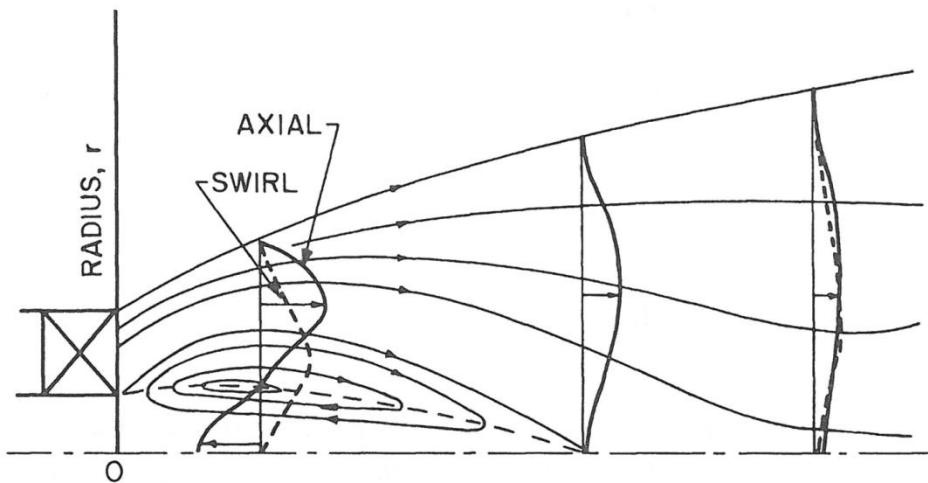


Figure 98: Typical profiles of axial and swirl velocity components in a strongly swirling flow [15]

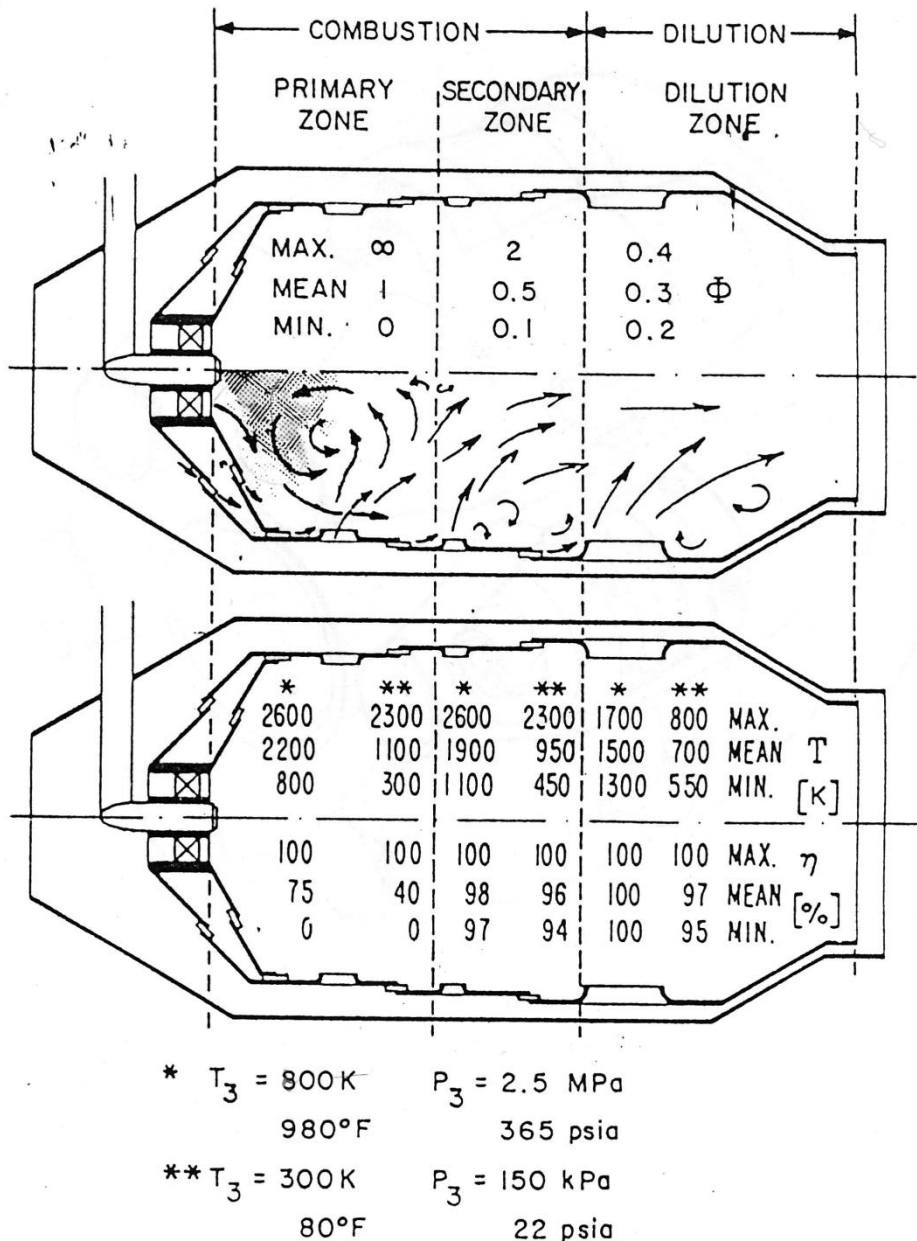


Figure 99: Typical combustion chamber flow schematic diagram and values [27]

The above-mentioned features are shown in the velocity data measured using the PIV system and are reported in Section 4.2. The typical flow features present are the recirculation zone in the primary zone as well as typical axial and azimuthal velocity profiles in the primary zone. The velocity profile at the outlet of the primary zone also has a typical shape.

### 3.4.2 PIV-Pitot comparison

A simple verification of the PIV measurement method was performed by comparing one velocity component measured using PIV with a well-established velocity measurement method using a Pitot tube (see Figure 100). In order to get an indication of the validity of the PIV data for this study, it was compared with a known technique of velocity measurement. A comparison of uniform flow coming out of the test rig without a liner was measured using a Pitot tube and the PIV system. Only the axial velocity component of the PIV measurements was used for comparison to the Pitot tube results. The velocity measurements were taken

after the outlet of the test rig in the jet of air provided by the fan. The Pitot tube tip was aligned with the laser sheet that was used to measure the PIV velocities on an axial plane. A slice was taken from the PIV plane, which lined up with the position of the tip of the Pitot tube. The two velocity profiles for comparison were thus at the same position in the flow and could thus be compared. The velocity profile comparison is shown in Figure 100. The Pitot tube velocity profile has error bands consisting of the instrument error of the Pitot tube ( $\pm 1.05\%$ ) and the uncertainty of the velocity due to the uncertainty involved with setting up a repeated air mass flow rate ( $\pm 0.4\%$ ). The Pitot tube values are corrected for the difference in velocity due to a difference in air mass flow rate, measured with the orifice plate, between the two tests. The PIV velocity profile at the same cross-section obtained from an average of 735 PIV points per cell is plotted on the same graph. The scatter bands on the PIV profile show a 95% confidence interval (1.96 standard deviations of the sample at each point) for the PIV sample at each cell.

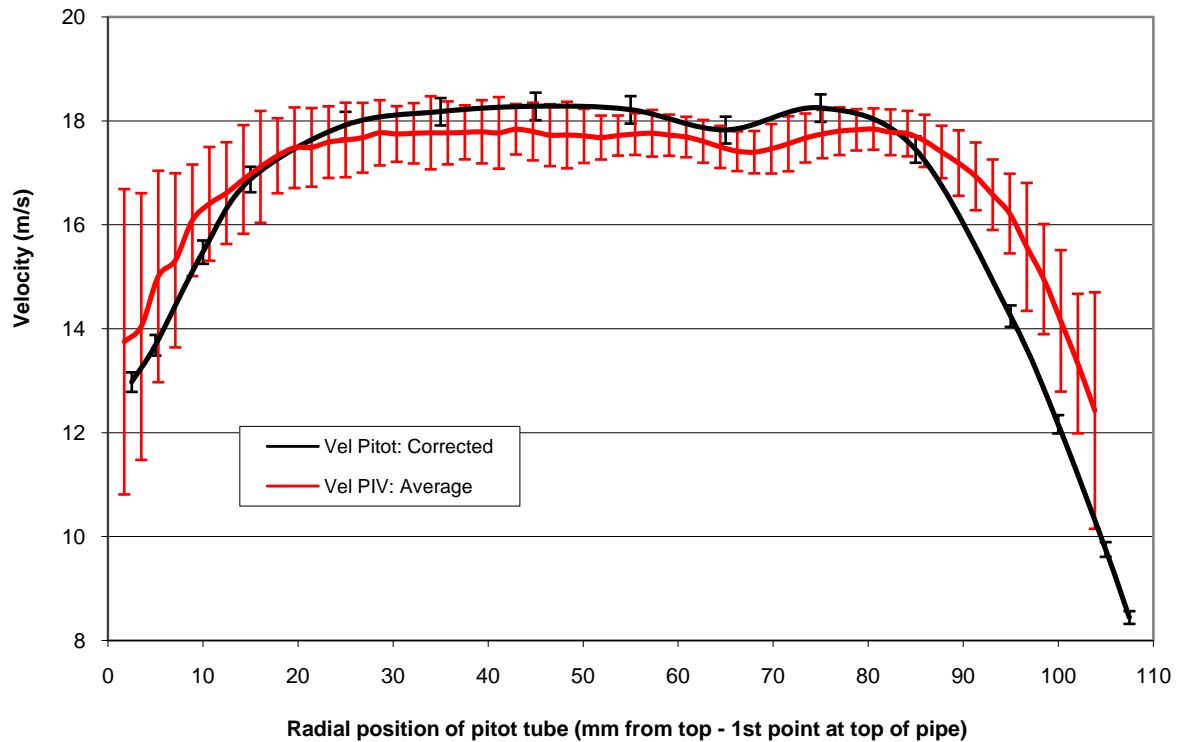


**Figure 100: Comparison of the velocity profiles after the outlet of the test rig**

At the core of the flow, the Pitot tube and the PIV profile lie reasonably close with the Pitot tube lying within the PIV scatter band, which has an average of 3.2% in this region. Near the edge of the flow, the PIV scatter bands increase in size because the flow on the edge of the jet is more unsteady than the core due to mixing with the ambient air. However, the profiles do follow a similar trend even at the edges of the flow.

### 3.4.3 Calibration and Instrument Uncertainty

Further, the rest of the data was collected using calibrated instruments. Table 5 shows the uncertainties of the various instruments and properties (measured or calculated) and indicates the method used to calculate them. The uncertainty analysis methods used are described in Appendix 6D.

**Table 5: The uncertainties of the various pieces of equipment used**

Equipment	Variable	Units	Typical measured value	Uncertainty	Method used
300° mercury thermometer	$T_{atm}$	°C	5 - 25	$\pm 1$ °C	½ scale reading
100° mercury thermometer	$T_{atm}$	°C	5 - 25	-30 to 50 °C → $\pm 0.7$ °C 50 to 100 °C → $\pm 0.6$ °C	Calibration certificate
Fortin barometer	$P_{atm}$	mmHg →Pa	87 000	$\pm 30.2$ Pa	Kline-McClintock [28]
Digital barometer	$P_{atm}$	Pa	87 000	$\pm 200$ Pa	Manufacturer
Kews barometer	$P_{atm}$	mmHg →Pa	87 000	$\pm 17.3$ Pa	Kline-McClintock [28]
dpm t-series digital manometer	$\Delta p$	Pa	1000 - 5800	$\pm 2\%$	Manufacturer
PT103	$T_1$	°C	5 - 45	$\pm 1.2$ °C	Calibration SEE
Wika fuel pressure gauge	$P_F$	kPa	900	$\pm 25$ kPa	½ scale reading
K-type thermocouple	$T_3$	K	278 - 320	$\pm 1.1$ °C or K	Calibration SEE
K-type thermocouple	$T_4$	K	400 - 900	$\pm 3.4$ °C or K	Calibration SEE
Timer on video camera	$\Delta t$	s	293.15	$\pm 0.41$ s	Full-scale reading and video frame rate
Terrailon digital scale	$m_F$	g	230	$\pm 1.96$ g	Calibration SEE
Air mass flow rate result	$\dot{m}_A$	kg/s	0.055 - 0.118	$\pm 1.01\%$	Kline-McClintock [28]
Fuel mass flow rate result	$\dot{m}_F$	kg/s	0.000785	$\pm 6.7 \times 10^{-6}$ kg/s	Kline-McClintock [28]
Velocity profile Pitot result	$U$	m/s	0 - 50	$\pm 1.05\%$	Kline-McClintock [28]



Equipment (Continued)	Variable (Cont.)	Units (Cont.)	Typical measured value (Continued)	Uncertainty (Continued)	Method used (Continued)
Velocity profile PIV result	$U, V, W$	m/s	0 - 110	$\pm 3.2-10\%$	Standard deviation and Pitot comparison and Li and Gutmark <sup>1</sup>
Air/Fuel ratio	AFR	-	116	$\pm 1.32$	Kline-McClintock [28]
Pressure loss factor	-	-	80 - 132	$\pm 2.15\%$	Kline-McClintock [28]
Overall pressure loss	-	%	1.7 - 4.6	$\pm 1.97\%$	Kline-McClintock [28]
Pattern factor	-	-	0.56 - 0.71 0.64 - 0.66	$\pm 0.0068^2$ $\pm 0.0115^3$	Kline-McClintock [28]
Profile factor	-	-	0.49 - 0.54 0.51 - 0.54	$\pm 0.0017^4$ $\pm 0.003^5$	Kline-McClintock [28]
Swirl number	-	-	0 - 1.28	$\pm 2.2 - 11.4\%$ (Average = 3.83%)	Kline-McClintock [28]

The uncertainty of PIV velocities is very complex to calculate from first principles due to the digital nature of the data acquisition and the number of digital components used in the PIV equipment arsenal before the data is produced. Li and Gutmark [11] state that the uncertainty of PIV is greater than that of LDV, which is taken as  $\pm 5\%$  and thus was assumed to be of the order of  $\pm 5 - 10\%$ .

<sup>1</sup> Li and Gutmark [11] state that the uncertainty of PIV is greater than that of LDV, which is taken as  $\pm 5\%$  and thus was assumed to be of the order of  $\pm 5 - 10\%$ .

<sup>2</sup> Uncertainty for the pattern factor for the set-ups with three experiments used to calculate the outlet profile and pattern factor, etc. (No WR (base case), Both 0.3 WR, Both 0.1 WR, Pz 0.1 WR, Sz 0.1 WR)

<sup>3</sup> Uncertainty for the pattern factor for the set-ups with only one experiment used to calculate the outlet profile and pattern factor, etc. (Pz 0.3 WR, Sz 0.3 WR)

<sup>4</sup> Uncertainty for the profile factor for the set-ups with three experiments used to calculate the outlet profile and profile factor, etc. (No WR (base case), Both 0.3 WR, Both 0.1 WR, Pz 0.1 WR, Sz 0.1 WR)

<sup>5</sup> Uncertainty for the profile factor for the set-ups with only one experiment used to calculate the outlet profile and profile factor, etc. (Pz 0.3 WR, Sz 0.3 WR)

## 4 RESULTS

### 4.1 Reacting experiment

The reacting experiment base case is the setup without any of the wedge rings inserted. It is shown in Table 6 (same as Table 2) with a green border.

**Table 6: The experimental test matrix for the reacting experiments**

Data types measured	Wedge ring configuration →	Both wedge rings	Pz wedge rings	Sz wedge rings	No wedge rings (base case)
Wedge ring set ↓		<ul style="list-style-type: none"><li>• Outlet plane temperature contours</li><li>• Outlet Velocity profile with combustion</li><li>• Outlet Velocity profile without combustion</li></ul>			
10%					
30%					



= Reacting flow base case

The following data is the reacting base case results.

#### 4.1.1 Outlet temperature profile

The normalised temperature results (see Equation [9] in section 2.3.2) measured with the thermocouples are plotted in Table 7 as a contour plot on the outlet plane to the combustor liner. The relevant characteristic values and factors are also noted in Table 7. The air mass flow rate was 0.091 kg/s.

The outlet temperature profile was not as symmetrical as expected from the symmetrical geometry. There were hot regions from about 45° to 135° and from about 260° to 340°. The cold region pushed from the centre through to the walls in between the hot spots. There was also an undulation in the hot region in the 45° to 135° sector.

Figure 101 shows a comparison between a simple CFD run performed on this combustor in a previous project [2] and the experimental result above. Note that the scale of the CFD results (bottom left and top) is about twice that of the scale in the experimental result image (bottom right). It can be seen that the general shape of the outlet profile is matched. The flow was hotter in the outer region than in the centre and there were two cooler “bubbles” just off centre on the opposite sides of each other in both results. An undulation or hot protrusions are also shown in the CFD results as in the experimental results. The experimental results, however, did not have an undulation in the lower hot region but one was present in the CFD results. The CFD temperature results were also about 200 K hotter than the experimental results, which is a too large an error to be acceptable.

Possible reasons for the CFD predicting incorrect flow features is that the common turbulence model is usually designed to model either swirling flows or jet flows correctly and thus when both are present the model falls short. Turbulence models also often assume isotropic turbulence properties which is not realistic for gas turbine combustors. This assumption could also be a main factor in the poor performance of the combustion model since the combustion model is dependent on the turbulence model to a great extent. The

<sup>6</sup>  $\alpha$  is measured from the dashed horizontal line shown in Table 7 in an anti-clockwise direction for all angle references in this dissertation

combustion models are also gross over-simplifications of the combustion process and often hundreds of the combustion steps are not modelled.

**Table 7: The normalised temperature results for the base case**

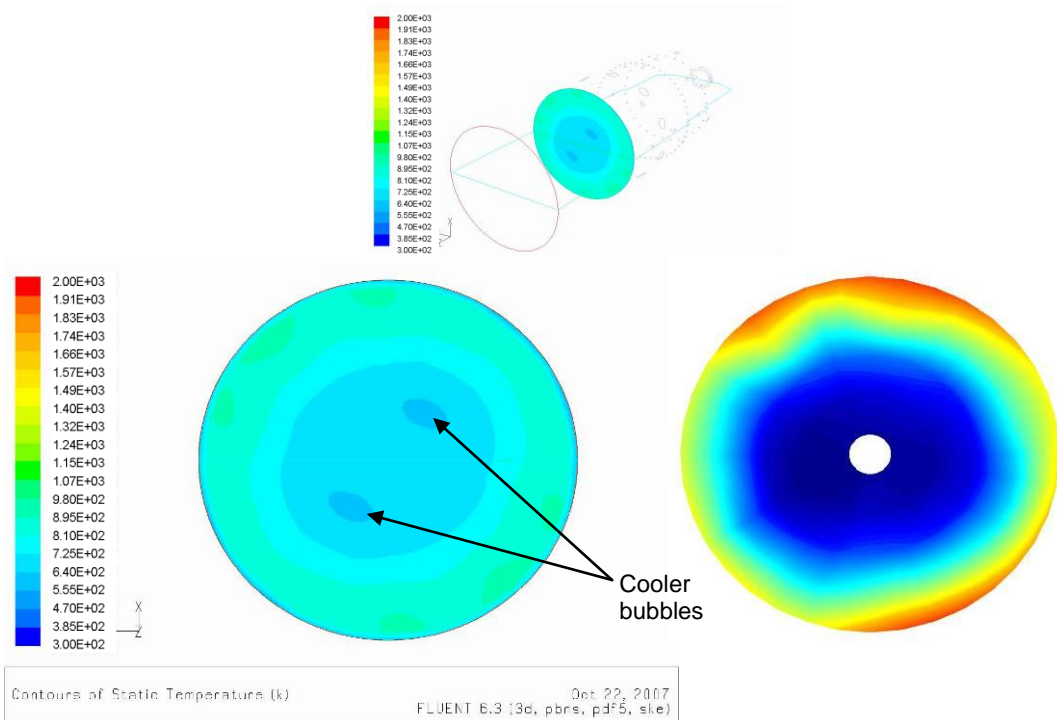
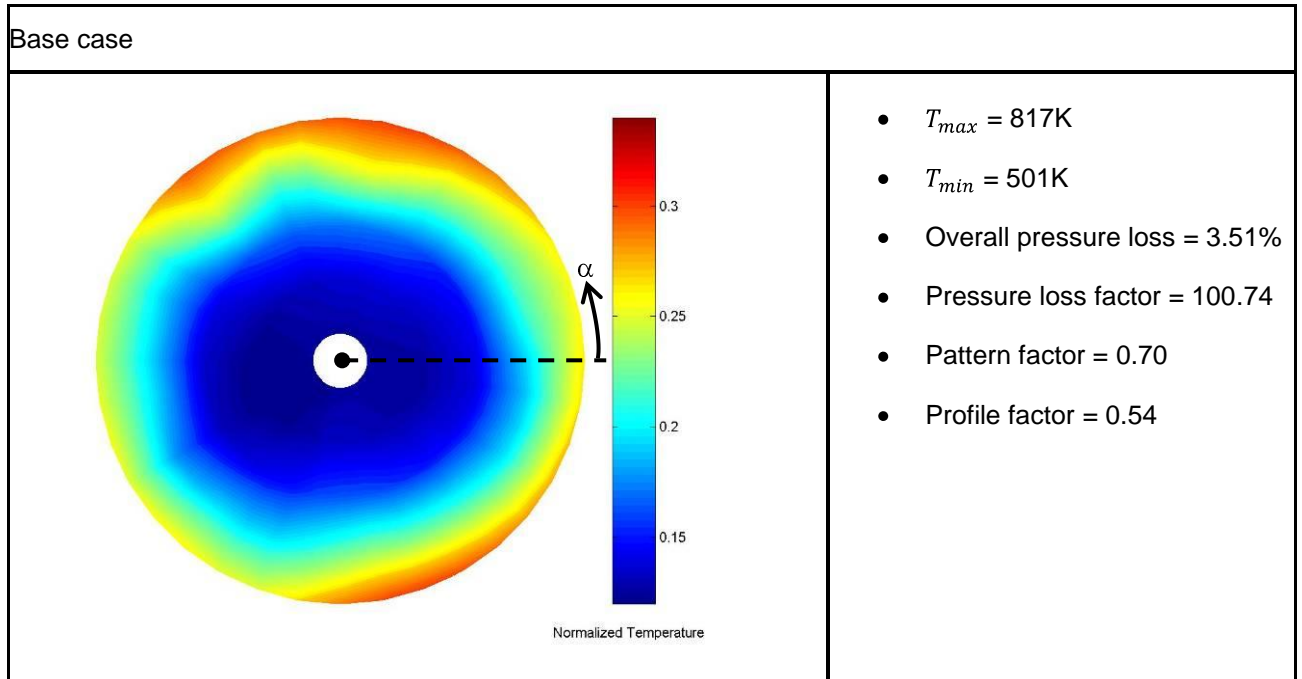


**Figure 101: A comparison between the experimental and simulated outlet temperature profile**

### 4.1.2 Qualitative data

In order to help interpret the measured data, some qualitative data was collected. Photos were taken of the flames during a combustion run. As can be seen in Figure 102, there were both blue flames and orange

flames. The blue flames indicate regions of combustion reactions close to stoichiometric while the orange flames represent off stoichiometric combustion most likely in the rich regime. During the experiments the blue parts of the flames were “stationary” and did not seem to move or vary much in shape throughout the experiment. The orange flames, however, were constantly moving, wrapping around, growing and then shrinking. There did, however, seem to be a periodic pattern to the orange flame movement.

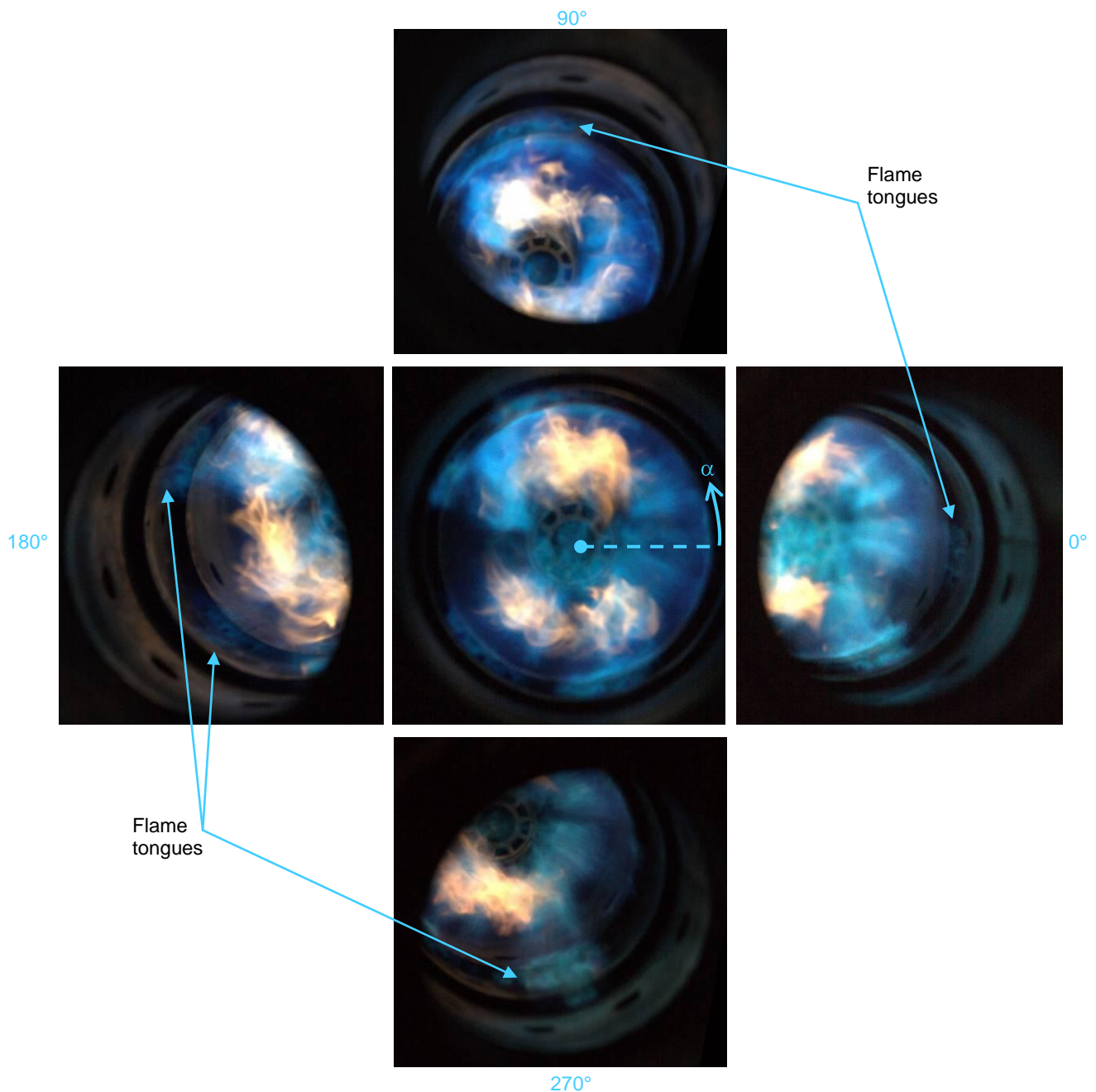


**Figure 102: The flame photos viewed from straight downstream and from angles of 0, 90, 180 and 270°**

In the left and centre images on the left side of the combustor, from about 135° to 225°, a wedge of “no flame” can be seen. This missing flame was a constant feature and corresponds to part of the colder region between 135° and 260° seen in the outlet profile in Table 7. In the top and bottom images, flame tongues that extend along the wall almost to the second cooling ring correspond to the hot protrusion or undulation at the top hot sector and the thick part of the bottom hot sector in Table 7. The flame tongue in the right image is not as long or as thick as the other two but seems to be in a position to extend the bottom hot region up the right side of the combustor wall all the way up to about 340° as seen in Table 7. The same features in the

outlet profiles corresponding to the phenomena in the flames mentioned above are present and discussed in the wedge ring results in Section 4.3 and in Table 18.

In Figure 103, a combination of flow and combustion patterns are evident on the walls. The regions where there is no carbon indicate where the carbon was burned away or physically dislodged. In the bottom and right images, there are regions where the carbon was burned away, which correspond to the flame tongues that are evident in the corresponding flame images in Figure 102. This also corresponds to the hotter regions in the outlet temperature profiles.

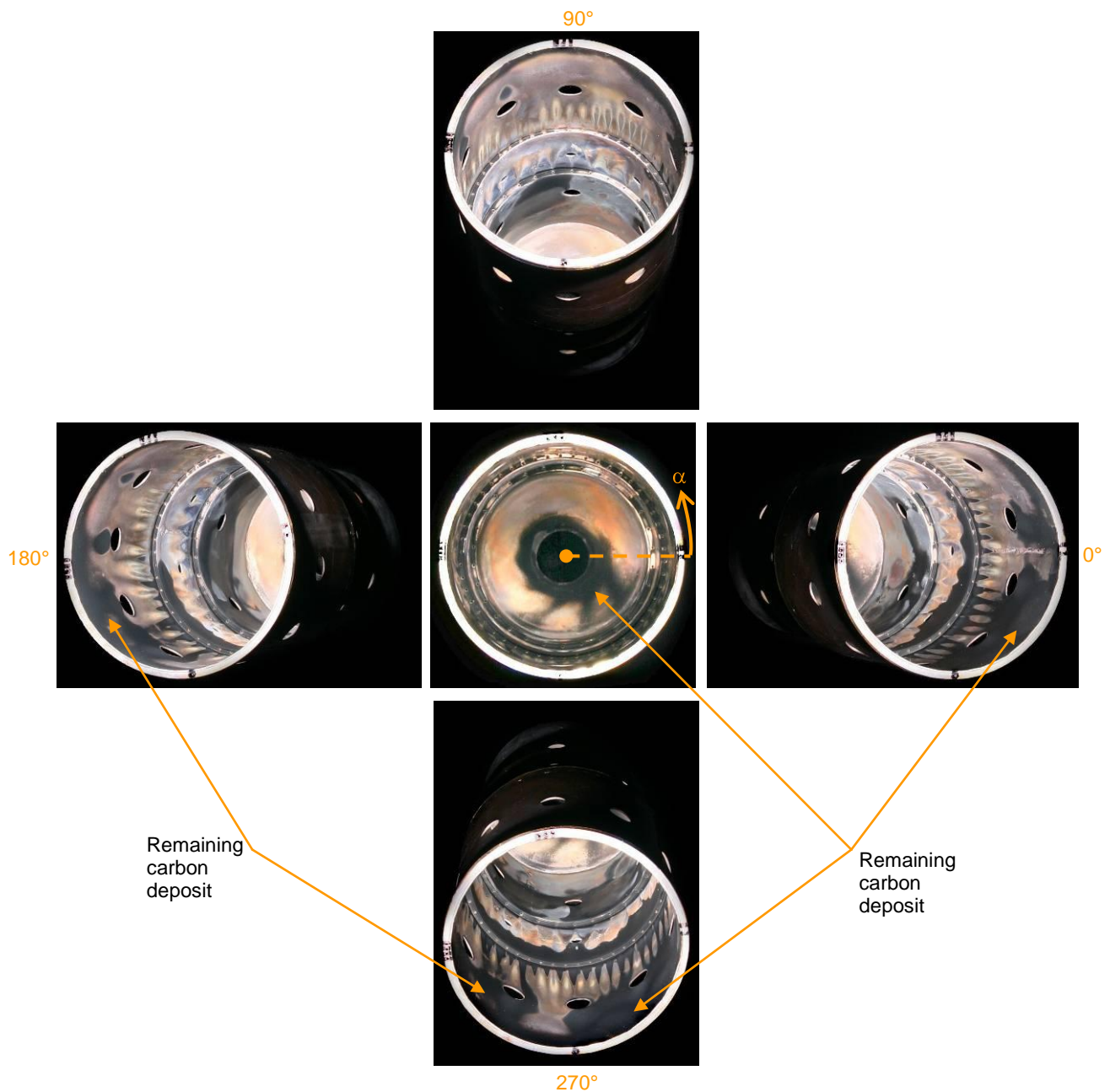


**Figure 103: Carbon deposits on the liner walls viewed from straight downstream and from angles of 0, 90, 180 and 270°**

The central image shows carbon deposit in the bottom right quadrant of the dome. This indicates that the flow is skewed from the dome region already and this then contributes to the skewed outlet temperature profile. The top image too shows that the carbon has been burned away in a sector that corresponds to flame tongues and the hot regions in the outlet temperature profile. The image on the left, however, does not show such a correlation. Since that region has no visible flame and is cold, one would expect there still to be carbon deposits on this sector of the liner but there is not. There are two main inputs that are required for the

combustion of the carbon: these are the presence of enough oxygen and a high enough temperature. If these are present in the correct combination, then the carbon can be burned away. Also it may be possible that a non-visible flame is present and the carbon is burned away in this way. A further reason could be that asymmetrical flow could cause a higher velocity air flow along the left wall which could physically cause the carbon to be dislodged and cause a lack of flame on the left at the same time. It could also have been that the flame structure at start up was such that the carbon was burned away on this side before test conditions were reached. It is evident that the reason is not as straightforward as it might seem originally and any one of the reasons mentioned may explain the discrepancy in the carbon and flame images on the left in Figure 102 and Figure 103. Also shown in the four outer images of Figure 103 is the distance downstream that the cooling holes affect the liner wall. This is indicated by the longitudinal stripes of missing carbon in line with the cooling holes.

### 4.1.3 Outlet velocity profile

The velocity profiles measured with the Pitot tube 60 mm downstream to the outlet plane of the combustor are presented in Figure 104. The velocity profile with the empty markers was measured with combustion while the one with filled markers was measured without combustion (NC). The two empty markers on the combustion profile are negative indicating that a negative pressure drop was measured across the Pitot tube at these points. This is an artificial negative and only indicates a region where the pressure drop across the Pitot tube was negative. This indicates that a larger component is perpendicular to the Pitot tube than parallel with it. As expected, the velocity profile with combustion has a higher velocity than the profile without combustion. The maximum velocity with combustion at 44.5 m/s is almost double that without combustion which is at 26.5 m/s. In the graph, the base case is referred to as the “No WR” or No Wedge Ring case.

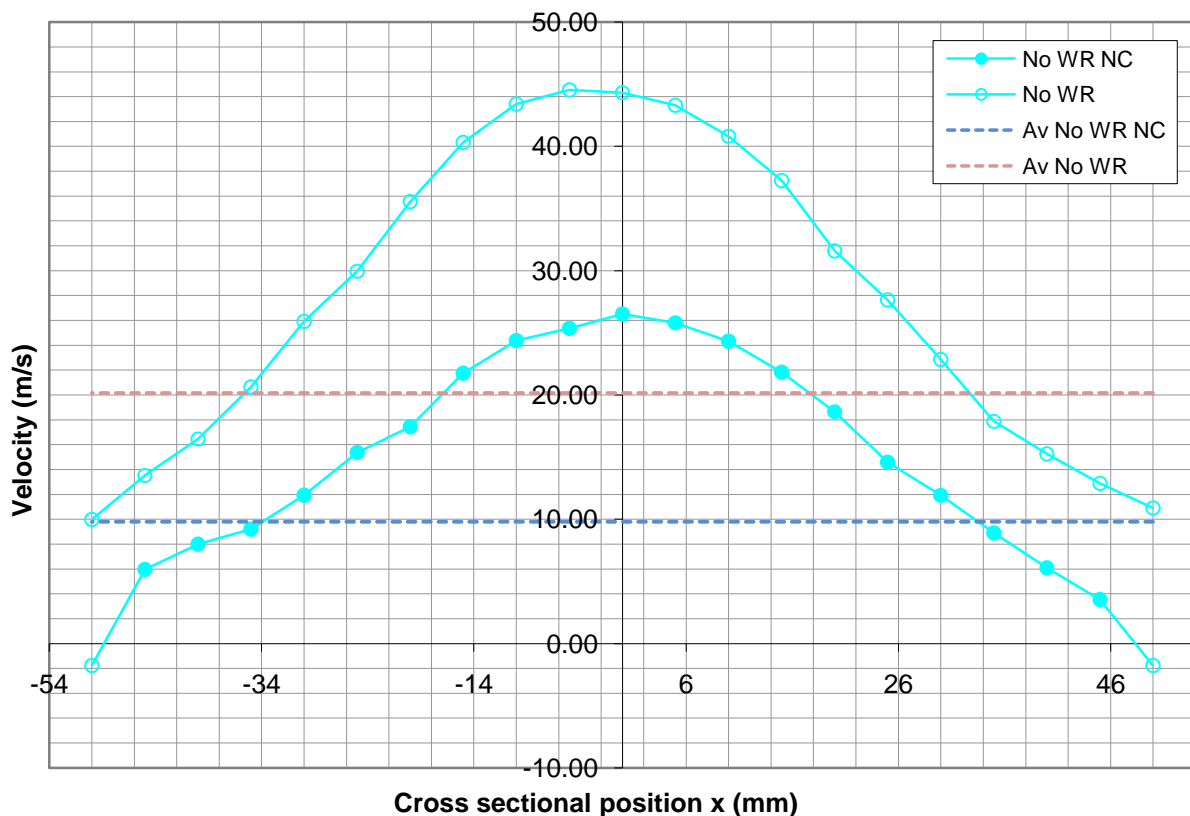


**Figure 104: The outlet velocity profile comparison for the base case set-up**

The two dotted lines at 9.76 and 20.12 m/s are the calculated average velocities (Av), without wedge rings and no combustion (Av No WR NC) and without wedge rings and with combustion (Av No WR), respectively,

at the outlet of the combustor based on the measured mass flow rate and the diameter of the outlet. The addition of the fuel and combustion increases the velocities exiting the combustor.

## 4.2 Non-reacting experiment

The PIV experimental test matrix is shown in Table 8 (same as Table 3). In the cells of the test matrix, it is stated whether a two- or three-dimensional test was done as well as the time between laser pulses used for that run. The two-dimensional experiments were performed in order to check the three-dimensional results. The results for the three-dimensional experimental set-ups are shown after the test matrix and discussed below.

**Table 8: The experimental test matrix for the PIV experiments**

PIV Test matrix	Air mass flow rate →	$\dot{m}_A = 0.056$ kg/s		$\dot{m}_A = 0.059$ kg/s		$\dot{m}_A = 0.064$ kg/s		$\dot{m}_A = 0.070$ kg/s		$\dot{m}_A = 0.078$ kg/s		$\dot{m}_A = 0.091$ kg/s	
	Laser Position →												
Section ↓	Camera Angle ↓	In line Holes	In between	In line Holes	In between	In line Holes	In between	In line Holes	In between	In line Holes	In between	In line Holes	In between
Pz	T = 5° B = 20°	3D: 15 $\mu$ s	3D: 15 $\mu$ s	3D: 15 $\mu$ s									
	T = 0° B = 23°	2D: 15 $\mu$ s	2D: 15 $\mu$ s										
Sz	T = 5° B = 20°	3D: 5 $\mu$ s	3D: 5 $\mu$ s					3D: 2.5 $\mu$ s				3D: 2 $\mu$ s	
	T = 0° B = 23°	2D: 15 $\mu$ s	2D: 15 $\mu$ s										
Dz	T = 5° B = 20°	3D: 5 $\mu$ s	3D: 5 $\mu$ s					3D: 4 $\mu$ s				3D: 2 $\mu$ s	
	T = 0° B = 23°	2D: 5 $\mu$ s	2D: 5 $\mu$ s										

- = Completed PIV Experiments
- = Experimental setup for combustion tests (see Table 3)
- = Not planned for this project
- = Experimental setup for isothermal base case tests
- Pz = Primary zone
- Sz = Secondary zone
- Dz = Dilution zone
- $\dot{m}_A$  = Air mass flow rate
- T = Top camera
- B = Bottom camera

Some of the base case flowfield data shown in Section 4.2.1 was presented at the 19<sup>th</sup> International Symposium on Air Breathing Engines Conference in Montréal, Canada and is available on the proceedings as document number ISABE-2009-1108 with the title “Three-dimensional Particle Image Velocimetry in a Generic Can-type Gas Turbine Combustor”.

### 4.2.1 Base case flowfield

Due to experimental limitations, the flow rate where the most PIV data was collected was not that of the hot tests but at a lower flow rate of 0.056 kg/s. At this flow rate, almost full planes of data were collected in line with and in between the holes of each of the zones.

The velocity magnitude contours and streamlines are shown in a perspective view of the combustor liner in Figure 105. In Figure 105, the data planes are in line with the holes of all three zones. Figure 106 shows a normal view of the same data as in Figure 105.

Figure 107 and Figure 108 show the velocity vector field viewed from the side for each of the three zones in line with the holes. The velocity magnitude is also shown. Figure 109, Figure 110 and Figure 111 show the axial, radial and azimuthal velocity profiles at 19 slices along the length of the combustor. The X = 0 mm position is at the inlet plane of the swirler. The positions of the various profiles shown are at the axial positions X = -9, -1, 12, 29, 48, 64, 72, 81, 93, 113, 126, 138, 151, 163, 178, 185, 193, 204 and 214 mm. The swirl number at 10 of the slices (X = 12, 29, 48, 64, 72, 81, 126, 163, 178 and 214 mm) was calculated and included in the figures below the axial position of the corresponding slice in each of the figures. A CHC contour map for each section is also included in Figure 112.

Figure 113 to Figure 120 show the same type of data as discussed for Figure 105 to Figure 112 but this data lies on the planes in between the holes of each of the three zones. All of the images from Figure 105 to Figure 121 have the vectors with velocity magnitude greater than 80 m/s removed. Above 80 m/s the velocity vectors were found to have directions that were inconsistent with the surrounding vectors and thus were considered to be non-real.

Lastly, Figure 121 is a side-by-side comparison of the general flow features in the combustor both in line with the flow and in between the holes.

The black arrow in all the images shows the direction of the bulk inlet flow.

The primary zone features mentioned in Section 3.4.1 can be seen in Figure 105 to Figure 112.

In Figure 105, the data is shown in an isometric view of the combustor liner. In this view, the orientation and position of the data planes can be seen more clearly and the alignment with the holes is shown.

Figure 106 is a normal view of the planes lying in line with the holes. This figure shows the velocity magnitude in the contour plot with streamlines superimposed over the contours. At the position marked with a (1), the uniform bulk flow from the fan is converging in order to enter the annulus around the combustor liner. The bulk flow is also shown at (2) to curve downwards so as to enter the swirler.

In the primary zone, the recirculation zone that would aid combustion is present at (3) in both the streamlines in Figure 106 and the vectors in Figure 107. The recirculation zone is toroidal in shape and circles the primary zone of the combustor liner. At the centre of the primary zone is the reverse flow zone shown at (4). The reverse flow zone in this combustor is quite rectangular in shape, which is slightly atypical because the reverse flow zone is usually "V"- or "Y"-shaped [10]. The rectangular shape could be an extreme "Y"-shaped reverse flow zone in that the angle between the two arms of the Y tends to 0°. At (5), the stagnation point between the jets, combustor main flow and reverse flow zone occurs. The main cause of this stagnation point is the jets at (6) in Figure 106 and Figure 108. The jets of the primary zone receive 22.5% of the total mass flow supplied [2]. The primary zone jets show a 100% penetration depth. The penetration depth in this report is determined by the radial distance from the wall, as a percentage of the radius, at which the streamlines from the jets become asymptotic to the main combustor flow. Similar flow features shown in this zone and the flow patterns formed by the streamlines can be seen in Figure 95, Figure 96 and Figure 99.

The secondary zone streamlines (Figure 106) diverge outwards soon after the inlet to the zone (7). The jets entering the flow at (8) cause the flow to converge towards the centre again. The secondary zone jets only receive 8.8% of the total mass flow [2]. Due to the lower mass flow, the secondary jet penetration is approximately 60% of the radius. After the jets, the streamlines diverge again at (9).

In the dilution zone, the presence of an atypical recirculation zone at (10) is shown. It is unusual for a recirculation zone to be present in the dilution zone, which can be seen by the lack of a recirculation zone in the typical combustor flow in Figure 99. The presence of this recirculation zone is assumed to be due to the high mass flow rate of the dilution zone jets (11), which get 50% of the total mass flow [2]. It is assumed that the jets form a partial barrier, which then induces a recirculation zone. The dilution zone jets also have a 100% jet penetration depth, which contributes to the creation of a recirculation zone in the dilution zone. A stagnation point is also present in the dilution zone at (12). At (13), the streamlines converge towards the centre before leaving the combustor liner. The outlet velocity profile measured with the PIV can be seen at (14) in Figure 107 and Figure 108.

Small parts of the annulus flow around the combustor liner were also picked up during the PIV measurements. In Figure 107, the straight annulus flow along the secondary zone annulus can be seen at (15). At (16) in Figure 108, the annulus flow curving towards the holes to enter the liner in the primary and secondary jets can be seen. Also evident is the annulus flow curving around the step on the outside of the combustor liner to enter the next zone annulus at (17).

Figure 109 shows the axial velocity profile at various positions along the length of the combustor. At Profile A ( $X = -9$  mm) the bulk flow axial velocity is shown with quite a smooth and steady nominal velocity of 5,8 m/s (maximum velocity of 7 m/s). Moving downstream to Profile B ( $X = -1$  mm), the velocity profile near the lower 10 points shows fluctuations and a decrease in magnitude indicating a decrease of axial momentum to enter the swirler. Inside the primary zone, the velocity profiles C to F at  $X = 12, 29, 48$  and 64 mm show the profile shapes in the recirculation zone with a negative value in the core of the combustor and a positive value around the edge of the combustor flow. This profile shape is very typical of the recirculation region of the primary zone and similar profiles can be seen in the recirculation zone of Figure 98 and in the work of Cameron *et al.* [14] in Figure 2. Just before the jets on Profile F, at  $X = 64$  mm, the core of the profile is still negative but is becoming more positive. This trend in the centre can also be seen just before the jets in Figure 2. Profile G at  $X = 72$  mm goes through the jets that are seen in the velocity vector field in Figure 108. In this profile, the velocity in the positive direction increases in magnitude at the outer region and the flow is

positive for a wider band moving into the core. At Profile H after the jets (at  $X = 81$  mm), the whole profile is positive and the flow is on its way to having a large positive core in the secondary zone. The three Profiles F, G and H at  $X = 64$ , 72 and 81 mm, respectively, show an increase in fluctuations on the profile especially near the core of the flow. This is an indication either of the turbulence and unsteadiness of the flow in and around the jets or of low sample sizes (most likely due to the unsteadiness and the turbulence in this region) in the interrogation regions in this sector.

At the secondary zone inlet (Profile J), the axial velocity is exclusively positive and there is a high positive peak in the core and almost zero value at the outer region. The shape of this profile at  $X = 93$  mm is very similar to that shown before the jets in the secondary zone of Cameron *et al.* [14] ( $\frac{x}{R} = 2.50$ ) in Figure 2. Also as in Figure 2, the velocity profile magnitude begins to decrease after Profile J. In line with the jets at Profile K ( $X = 113$  mm), the top of the profile has a hump showing an increase in the positive axial velocity over a small sector of the radius. This peak is due to the jet at the top being angled more towards the combustor outlet than the bottom jet which can be seen in Figure 108. The profile thus passes through the centre of the top jet but not the bottom jet and only cuts through the edge of the bottom jet. At  $X = 126$  mm (Profile L), the axial velocity decreases after the secondary zone jets to become a much flatter profile and lower in magnitude as the flow transitions into the recirculation zone in the dilution zone.

In the dilution zone, the profiles before the jets are similar to those before the jets in the primary zone due to there also being a recirculation zone. After the dilution holes the velocity profile becomes positive at the core at  $X = 193$  mm (Profile S) and the whole profile moves positive at  $X = 204$  mm (Profile T). The outlet velocity profile (Profile U) at  $X = 214$  mm is a similar shape to that measured by the Pitot tube in Figure 104 and at ( $\frac{x}{R} = 5.00$ ) in Figure 2.

Figure 110 has the radial velocities at the same cross-sections as the axial velocity profiles in Figure 109. The bottom image has the profiles through the jets (Profiles G, K and R), which were removed from the top image for clarity. The left side of the zero lines, which is the negative side, indicates a downward-pointing vector whereas the positive side indicates an upward-pointing vector. From  $X = -9$  mm to  $X = -1$  mm, the radial velocity increases slightly from Profile A to Profile B. This is due to the flow turning upwards in this region to converge and enter the annulus around the combustor liner. At  $X = -1$  mm, the bottom 10 points of Profile B are negative, showing the flow turning downwards towards the swirler inlet. At  $X = 12$  mm to  $X = 64$  mm (Profiles C to F), the radial profiles are as expected in the recirculation zone with the flow moving apart at  $X = 12$  mm (Profile C) and towards the centre at  $X = 64$  mm (Profile F) and no radial flow at  $X = 48$  mm (Profile E). The primary jets are shown in the lower image of Figure 110 at  $X = 72$  mm (Profile G). The primary jets have a magnitude of approximately 50 m/s. Nine millimetres downstream at Profile H ( $X = 81$  mm), there is still radial velocity vectors of approximately 25 m/s but the radial velocity is dissipated rapidly after this profile to a fairly flat and low magnitude Profile J in the secondary zone at  $X = 93$  mm. At  $X = 113$  mm, Profile K passes through the secondary jet region. On this profile, the top jet magnitude is approximately 34.7 m/s and the bottom jet is approximately 24.6 m/s towards the centre of the combustor but the core of the profile is showing the diverging combustor main flow towards the outer region of the liner. The next cross-section (Profile L) shows diverging flow across the whole diameter of the combustor.

The dilution zone also has profiles typical of a recirculation zone with no radial vectors at  $X = 163$  mm (Profile O). The top jet has a radial velocity magnitude of approximately 47.2 m/s and the bottom jet 27.0 m/s. After the dilution jet region, there are minimal radial velocities at Profiles T and U ( $X = 204$  and 214 mm). The asymmetry of the jet magnitudes in the secondary and dilution zones may be due to the slice not intersecting the bottom jet exactly in the centre of its main flow.

Figure 111 shows the azimuthal velocity profiles throughout the combustor. For the bulk flow before the combustor liner at Profiles A and B, there is no azimuthal (tangential) component except for the small region at the swirler entrance on Profile B where the flow is starting to gain a tangential component on entering the swirler. Inside the primary zone, the profiles have negative sectors above the centreline and positive sectors below indicating a swirling flow. From Profile C ( $X = 12$  mm) to Profile F ( $X = 64$  mm), the swirl velocity increases in magnitude as one moves in the downstream direction. There is also a decrease in the swirl velocity as one moves towards the outer radius of the combustor on these profiles. At Profile G, in line with the jets at  $X = 72$  mm, there still seems to be evidence of swirl at the upper half of the profile but not the lower half.

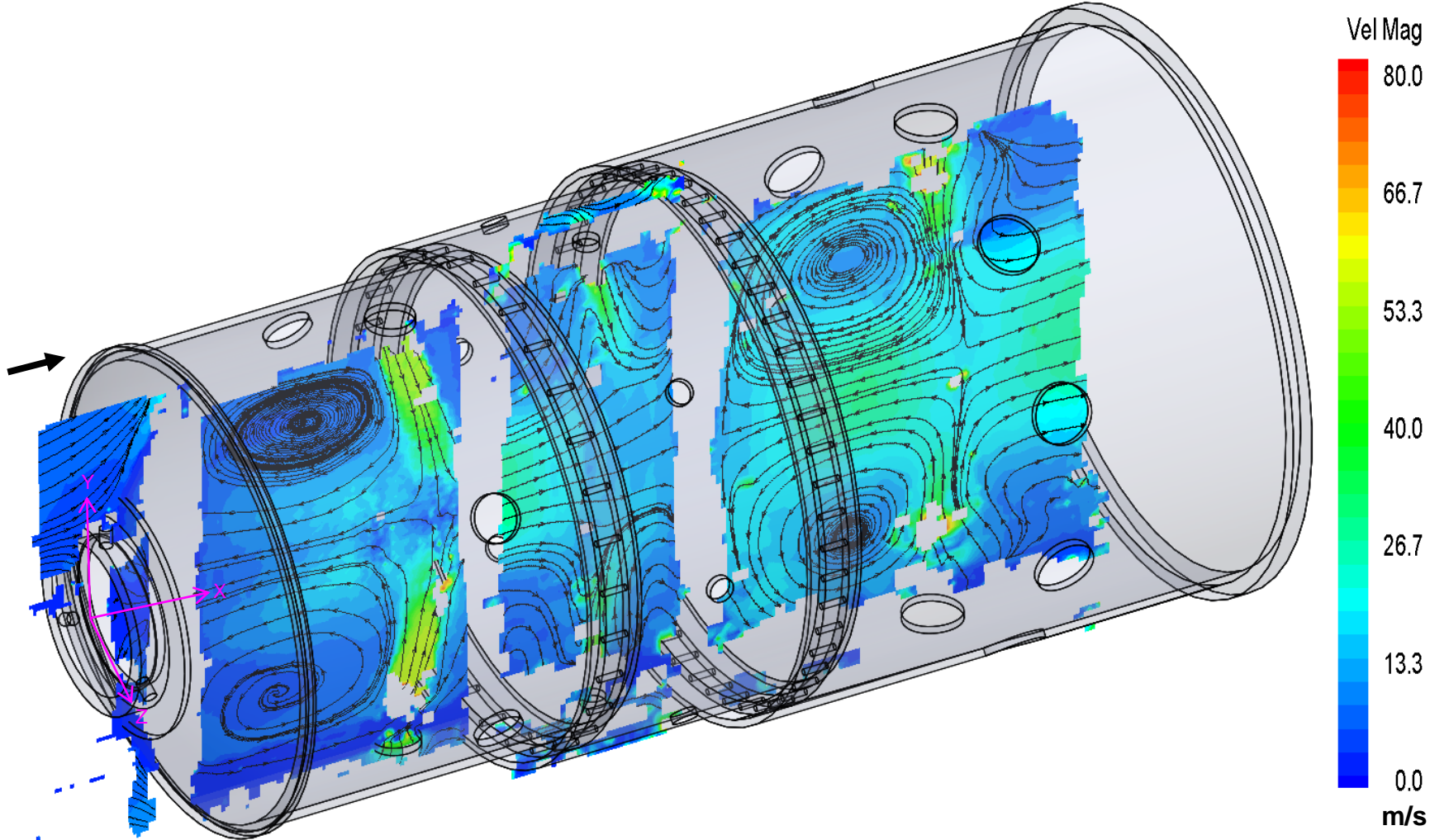


Figure 105: Isometric view of the combustor liner showing the velocity magnitude contours and streamlines in line with the holes

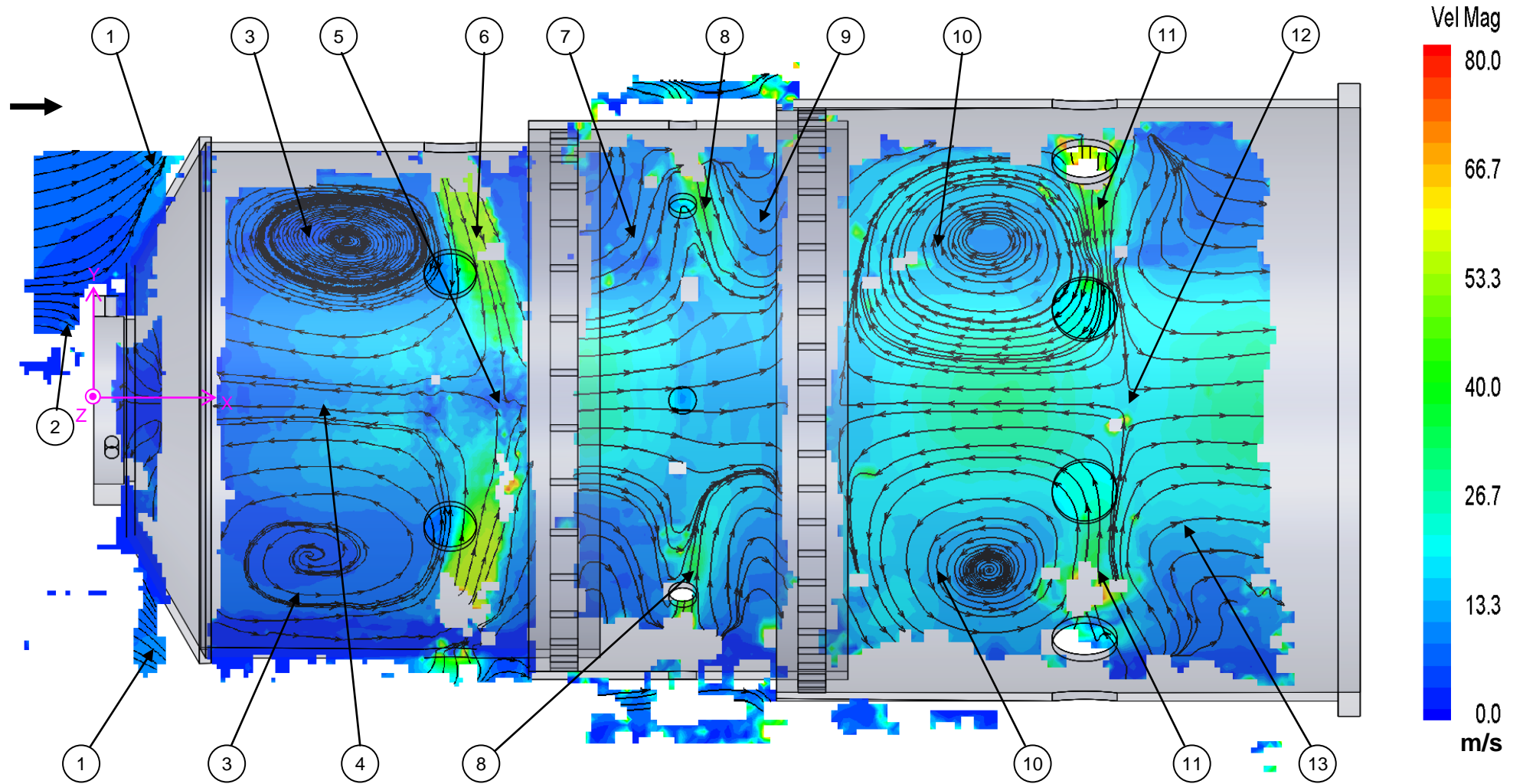


Figure 106: Normal view of the combustor liner showing the velocity magnitude contours and streamlines in line with the holes

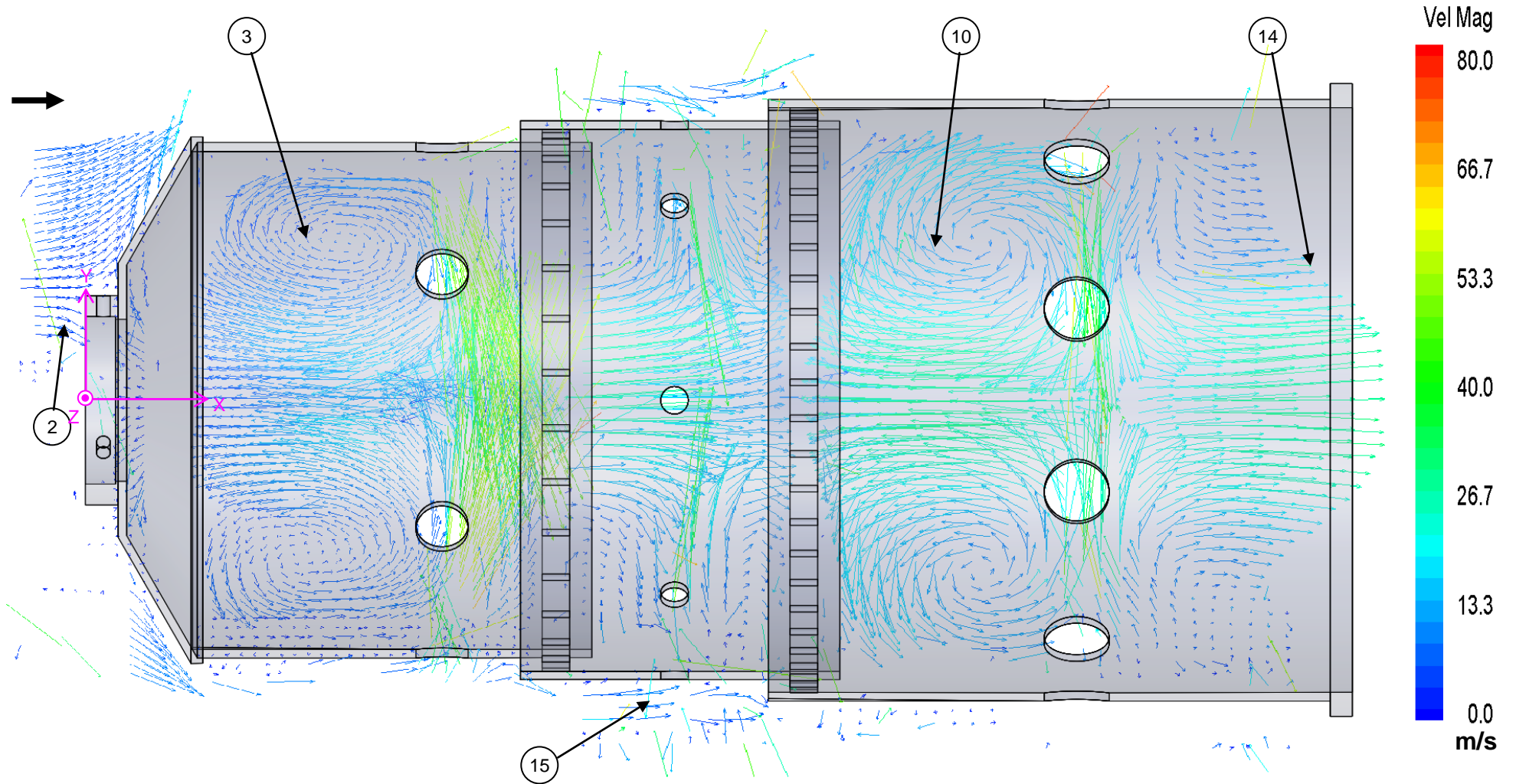


Figure 107: Normal view of the combustor liner showing the sparse velocity vectors in line with the holes

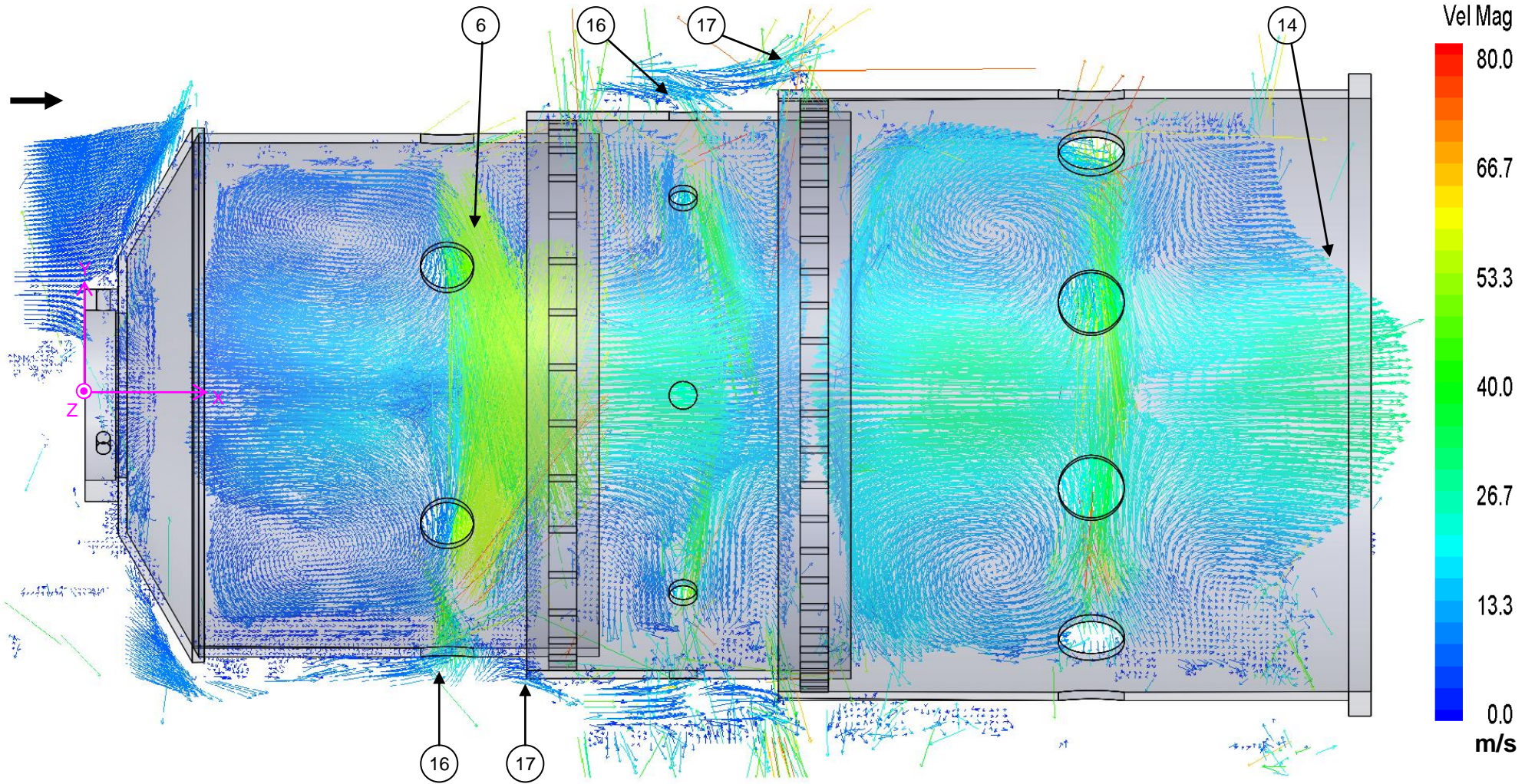


Figure 108: Normal view of the combustor liner showing the velocity vectors in line with the holes

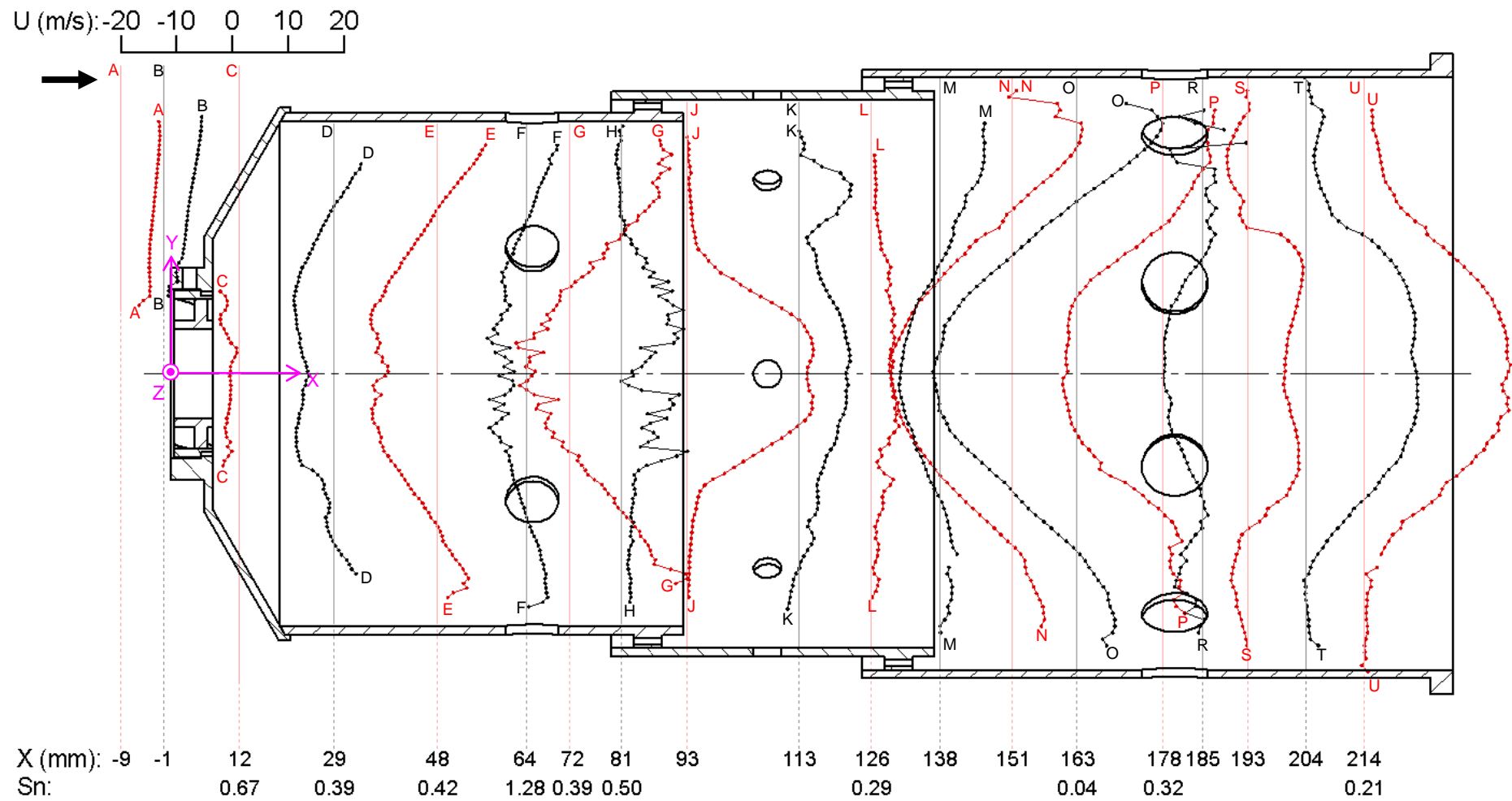
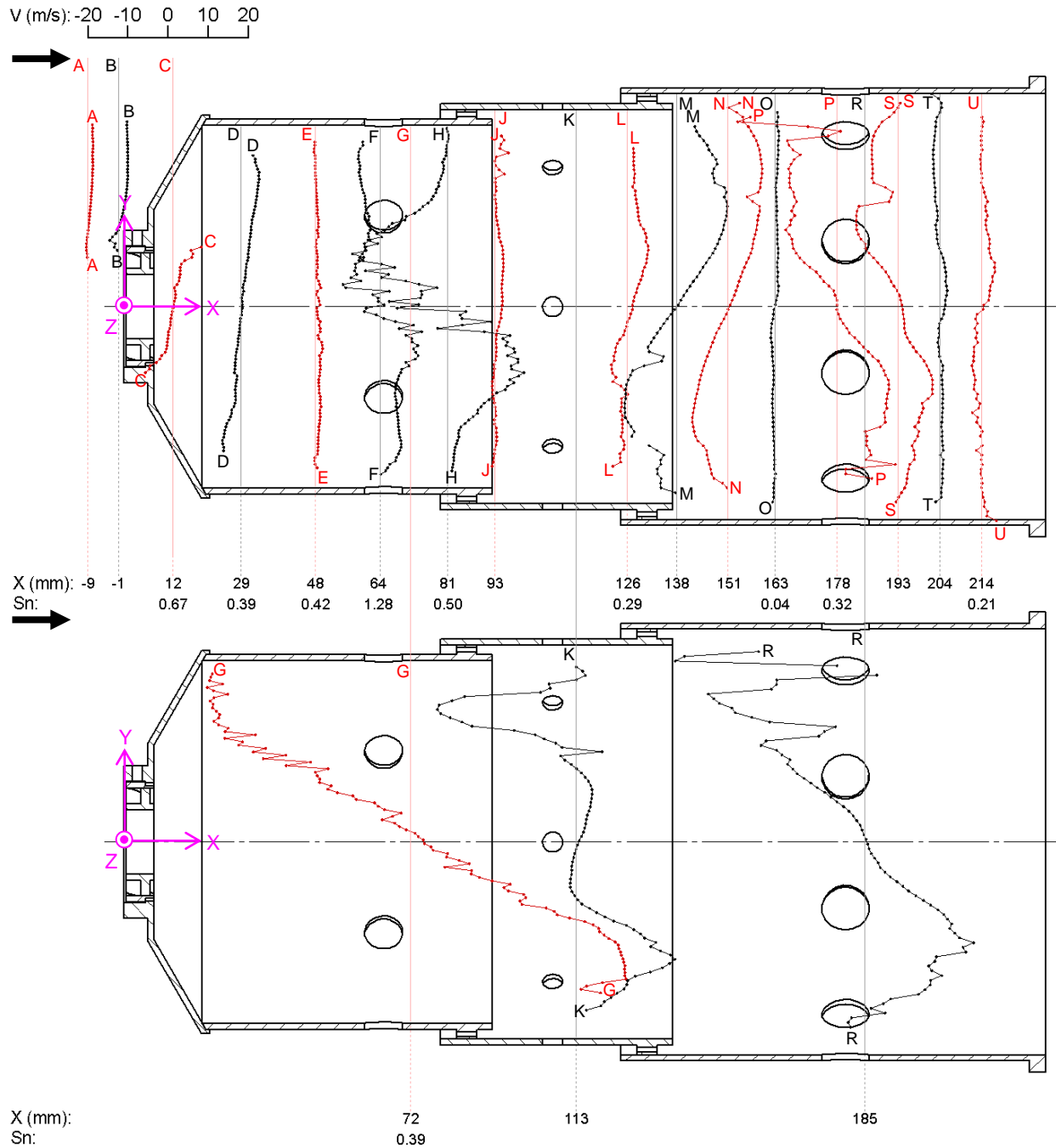


Figure 109: The axial velocity profiles at various positions in the plane in line with the holes



**Figure 110: The radial velocity profiles at various positions in the plane in line with the holes**

In the secondary zone just after the secondary jets (Profile L) through to the last profile in the dilution zone (Profile U), there is only a small amount of swirl left in the flow. The small amount of swirl left, however, still swirls in the same direction as the original swirl induced by the swirler.

Almost all the profiles in the primary zone have swirl numbers indicating moderate to high swirl ( $Sn > 0.4$ ). Just after the swirler and just before the jets (at Profiles C to F), high swirl numbers ( $Sn > 0.6$ ) are shown, which would induce reverse flow at the core. In the secondary and dilution zones, the swirl number has decreased and all the values indicate low swirl ( $Sn < 0.4$ ).

Figure 112 shows the choice code or CHC value of the fields measured. Optical obstruction due to the hole edges, loss of laser light and reflections are some of the reasons for low sample sizes at certain of the cells. At (18), the low sample size regions correspond in shape to the holes of the dilution and secondary zone.

W (m/s): -20 -10 0 10 20

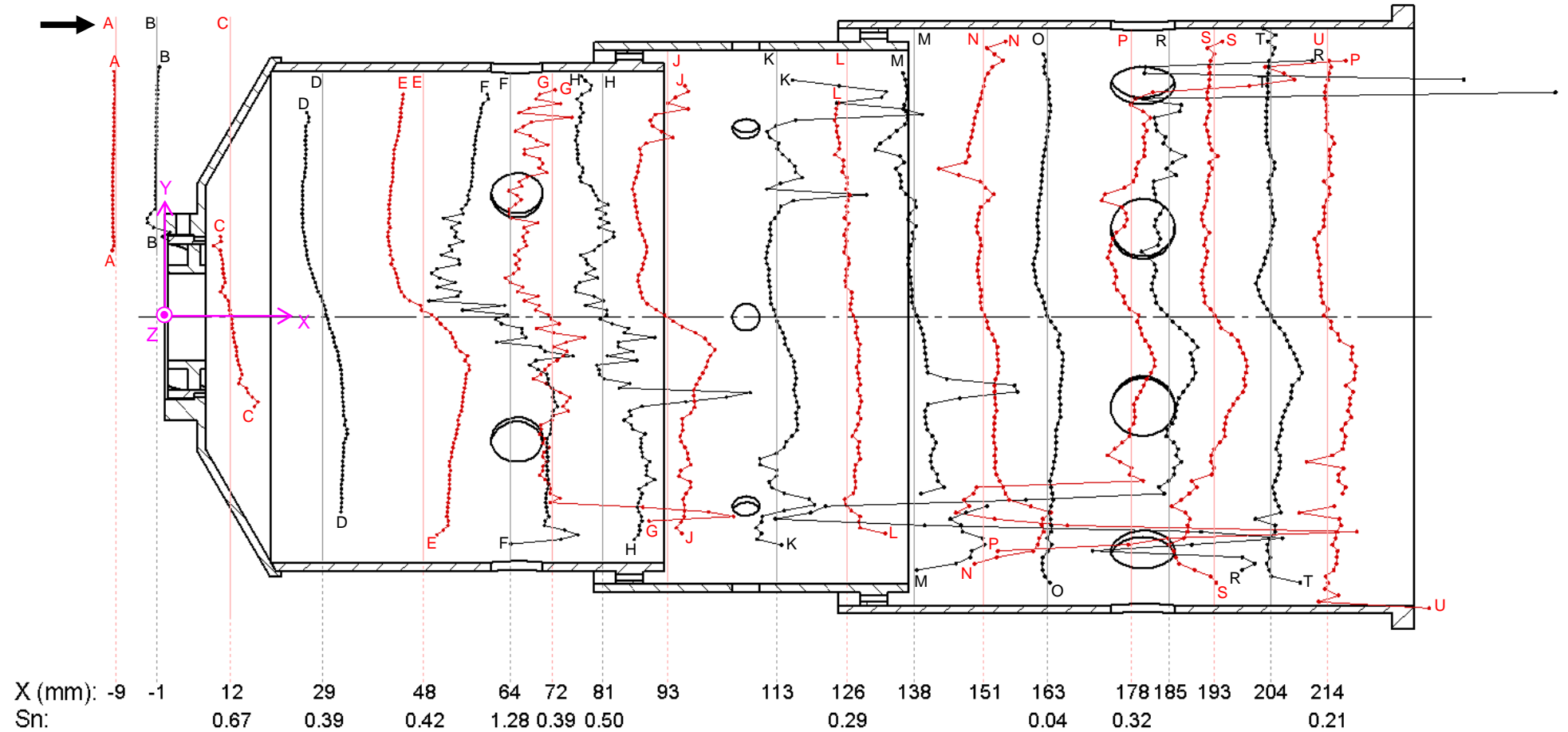


Figure 111: The azimuthal velocity profiles at various positions in the plane in line with the holes

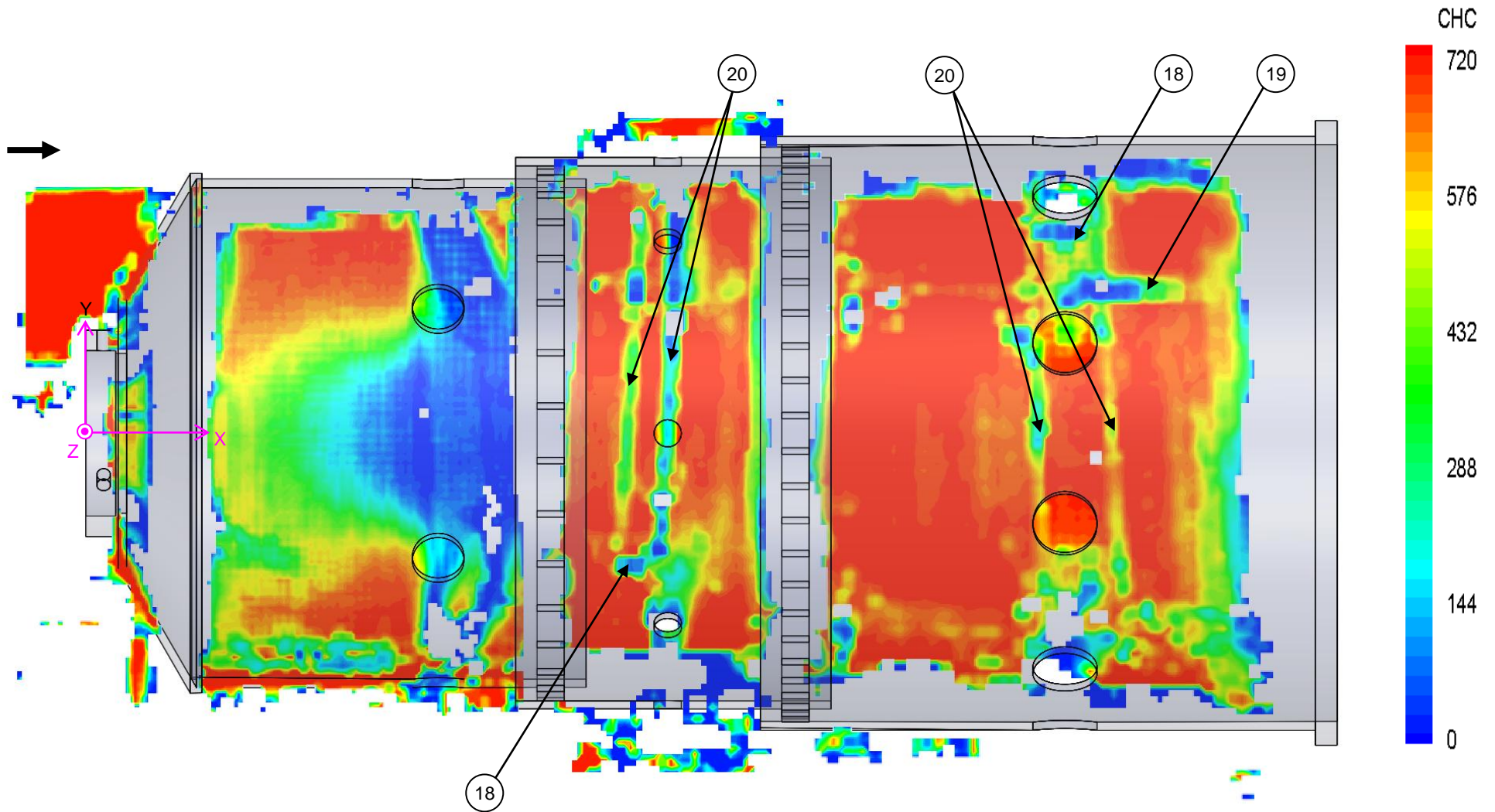


Figure 112: Normal view of the combustor liner showing the CHC contours in line with the holes

At (19), there is a horizontal band of low sample values, which are due to reflections that were present on the back of the liner. The vertical stripes at (20) are due to low laser light from the edges of the holes obstructing the laser light. Other reasons for low sample values are that the flow in that region has high shear and/or is turbulent and unsteady thus creating difficulty in tracking particles or in keeping particles in the laser sheet as in the jet regions of the three zones. High shear, high turbulence and highly unsteady regions also result in high gradients in an interrogation region which means that the vector calculated for that interrogation region is not fully representing the flow in the region because there is not enough detail being captured. This is equivalent to there being too large a cell size in CFD. These flow features also give a high scatter or standard deviation to the vector sample for that interrogation region. In Figure 109 to Figure 111, there are fluctuations or noise seen on some of the velocity profiles (Profiles F, G, H, K, M, P and R), which could be due to many reasons. The main reason that can be seen is that the regions where these fluctuations occur are where low sample sizes are shown in Figure 112. These regions have low sample sizes due to various reasons explained above.

Figure 113 to Figure 120 show the velocity vector field, velocity profiles, CHC value and velocity magnitude for each of the three zones in between the holes of the respective zones. The primary zone plane is at  $30^\circ$  to the plane in line with the holes, the secondary zone is at  $22.5^\circ$  and the dilution zone is at  $18^\circ$  (Planes shown in Figure 83).

In the primary zone, the flow structure is very similar to the flow in line with the holes except that the jets are missing in this flowfield. The following features which are still evident in between the holes are: the bulk flow converging into the annulus, the bulk flow curving to enter the swirler, the primary toroidal recirculation zone at (21) in Figure 114 and Figure 115, the rectangular reverse flow zone and a stagnation point at (23) in Figure 114.

The jets are missing, which is shown at (22) in Figure 114, however, the flow in the jet region still follows a similar path to the jets with some flow following the recirculation zone and some joining the main axial combustor flow.

The secondary zone shows a diverging streamline pattern without the jets interrupting the flow divergence. At (24), the streamlines start to diverge as with the flow in line with the holes but the missing jets evident at (25) allow further divergence and there is no convergence of the flow at the centre of the zone. At (26), the diverging flow is starting to straighten out and become more axial in nature.

The dilution zone flow also shows similar features to the flow in line with the jets. The following features are in the dilution zone in between the holes: the dilution toroidal recirculation zone at (27) in Figure 114 and Figure 115, a stagnation point at (29) in Figure 114, and a similar velocity profile shape to that in line with the holes (see Figure 107 and Figure 108) at the outlet (31) in Figure 115 and Figure 116.

The missing dilution jets are shown at (30) in Figure 114. There is, however, a significant difference in the dilution zone at (28). At (28), the flow from the recirculation zone continues downstream along the wall towards the outlet of the combustor. This feature as well as the diverging flow in the secondary zone both in line with and in between the holes could be the reason for the hottest temperatures being measured at the outer region of the outlet plane. The diverging flow at the outlet of the secondary zone both in line with and in between the holes infers that the flow diverges around the full outlet plane of the secondary zone. The hot combustion products from the primary zone would be carried into the secondary zone where there is an outward tendency to the flow. The flow then enters the dilution zone where the recirculation zone forces the hot air to the outer region by both blockage of the core as well as entrainment. In between the holes, the hot gasses then flow along the wall and leave the recirculation region on the outer edge at (28) to form a ring of hot gas along the walls at the outlet. This is reinforced by the cooler core formed by the dilution jets impinging on one another at the centre on the plane in line with the holes. The hot flow then leaves the combustor along the wall while the cooler air from the dilution jets leave the combustor in the centre. This hot ring of combustion products at the outer edge can be seen in Table 7.

The velocity profiles in between the holes shown in Figure 117 to Figure 119 also do not show very many differences from those in line with the holes except where the jets were (Profiles G, K and R). There is also a kink in the middle of the bulk flow velocity profiles at  $X = -9$  and  $X = -1$  mm (Profiles A and B, respectively). This is not a true flow feature but due to a problem with the optical features in a small spot in this region. This is evident by the decrease in CHC values in this area shown at (36) in Figure 120. At Profile G, in line with the jet positions ( $X = 72$  mm), the velocity profile in all three of the directions is just a transition shape between the profiles either side of it. These profiles (Profiles G, K and R) also have the same fluctuations at

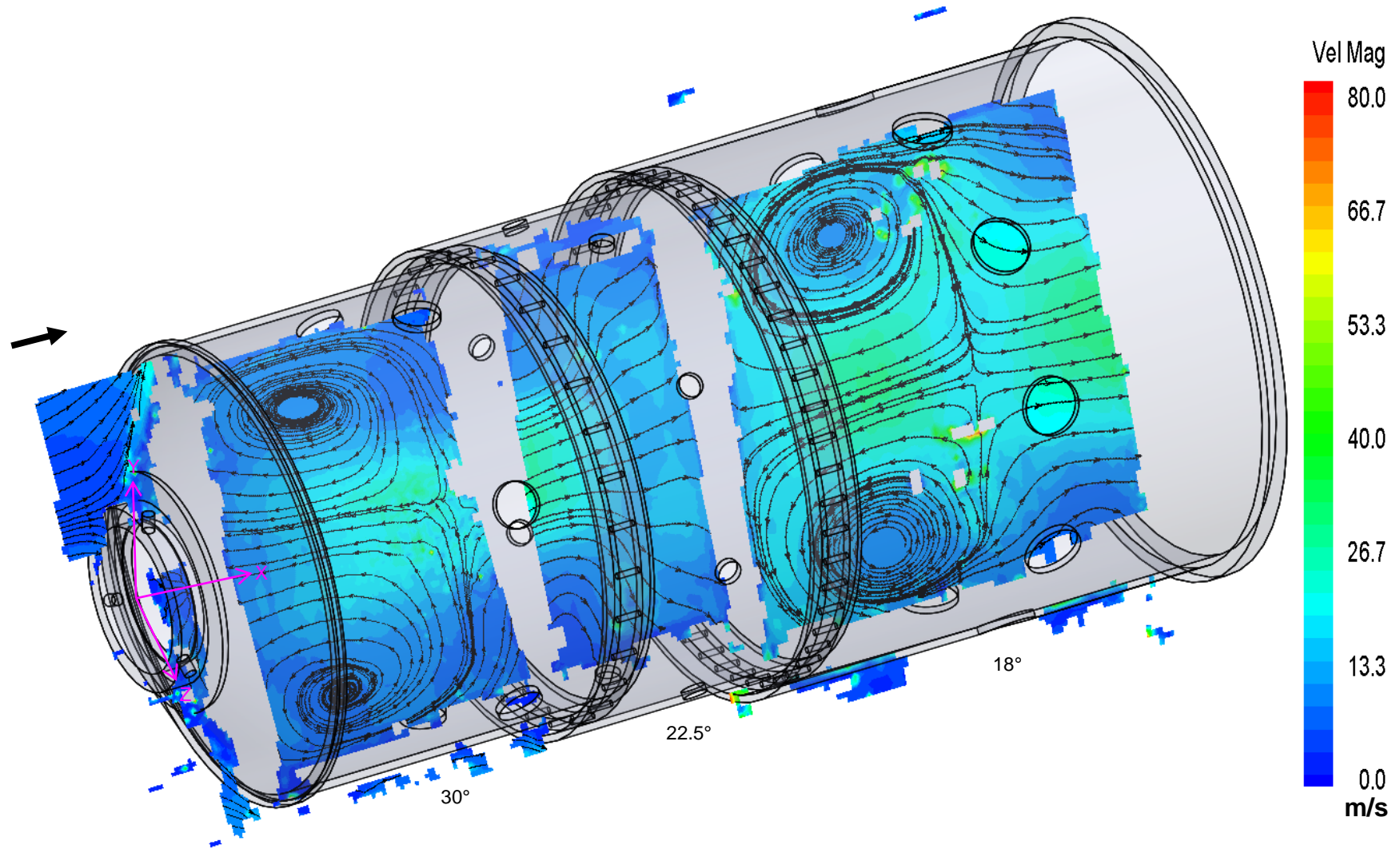


Figure 113: Isometric view of the combustor liner showing the velocity magnitude contours and streamlines in between the holes

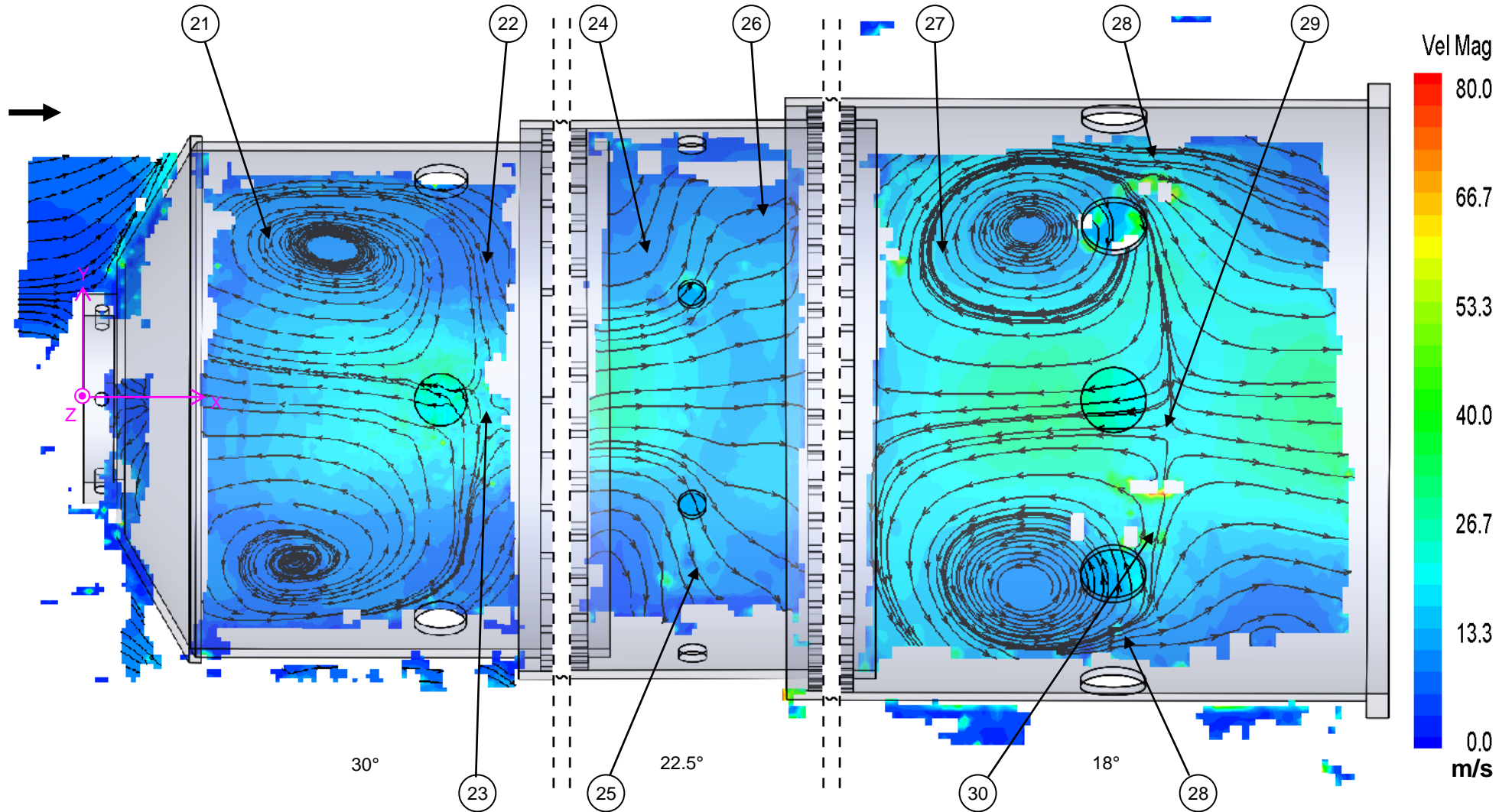


Figure 114: Normal view of the combustor liner showing the velocity magnitude contours and streamlines in between the holes



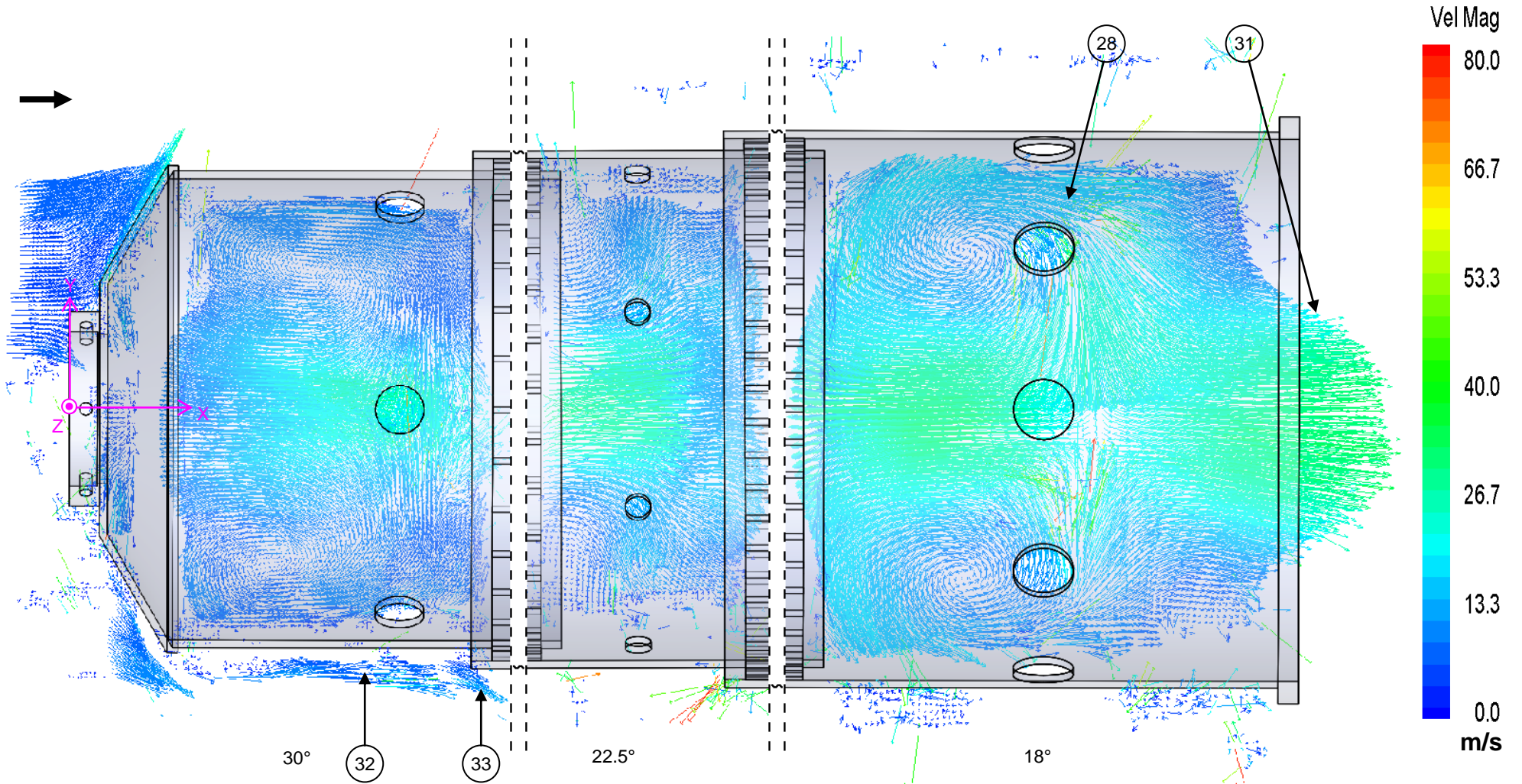


Figure 116: Normal view of the combustor liner showing the velocity vectors in between the holes

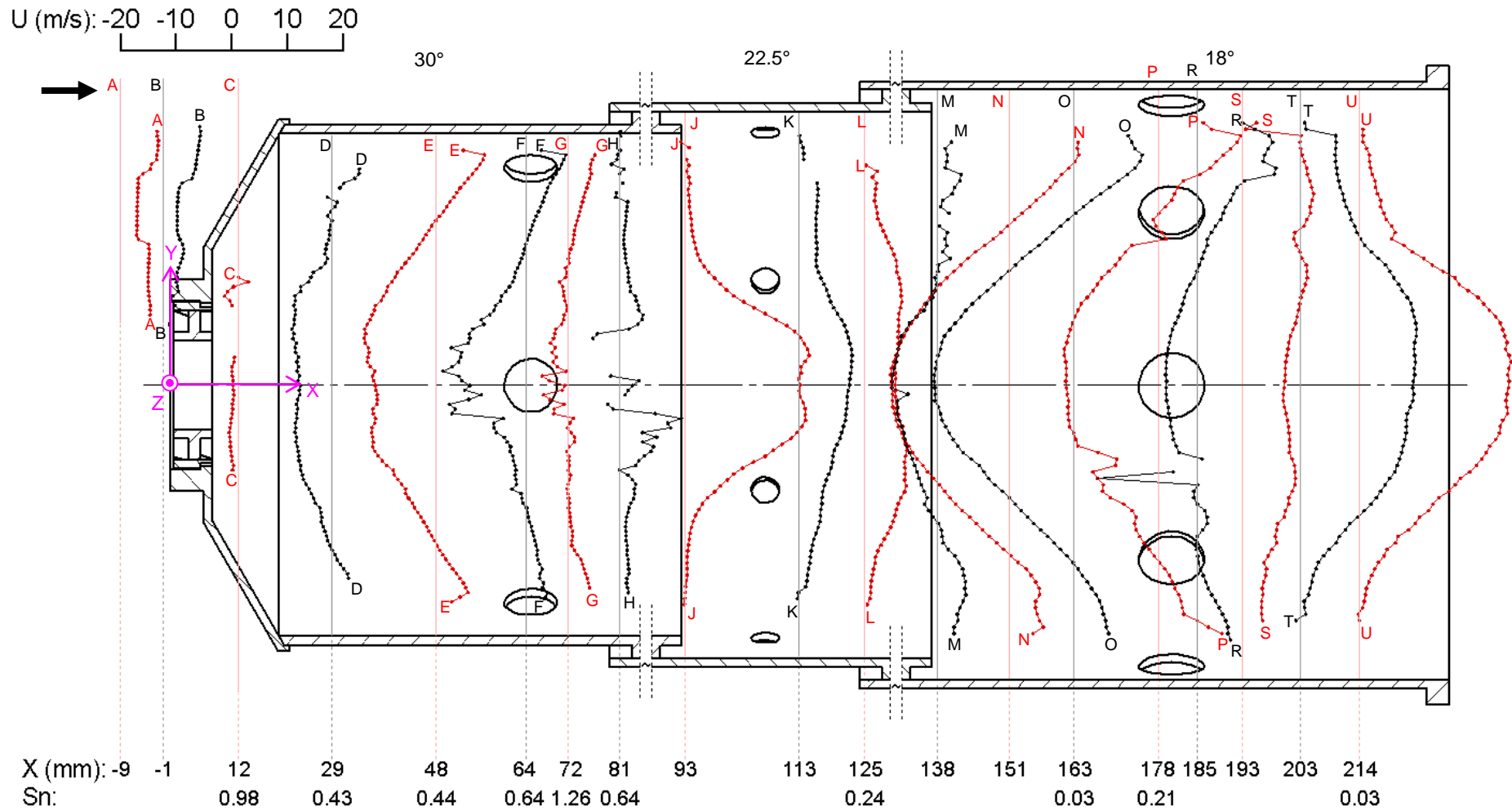


Figure 117: The axial velocity profiles at various positions in the plane in between the holes of the respective zones

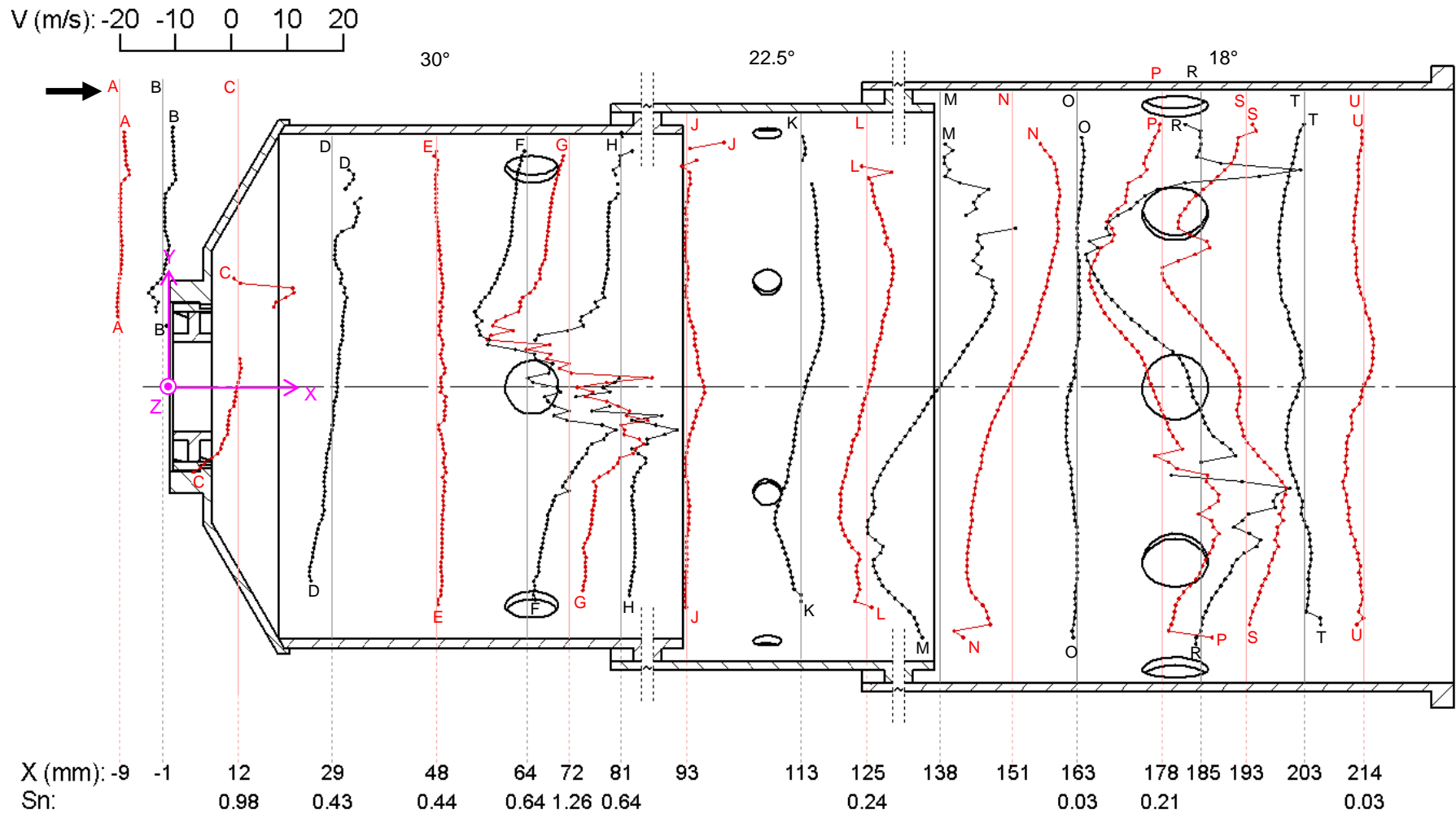


Figure 118: The radial velocity profiles at various positions in the plane in between the holes of the respective zones

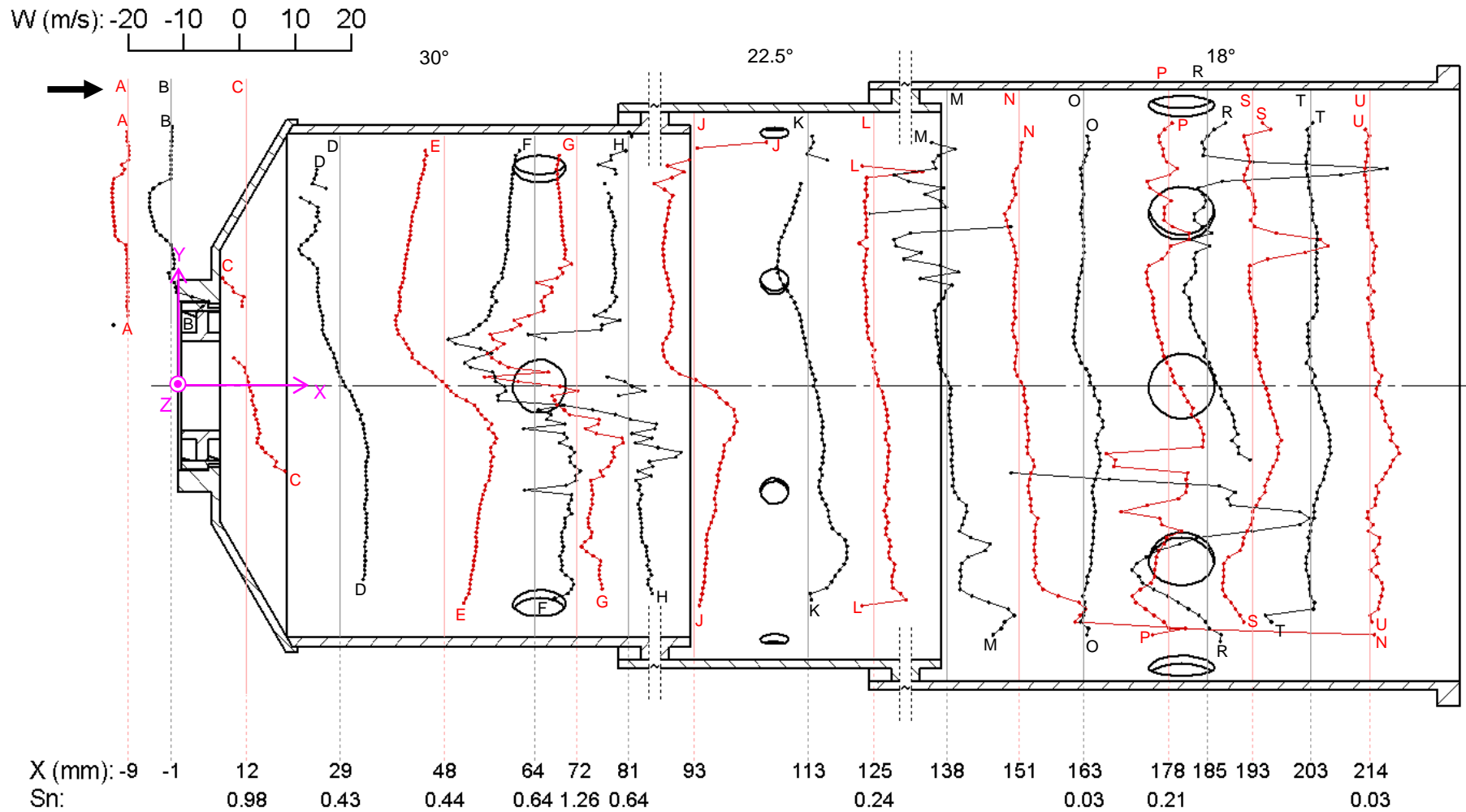


Figure 119: The azimuthal velocity profiles at various positions in the plane in between the holes of the respective zones

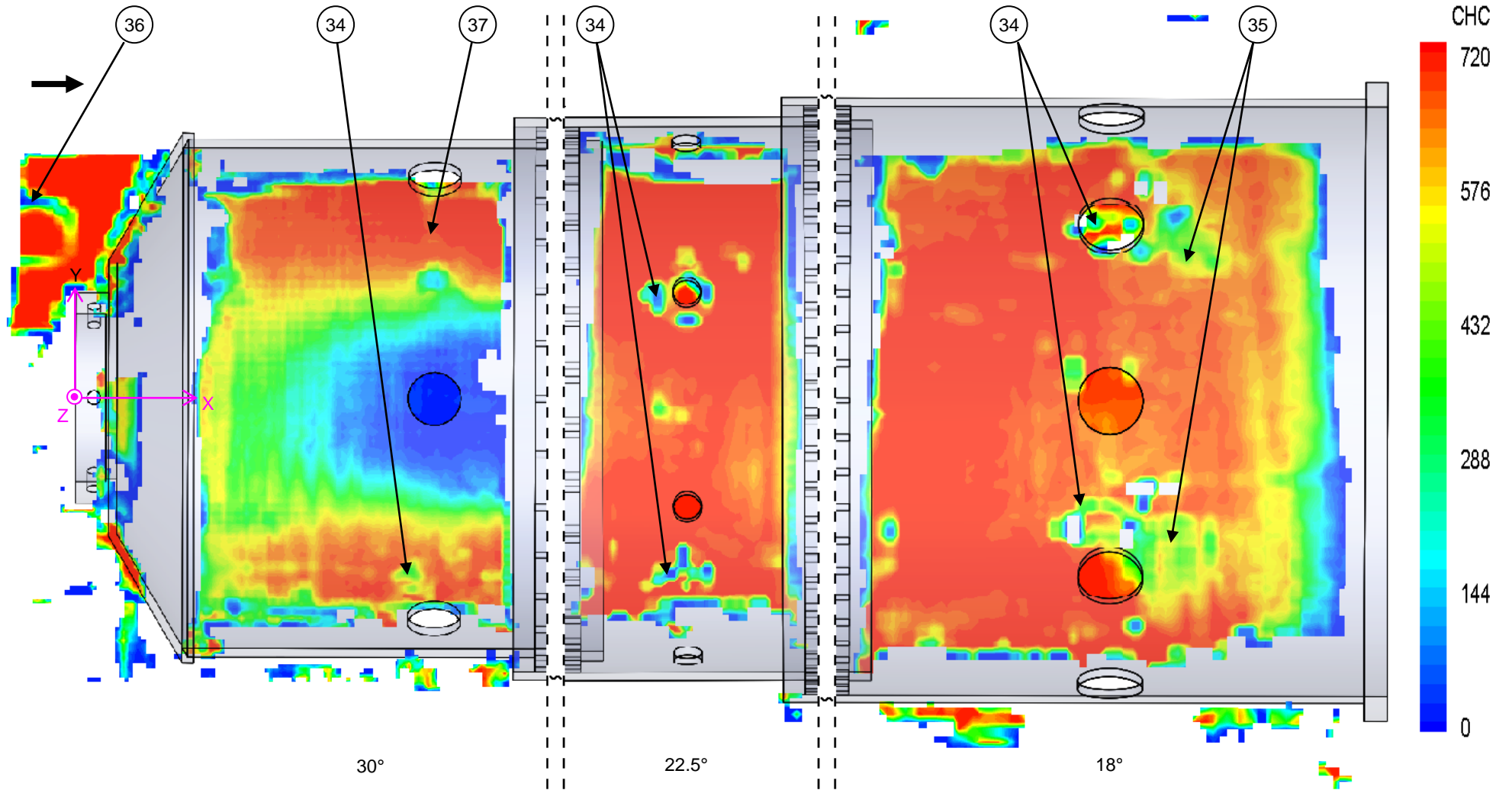


Figure 120: Normal view of the combustor liner showing the CHC contours in between the holes

the same positions as those in line with the jets indicating that the turbulence and unsteadiness does not decrease significantly even though the jets are not present in these planes.

The swirl numbers were also calculated at the same cross-sections as in line with the holes. In these planes, all of the primary zone swirl numbers are above 0.4 indicating moderate and strong swirl is still present in between the holes. The peak swirl number of  $Sn = 1.26$  now occurs at  $X = 72$  mm (Profile G) instead of before the jets at  $X = 64$  mm (Profile F with  $Sn = 1.28$ ) as it was in line with the holes. The swirl number in the mid-region of the recirculation zone (Profile E) has almost the same values as the corresponding cross-sections in line with the holes. At Profile C, just after the swirler, the swirl number shows an increase but due to the missing data above the centreline no significance is placed on this increase. Downstream in the secondary and dilution zone, the swirl numbers are again all below 0.4 as the swirl numbers were in line with the holes.

It is expected for the swirl numbers that are not near the jets to have similar valued on both the planes in line with and in between the holes. The swirl number definition in equation [13](#) is based on the assumption of constant fluid properties ( $U$ ,  $W$ ,  $\rho$  etc) at each radius on the cross sectional plane which is the case when not near the jets.

In Figure 120, the CHC values of the planes in between the holes are shown. The position where the holes obstructed the camera view is shown at (34) while the reflection positions are shown at (35). An increase in the CHC values where the jets used to be is shown at (37).

In Figure 121, a side-by-side comparison is made between the flowfield in line with the holes and in between the holes. The flow in between the holes from above the centreline is mirrored about the centreline and placed at the bottom half of each of the images. Figure 121b shows a simplified flow representation of the two experimental flowfields. The flow in between the holes has much smoother transitions and less sharp direction changes in the flow than the flow in line with the holes. This can be seen at (38) and (39) in Figure 121.

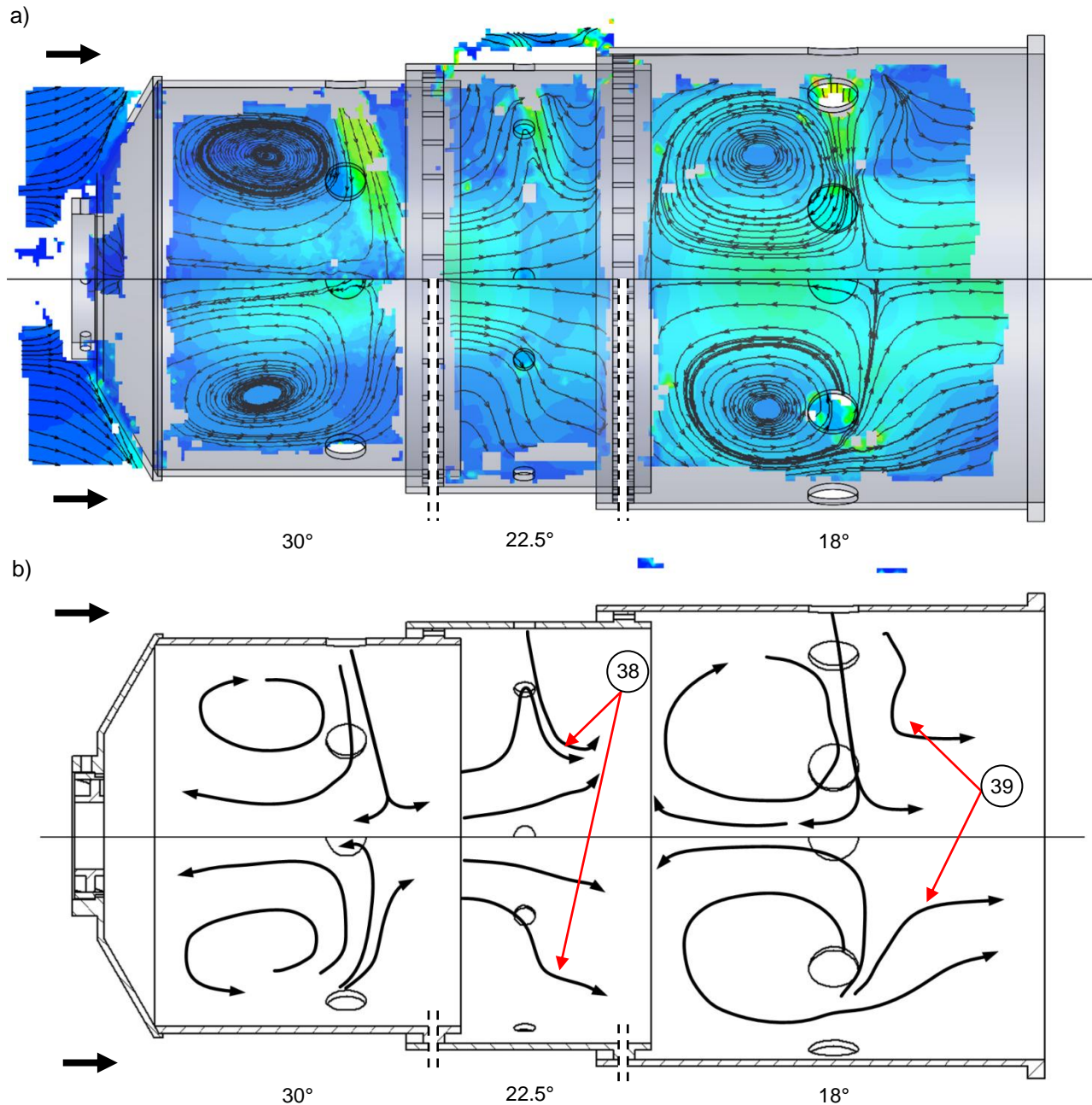


Figure 121: A comparison of the flow in line with the holes and in between the holes of all the zones

#### 4.2.2 Change in flow rate

Since the data showing the most information is collected at a lower flow rate than the designed flow rate of the combustor, the flow rate was increased and what little data was available at the higher flow rates is shown in Table 9 to Table 12 and in Figure 122 to Figure 129. In these tables and figures, the data is shown in increasing order of flow rate for comparison purposes. Note that the velocity magnitude key goes from 0 to 110 m/s in this section as opposed to 80 m/s maximum in the previous section.

Table 9 to Table 12 show only the primary zone data in line with the holes but at six flow rates from 0.056 kg/s to 0.091 kg/s. Figure 122 to Figure 129 show the data in the whole combustor liner but at only three flow rates, i.e. 0.056 kg/s, 0.070 kg/s and 0.091 kg/s.

It can be seen in Table 9 to Table 12 that the data is sparser in sections of higher flow rates such as in the jets. The data sets are also less populated in the bottom recirculation section. This is due to reflections and camera angles making the particles difficult to pick up to perform PIV in those sections at the higher velocities. Despite the decrease in data, trends can still be shown, which are due to an increase in the flow rate.

In Table 9, a comparison of the velocity contours as the flow rate increases shows that the higher velocity section in the reverse flow region extends further upstream as the flow rate increases. This can be seen by the colour near the dome region shifting away from the blue and towards the cyan colour. Also as the flow rate increases, the streamlines in the reverse flow zone near the jets start to pull further apart and finally a “Y”-shaped reverse flow zone does appear to form.

In Table 10 and Table 11, the increase in the jet magnitude is evident as the flow rate increases. In the lowest three flow rates from 0.056 to 0.064 kg/s, the jet magnitudes are approximately 50 m/s. When the flow rate reaches 0.070 kg/s, the jet velocity increases to about 75 m/s with a further increase to approximately 85 m/s at a flow rate of 0.078 kg/s and a jet velocity of approximately 95 m/s at the highest mass flow rate of 0.091 kg/s. Also shown in these pictures are the centres of the recirculation zones of the increased mass flow rate set-ups relative to the centres of the recirculation zones of the base case PIV data set at 0.056 kg/s. The centre markings are shown following the right-hand curl rule with an X marking the inward direction of the thumb when the fingers curl in a clockwise direction and a dot (•) marking an anti-clockwise direction. The positions of the base case centres are marked on all the data sets with black markings while the magenta markings show the positions of the centres of that particular data set (where it was possible to determine). The centre of the clockwise recirculation zone (top) tends to move upstream as the flow rate is increased but only by a few millimetres ( $\pm 5$  mm). The anti-clockwise recirculation zone centre (bottom) shows a slight tendency to move in the downstream direction but there are only two determinable centres on this vortex on the lower flow rates and thus a centre movement direction cannot really be determined for this recirculation zone.

Table 12 shows that fewer vectors are picked up in the interrogation regions as the flow rate increases. The fewer vectors are most likely due to an increase in velocity thus the particles move out of the plane before the second laser pulse giving fewer particles to track. For the primary zone experiments, the time between frames was set at 15  $\mu$ s. At the time of these experiments, the time between frames could not be decreased due to synchroniser errors. Some of the statistics of the data could improve if the timing between Frame A and Frame B could be decreased. It is now possible to decrease the timing between the laser pulses due to the synchronizer errors being overcome. Lower times between pulses were used for the secondary and dilution zone experiments as indicated in Table 8.

Figure 122 to Figure 129 are comparisons of the various flowfield characteristics in line with the holes in the whole combustor at flow rates of 0.056 kg/s, 0.070 kg/s and 0.091 kg/s. For the figures with contour plots, all of the cells were plotted but in the vector plots the non-real vectors above 110 m/s were removed for clarity.

In Figure 122, the overall increase of velocity magnitude can be seen in all three of the zones. The increase of angle between the reverse flow stream lines in the primary zone can again be seen in this figure.

In the vector plots in Figure 123 and Figure 124, the centres of the primary recirculation zone are plotted again as well as the centres of the dilution recirculation zone. There is very little movement of the dilution recirculation zone centre. The outlet velocity vectors start to fan out slightly in the 0.091 kg/s data set. The bottom jet of the secondary zone also starts to angle more towards the downstream direction in the higher two flow rates. This can also be seen by a hump presenting on both sides of the cross-sectional slice at  $X = 113$  mm (Profile K) for the higher two flow rates instead of only on one side as for 0.056 kg/s.

Figure 125 has the axial velocity profiles for comparison. The maximum value on the bulk flow inlet profile, Profile A ( $X = -9$  mm), for 0.056 kg/s is 7 m/s while this value increases to 8.5 m/s at the 0.070 kg/s flow rate. The corresponding value for the highest flow rate could not be read due to missing data. At  $X = 48$  mm (Profile E), the velocity at the edges in the positive direction<sup>7</sup> stays between 7 to 8.5 m/s while the reverse flow magnitude increases from 12 to 15 then 17 m/s as the flow rate increases.

<sup>7</sup> The positive and negative direction in Chapter 4 is with respect to the X-axis directions.

Table 9: Comparison of velocity magnitude contours and stream lines in the primary zone as the air mass flow rate is increased from 0.056 to 0.091 kg/s

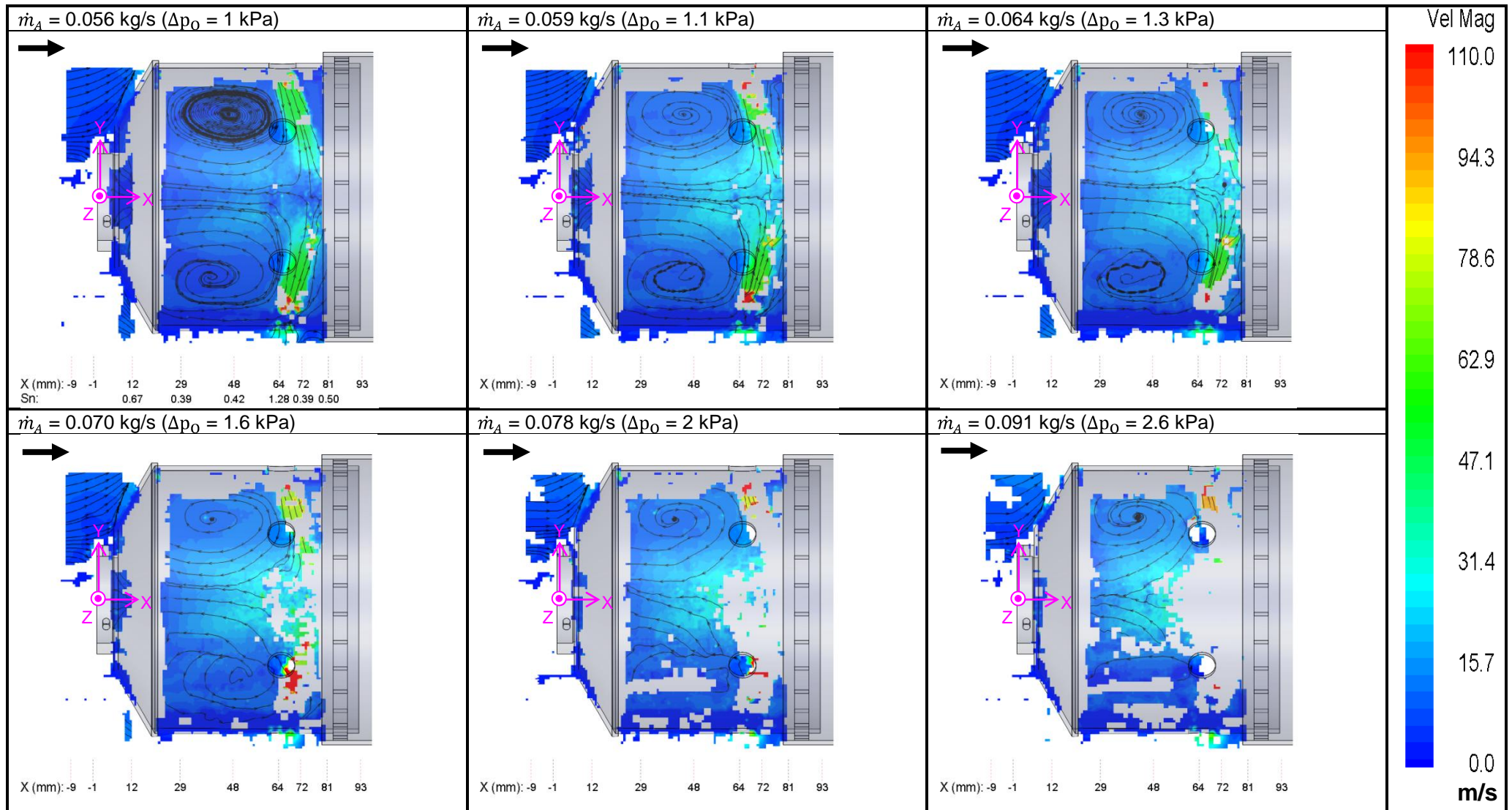


Table 10: Comparison of sparse velocity vectors in the primary zone as the air mass flow rate is increased from 0.056 to 0.091 kg/s

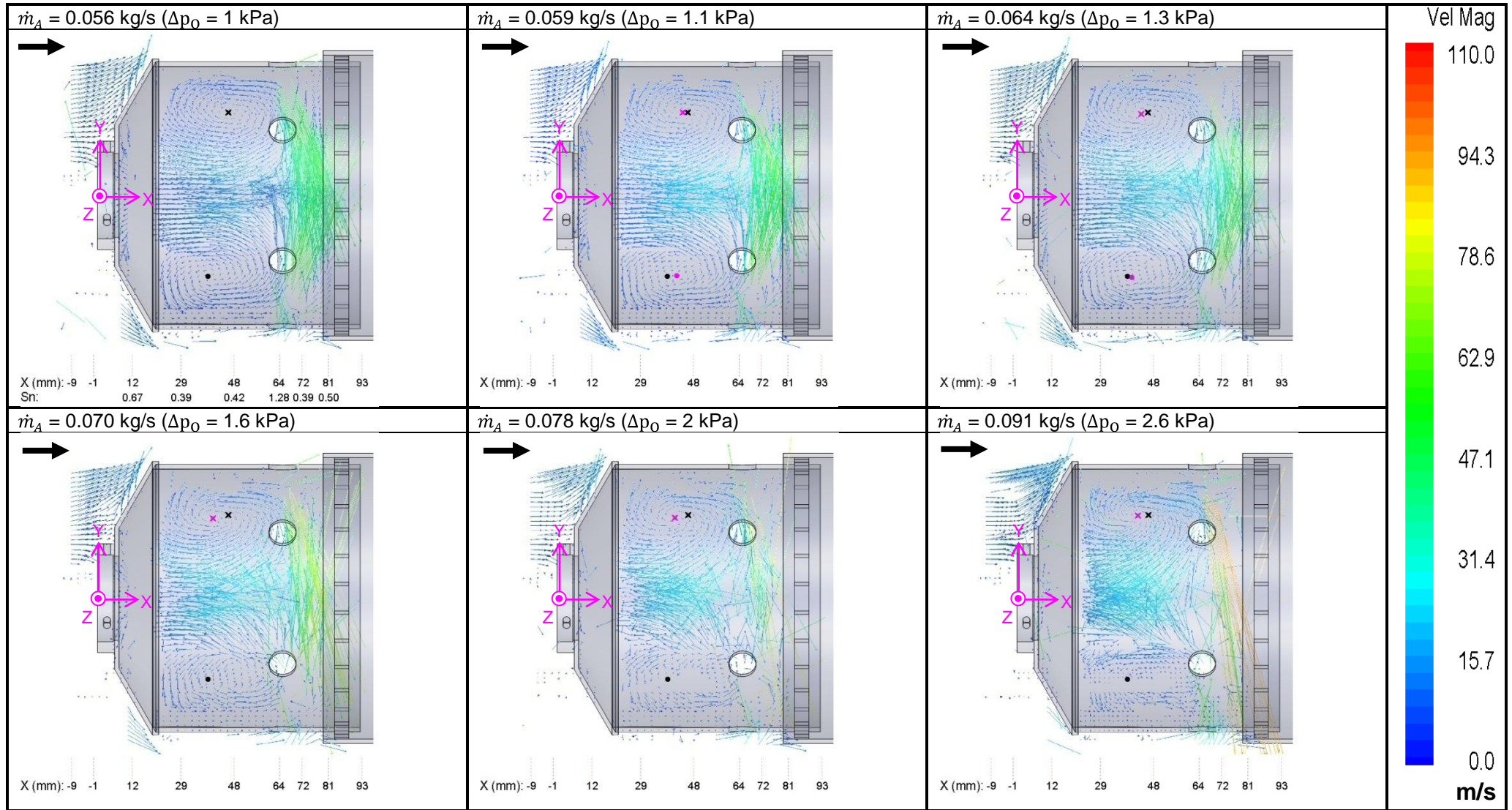


Table 11: Comparison of velocity vectors in the primary zone as the air mass flow rate is increased from 0.056 to 0.091 kg/s

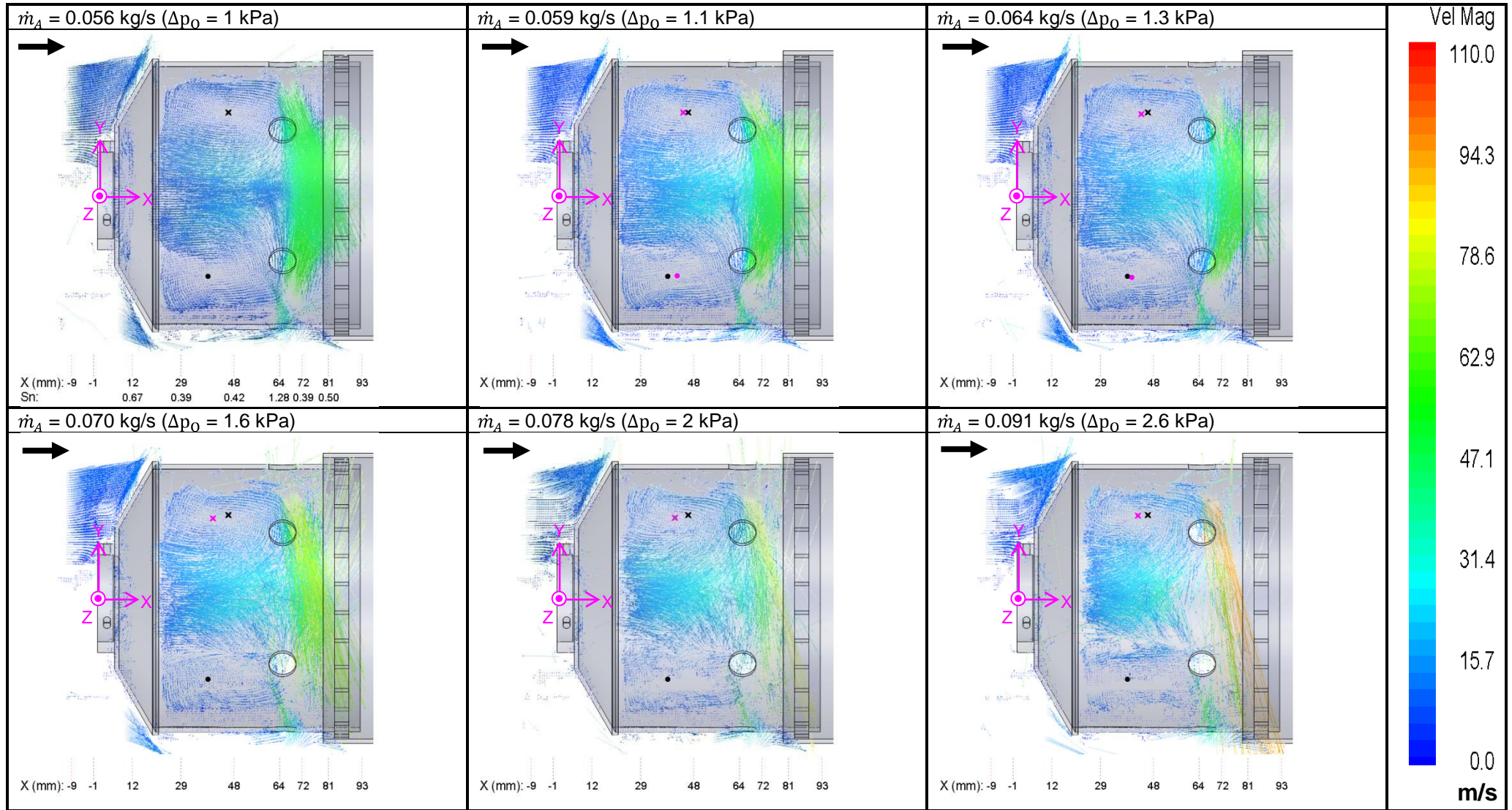
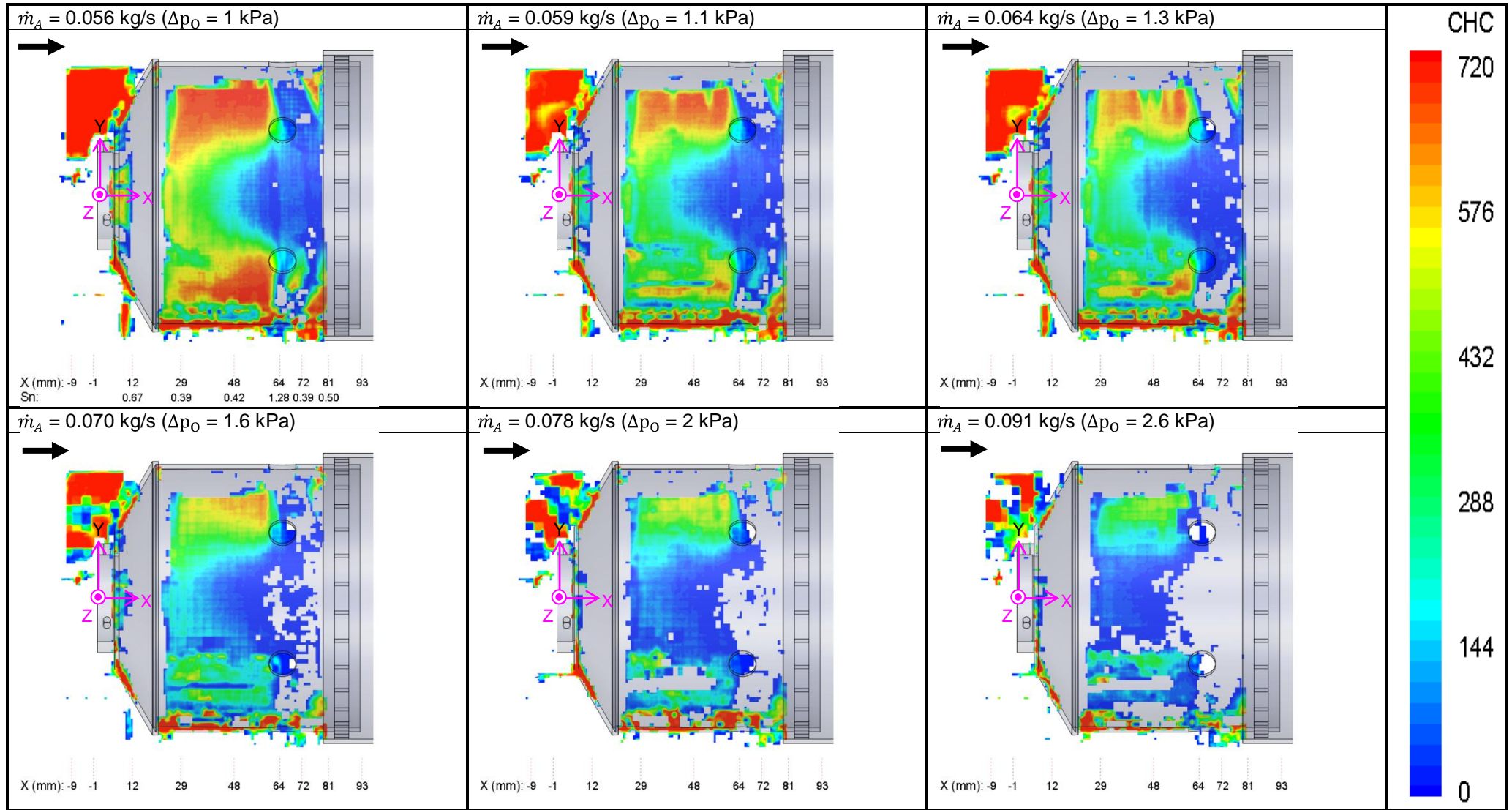


Table 12: Comparison of CHC values in the primary zone as the air mass flow rate is increased from 0.056 to 0.091 kg/s



The maximum magnitude of the flow entering the secondary zone starts at 22.7 m/s at 0.056 kg/s with an increase to 28.5 m/s at 0.070 kg/s and 36 m/s at 0.091 kg/s.

In the dilution zone, there is very little change in the magnitude in the positive direction of Profile O, which is the velocity profile through the centre of the recirculation zone (at  $X = 163$  mm), with the maximum magnitude in this direction ranging between 15 and 16 m/s. In the negative direction, however, the axial velocity magnitude started at 25.8 m/s for the lowest flow rate then increased to 32.3 m/s for the intermediate flow rate then finally to 35.9 m/s for the highest flow rate set-up. The outlet profile also increased with increasing flow rate giving a maximum outlet velocity of 26 m/s, 35.8 m/s and 44 m/s for the 0.056 kg/s, 0.070 kg/s and 0.091 kg/s, respectively.

The radial velocities are presented without the slices through the jets in Figure 126. Figure 127 has the jet cross-sections only. In the secondary and dilution jets (Profile K and R, respectively), the top jet velocity is higher than the velocity through the bottom jet. This again is due to the jets not being perfectly symmetrical and thus the slice only passes through the edge of the bottom jets in these zones.

In the primary zone, the top and bottom jets on Profile G seem to be more symmetrical and thus the slice show peaks that are closer in magnitude between the two sides. For the 0.056 kg/s flow rate, the primary zone jets are 50.8 m/s at the top and 53.7 m/s at the bottom. In the 0.070 kg/s flow rate profile, there are a lot of fluctuations and the profile is not well defined. The maximum velocity magnitudes in the two directions seem to be about 70 m/s. No values could be read in the 0.091 kg/s primary jets.

At Profile K ( $X = 113$  mm), the maximum velocity in the negative direction is 34.7 m/s, 45.5 m/s and 60.4 m/s for the 0.056 kg/s, 0.070 kg/s and 0.091 kg/s, respectively. In the positive direction the maximums are 24.6 m/s, 37 m/s and 47.6 m/s for the 0.056 kg/s, 0.070 kg/s and 0.091 kg/s, respectively.

In the dilution zone (Profile R), the negative and positive peaks were measured at 47.2 m/s and 27 m/s for the lowest flow rate, 47.8 m/s and 36.7 m/s for the intermediate flow rate, and 58.5 m/s and 49.7 m/s for the highest flow rate. It should be noted that the 0.091 kg/s flow rate data is sparse and erratic and the velocity magnitudes given are only the maximum point of the data that is present in that particular slice.

For the swirling flow in Figure 128, the Profile E shows an increase in the negative velocity magnitude from 6.6 to 8.4 up to 13.4 m/s while the positive magnitude increased from 8.3 to 10.5 to 11 m/s as the flow rate increased.

For all the component profiles, throughout the flow rate increase, the tendency is for the shape of the profile to remain almost the same with the magnitudes of the velocities increasing. The fluctuations on the profiles in all the zones also increase with increasing flow rate.

In a comparison of the CHC values in Figure 129, it can be seen that the amount of missing data does not increase in the secondary and dilution zone as much as occurred in the primary zone. The main reason is that the time between the laser pulses is quite large (15  $\mu$ s) in the primary zone experiments while it is only 5  $\mu$ s or less in the secondary and dilution zone experiments. Also the primary zone jets increase to higher flow rates than the secondary and dilution jets thus an even shorter time between laser pulses would be required.

In conclusion, the most significant changes in the flowfield due to a change in flow rate are the changes in the shape of the reverse flow zone in the primary zone and the magnitude of the velocity vectors. Besides this there are only slight variations in the rest of the flowfield features. There are no missing or additional features due to the change in flow rate as well as no changes in flow regimes, thus the data at the lower flow rates is sufficient to use as a CFD test case.

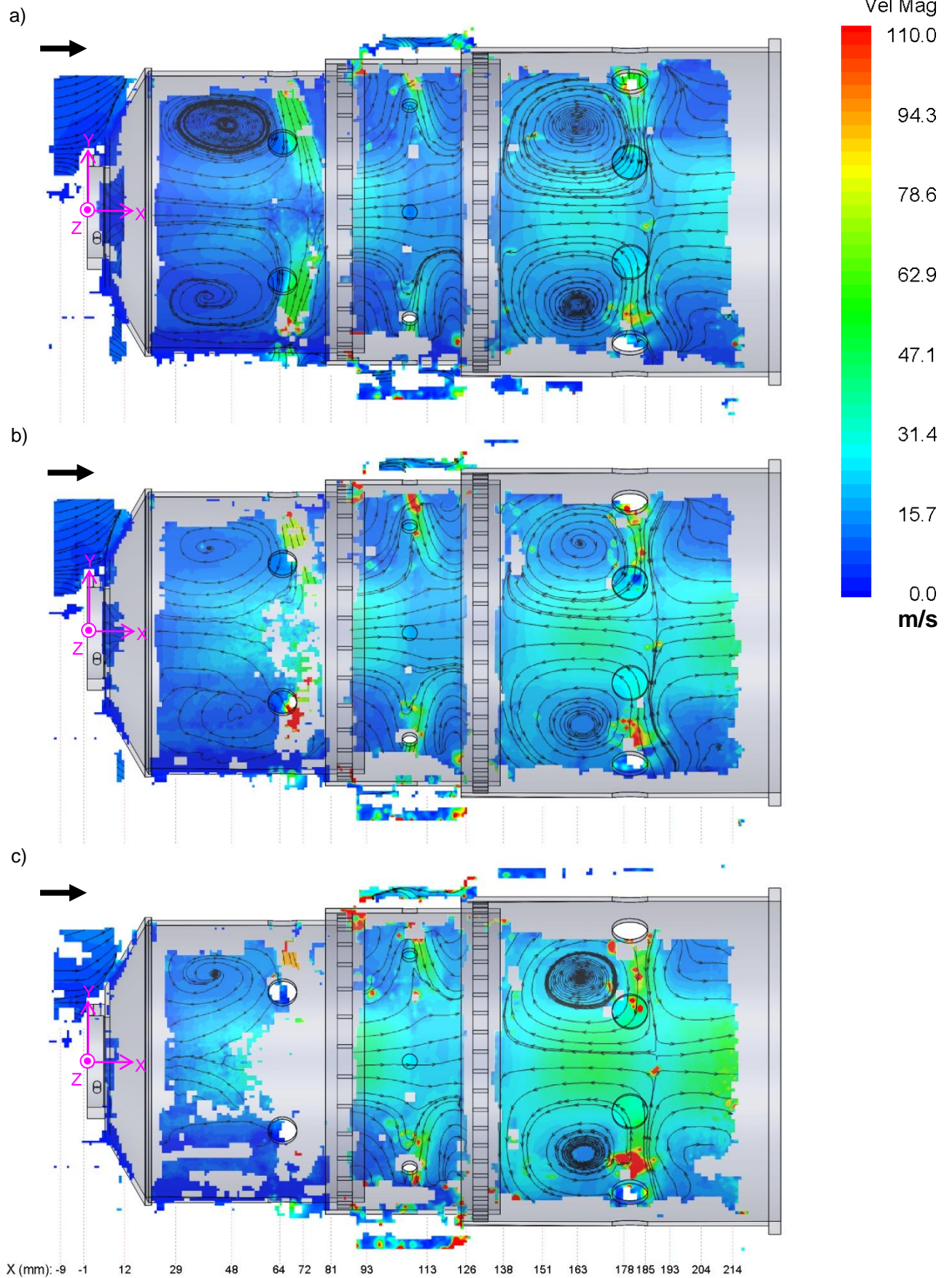


Figure 122: A comparison of the velocity magnitude and streamlines in line with the holes at a)  $\dot{m}_A = 0.056$  kg/s, b)  $\dot{m}_A = 0.070$  kg/s and c)  $\dot{m}_A = 0.091$  kg/s

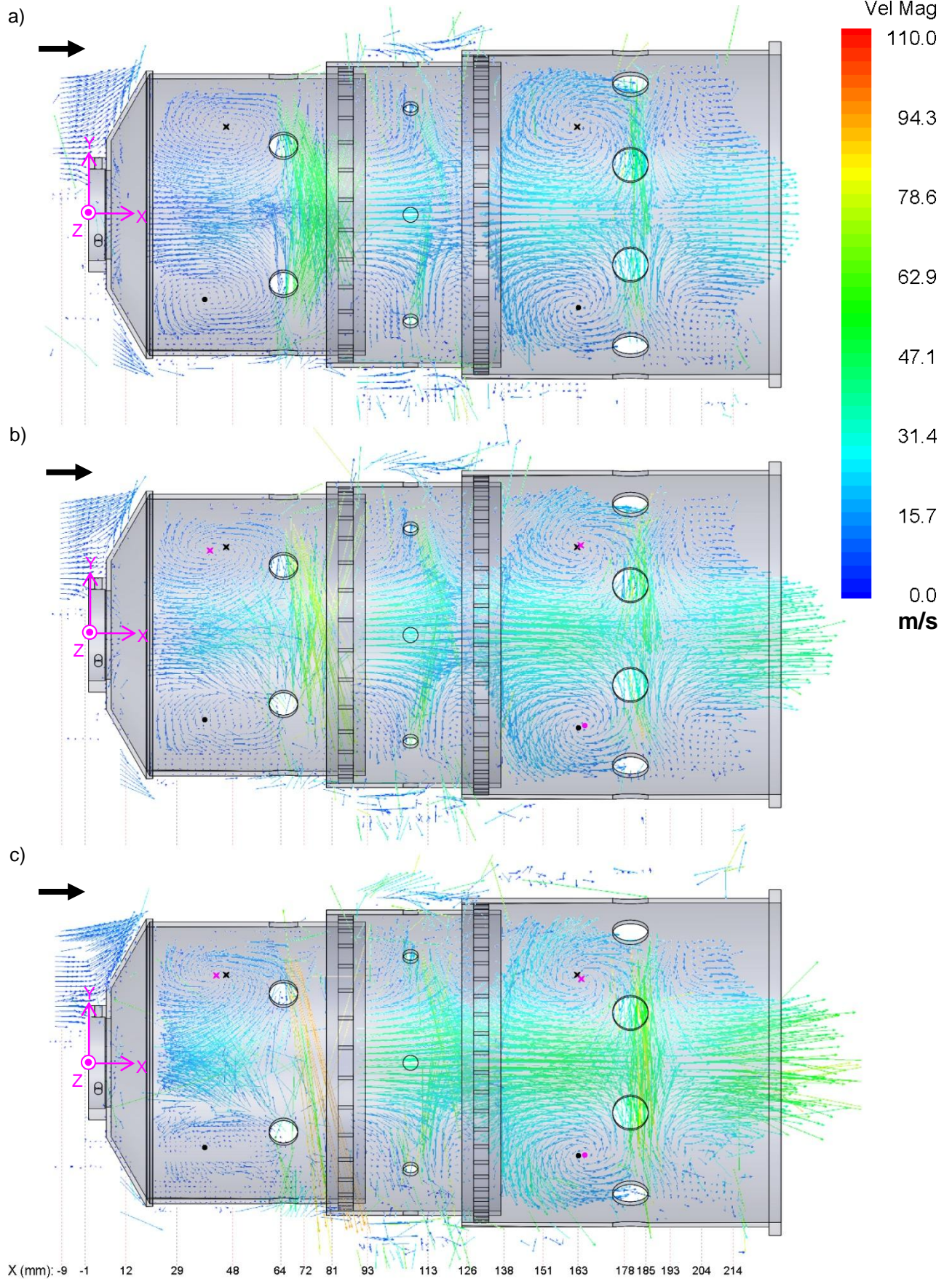


Figure 123: A comparison of the sparse velocity vectors in line with the holes at a)  $\dot{m}_A = 0.056$  kg/s, b)  $\dot{m}_A = 0.070$  kg/s and c)  $\dot{m}_A = 0.091$  kg/s

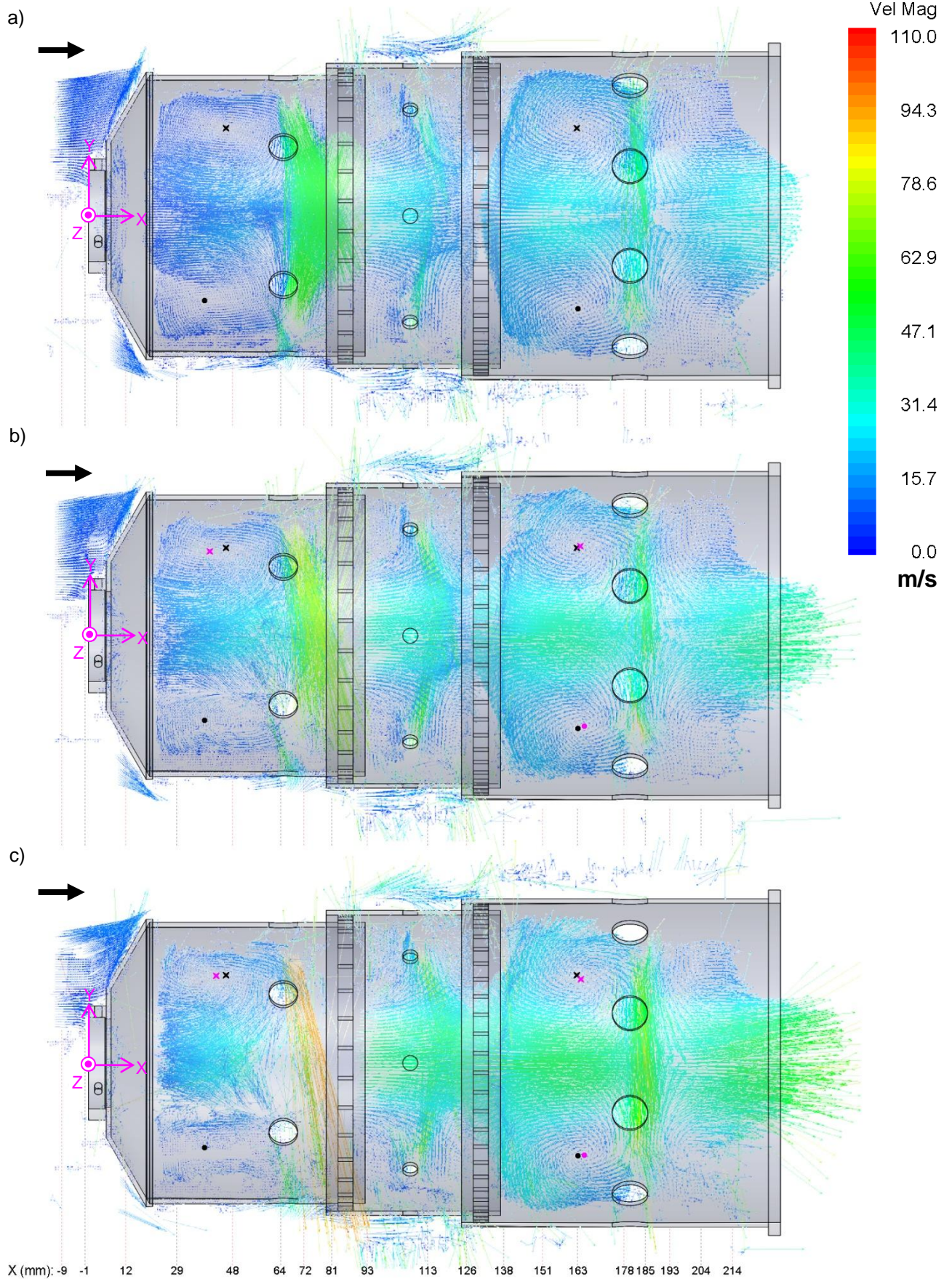


Figure 124: A comparison of the velocity vectors in line with the holes at a)  $\dot{m}_A = 0.056$  kg/s, b)  $\dot{m}_A = 0.070$  kg/s and c)  $\dot{m}_A = 0.091$  kg/s

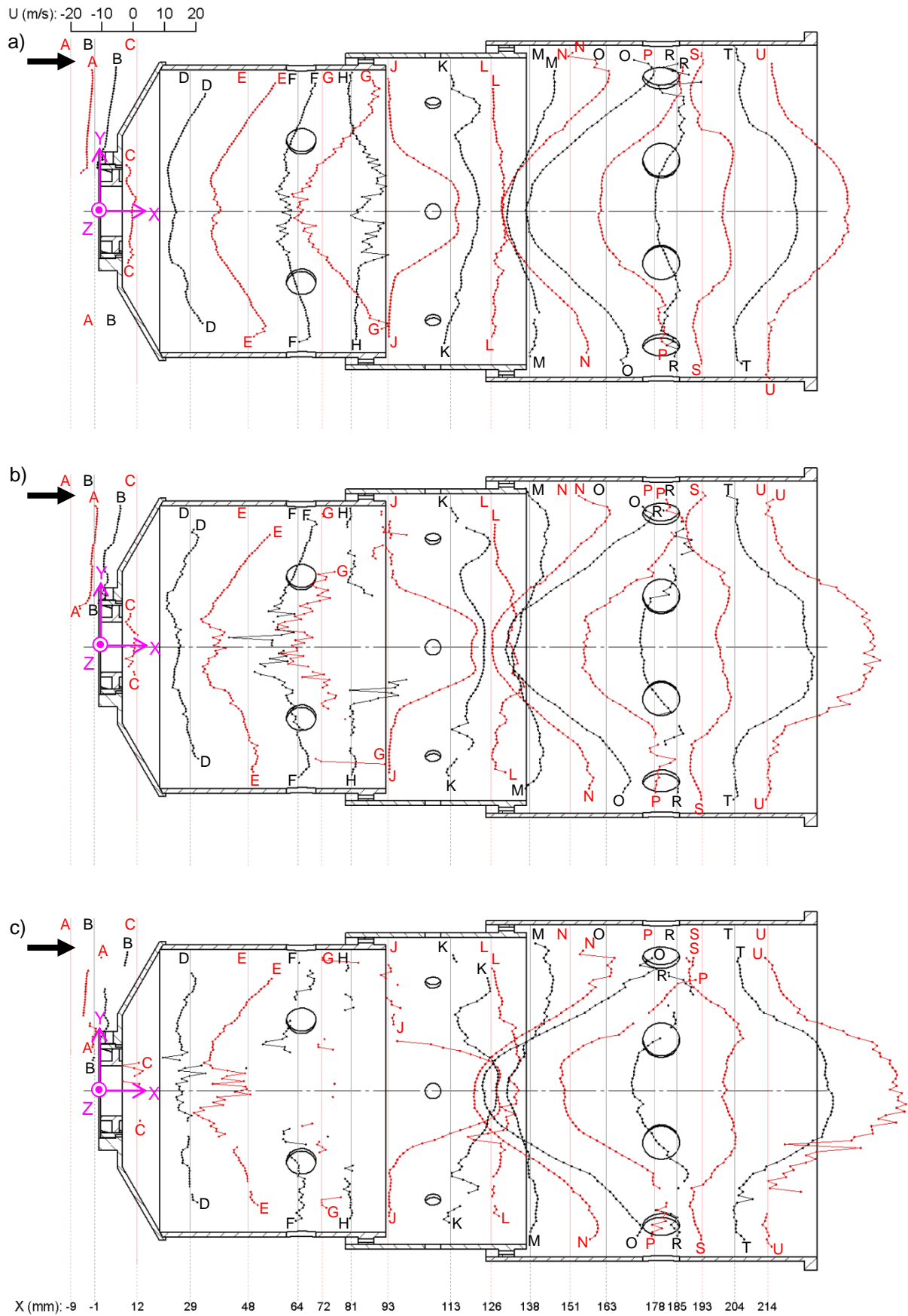


Figure 125: A comparison of the axial velocity profiles in line with the holes at a)  $\dot{m}_A = 0.056$  kg/s, b)  $\dot{m}_A = 0.070$  kg/s and c)  $\dot{m}_A = 0.091$  kg/s

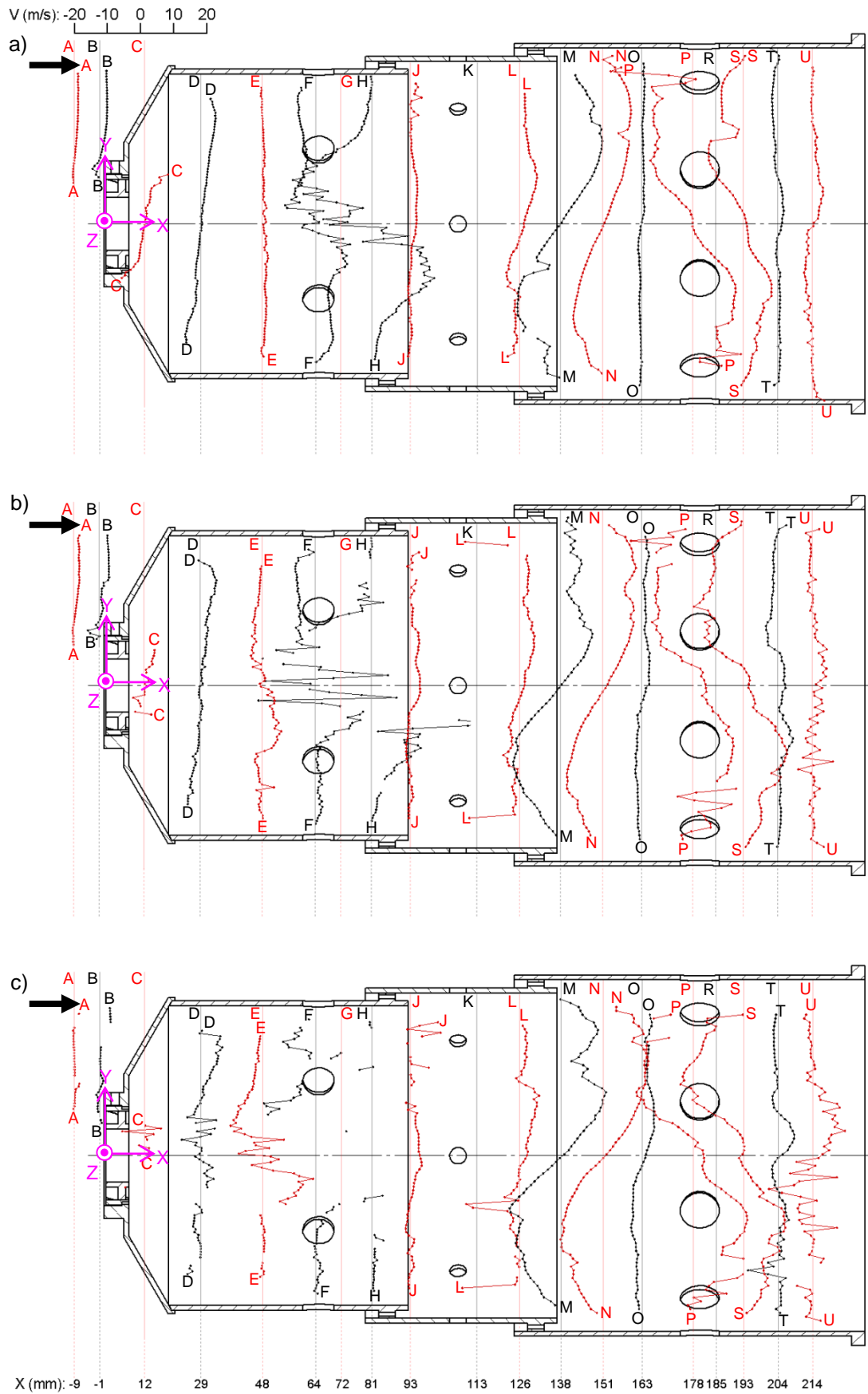


Figure 126: A comparison of the radial velocity profiles in line with the holes but excluding the jets at a)  $\dot{m}_A = 0.056$  kg/s, b)  $\dot{m}_A = 0.070$  kg/s and c)  $\dot{m}_A = 0.091$  kg/s

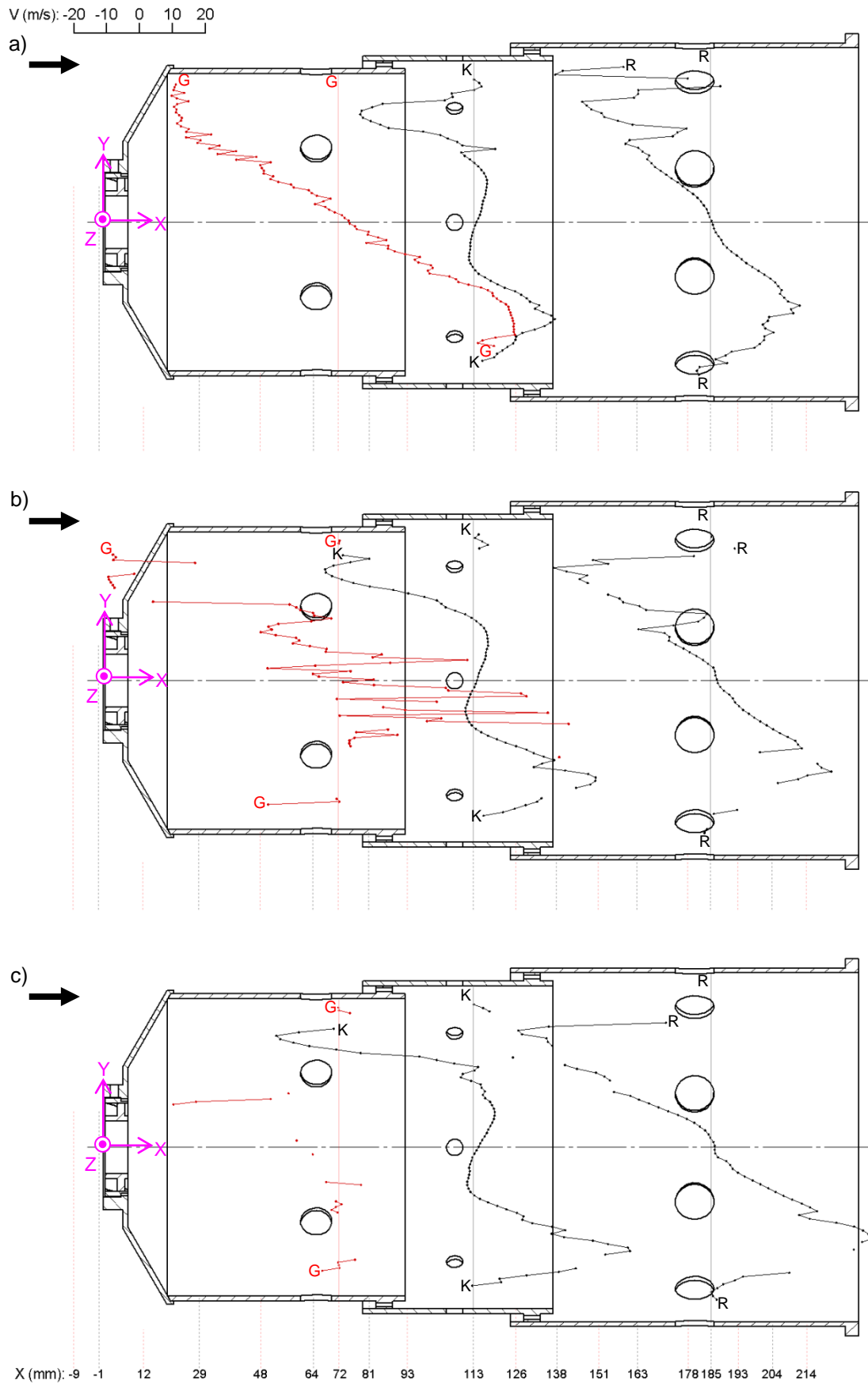


Figure 127: A comparison of the radial velocity profiles in line with the holes at the jets at a)  $\dot{m}_A = 0.056$  kg/s, b)  $\dot{m}_A = 0.070$  kg/s and c)  $\dot{m}_A = 0.091$  kg/s

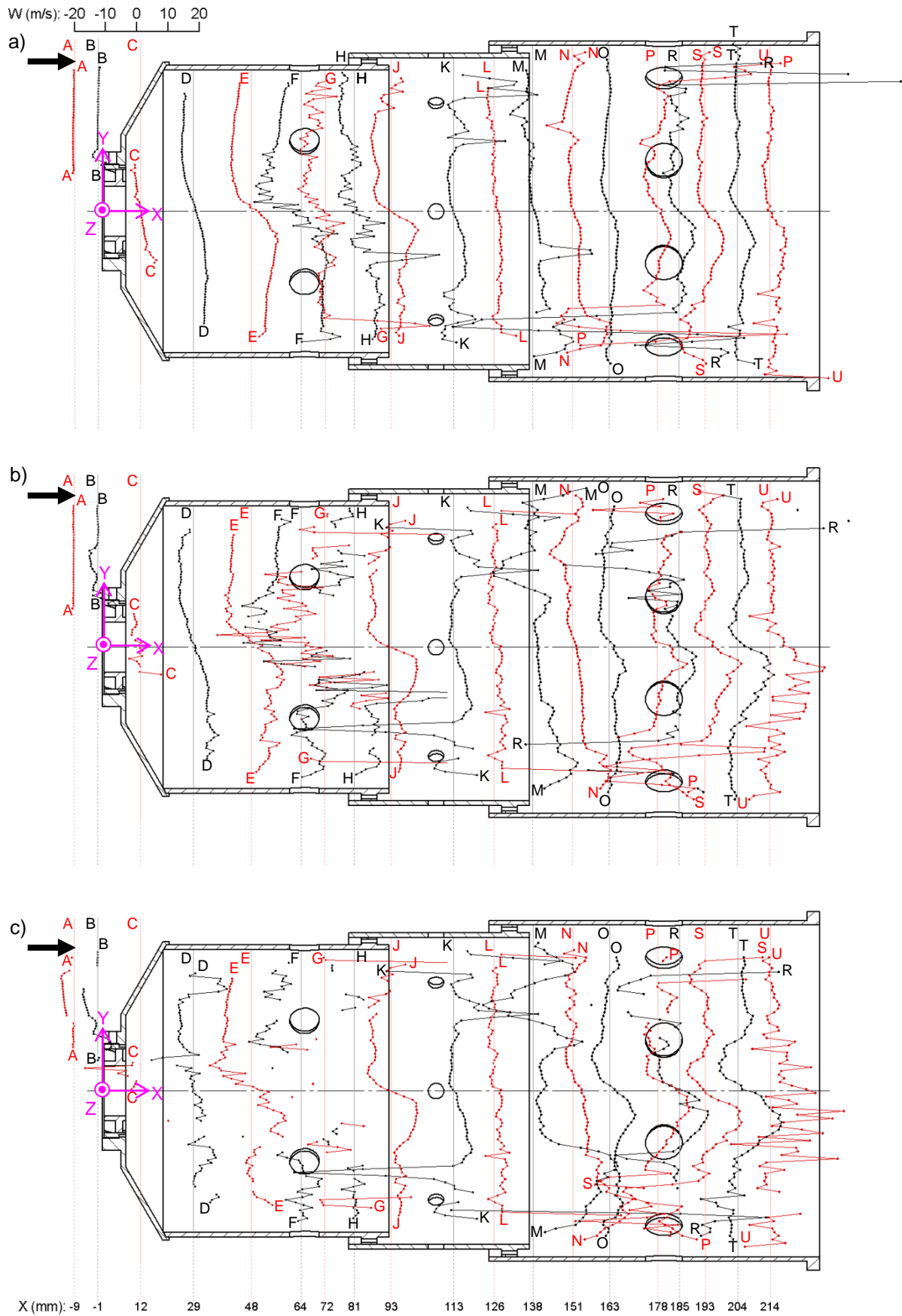


Figure 128: A comparison of the azimuthal velocity profiles in line with the holes at a)  $\dot{m}_A = 0.056$  kg/s, b)  $\dot{m}_A = 0.070$  kg/s and c)  $\dot{m}_A = 0.091$  kg/s

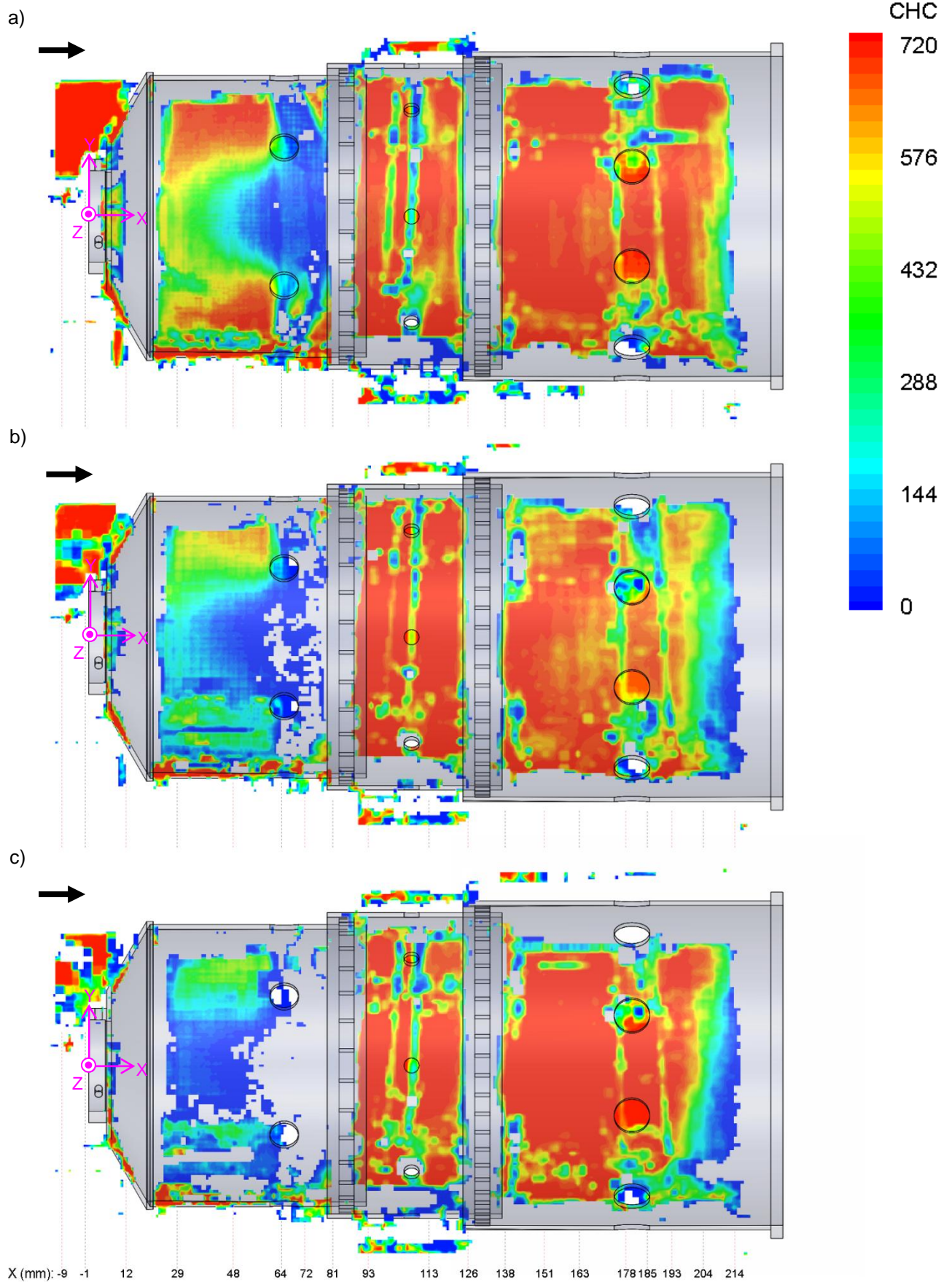


Figure 129: A comparison of the velocity vectors in line with the holes at a)  $\dot{m}_A = 0.056$  kg/s, b)  $\dot{m}_A = 0.070$  kg/s and c)  $\dot{m}_A = 0.091$  kg/s

### 4.2.3 Temporal indication

The data presented in the previous sections are averages of many captures and are thus steady-state results of a highly turbulent and unsteady flowfield. The hardware of the PIV system as it stands cannot sample that many images at a fast enough rate to evaluate the turbulent fluctuations in this flowfield. However, an indication of the turbulence and unsteadiness can be seen if consecutive two-dimensional images are observed. Figure E.1 to Figure E.6 in Appendix 6E show the last six consecutive captures of the 0.056 kg/s primary zone run in line with the holes. These images are captured approximately 1.5 seconds apart. If one looks at particular features in all the captures, the unsteadiness of the flowfield becomes evident. Table 13 to Table 15 focus on the top recirculation zone, the bottom jet and the reverse flow section to highlight the unsteady nature of the flow. It is important to note that the sample rate is very slow and thus the features pointed out in adjacent images are not necessarily a direct follow-on from each other and may be at different places in a cycle, in the incorrect order, sampled many cycles apart. The red square in the combustor primary zone diagram at the top of the tables indicates the position of the images shown.

In Table 13a, the top recirculation zone is shown, which has a flowfield similar to the recirculation zone calculated in the steady-state results. If one looks at b), which is 1.5 s after a), the reverse flow section of the recirculation at the bottom becomes weak and an upward flow across the reverse path starts to appear. In c), the recirculation zone has been cut in half by an upward flow path and a larger flow pulse has appeared at the top left corner of the image. In d), there seems to be a complete breakdown of the recirculation zone and many small weak vortex-like structures are in its place. On the bottom right-hand corner, the velocity vectors are pointing in the opposite direction to when the recirculation zone is established and there is no evidence of a strong reverse flow zone. In e), the reverse flow zone is re-established and is larger than the average reverse flow zone extending upwards to almost take up the full area where the recirculation zone was. In the next image, f), the recirculation zone has almost re-established with reverse flow at the bottom and forward flow at the top.

Table 14 shows a close-up of the bottom primary zone jet. The angle of the jet changes with respect to the combustor wall normal. The jet angles in the images from a) to f) are approximately 25°, 18°, 20°, 16°, 27° and 23°, respectively. This change in jet angle indicates that the jets fluctuate left and right in the flow by as much as 11°.

In Table 15, the reverse flow zone is shown to have fluctuating intensities and the occasional interference or breakdown. In a), there is a full intense reverse flow zone shown. In b), there is some decrease in the velocity magnitudes at the bottom right and top left. There is almost a complete breakdown of the top half of the reverse flow zone in c) and d). In e), an intense reverse flow zone has been re-established while in f), the left portion of the reverse flow zone has been cut through by a downward non-uniform flow.

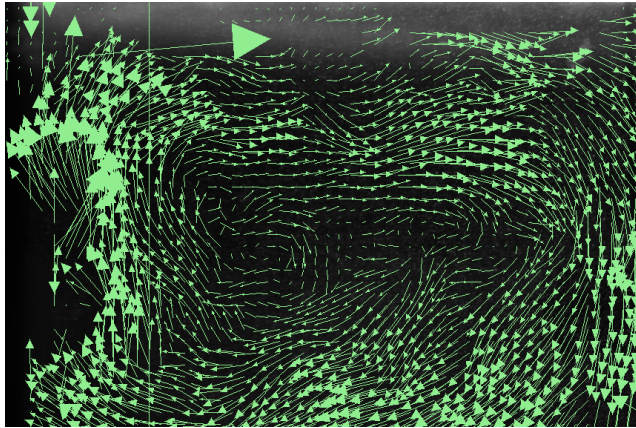
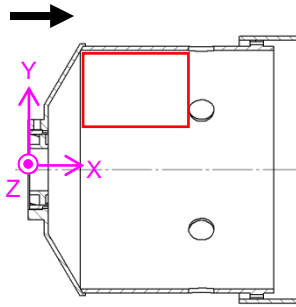
Various other features fluctuate in the primary zone especially visible in the recirculation zones. The full two-dimensional vector fields for the primary zone are shown in Figure E.1 to Figure E.6 in Appendix 6E.

The secondary zone (Figure E.7 to Figure E.12 in Appendix 6E) and dilution zone (Figure E.13 to Figure E.18 in Appendix 6E) also show unsteadiness and fluctuating features.

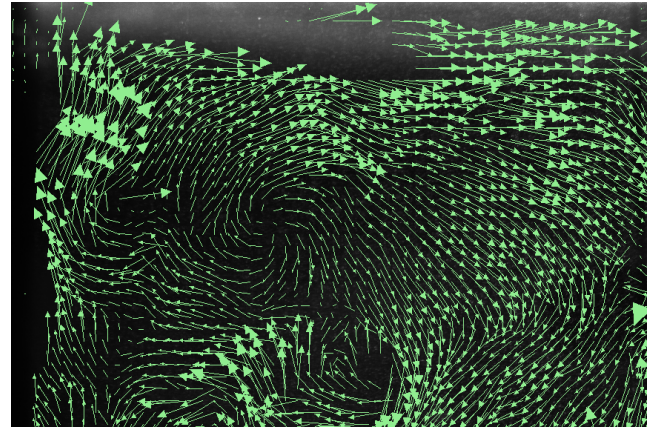
In the secondary zone images, the unsteadiness is seen in the varying nature of the jet path and extent. The central forward flow zone in the secondary zone also has instances where it recedes from the right and a weak reverse flow patch occurs. The direction of the central flow also changes from image to image.

The dilution recirculation zone has similar fluctuations to the primary recirculation zone. The recirculation zone breaks down in certain images to show many small patches of vectors in many directions. The jet velocity vectors vary in the extent to which they impinge as well as the angle at which they enter the flow. The outlet velocity vectors also vary between pointing slightly upwards and downwards and sometimes both.

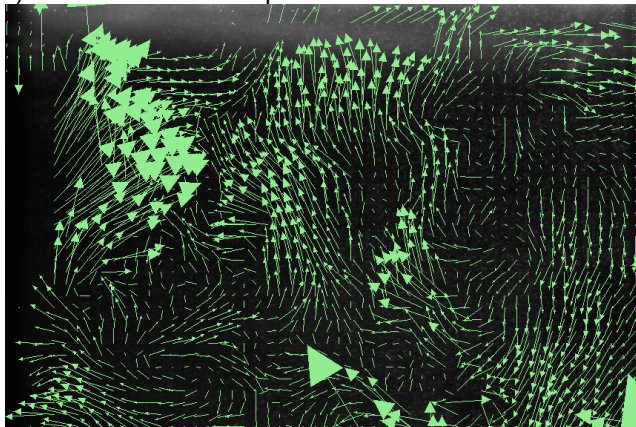
Table 13: The primary zone vectors at the top recirculation zone at times starting at  $t = 1\ 188\ 625\ 000\ \mu\text{s}$  to  $t = 1\ 196\ 531\ 250\ \mu\text{s}$



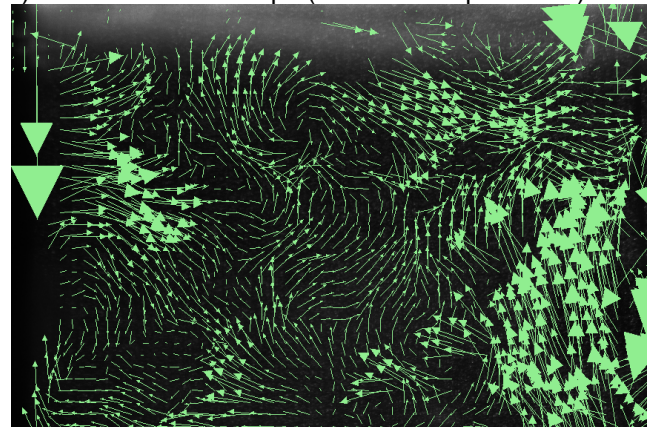
a)  $t = 1\ 188\ 625\ 000\ \mu\text{s}$



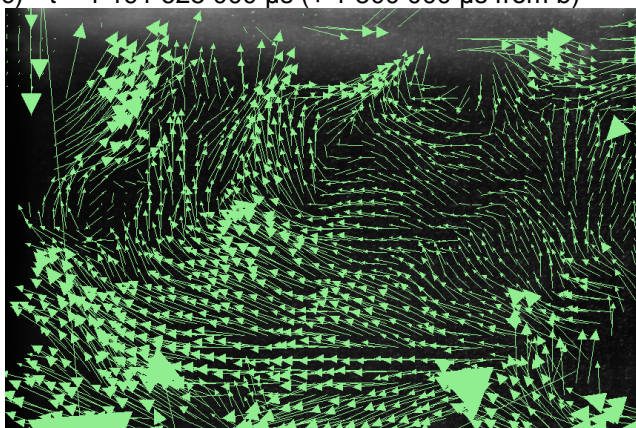
b)  $t = 1\ 190\ 125\ 000\ \mu\text{s}$  (+ 1 500 000  $\mu\text{s}$  from a)



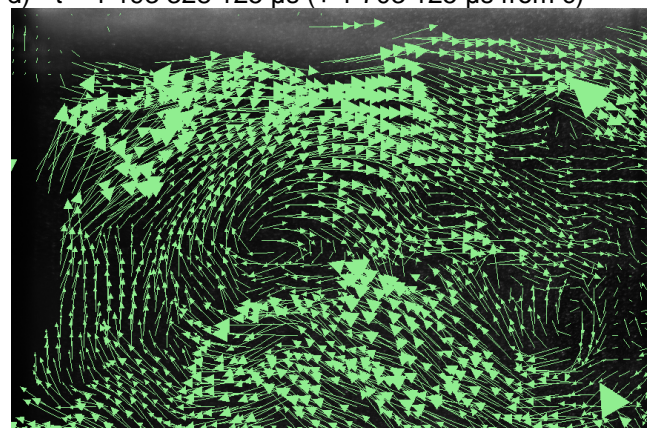
c)  $t = 1\ 191\ 625\ 000\ \mu\text{s}$  (+ 1 500 000  $\mu\text{s}$  from b)



d)  $t = 1\ 193\ 328\ 125\ \mu\text{s}$  (+ 1 703 125  $\mu\text{s}$  from c)

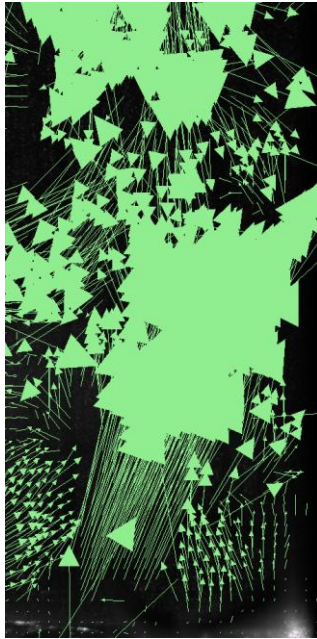
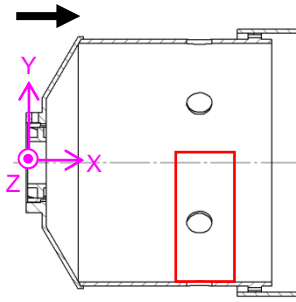


e)  $t = 1\ 195\ 031\ 250\ \mu\text{s}$  (+ 1 703 125  $\mu\text{s}$  from d)



f)  $t = 1\ 196\ 531\ 250\ \mu\text{s}$  (+ 1 500 000  $\mu\text{s}$  from e)

Table 14: The primary zone vectors at the bottom jet region at times starting at  $t = 1\ 188\ 625\ 000\ \mu\text{s}$  to  $t = 1\ 196\ 531\ 250\ \mu\text{s}$



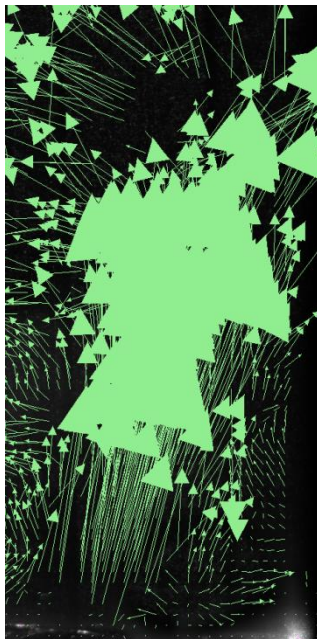
a)  $t = 1\ 188\ 625\ 000\ \mu\text{s}$ ,  
Jet angle =  $\pm 25^\circ$



b)  $t = 1\ 190\ 125\ 000\ \mu\text{s}$   
(+  $1\ 500\ 000\ \mu\text{s}$  from a),  
Jet angle =  $\pm 18^\circ$



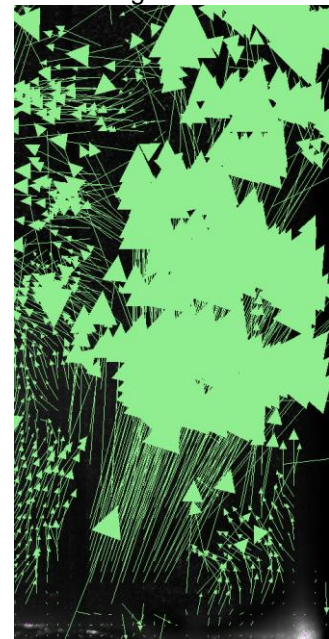
c)  $t = 1\ 191\ 625\ 000\ \mu\text{s}$   
(+  $1\ 500\ 000\ \mu\text{s}$  from b),  
Jet angle =  $\pm 20^\circ$



d)  $t = 1\ 193\ 328\ 125\ \mu\text{s}$   
(+  $1\ 703\ 125\ \mu\text{s}$  from c),  
Jet angle =  $\pm 16^\circ$

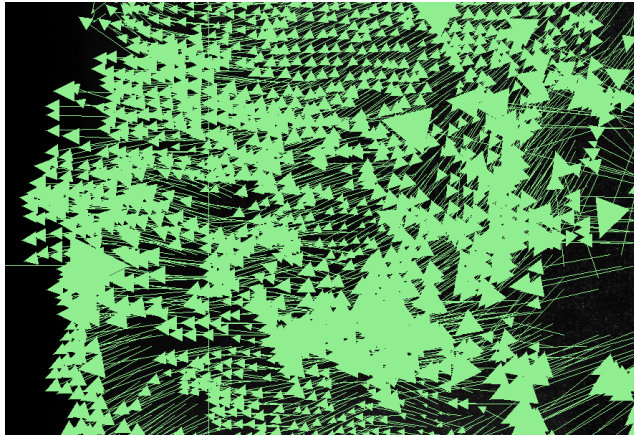
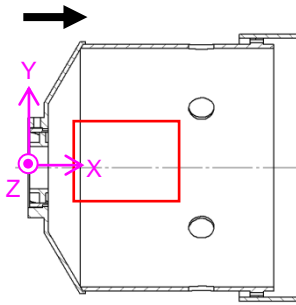


e)  $t = 1\ 195\ 031\ 250\ \mu\text{s}$   
(+  $1\ 703\ 125\ \mu\text{s}$  from d),  
Jet angle =  $\pm 27^\circ$

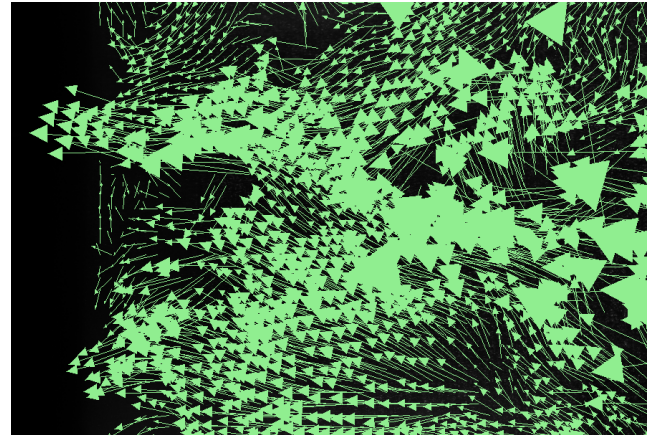


f)  $t = 1\ 196\ 531\ 250\ \mu\text{s}$   
(+  $1\ 500\ 000\ \mu\text{s}$  from e),  
Jet angle =  $\pm 23^\circ$

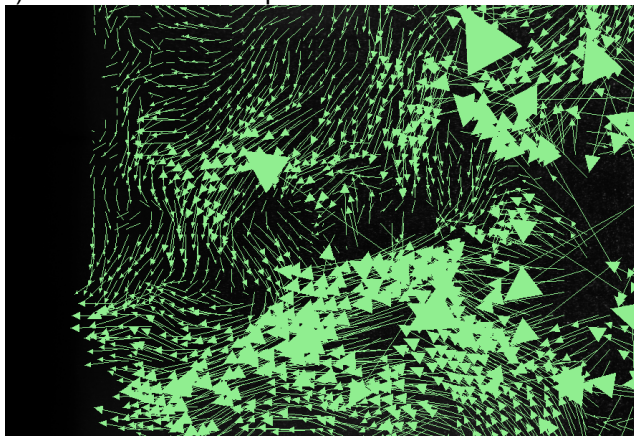
Table 15: The primary zone vectors at the reverse flow region at times starting at  $t = 1\ 188\ 625\ 000\ \mu\text{s}$  to  $t = 1\ 196\ 531\ 250\ \mu\text{s}$



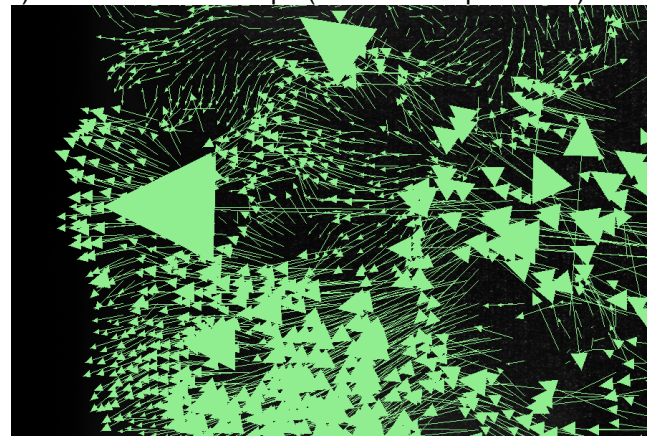
a)  $t = 1\ 188\ 625\ 000\ \mu\text{s}$



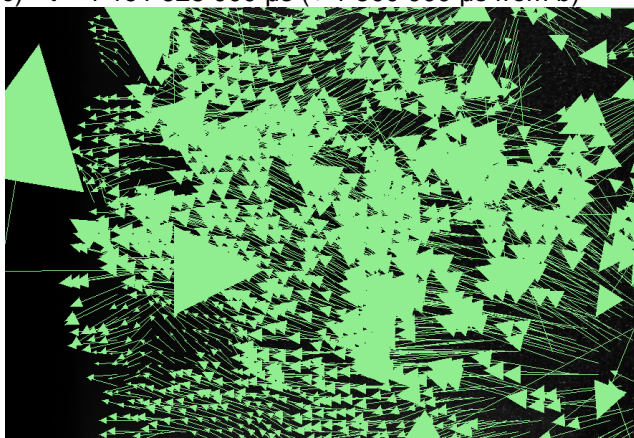
b)  $t = 1\ 190\ 125\ 000\ \mu\text{s}$  (+  $1\ 500\ 000\ \mu\text{s}$  from a)



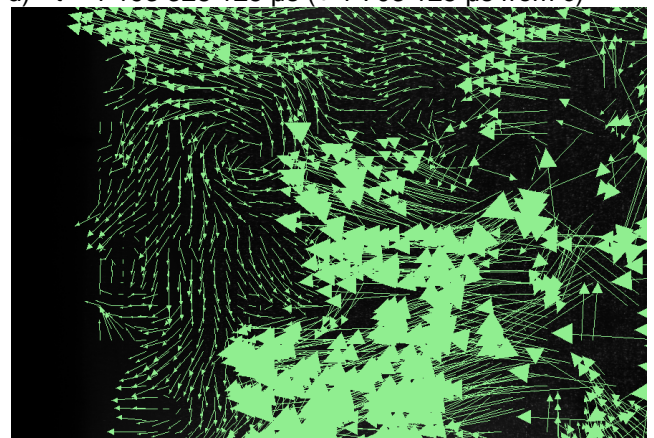
c)  $t = 1\ 191\ 625\ 000\ \mu\text{s}$  (+  $1\ 500\ 000\ \mu\text{s}$  from b)



d)  $t = 1\ 193\ 328\ 125\ \mu\text{s}$  (+  $1\ 703\ 125\ \mu\text{s}$  from c)



e)  $t = 1\ 195\ 031\ 250\ \mu\text{s}$  (+  $1\ 703\ 125\ \mu\text{s}$  from d)



f)  $t = 1\ 196\ 531\ 250\ \mu\text{s}$  (+  $1\ 500\ 000\ \mu\text{s}$  from e)

### 4.3 Wedge ring tests

The reacting wedge ring experiments are performed with varying combinations of wedge rings inserted. The experimental test matrix for the wedge ring tests is shown in Table 16 (same as Table 2) with a red border.

**Table 16: The experimental test matrix for the reacting experiments**

Data types measured	Wedge ring configuration →	Both wedge rings	Pz wedge rings	Sz wedge rings	No wedge rings (base case)
Wedge ring set ↓		<ul style="list-style-type: none"> <li>• Outlet plane temperature contours</li> <li>• Outlet Velocity profile with combustion</li> <li>• Outlet Velocity profile without combustion</li> </ul>			
10%					
30%					

= Reacting flow base case

The following data shows a comparison between the wedge ring configurations and the reacting base case results.

#### 4.3.1 Outlet temperature profile

The outlet temperature profile that was measured with no wedge rings inserted is used as the base case for comparison. All the effects of the wedge ring inserts were monitored with comparison with this no ring base case which is presented again in Table 17 (same data as Table 7).

**Table 17: The normalised temperature results for the no wedge ring case**

No wedge rings	
<p style="text-align: center;">Normalized Temperature</p>	<ul style="list-style-type: none"> <li>• <math>T_{max} = 817</math> K</li> <li>• <math>T_{min} = 501</math> K</li> <li>• Overall pressure loss = 3.51%</li> <li>• Pressure loss factor = 100.94</li> <li>• Pattern factor = 0.70</li> <li>• Profile factor = 0.54</li> </ul>

**Table 18: A comparison of the normalised outlet temperature profiles for the seven configurations**

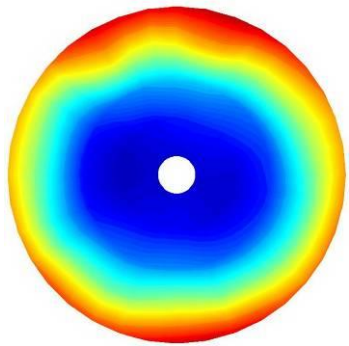
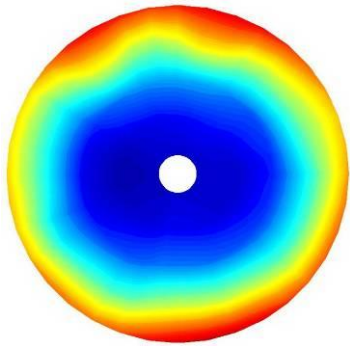
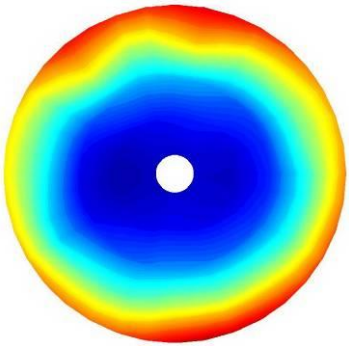
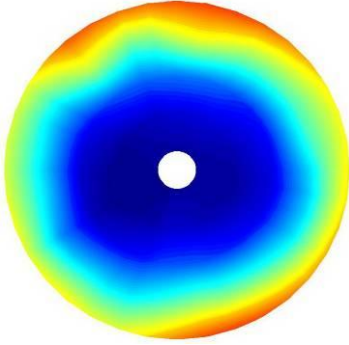
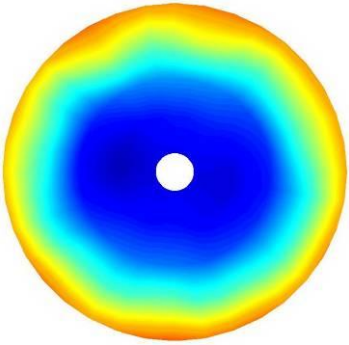
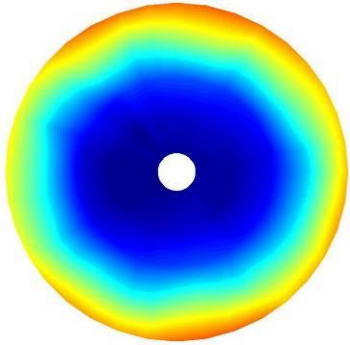
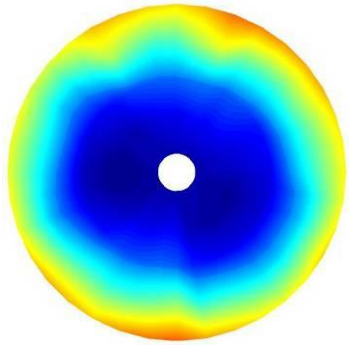
	Both wedge rings	Primary zone wedge ring	Secondary zone wedge ring	No wedge rings
10%				
30%				

Table 18 has a comparison of the seven outlet profiles. The scales of all the profiles are the same as that in Table 17. All the profiles are also presented in the same orientation. The outlet profiles as well as the graph in Figure 130 show a higher maximum temperature for the 10% wedge rings than for the 30% wedge rings.

The hot region extends all the way around the combustor circumference if both wedge rings are in although it is smoother for the 30% wedge rings. The undulation or hot protrusion is also not as steep for the 30% wedge rings as for the 10% wedge rings. For the 30% wedge rings, it seems that inserting both rings or only the primary zone ring has the same effect while only inserting the 30% secondary wedge ring seems to have very little effect since the outlet profile is the same as if no wedge rings are inserted. For the 10% wedge rings, except for the extension of the hot section as mentioned above, there is very little difference between the different 10% wedge ring configurations and no wedge rings. This can also be seen in the light markers in Figure 131 to Figure 134 where they are closer to the no wedge ring values than the 30% wedge ring markers (bright markers).

The graphs in Figure 130 to Figure 134 are comparisons of the combustor characteristic factors reported in Table 17 for the base case. The key to the graphs is as follows:

- Blue marker ( $\diamond$ ) = Both the primary zone and secondary zone wedge ring inserted (set-up 1 & 5)
- Pink marker ( $\square$ ) = Only the primary zone wedge ring inserted (set-up 2 & 6)
- Gold marker ( $\triangle$ ) = Only the secondary zone wedge ring inserted (set-up 3 & 7)
- Cyan marker ( $\circ$ ) = No wedge rings inserted (set-up 4 & 8)

Set-ups 1 to 4 are experiments with no combustion while 5 to 8 are experiments with combustion.

Finally, the light markers are the 10% wedge ring experiments while the bright markers are the 30% wedge ring experiments.

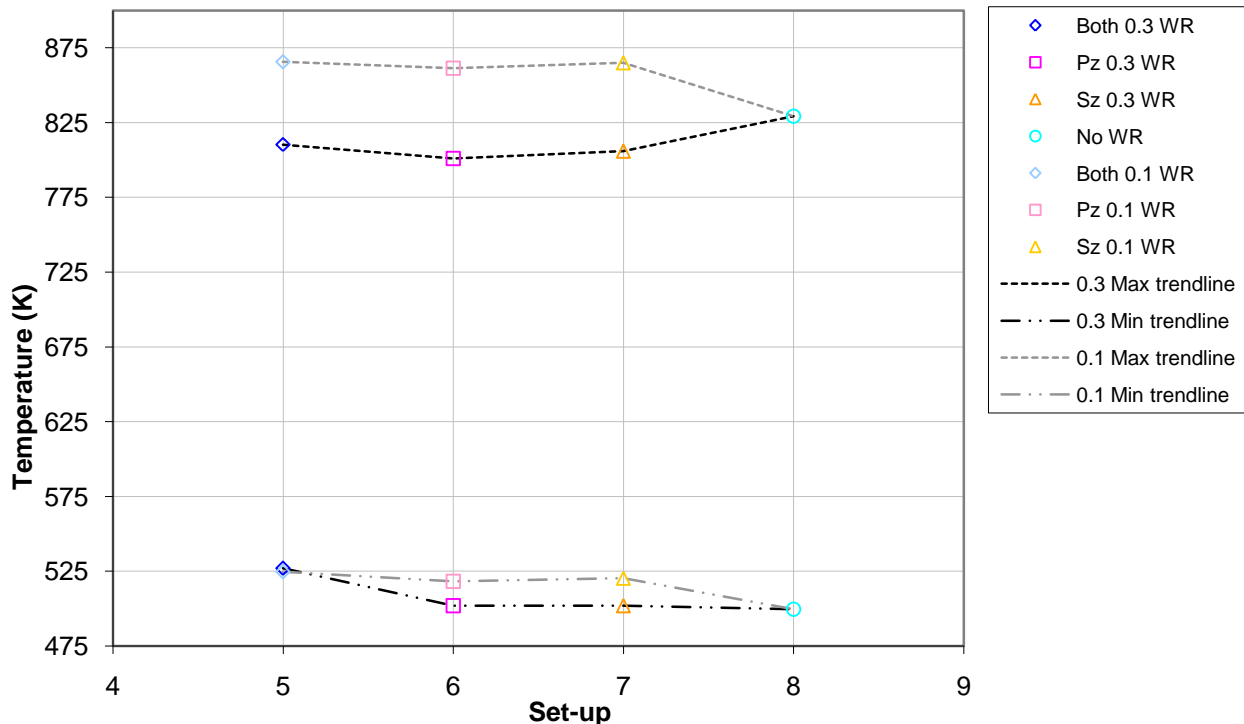


**Figure 130: The average maximum and minimum temperatures for each experimental set-up**

It can be seen from Figure 130 that the maximum values for the 10% wedge rings are higher than that of the 30% wedge rings and the no wedge rings configurations but the minimum temperatures have more or less the same values for all configurations. The maximum values for the 30% wedge ring configurations are slightly lower than that of the maximum temperature with no wedge rings.

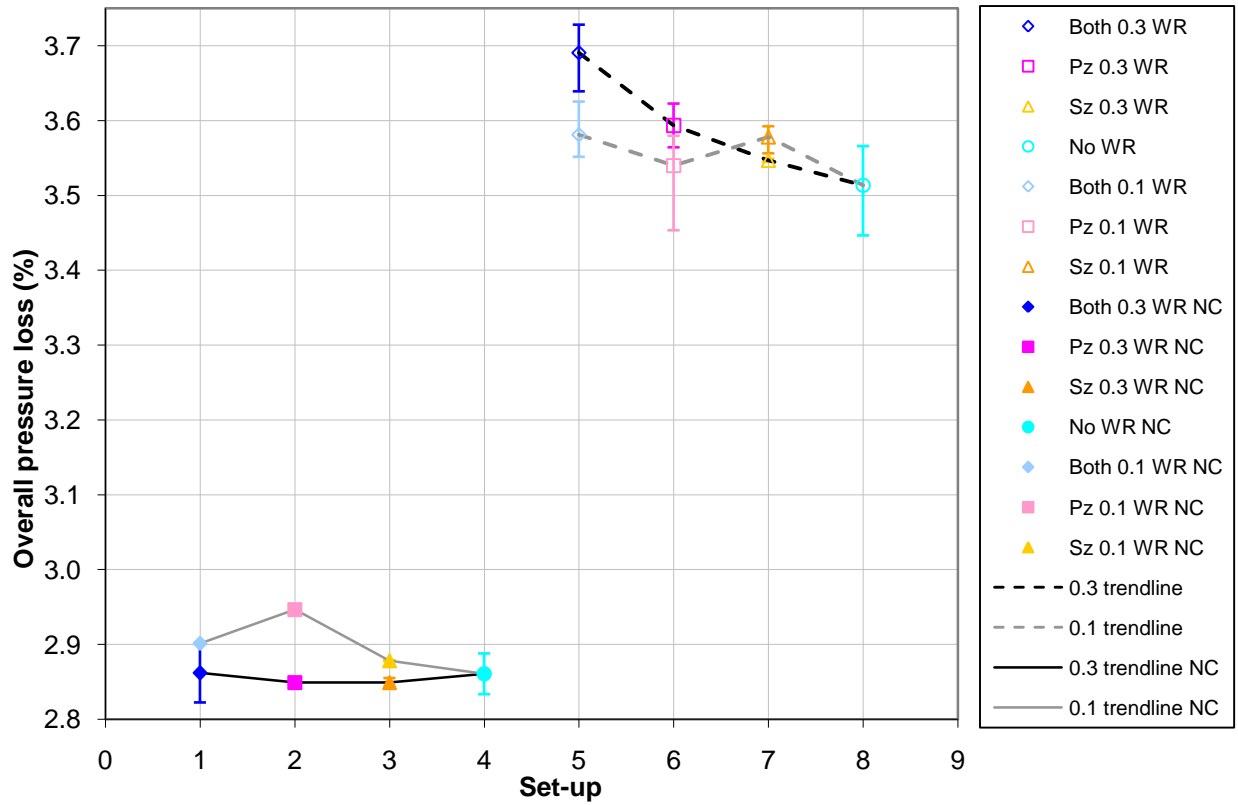


Figure 131: The average overall pressure loss for each experimental set-up

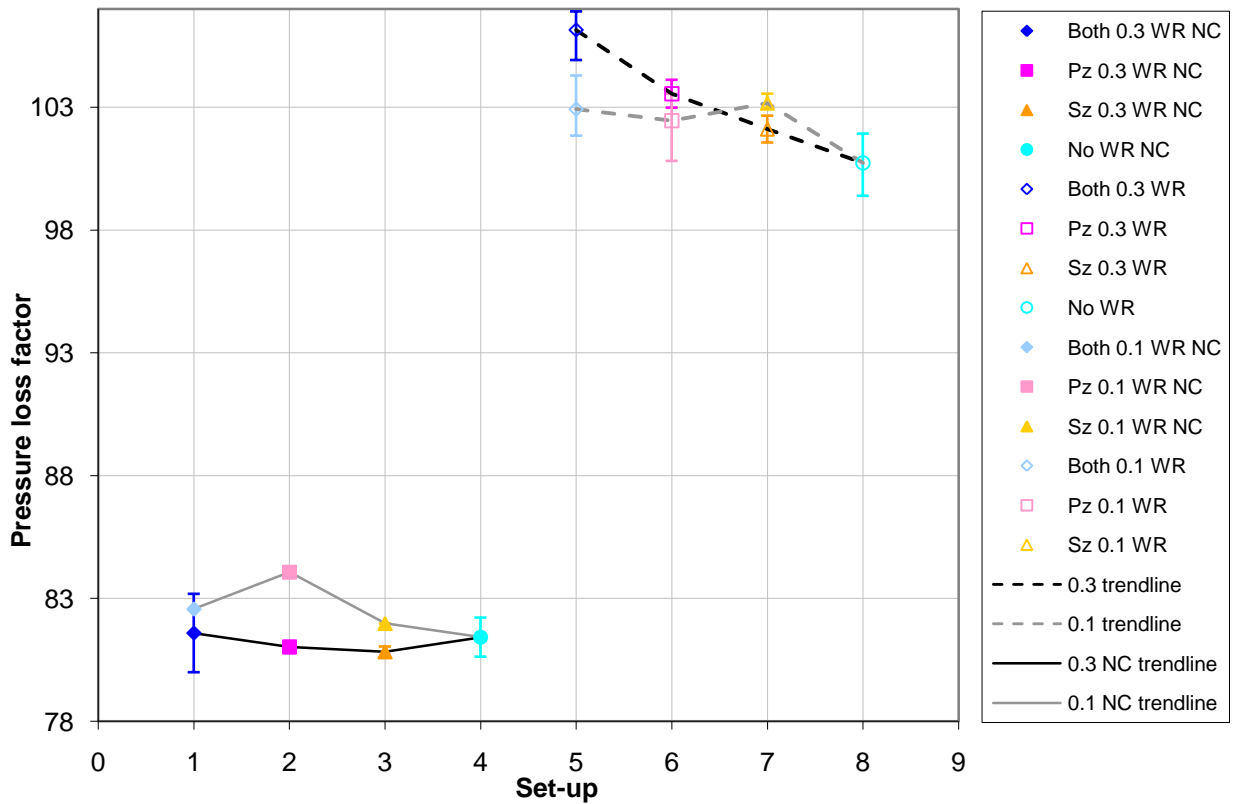


Figure 132: The average pressure loss factor for each experimental set-up

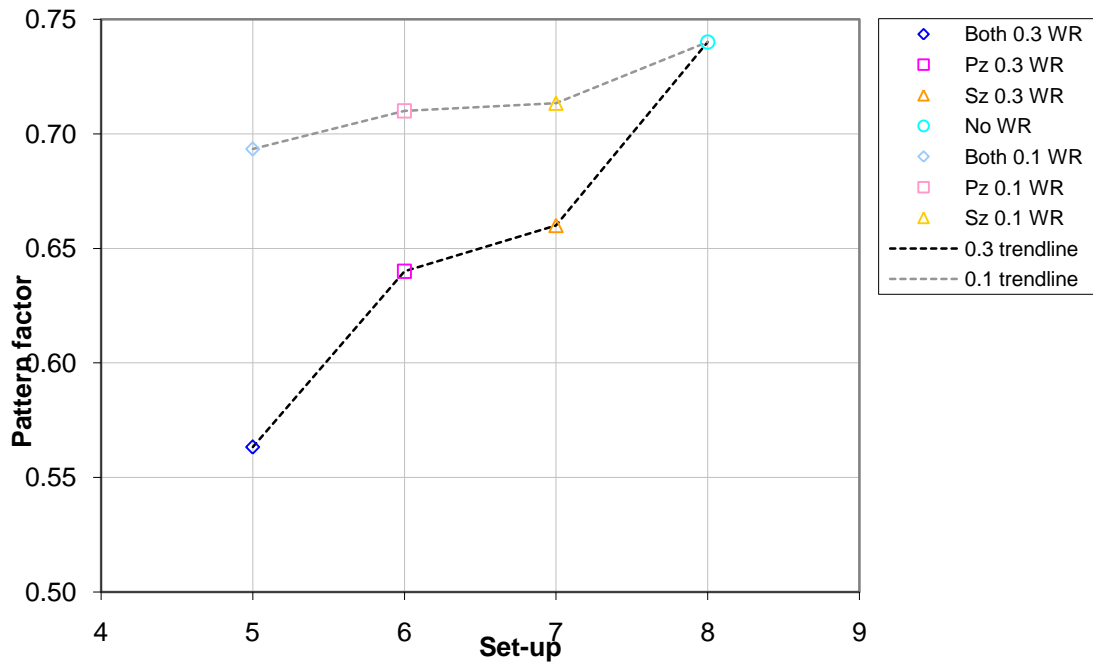


Figure 133: The average pattern factor for each experimental set-up

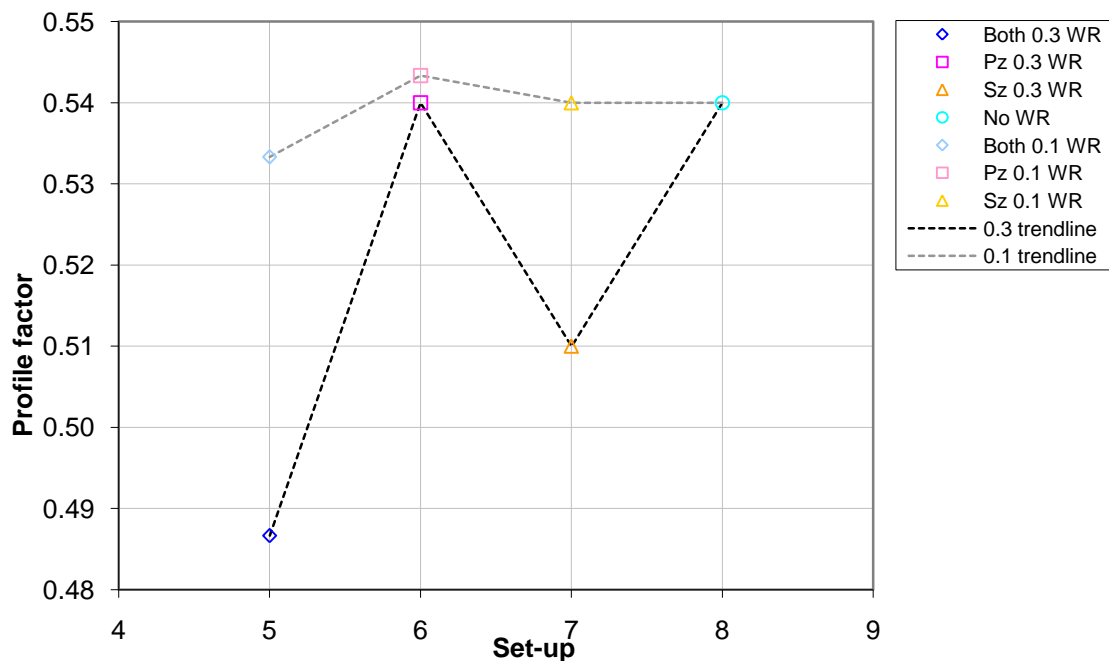


Figure 134: The average profile factor for each experimental set-up

Figure 131 and Figure 132 are pressure characteristic graphs. These factors without combustion (set-up 1 to 4) do not show any trends that explain any phenomena but with combustion (set-up 5 to 8) some trends are visible. Both figures indicate a higher pressure loss for the cases with combustion than without. This is due to the combustion of the fuel providing expansion in the combustion products which increases the velocity and thus dynamic pressure of the flow exiting the combustor. For the 30% wedge rings, there is a definite increase in both the overall pressure loss and the pressure loss factor as the blockage increases. This is expected since the secondary zone wedge ring introduces a higher blockage than no wedge rings, the primary zone wedge ring introduces even more of a blockage than that and having both the wedge rings in would introduce even more blockage than that. This is definitely seen by an increase of the pressure factors. The 10% wedge rings, however, do not seem to have a definite trend and only seem to increase the

blockage slightly compared with no wedge rings but there is no significant difference whether one or both of the 10% wedge rings are in.

Figure 133 and Figure 134 are the pattern and profile factor graphs. These two graphs like the pressure characteristic graphs also show very little effect from inserting any of the 10% wedge ring configurations. This may be partly due to the maximum temperature increase for the 10% wedge rings. The 30% wedge rings, however, show a definite downward trend in pattern factor with the increase in wedge ring insertion. There is a 0.14 decrease in pattern factor when using both 30% wedge rings at a cost of 0.2% increase in overall pressure loss. This may be due to increased mixing because of recirculation zones created after the wedge rings or possibly due to the wedge rings heating up and radiating heat performing a slight smoothing or evening of the temperature profile. It could also be due to the maximum temperature decrease which would then cause a decrease in the pattern factor. This would cause a false indication of improvement.

Having noted the above-mentioned variations found when using the wedge rings, overall the effect of the wedge rings was small and the general unevenness in the radial direction of the thermal distribution is still not ideal, thus, the wedge rings were not considered a success.

### 4.3.2 Outlet velocity profile

The velocity profiles measured 60 mm downstream to the outlet of the combustor liner are presented in Figure 135. The velocity profiles with the open markers were measured with combustion while the ones with filled markers were measured without combustion. As expected, all the velocity profiles with combustion have a higher velocity than the profiles without combustion due to the added energy from the burning of the fuel. The maximum velocities with combustion are almost double that without combustion. It is evident that the different wedge ring configurations have little or no effect on the velocity profile. The only variation in the velocity profile is for the 30% primary zone ring with no combustion. As can be seen in the graph, there is a negative section in the graph on the left-hand side. As in the base case, this is an artificial negative and only indicates a region where the pressure drop across the Pitot tube was negative. This indicates that a larger component is perpendicular to the Pitot tube than parallel with it. It is speculated that there may have been a recirculation or reverse flow region at this point.

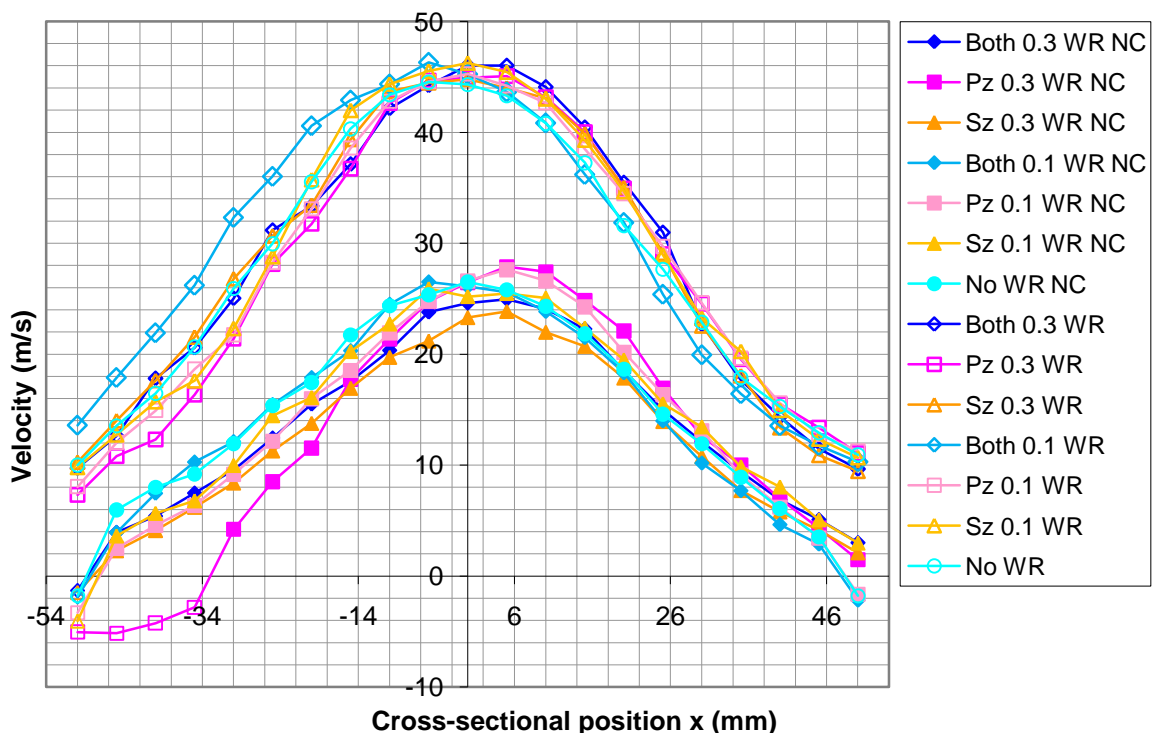


Figure 135: The outlet velocity profile comparison for each experimental set-up

## 5 CONCLUSIONS

### 5.1 Summary

Due to inaccuracies in both flow and combustion modelling in CFD, the simulations of gas turbine combustor flow often compare poorly with experimental results. Due to this poor comparison, CFD is not a reliable design tool for gas turbine combustors.

Furthermore, during past experiments on the combustor used in this study, it was found that the outlet temperature profile was somewhat undesirable, with a hot outer region and a cold core.

The first and main purpose of this dissertation is to create an experimental test case for CFD result validation as well as for evaluating the models used in CFD simulations. Velocity field data was required for comparison to non-reacting CFD runs for the evaluation of the turbulence modelling and flow feature simulation. Temperature data was required to evaluate the accuracy of the combustion models. A secondary purpose was to attempt to improve the outlet temperature profile of the current test rig. The test case also serves the purpose of being a base case for comparison if modifications are applied to the combustor test rig.

The CFD test case was made up of three-dimensional velocity field data measured using a PIV system. The velocity field data was captured on planes in line with the holes and in between the holes of each of the three combustor zones. A transparent perspex combustor was manufactured to enable the PIV measurements. The velocity profile at the outlet to the test rig was measured using a Pitot tube both with and without combustion. The temperature profile at the outlet of the combustor liner was measured using a thermocouple rake which consisted of five K-type thermocouples.

Passive inserts were used to attempt to improve the outlet temperature profile of the combustor. The Passive inserts were stainless steel wedge shaped rings that were manufactured and fitted into the primary and secondary zone in line with the cooling rings. The outlet temperature profile was measured using the thermocouple rake for each of the six wedge ring configurations (Both 10%, Both 30%, Pz 10%, Sz 10%, Pz 30%, Sz 30%) and compared to the base case (No wedge rings) configuration. The velocity profiles both with and without combustion were also measured with a Pitot tube and also compared to the base case configuration.

### 5.2 Results

#### 5.2.1 Reacting experiment

Even though the outlet temperature profile indicates a non-ideal combustor with a hot ring-like sector around the outer edge, the data collected can be used for creating a test case for CFD and an ideal combustor is not needed. This is concluded because all the typical flow features of a combustor are shown to be present in the PIV measurements. The comparison between the CFD and experimental outlet temperature profile also reveals one of the many reasons that a validation case is needed due to the large discrepancy in the temperature values.

The thermocouple measurements produced the outlet temperature contour profile showing the temperatures on the outlet plane of the combustor liner. An asymmetrical temperature distribution was present at the outlet to the combustor. A hot region was formed around the outer region of the combustor while a cooler region in the core of the flow was present. The maximum temperature, which was present in the outer region of the outlet plane, was 817 K while the minimum, near the centre, was 501 K. In the outer hot ring-like region the temperature was not distributed evenly with the hottest sectors between 45 and 135° and between 260 and 340°. The coolest sector of the outer ring was on the left side of the outlet profile between 135 and 260°.

The qualitative data, especially the flame photographs, help to explain the outlet temperature profile and also validate it. In the sector between 135 and 260°, there was no flame visible in the flame images. This sector coincided with the cooler region in the outer hot ring shown in the thermocouple measurements. The correspondence between the flame tongues and the hottest regions at the top and bottom of the liner outlet is quite evident as well. The carbon deposit photographs showed that the sectors of carbon burned away on the top, bottom and right side corresponded to the flame tongues' position. The carbon on the left, however, where no flame was visible, was also burned away which does not correspond to the flame photographs. The reason for this lack of correlation on the left is unknown. Possible reasons for the lack of correlation on the left are that there may have been enough heat and oxygen to combust the carbon, there may be a non-visible flame, there may have been a jet of air that caused both the physical removal of the carbon deposit and the lack of flame on the left side or the flow structure could have been such in the startup of the rig to have been able to burn this carbon away.

The velocity profiles indicated that the maximum velocity almost doubled with the addition of combustion going from the maximum outlet velocity of 26.5 m/s without combustion to 44.5 m/s with combustion. The general shape of the profile was similar to that without combustion but the profile as a whole increased in magnitude due to the energy addition from combustion which caused an expansion of combustion products thus increasing the velocities and thus dynamic pressure of the flow leaving the combustor liner.

## 5.2.2 Non-reacting experiment

A large amount of flowfield data has been collected and the main typical and atypical flow features are shown. The data collected shows the positions, shapes and sizes of the main features in the combustor and can thus be used for the comparison of CFD data to ensure the modelling of flow features is correct.

The size and position of the primary recirculation zone and the swirling profiles are required to check how well the turbulence model simulates swirl and jets together.

On the planes in line with the holes, the primary recirculation zone shows a rectangular reverse flow region for the 0.056 kg/s flow rate. This region is typically "V"- or "Y"-shaped and has an atypical shape at this flow rate.

The azimuthal profiles indicate that the swirl velocities decreased towards the outer radii positions while they increased as one moved downstream in the primary zone. The swirl number, calculated at various cross-sections, was greater than 0.4 for a majority of the primary zone indicating moderate to high swirl while in the secondary and dilution zones had swirl numbers below 0.4 indicating weak swirl intensities. Just before the primary zone jet, the swirl number was 1.28 indicating the strongest swirl in this region.

The jet penetration depths should be well modelled because the jet penetration depths influence the mixing, which influences the combustion process. The primary and dilution zone jets have a 100% penetration depth. It is thought that the high penetration depths of the jets form a partial barrier to the flow and thus help to induce the recirculation zones in these two regions. The secondary zone jet penetration depths are only about 60%. This is most likely due to the secondary holes only receiving 8,8% of the total supplied mass flow where as the primary and dilution holes each receive 22.5 and 50% of the total mass flow, respectively.

In between the holes, the flow structures are largely similar to those in line with the holes except for where the jets were. The jets are not present due to the plane not being aligned with the holes. Even though there are no jets, the flow in the hole region on these planes still follows a similar path as to when the plane was in line with the holes. The other main differences are that the secondary zone flow only diverges and does not converge in the centre as when the jets were present, and the dilution zone flow leaves the recirculation zone at the outer edge along the combustor wall.

The swirl numbers in the primary zone still indicate a moderate to strong swirl in the primary zone as with in line with the holes, but the maximum swirl number occurred 8 mm downstream on the cross-section in line with the holes instead of before the holes. After the primary zone the swirl numbers all indicated weak swirl.

The streamlines in between the holes tend to have much smoother changes in direction and have less sharp turns in the flow path. This is especially evident in the secondary and dilution zones.

The CHC values show that in the regions with high shear and turbulence, where the jets interact with the main combustor flow, the particles are more difficult to track and thus lower sample sizes are used in these regions. These regions need many more image captures to obtain statistically relevant sample sizes. The CHC values also indicate the presence of optical obstructions and reflections which further decrease the particle tracking ability of the PIV system.

Except for the recirculation zone in the dilution zone, all the velocity features and profiles in this combustor are similar to those shown in the typical flow of a can type combustor in the literature (Lefebvre [15]) as well as similar to other experimental data collected such as that of Cameron *et al.* [14]. The outlet velocity profile measured with the PIV system has a similar shape to the profile measured with the Pitot tube without combustion as well as to the outlet profile of Cameron *et al.* [14].

The atypical dilution recirculation zone, however, can be used to evaluate whether the CFD is modelling real flow features. This recirculation zone could also be part of the reason for the hot ring-like region at the outer radius of the combustor outlet. The 100% penetration of the cooler dilution jets could further help to create a cooler core and hotter outer ring at the outlet of the combustor. The hot combustion flow from the primary zone enters the secondary zone in the central region of the combustor and then diverges in the secondary zone as the streamlines diverge. The hot gasses then enter the dilution zone and are further forced towards the combustor walls by the dilution recirculation zone. The hotter flow then moves along the combustor wall. These hot gasses then leave the combustor along the wall in between the dilution holes and exit the combustor forming the hot ring of gasses on the outer flow region. The cooler air from the jets leave the combustor in the centre.

The comparison of the data as the flow rate increases ( $\dot{m}_A = 0.056$  kg/s,  $\dot{m}_A = 0.070$  kg/s and  $\dot{m}_A = 0.091$  kg/s) shows that none of the flow features are lost due to the lower flow rate and that the positions of the features are only slightly affected. The largest flow feature variation occurs in the reverse flow region which changes from a rectangular to a “Y”-shaped region as the flow rate increases. The velocity magnitudes in all the flow features throughout the combustor are increased as the flow rate increases. There are some minor variations in the primary recirculation zone centre positions and the jet angles, mainly in the secondary zone. The centres of the primary recirculation zone move upstream by approximately 5 mm and the secondary zone jets tend to angle more downstream as the flow rate increases.

The increase in flow rate showed a decrease in CHC value and a sparser data set. Due to this it would be preferable to use the lowest flow rate data for comparison due to the data set being more complete. Since the changes due to flow rate are slight and easily recognisable, the lower flow rate data is adequate for a CFD test case.

A comparison of consecutive captures showed variations in the flow features which showed an indication of the temporal nature of the flow inside the combustor. The primary recirculation zone tended to breakdown then re-establish periodically while the primary zone jet angle varied by  $11^\circ$  over the six images shown. The secondary zone images showed a variation in the jet angles and penetrations depths as well as pulsing in the central forward flow region. The dilution recirculation zone also broke down and re-established periodically and the dilution jets showed similar fluctuations as in the secondary zone.

### 5.2.3 Wedge rings

For the wedge ring tests, there are a few minor improvements, namely a decrease in pattern factor of 0.14 using both 30% wedge rings at a cost of only 0.2% increase in overall pressure loss as well as lesser pattern factor decreases in the other 30% wedge ring configurations. The increase in the overall pressure loss was small and the overall pressure loss was still below the 5% maximum allowed value. There was, however, no significant improvement in the profile factor indicating that the undesirable gradients have not been improved. This is evident just by looking at the outlet temperature profile. The wedge rings also did not significantly affect the position of the hot and cold regions. In order to improve the outlet temperature profile, the aerodynamic design of the combustor should rather be revised.

The reason for the pattern factor improvements may be due to the slight drop in maximum temperature, which is then actually a false improvement since the overall “peakiness” of the profile has not been flattened

significantly. From this it is shown that an improvement in the factors may not necessarily mean an improved overall outlet profile.

Overall, the experiments performed produced a large variety of data that can be used in the various stages of combustor simulation using CFD. The non-reacting experimental data can be used to validate the numerical turbulence models and to evaluate how well the flow features are modelled or captured during the non-reacting stage of the combustor simulation process. The typical flow features such as jet penetration depths and the position and size of the recirculation regions are provided for effective comparison. The thermal results presented on the outlet plane of the combustor can be used for comparison with the CFD results simulating the combustion process.

### 5.3 Recommendations for future work

The current data set could be improved by re-measuring the primary zone PIV data with a smaller time between laser pulses since this was not possible at the time of the first data capture. More axis-symmetric data planes could be measured around the whole combustor liner providing a fuller set of combustor data. This data would be more useful if the combustor remained stationary and the PIV system rotated around it.

Temperature data measured in the primary zone and other internal positions would provide valuable data about the combustion process, even if the method is intrusive.

A glass combustor would enable the measurement of the flow field during a combusting experiment and would then enable one to evaluate the effect of combustion on the flowfield. PLIF and other optical temperature measurement techniques could then also be performed to gain non-intrusive temperature data inside the combustor liner and not just at the outlet. Visual evaluation of the flame would also be enabled in this way.

Turbulence data is required for CFD input as well as for result evaluation thus it would be hugely beneficial if hot-wire anemometer measurements were performed within the combustor liner.

Lastly the combustor liner could be aerodynamically redesigned to improve the outlet temperature profile since this would be the correct method to improve the outlet profile. Since an optimal or perfect combustor is not essential for test case purposes, this last recommendation would be for more academic purposes.

## 6 REFERENCES

- [1] Mbatha, M.N., "The Design, Manufacturing and Testing of a Fuel Injection System for a Gas Turbine Combustor," University of Pretoria, South Africa, Final Year Project Report 2003.
- [2] Meyers, B.C., "The Design, Manufacture and Testing of the Dilution Zone of a Gas Turbine Combustor," University of Pretoria, South Africa, Final Year Project Report 2003.
- [3] Scheepers, G., "Design of a Swirler for an Existing Gas Turbine Combustor," University of Pretoria, South Africa, Final Year Project Report 2003.
- [4] Vakil, S.S., Thole, K.A., "Flow and Thermal Field Measurements in a Combustor Simulator Relevant to a Gas Turbine Aeroengine," *Journal of Engineering for Gas Turbines and Power*, vol. 127, pp. 257-267, April 2005.
- [5] Archer, S., Gupta, A.K., "Confinement Effects on Flow and Combustion under Fuel Lean Conditions," in *Proceedings of IMECE04 2004 ASME International Mechanical Engineering Congress and Exposition*, Anaheim, California, USA, 13 - 20 November 2004, pp. 87-96.
- [6] Eggels, R.L.G.M., Brown, C.T., "Comparison of Numerical and Experimental Results of a Premixed DLE Gas Turbine Combustor," in *Proceedings of ASME Turbo Expo*, New Orleans, Louisiana, USA, 4 - 7 June 2001, pp. 1-10.
- [7] Mandai, S., Nishida, H., "Application of Turbulent Reacting Flow Analysis for Gas Turbine Combustor Development," *JSME International Journal*, vol. 47, no. 1, 2004, Series B.
- [8] Carl, M., Behrendt, T., Fleing, C., Frodermann, M., Heinze, J., Hassa, C., Meier, U., Wolff-Gassmann, D., Hohmann, S., Zarzalis, N., "Experimental and Numerical Investigation of a Planar Combustor Sector at Realistic Operating Conditions," *Journal of Engineering for Gas Turbine and Power*, vol. 123, pp. 810-816, October 2001.
- [9] Janus, B., Dreizler, A., Janicka, J., "Flow Field and Structure of Swirl Stabilized Non-Premixed Natural Gas Flames at Elevated Pressure," in *Proceedings of ASME Turbo Expo 2004 Power for Land, Sea and Air*, Vienna, Austria, 14 - 17 June 2004, pp. 1-10.
- [10] Li, G., Gutmark, E.J., "Geometry Effects on the Flow Field and the Spectral Characteristics of a Triple Annular Swirler," in *Proceedings of ASME Turbo Expo 2003 Power for Land, Sea and Air*, Atlanta, Georgia, USA, 16 - 19 June 2003, pp. 1-10, GT2003-38799.
- [11] Li, G., Gutmark, E.J., "Boundary Condition Effects on Nonreacting and Reacting Flows in a Multiswirl Combustor," *AIAA Journal*, vol. 44, no. 3, pp. 444-456, March 2006.
- [12] Diers, O., Koopman, J., Fischer, M., Hassa, C., "Investigation of Two Advanced Cooling Mixing Concepts for a Rich Quench Lean Combustor," *Journal of Engineering for Gas Turbine and Power*, vol. 124, pp. 784-791, October 2002.
- [13] Weigand, P., Meiers, W., Duan, X., Aigner, M., "Laser Based Investigations of Thermo-acoustic Instabilities in a Lean Premixed Gas Turbine Model Combustor," in *Proceedings of ASME Turbo Expo 2006 Power for Land, Sea and Air*, Barcelona, Spain, 8 - 11 May 2006, pp. 1-9.
- [14] Cameron, C.D., Brouwer, J., Wood, C.P., Samuelsen, G.S., "A Detailed Characterization of the Velocity and Thermal Fields in a Model Can Combustor With Wall Jet Injection," *Journal of Engineering for Gas Turbines and Power*, vol. 111, pp. 31-35, January 1989.
- [15] Lefebvre, A.H., *Gas Turbine Combustion*, Hemisphere Publishing Corporation, United States of America, 1983.
- [16] Website of the South African Weather Service, (Accessed April, 2007).
- [17] White, F.M., *Fluid Mechanics*, 4th ed., McGraw-Hill Companies, Inc., Singapore, 1999.
- [18] Northern Research and Engineering Corporation, *The Design and Development of Gas Turbine Combustors; Volume II; Design Methods and Development Techniques*, Northern Research and Engineering Corporation, Woburn, Massachusetts, United States of America, 1980.
- [19] TSI Incorporated, "TSI Particle Image Velocimetry System Training," December 3-7, 2007.
- [20] TSI Incorporated, "Insight™ 3G v 7.2.2.0," 2004.
- [21] TSI Incorporated, "PowerView™ Stereoscopic PIV System," 2002.
- [22] TSI Incorporated, "INSIGHT 3G™ Data Acquisition, Analysis and Display Software User's Guide,"



- 
- [23] TSI Incorporated, "Installing the Model 630059 POWERVIEW™ Plus 4MP PIV Camera,".
- [24] TSI Incorporated, "Model 640050 Stereoscopic PIV Camera System," August 1999.
- [25] The MathWorks, Inc., "MATLAB® v6.0.0.88," September 2000.
- [26] Tecplot Incorporated, "Tecplot v 10.0-6-012," 1988.
- [27] Northern Research and Engineering Corporation, *The Design and Development of Gas Turbine Combustors; Volume I; Component Theory and Practice*, Northern Research and Engineering Corporation, Woburn, Massachusetts, United States of America, 1980.
- [28] Kline, S.J., McClintock, F.A., "Describing Uncertainties in Single-Sample Experiments," *Mechanical Engineering*, vol. 75, pp. 3-8, January 1953.



## APPENDICES

### APPENDIX A: SPECIAL NOMENCLATURE

**Cameron *et al.* [14] (Figure 1 to Figure 10):**

#### NOMENCLATURE

Technical characters:

$\bar{T}$	Mean temperature
$\bar{U}$	Mean axial velocity
$\bar{W}$	Mean tangential velocity
$\infty$	Infinite

Latin characters:

R	Radius
U	Axial velocity
W	Tangential velocity
X	Axial distance
x	Axial distance

Subscripts:

rms	Root-mean-squared
-----	-------------------

#### ABBREVIATIONS

AFR	Air/Fuel ratio
DIA.	Diameter
Dz	Dilution zone
JP-4	Jet propellant 4
Pz	Primary zone

**Egges and Brown [6] (Figure 12 to Figure 14):**

#### NOMENCLATURE

Latin characters:

T	Temperature
---	-------------

#### ABBREVIATIONS

CFD	Computational fluid dynamics
FGM	Flame generated manifold
GRM	Global reaction mechanism



k- $\epsilon$	A turbulence model
LDA	Laser Doppler anemometry

**Carl *et al.* [8] (Figure 15 to Figure 18):**

NOMENCLATURE

Latin characters:

v	Velocity
x	Horizontal distance
y	Vertical distance

Subscripts:

x	Referring to the horizontal velocity component
---	--

ABBREVIATIONS

AFR	Air/Fuel ratio
CFD	Computational fluid dynamics
k- $\epsilon$	A turbulence model
LDA	Laser Doppler anemometry
LIF	Laser-induced fluorescence
OH*	Hydroxide radical

**Diers *et al.* [12] (Figure 19 to Figure 24):**

NOMENCLATURE

Latin characters:

U	Axial velocity
X	Axial distance
x	Axial distance
y	Height/radial distance
Z	Spanwise/tangential distance
z	Spanwise/tangential distance

Subscripts:

pZ	Primary zone
----	--------------

ABBREVIATIONS

AFR	Air/Fuel ratio
CARS	Coherent anti-Stokes Raman scattering
CFD	Computational fluid dynamics
LDA	Laser Doppler anemometry



UHC Unburnt hydrocarbons

**Li and Gutmark [10] (Figure 25 to Figure 26):**

**NOMENCLATURE**

Latin characters:

D Diameter  
r Radius  
z Axial distance

**ABBREVIATIONS**

3D Three-dimensional  
CCD Charge-coupled device  
CTRZ Central toroidal recirculation zone  
Lm Mixing tube length  
PC Personal computer  
PIV Particle image velocimetry  
TARS Triple annular research swirler

**Li and Gutmark [11] (Figure 27 to Figure 29):**

**NOMENCLATURE**

Latin characters:

k Turbulent kinetic energy  
R Outer radius  
r Radius  
T Temperature  
V Velocity  
z Axial distance

Subscripts:

<sub>0</sub> Reference value  
<sub>θ</sub> Referring to the tangential velocity component  
<sub>inlet</sub> Referring to the inlet  
<sub>theta</sub> Referring to the tangential velocity component  
<sub>z</sub> Referring to the axial velocity component

**ABBREVIATIONS**

BC Boundary conditions  
CCD Charge-coupled device

---



---

CFD	Computational fluid dynamics
CH*	Methylidyne/methine radical
CRZ	Central recirculation zone
k	Turbulent kinetic energy
Lm	Mixing tube length
Lmt	Mixing tube length
OH*	Hydroxide radical
PC	Personal computer
TARS	Triple annular research swirler
Temp	Temperature
TKE	Turbulent kinetic energy

**Mandia and Nishida [7] (Figure 30 to Figure 31):**

NOMENCLATURE

Greek characters:

$\phi$  Diameter or equivalence ratio

Latin characters:

Ga Air supply mass flow rate

Pa Air supply pressure

Ta Air supply temperature

Tg Exhaust gas temperature

ABBREVIATIONS

CFD Computational fluid dynamics

EDC Eddy dissipation concept

MIN A combustion model

RANS Reynolds-averaged Navier-Stokes

**Janus *et al.* [9] (Figure 32 to Figure 35):**

NOMENCLATURE

Latin characters:

u Axial velocity

v Radial velocity

w Tangential velocity

X Axial distance

x Axial distance

Y Radial distance

y Radial distance



Z Radial/tangential distance

#### ABBREVIATIONS

LDA Laser Doppler anemometry  
LIQ Liquid  
PLIF Planar laser-induced Fluorescence  
RZ Recirculation zone  
SP Stagnation point  
TKE Turbulent kinetic energy  
URANS Unsteady Reynolds-averaged Navier-Stokes

#### Archer and Gupta [5] (Figure 36):

##### NOMENCLATURE

Greek characters:

$\rho$  Density

Latin characters:

d Diameter  
k Turbulent kinetic energy  
r Radius  
Sn Swirl number  
U Radial velocity  
u Axial velocity  
V Axial velocity  
W Tangential velocity  
w Tangential velocity

Subscripts:

<sub>rms</sub> Root-mean-squared

#### ABBREVIATIONS

3D Three-dimensional  
PIV Particle image velocimetry  
TKE Turbulent kinetic energy

#### Vakil and Thole [4] (Figure 37 to Figure 41):

##### NOMENCLATURE

Greek characters:

$\theta$  Non-dimensional temperature



Latin characters:

H	Height
L	Combustor length
T	Temperature
u	Axial velocity
w	Spanwise/tangential velocity
X	Axial distance
Z	Height/radial distance

Subscripts:

$\infty$	Free-stream conditions (primary flow)
c	Referring to the coolant condition (secondary flow)
in	Referring to the inlet

ABBREVIATIONS

LDV	Laser Doppler velocimetry
p	Plane perpendicular to the flow
s	Plane parallel to the flow

**Weigand *et al.* [13] (Figure 42 to Figure 47):**

NOMENCLATURE

Greek characters:

$\phi$	Diameter or equivalence ratio
--------	-------------------------------

Latin characters:

h	Height
p	Pressure
u	Axial velocity
w	Tangential velocity

Subscripts:

mean	Mean value
------	------------

ABBREVIATIONS

2D	Two-dimensional
AFR	Air/Fuel ratio
LDV	Laser Doppler velocimetry
OH*	Hydroxide radical
ph	Phase
phi	Equivalence ratio



## APPENDIX B: AIR MASS FLOW RATE

### NOMENCLATURE

Technical characters:

$\dot{m}$  Mass flow rate

Greek characters:

$\beta$  Diameter ratio

$\varepsilon$  Expansibility factor

$\kappa$  Isentropic exponent

$\mu$  Dynamic viscosity

$\rho$  Density

$\Delta$  Change in a value

Latin characters:

A Cross-sectional area

C Discharge coefficient

D Pipe diameter

d Orifice plate throat diameter

E Velocity of approach factor

k Uniform equivalent roughness

L Relative pressure tapping spacing

l Distance of pressure tapping from orifice plate surface

P Total pressure

p Static pressure

Q Volume flow rate

R Gas constant

S Sutherland constant

T Temperature

V Axial velocity

Superscripts:

' Referring to spacing w.r.t the downstream surface (no ' refers to spacing w.r.t the upstream surface)

Subscripts:

<sub>0</sub> Reference value or total value

<sub>1</sub> Referring to upstream of the orifice plate



2	Referring to downstream of the orifice plate at the vena contracta
A	Referring to air
atm	Referring to atmospheric values
O	Referring to the orifice plate
t	Referring to the throat of the orifice plate

## ABBREVIATIONS

EGL	Energy grade line
HGL	Hydraulic grade line

### B.1 Orifice plate theory

The orifice plate is a head loss flow measurement device. The method used is to obstruct the fluid flow causing a pressure drop, which is a measure of flux. There are two types of head loss devices, the Bernoulli-type device and the friction-loss device. An orifice plate is part of the former type.

Referring to Figure B.1, and using the continuity and Bernoulli equations below, the derivation of the equation used for calculating the mass flow rate from the pressure drop over an orifice plate will be shown.

Continuity: 
$$Q = \frac{\pi}{4} D^2 V_1 = \frac{\pi}{4} D_2^2 V_2 \quad \text{B-1}$$

Bernoulli: 
$$P_0 = p_1 + \frac{1}{2} \rho V_1^2 = p_2 + \frac{1}{2} \rho V_2^2 \quad \text{B-2}$$

The assumptions made are that the flow involved is incompressible, steady and frictionless.

Rearrange the continuity equation and writing  $V_1$  as a function of  $V_2$  gives

$$V_1 = \frac{D_2^2}{D^2} V_2 \quad \text{B-3}$$

Substituting **B-3** into **B-2** and rearranging into a function with  $V_2$  as the independent variable gives

$$\frac{Q}{A_2} = V_2 \approx \sqrt{\frac{2(p_1 - p_2)}{\rho \left(1 - \frac{D_2^4}{D^4}\right)}} \quad \text{B-4}$$

Making a further assumption that  $D_2 \approx d$  thus  $\frac{D_2}{D} \approx \frac{d}{D} = \beta$  and thus  $A_2 \approx A_t$ , where  $A_t$  is the throat area; and calibrate the orifice plate thus giving a loss compensation using a discharge coefficient. Thus

$$Q = A_t V_t = C A_t V_2 = C A_t \sqrt{\frac{2(p_1 - p_2)}{\rho(1 - \beta^4)}} \quad \text{B-5}$$

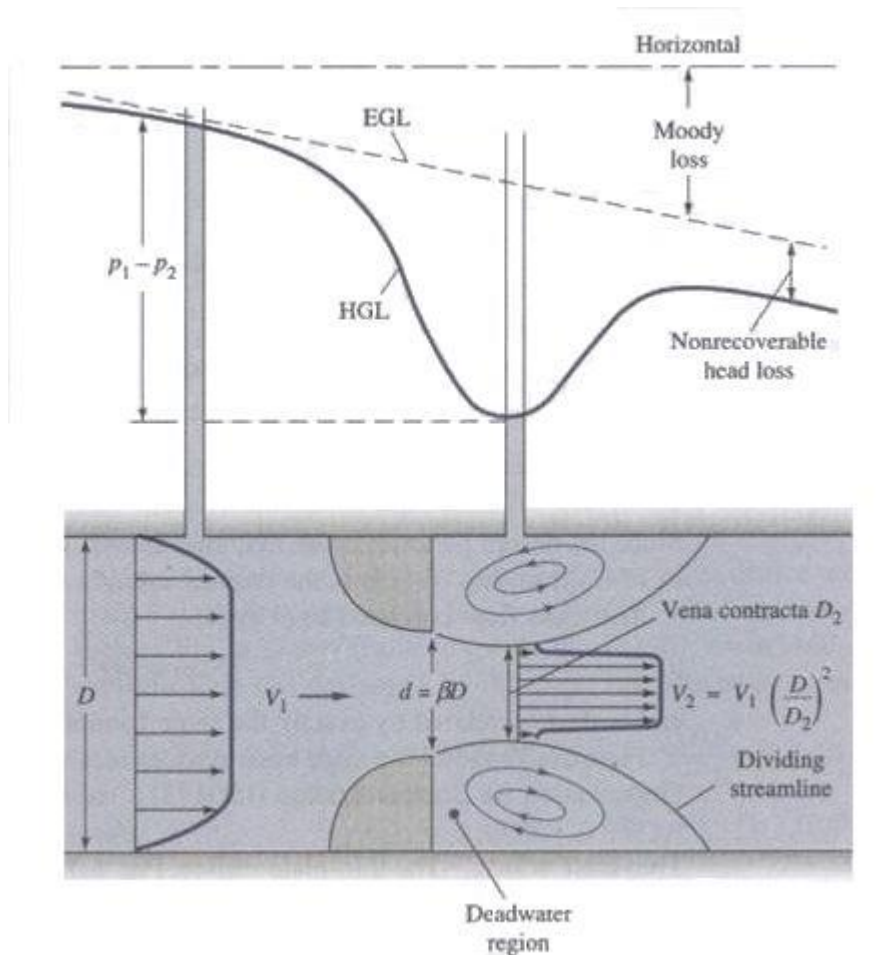


**Figure B.1: A generalised Bernoulli obstruction meter [B.1]**

The velocity of approach factor simplifies the mass flow rate equation under the square root. The velocity of approach factor is defined as follows:

$$E = \frac{1}{\sqrt{1 - \beta^4}} \quad \text{[B-6]}$$

Using the definition for the velocity of approach factor,  $E$ , in equation [B-5] above,

$$Q = CE A_t \sqrt{\frac{2(p_1 - p_2)}{\rho}} \quad \text{[B-7]}$$

and since

$$\dot{m} = \rho Q \quad \text{[B-8]}$$

$$\therefore \dot{m} = CE \frac{\pi}{4} d^2 \sqrt{2\rho \Delta p_0} \quad \text{[B-9]}$$

The discharge coefficient,  $C$ , is obtained from curve fit formulae, created from experimental data, performed by various standards institutes. The value for  $C$  is usually a little less than 0.6 for thin orifice plates [B.1].



In addition, in order to make equation [B-9] applicable to compressible flows and thus more realistic, a further factor can be multiplied called the expansibility factor,  $\varepsilon$ . If the fluid is incompressible, then  $\varepsilon = 1$ . The expansibility factor is calculated using the following equation:

$$\varepsilon = 1 - [0.41 + 0.35\beta^4] \times \left[ \frac{\Delta p_o}{\kappa(P_{atm} + \Delta p_o)} \right] \quad \text{[B-10]}$$

The empirical formula given in equation [B-10] above was calculated by the British Standards Institution from experimental data for use with equation [B-9]. If the expansibility factor is included, then the mass flow rate can be calculated using the following equation:

$$\dot{m} = CE\varepsilon \frac{\pi}{4} d^2 \sqrt{2\rho\Delta p_o} \quad \text{[B-11]}$$

In order to calculate the air mass flow rate, the British Standard [B.2] for the measurement of fluid flow in closed conduits was used.

In order to use this calculation method, the following variables were measured:

- Atmospheric temperature [ $T_{atm}$ ]
- Atmospheric pressure [ $P_{atm}$ ]
- Upstream orifice plate temperature [ $T_1$ ]
- Upstream orifice plate pressure [ $p_1$ ]
- Pressure drop over orifice plate [ $\Delta p_o$ ]
- Orifice diameter [ $d$ ]
- Pipe diameter [ $D$ ]

To check the applicability of the standard, the following aspects should be noted:

- Pressure tapping method
- Uniform equivalent roughness [ $k$ ]
- Relative roughness  $\left[ \frac{k}{D} \right]$
- Orifice pressure ratio  $\left[ \frac{p_2}{p_1} \right]$

Three pressure-tapping methods for orifice plates are covered in this standard, namely corner taps, flange taps and  $D$  and  $\frac{D}{2}$  pipe taps. For the experiment in this dissertation, the  $D$  and  $\frac{D}{2}$  pipe taps were used.

The uniform equivalent roughness is dependent on the type and condition of the piping used. The appropriate values for some example types are given in Table 6 of the British Standard [B.2]. For this experiment, new steel pipes that are welded longitudinally were used.

The relative roughness of the pipe section is an indication of the range of conduit types to which the British Standard applies. For the standard to apply, with the  $D$  and  $\frac{D}{2}$  pipe taps, then the relative roughness  $\frac{k}{D} \leq 10e^{-4}$ .

The orifice pressure ratio is used to determine the applicability of the expansibility factor equation used in this standard. For the expansibility factor equation to apply, the orifice pressure ratio of the orifice plate should be  $\geq 0.75$ .

Constants [B.3] required for the mass flow rate calculation were:

- Isentropic exponent [ $\kappa$ ]
- Gas constant for air [ $R$ ]
- Relative upstream pressure tapping spacing [ $L_1$ ]
- Relative downstream pressure tapping spacing [ $L'_2$ ]

$L_1$  is the relative upstream pressure tapping spacing used in the Stolz equation (equation [B-17]). It is the ratio of the distance of the upstream tapping from the upstream face of the orifice plate and the pipe diameter. It is given by

$$L_1 = \frac{l_1}{D} \quad \text{[B-12]}$$

The relative downstream pressure tapping spacing  $L'_2$  is the ratio of the distance of the downstream pressure tapping from the downstream orifice plate face to the pipe diameter. The apostrophe indicates that the distance was calculated from the downstream orifice plate surface. A lack of apostrophe indicates distances calculated from the upstream orifice plate surface.  $L'_2$  can be calculated using the following equation:

$$L'_2 = \frac{l'_2}{D} \quad \text{[B-13]}$$

Thus for  $D$  and  $\frac{D}{2}$  pipe taps,  $L_1 = 1$  and  $L'_2 = 0.47$ , however, according to the British Standard [B.2], if  $L_1 \geq 0.4333$  then  $L_1 = 0.039$ .

The following inputs were calculated before the mass flow rate calculation could commence:

- Upstream orifice plate density [ $\rho_1$ ]
- Upstream orifice plate dynamic viscosity [ $\mu_1$ ]
- Diameter ratio [ $\beta$ ]
- Expansibility factor [ $\varepsilon$ ]
- Velocity of approach factor [ $E$ ]

The method used to calculate  $\rho_1$  was to apply the ideal gas law from Sonntag *et al.* [B.3].

$$\rho_1 = \frac{p_1}{RT_1} \quad \text{[B-14]}$$

The Sutherland law [B.1] was used to calculate the dynamic viscosity  $\mu_1$ :

$$\frac{\mu_1}{\mu_0} = \left(\frac{T_1}{T_0}\right)^{3/2} \left(\frac{T_0 + S}{T_1 + S}\right) \quad \text{[B-15]}$$

$$\text{where } S_A \approx 110.4 \text{ K}$$

$$\mu_0 = 1.71e^{-5} \text{ kg/(ms)}$$

$$T_0 = 273.15 \text{ K}$$

The diameter ratio, which is used to calculate a number of other factors, is given by:



$$\beta = \frac{d}{D} \quad \text{[B-16]}$$

The discharge coefficient can be calculated using Stolz' equation below:

$$C = 0.5959 + 0.0312\beta^{2.1} - 0.184\beta^8 + [0.0029\beta^{2.5}] \left[ \left( \frac{\mu_1 \times 10^6}{V_1 D \rho_1} \right)^{0.75} \right] + \frac{L_1 \times 0.09 \times \beta^4}{1 - \beta^4} - 0.0337L_2' \beta^3 \quad \text{[B-17]}$$

Using the experimental results as inputs, the air flow rate can be solved iteratively using Stolz' equation and the flow rate equations [B-11] and [B-8] in the following formats:

$$\dot{m}_A = CE\varepsilon \frac{\pi}{4} d^2 \sqrt{2\rho_1 \Delta p_0} \quad \text{[B-18]}$$

and

$$\dot{m}_A = \rho_1 \frac{\pi}{4} D^2 V_1 \quad \text{[B-19]}$$

The iterative process involves the following steps:

1. Guess a value for  $V_1$
2. Calculate  $C$  using equation [B-17]
3. Calculate  $\dot{m}_A$  using equation [B-18]
4. Calculate a new  $V_1$  using equation [B-19]
5. Calculate new  $C$  using equation [B-17]
6. Calculate new  $\dot{m}_A$  using equation [B-18]
7. Repeat steps 4 to 6 until no change is observed in  $V_1$  and  $\dot{m}_A$

## REFERENCES

- [B.1] White, F.M., *Fluid Mechanics*, 4th ed., McGraw-Hill Companies, Inc., Singapore, 1999.
- [B.2] British Standards Institution, "Measurement of Fluid Flow in Closed Conduits; Part 1. Pressure Differential Devices; Section 1.1 Specification for Square-edged Orifice Plates, Nozzles and Venturi Tubes Inserted in Circular Cross-section Conduits Running Full," 1981.
- [B.3] Sonntag, R.E., Borgnakke, C., Van Wylen, G.J., *Fundamentals of Thermodynamics*, 5th ed., John Wiley & Sons, Inc., United States of America, 1998.



## APPENDIX C: MANUFACTURING DRAWINGS

### NOMENCLATURE

Technical characters:

d11	A shaft tolerance type
f8	A shaft tolerance type
h8	A shaft tolerance type
H8	A hole tolerance type
H11	A hole tolerance type

Greek characters:

$\Phi$	Diameter
--------	----------

Latin characters:

M	Metric
R	Radius

### ABBREVIATIONS

CSIR	Council for scientific and industrial research
DPSS	Defence, peace, safety and security
F.C.	Final cut
MEng	Master of engineering
N.B.	Nota bene
No.	Number
NR	Number
PCD	Pitch centre diameter
R.C.	Rough cut
rpm	Revolutions per minute
SS	Stainless steel

## C.1 Gas turbine combustor test case

### C.1.1 Non-reacting experiment

The drawings in Figure C.1 to Figure C.9 are the drawings used up until the end of the polishing stage in the manufacturing process.

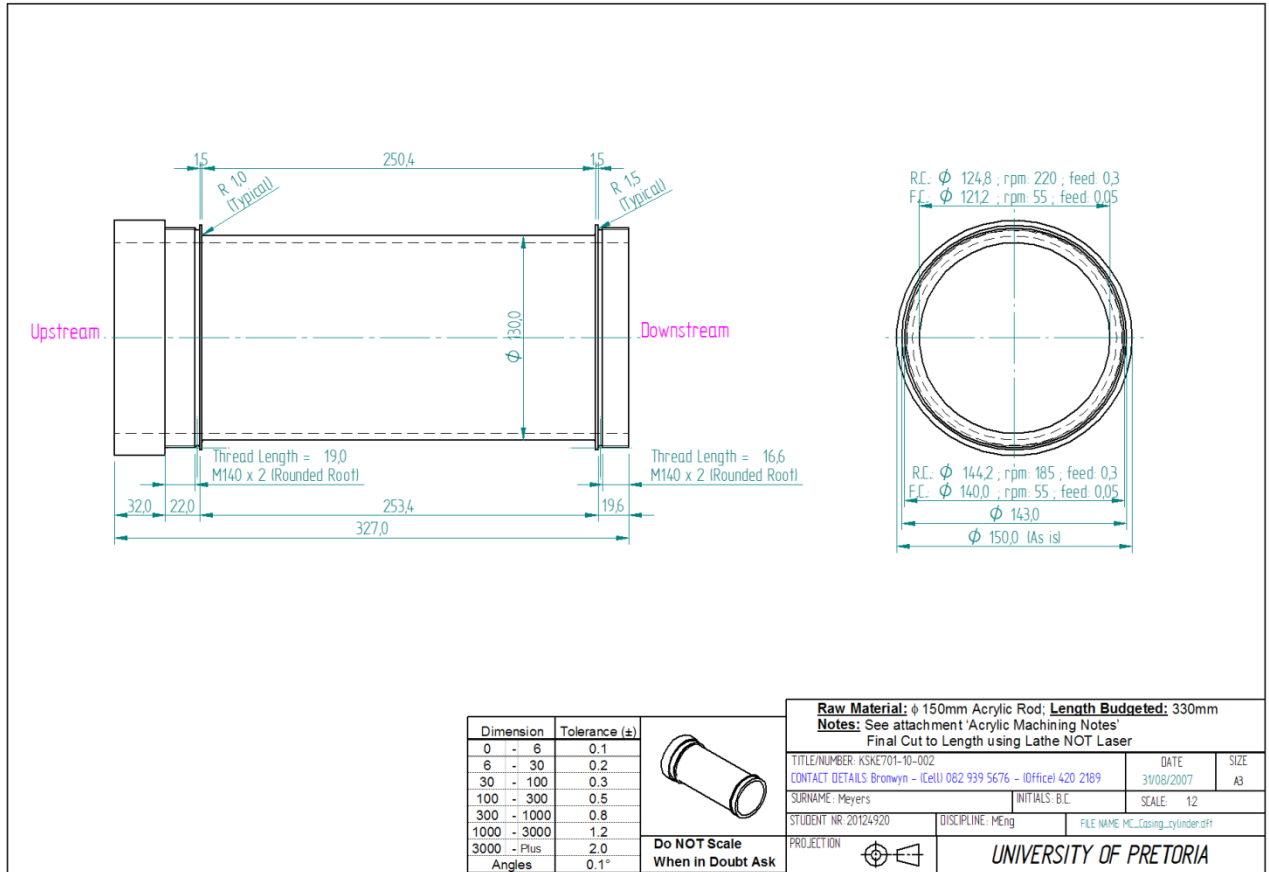


Figure C.1: The machining drawing of the casing

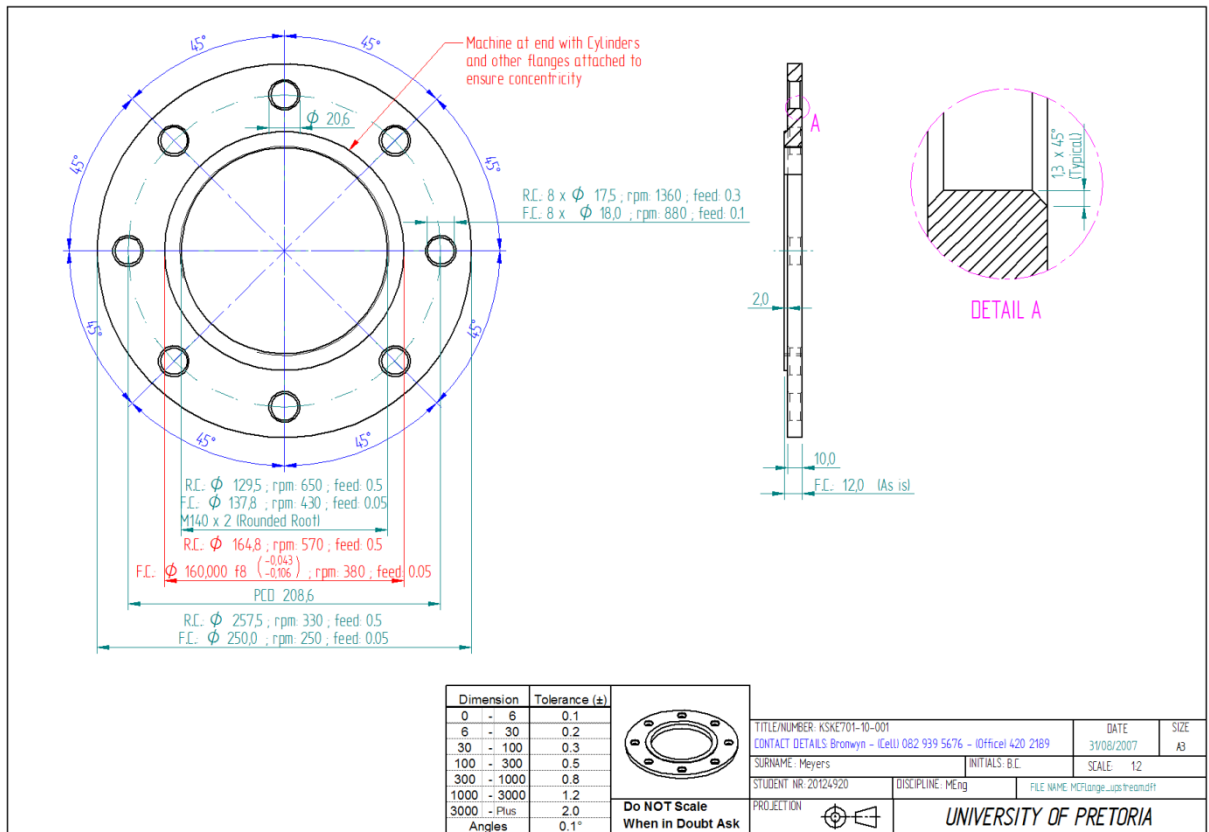


Figure C.2: The machining drawing of the upstream casing flange

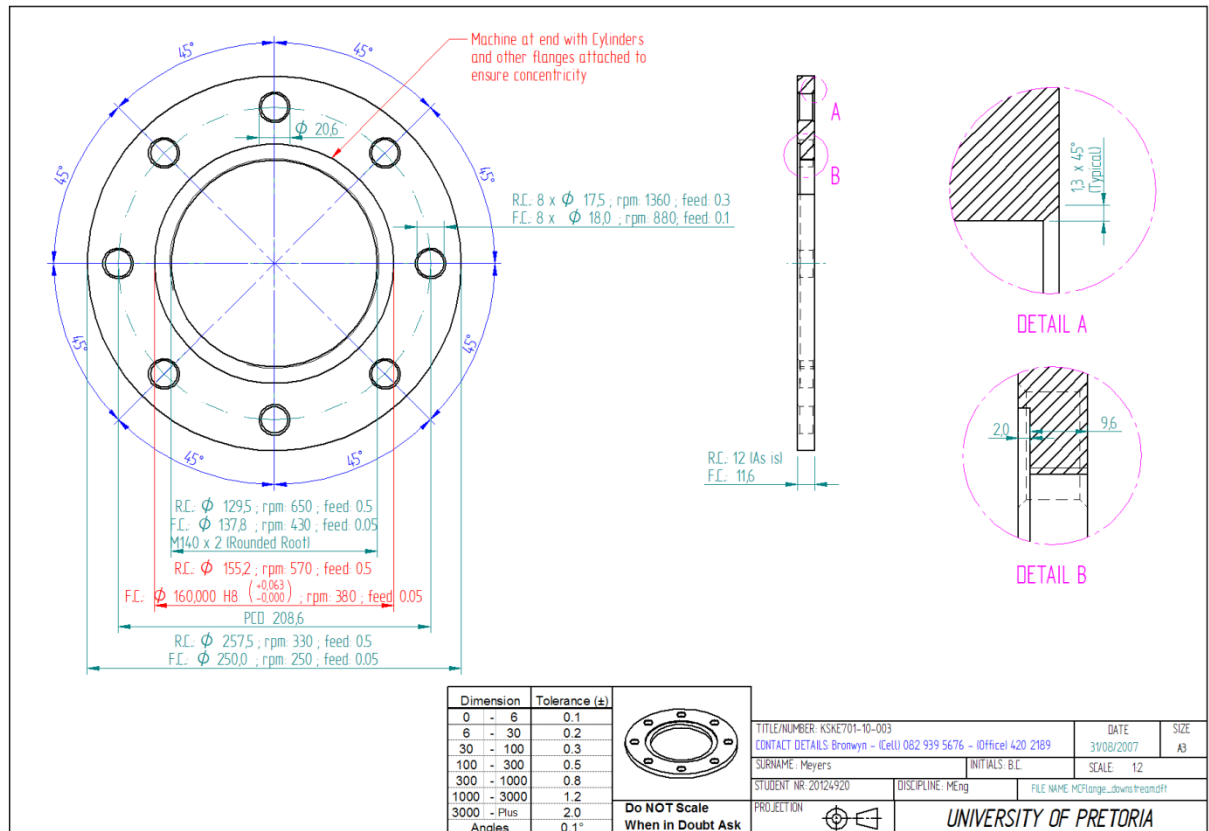


Figure C.3: The machining drawing of the downstream casing

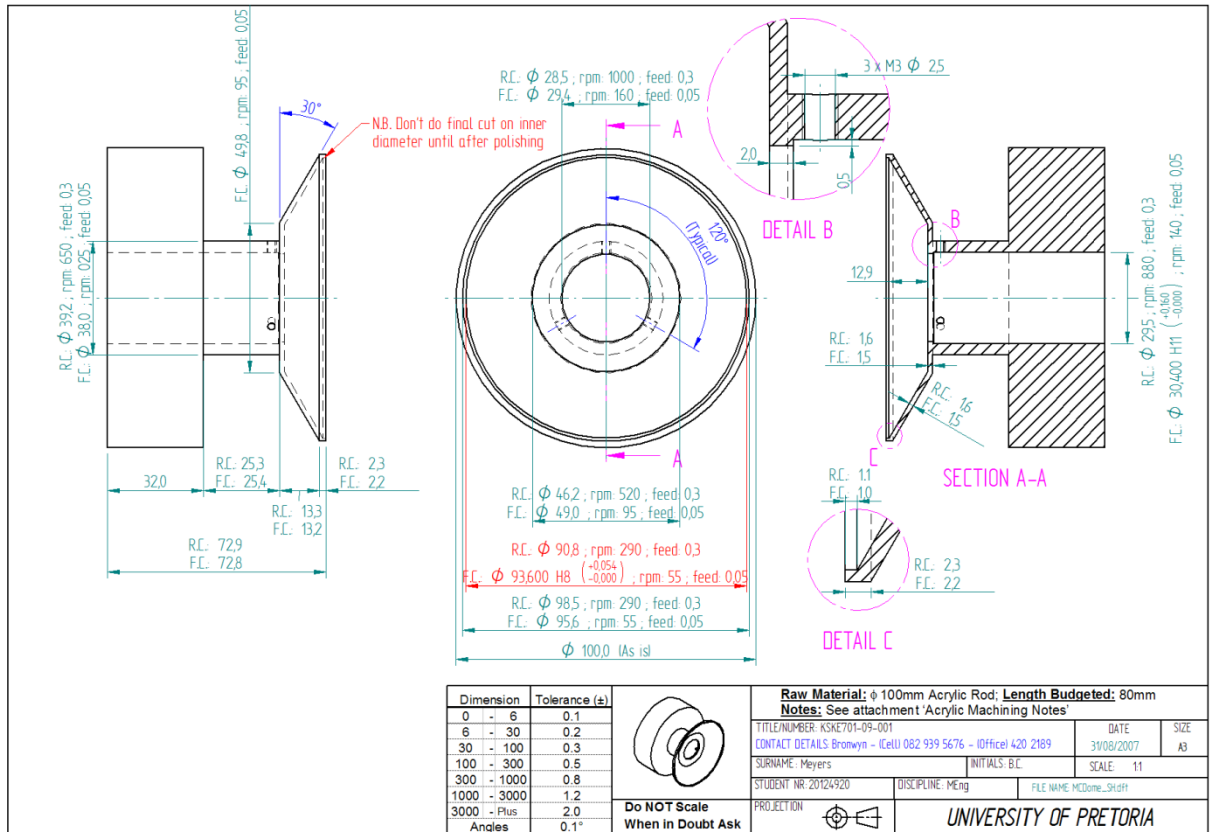


Figure C.4: The machining drawing of the combustor liner dome

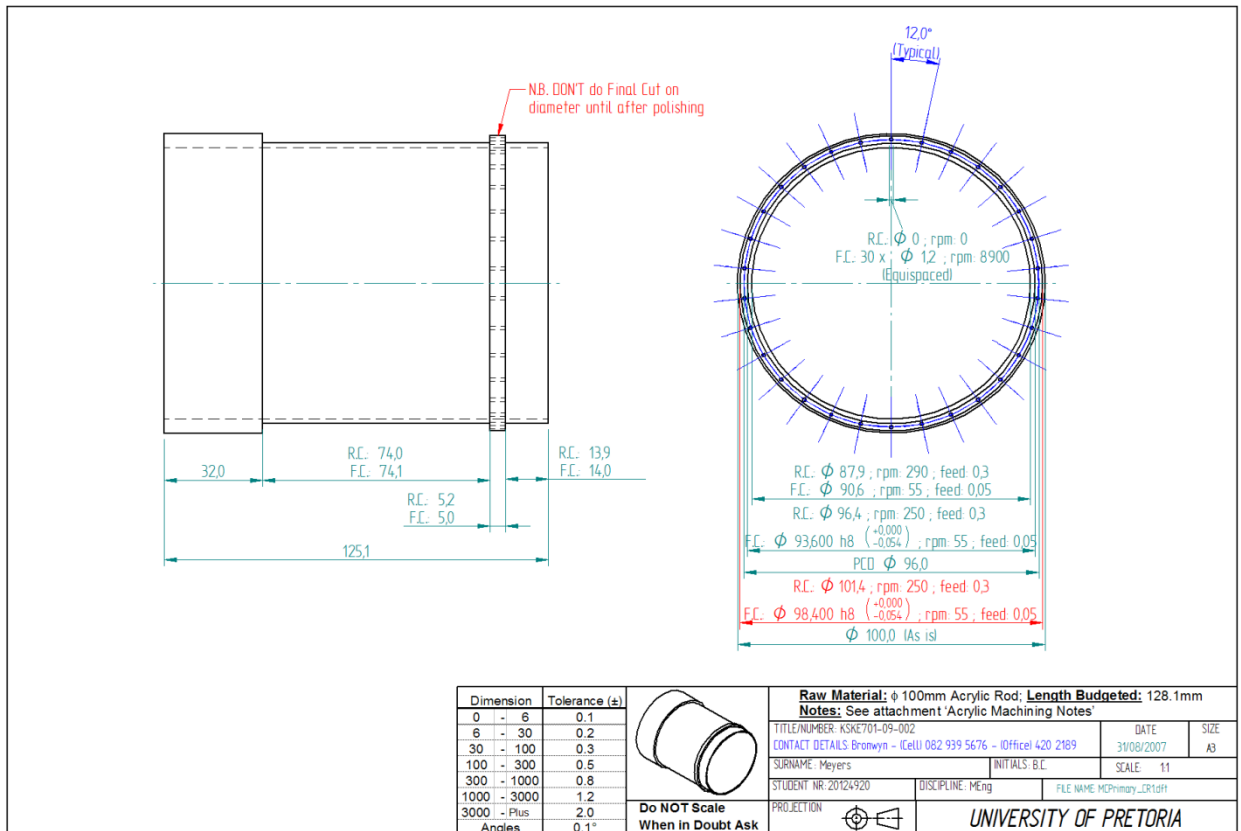


Figure C.5: The machining drawing of the combustor liner primary zone

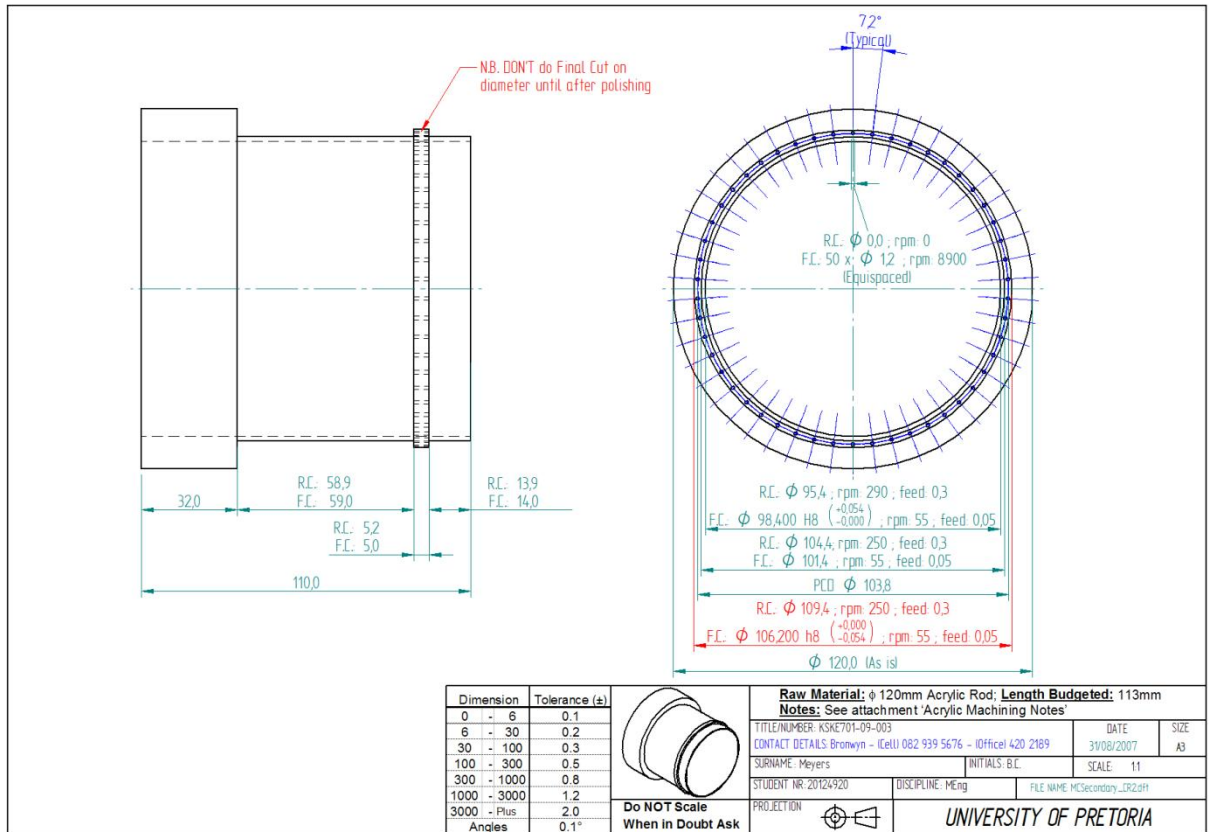


Figure C.6: The machining drawing of the combustor liner secondary zone

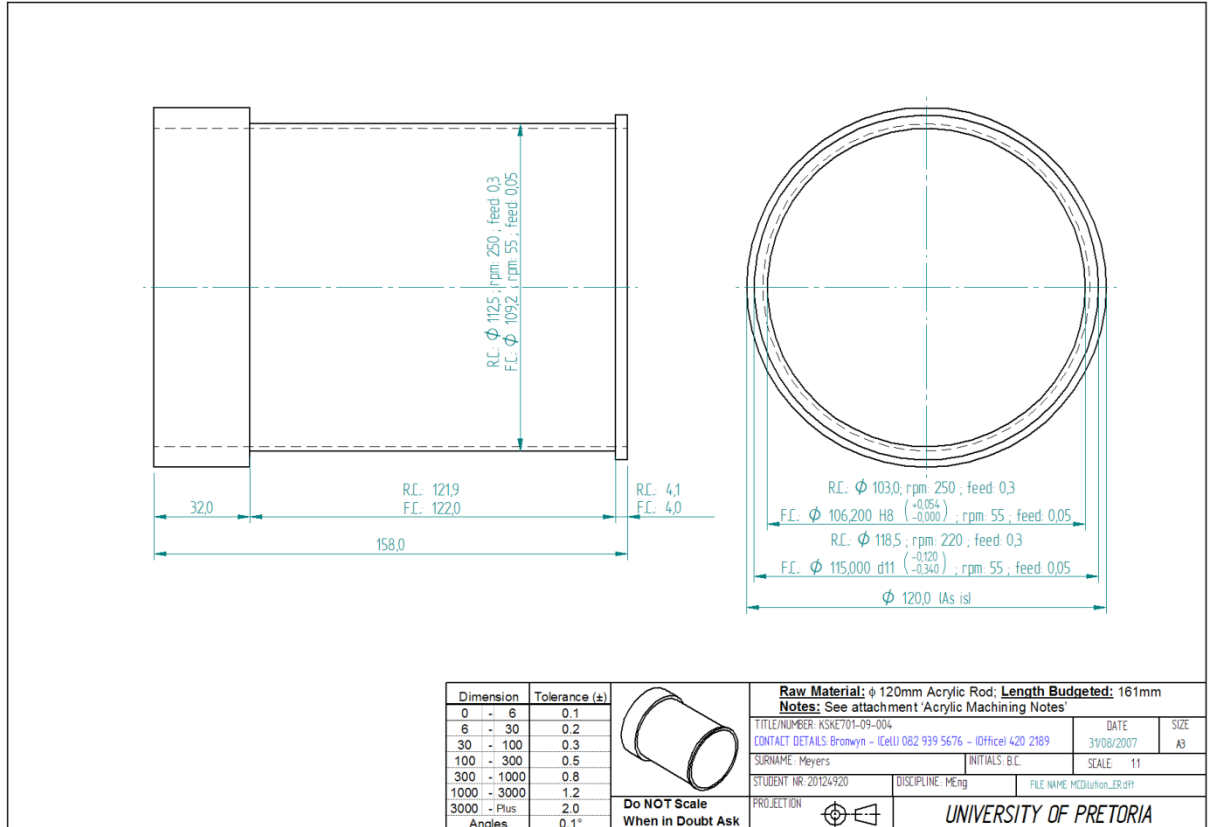


Figure C.7: The machining drawing of the combustor liner dilution zone

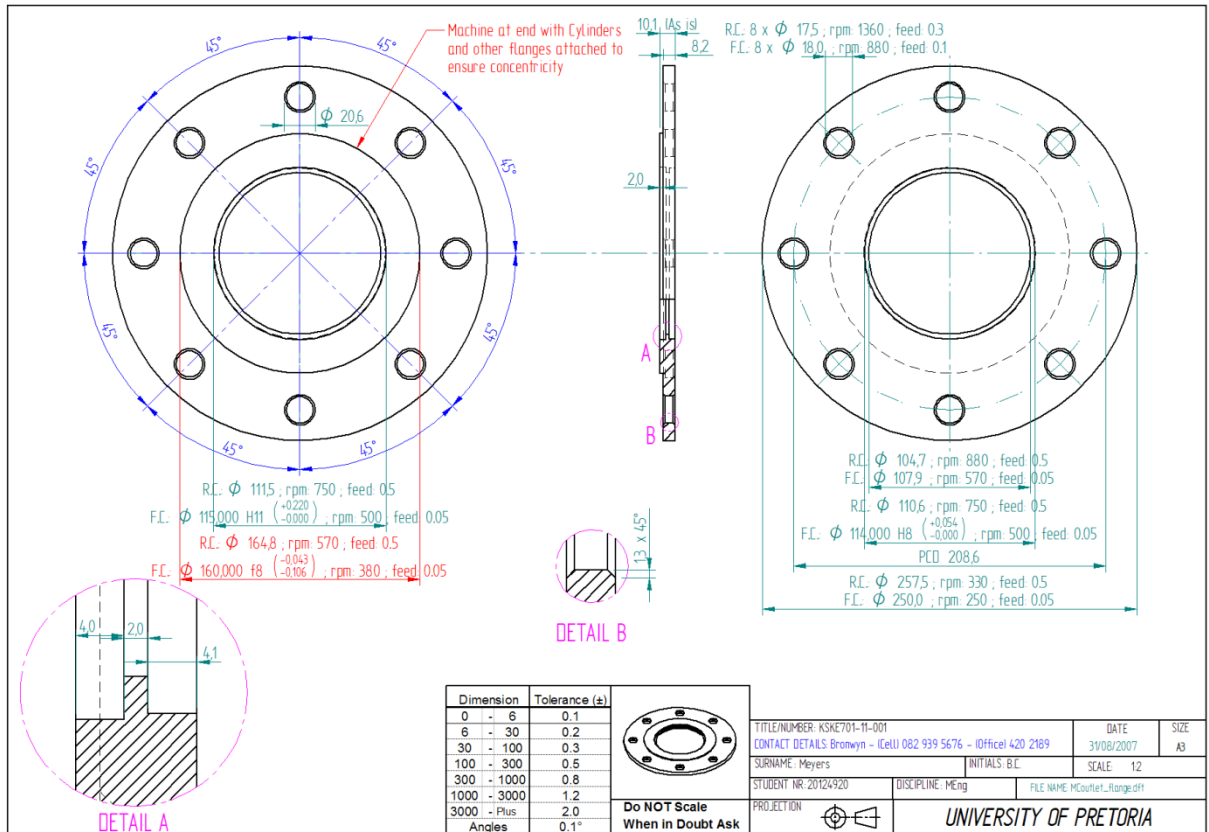


Figure C.8: The machining drawing of the outlet section flange

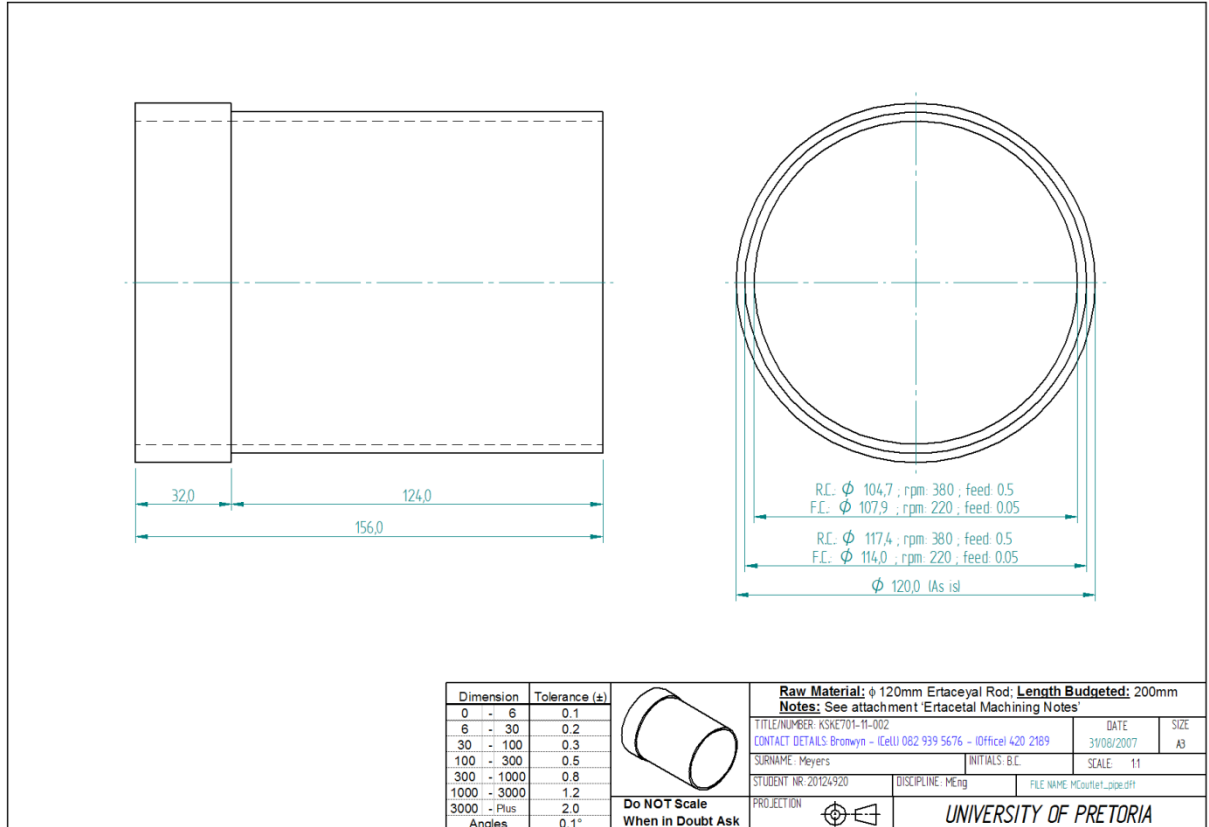


Figure C.9: The machining drawing of the outlet pipe

The drawings in Figure C.10 to Figure C.18 are of the assembly drawings and the part drawings of the parts that still needed to be laser cut after the manufacturing in the above drawings was completed.

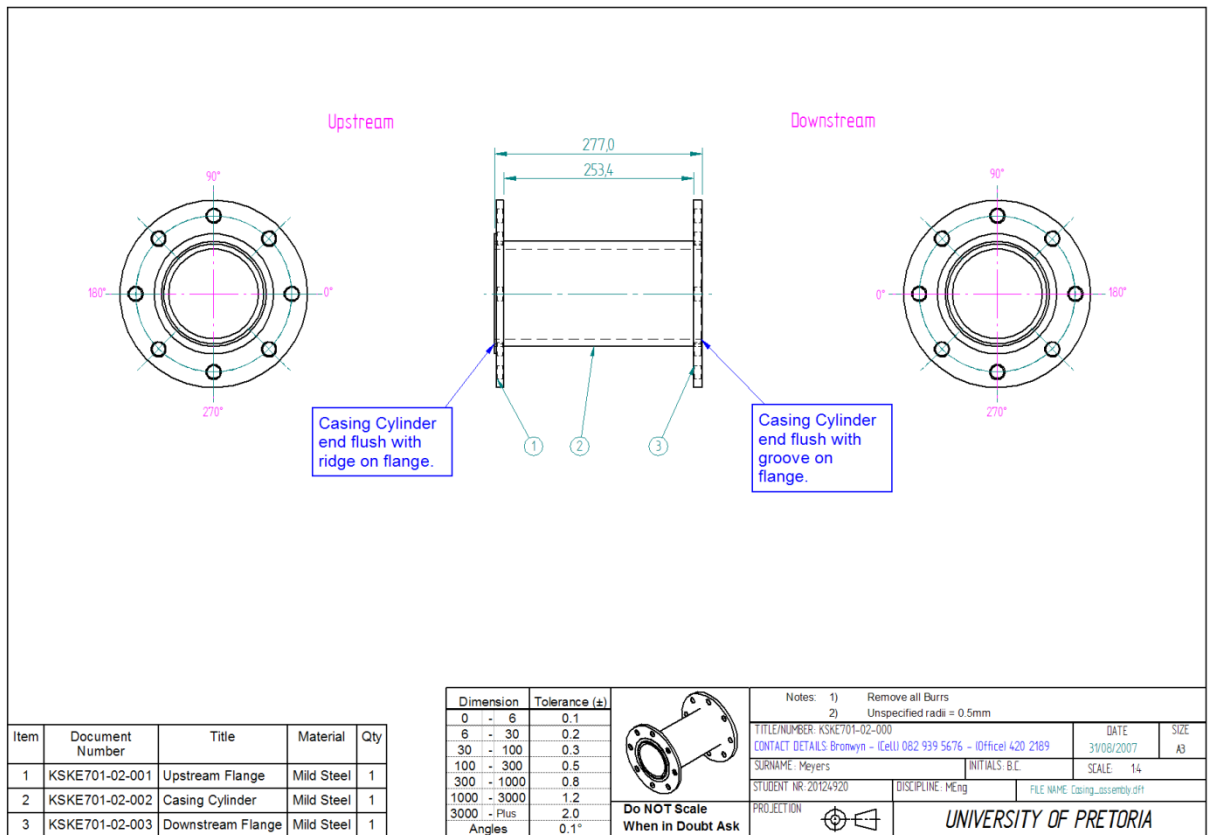


Figure C.10: The casing assembly drawing

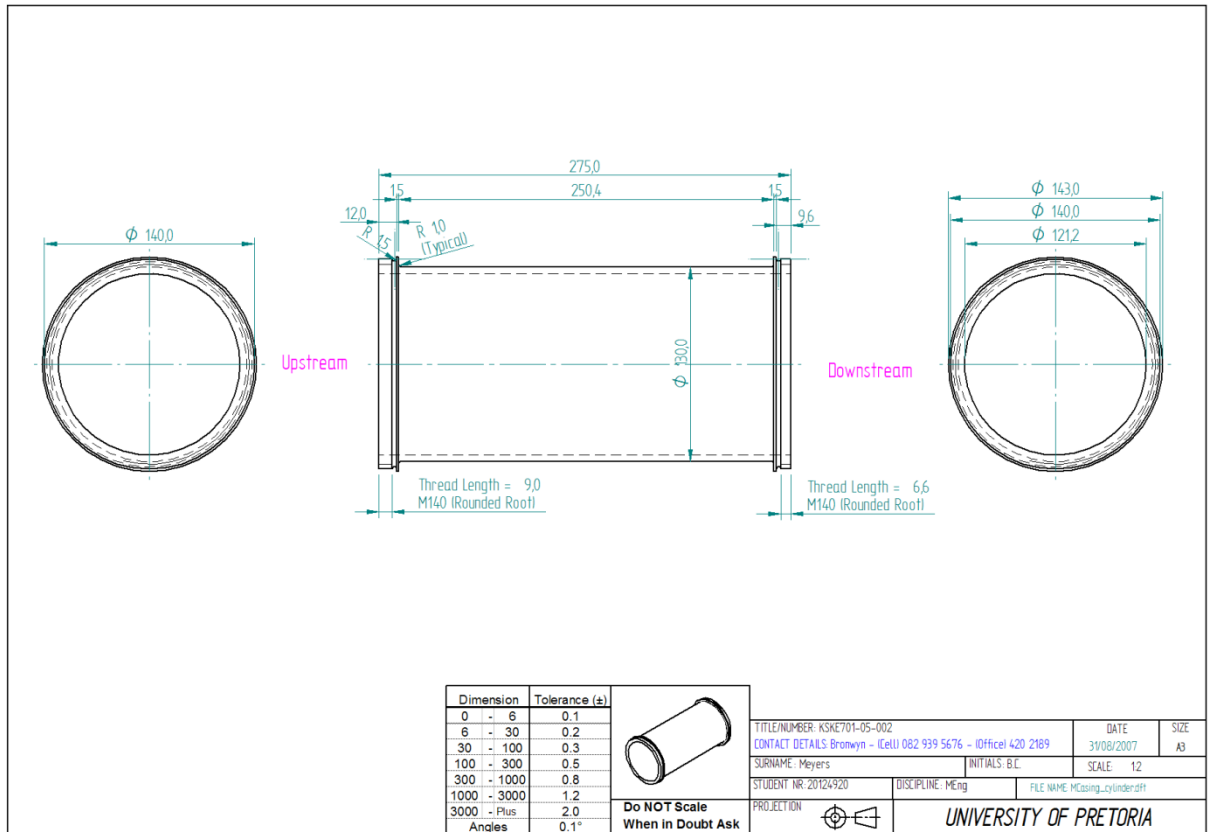


Figure C.11: The final casing tube after parting off

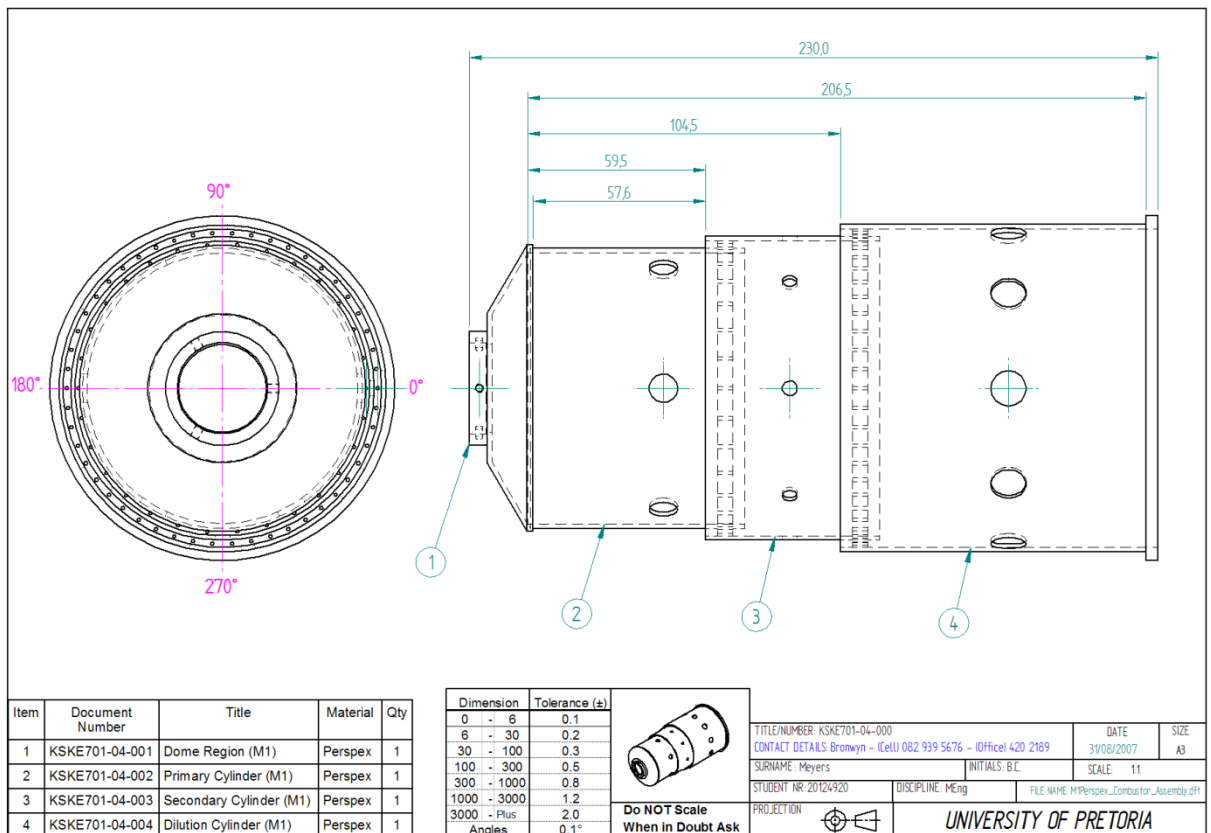


Figure C.12: The assembly drawing of the perspex combustor liner

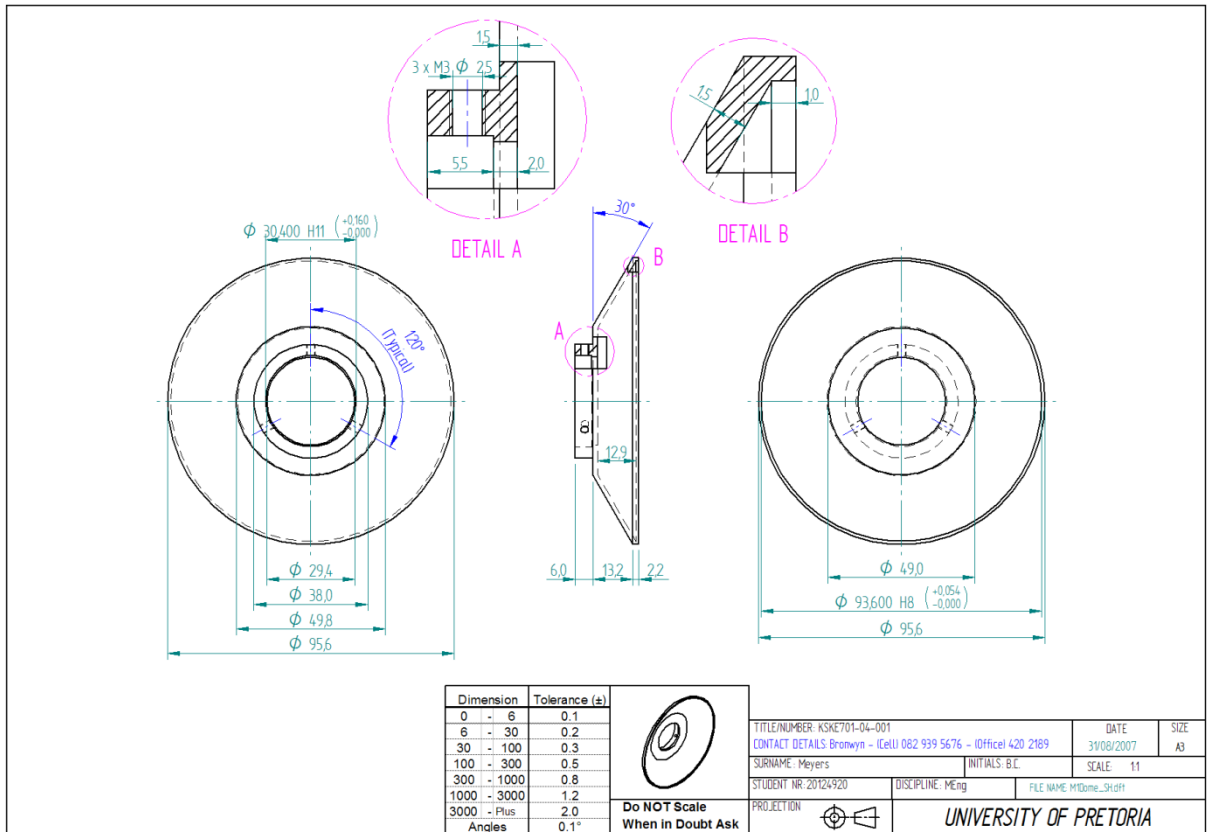


Figure C.13: The final combustor liner dome after parting off

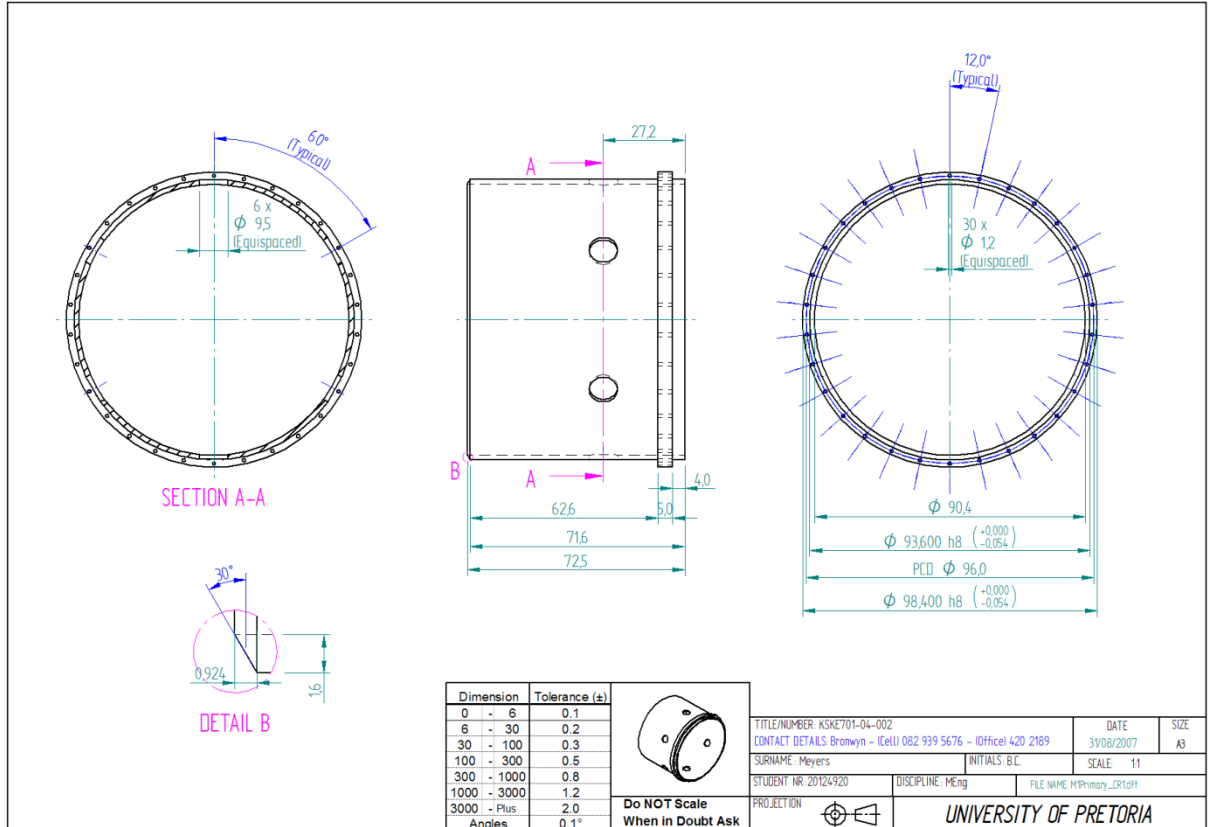


Figure C.14: The final combustor liner primary zone after parting off

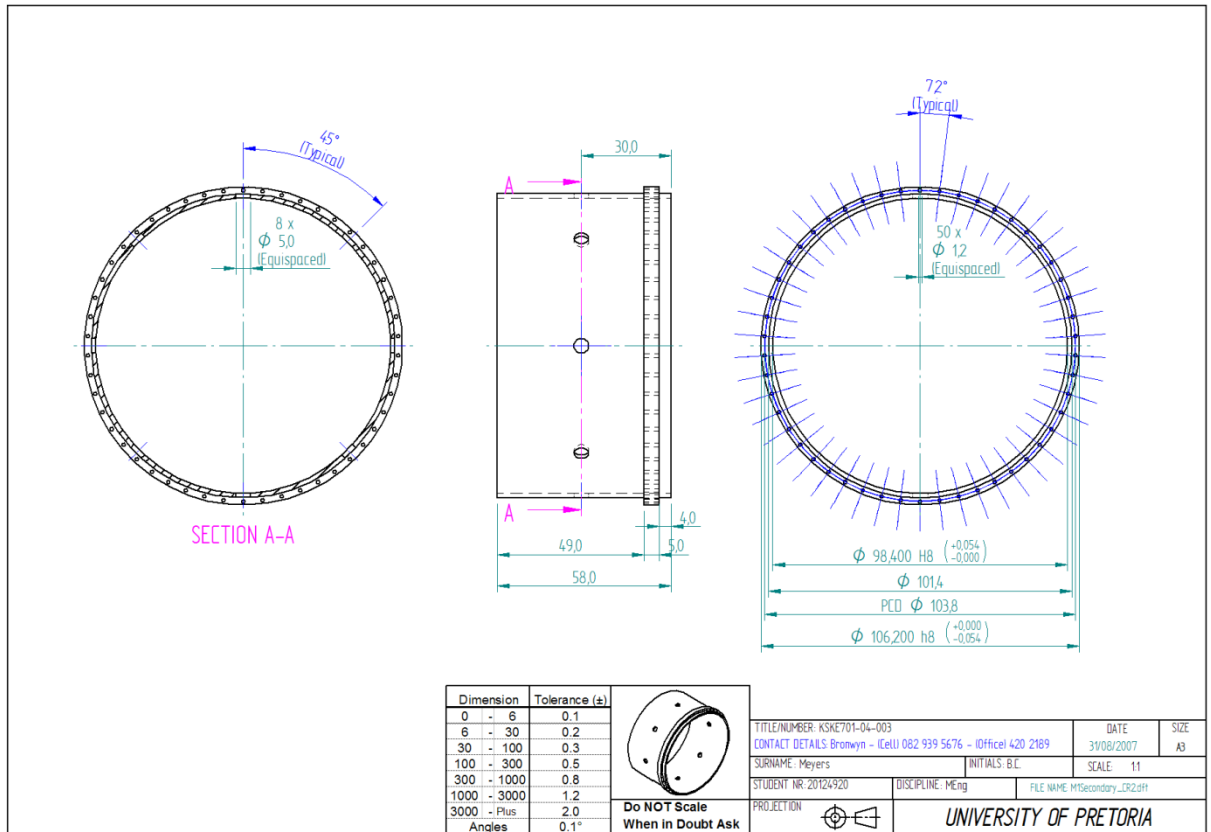


Figure C.15: The final combustor liner secondary zone after parting off

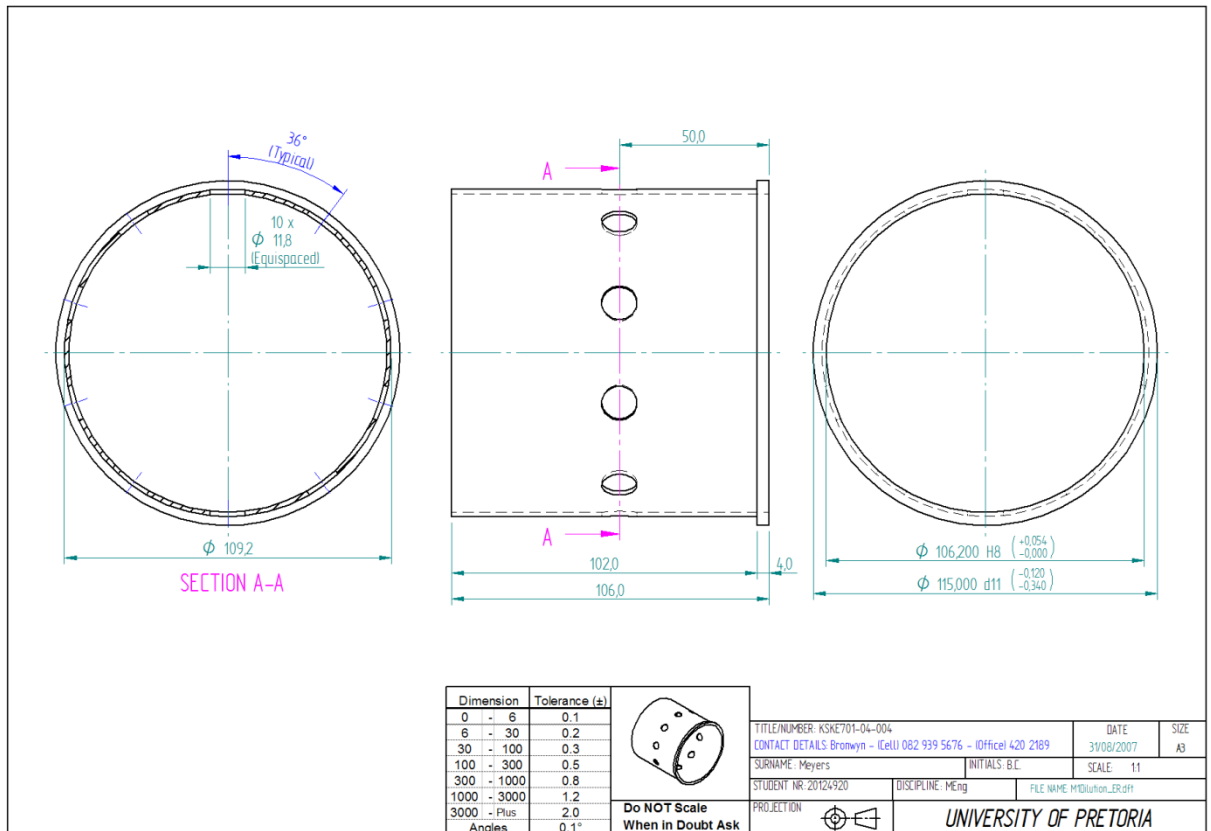


Figure C.16: The final combustor liner dilution zone after parting off

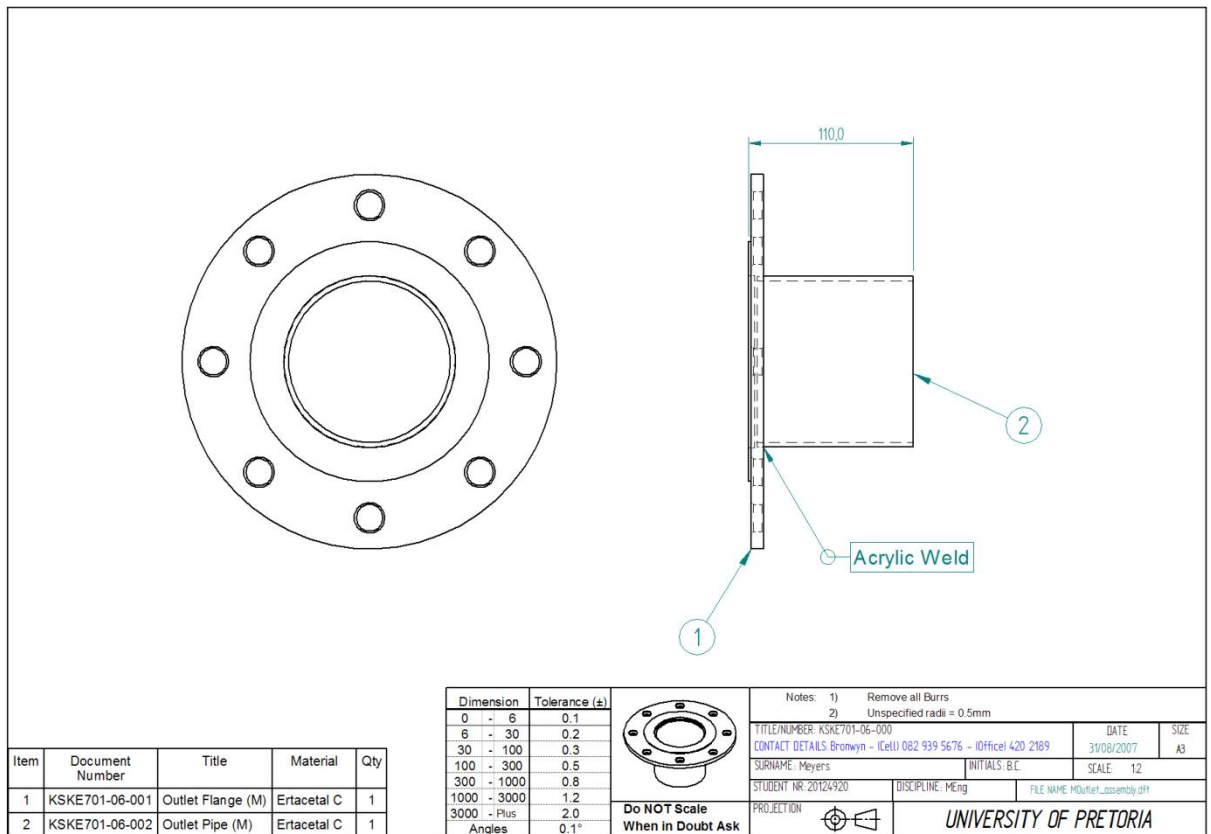


Figure C.17: The assembly drawing of the outlet section

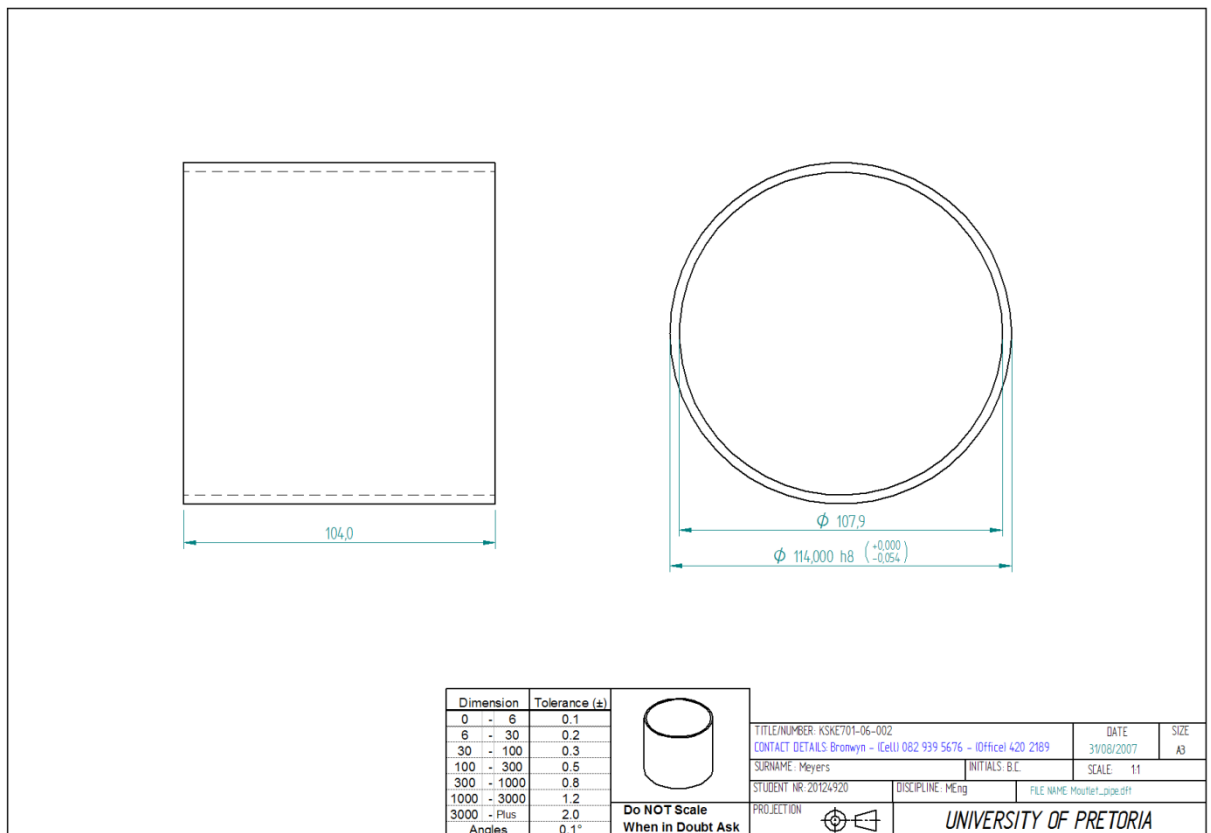


Figure C.18: The final outlet pipe after parting off

The next set of drawings (Figure C.19 to Figure C.21) is of the assembly and manufacturing drawing of the calibration target and mirror holder.

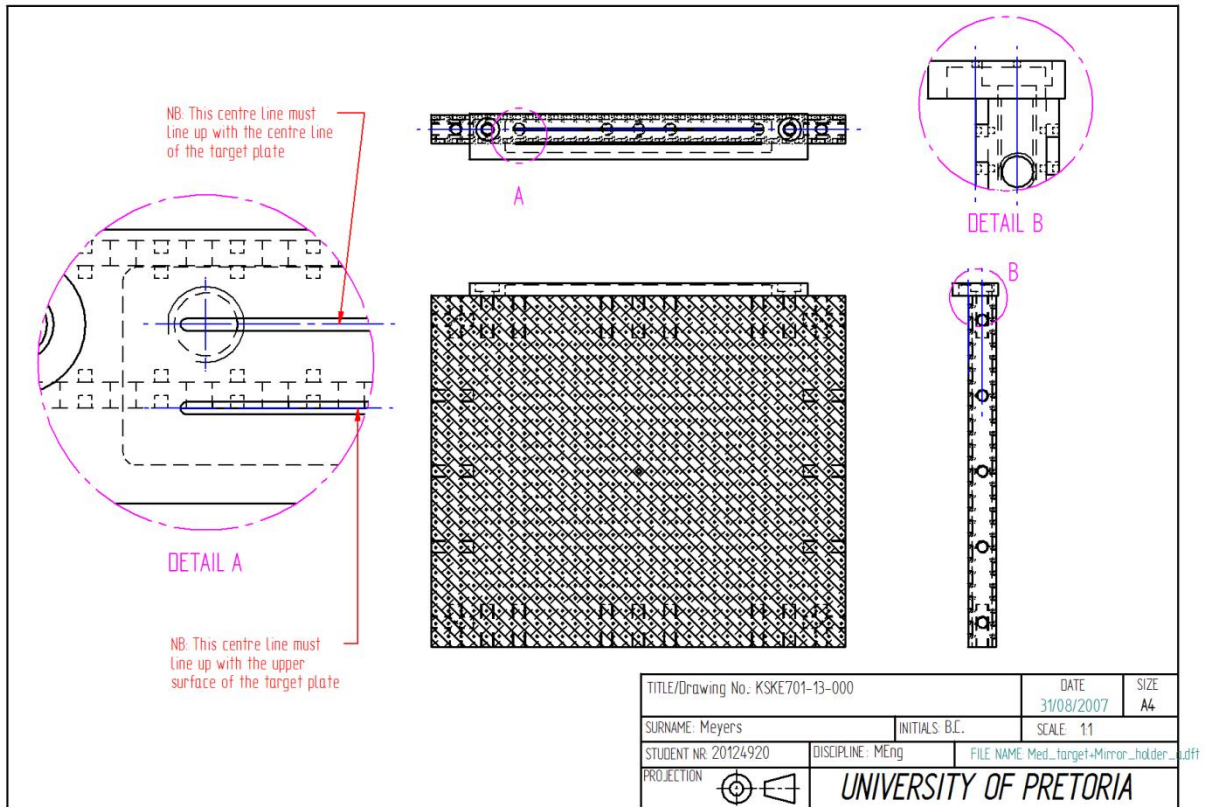


Figure C.19: The assembly drawing of the target and mirror holder

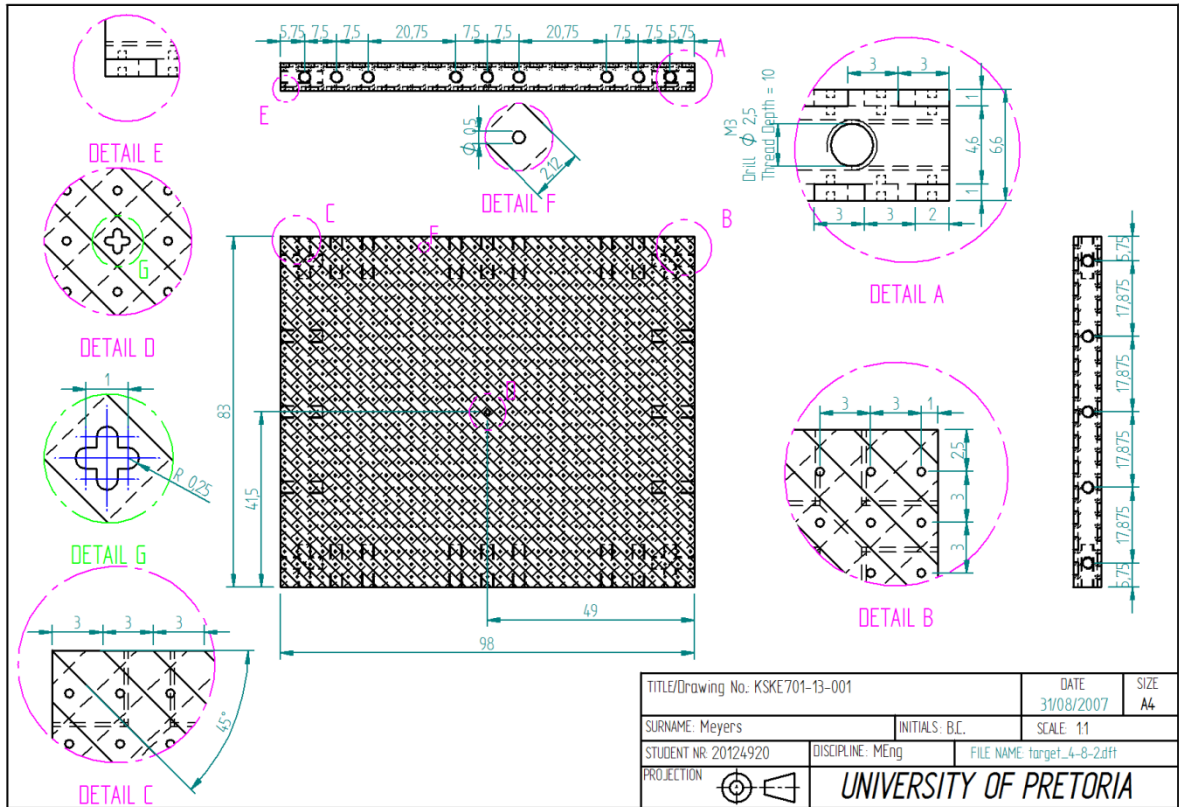


Figure C.20: Manufacturing drawing of the calibration target

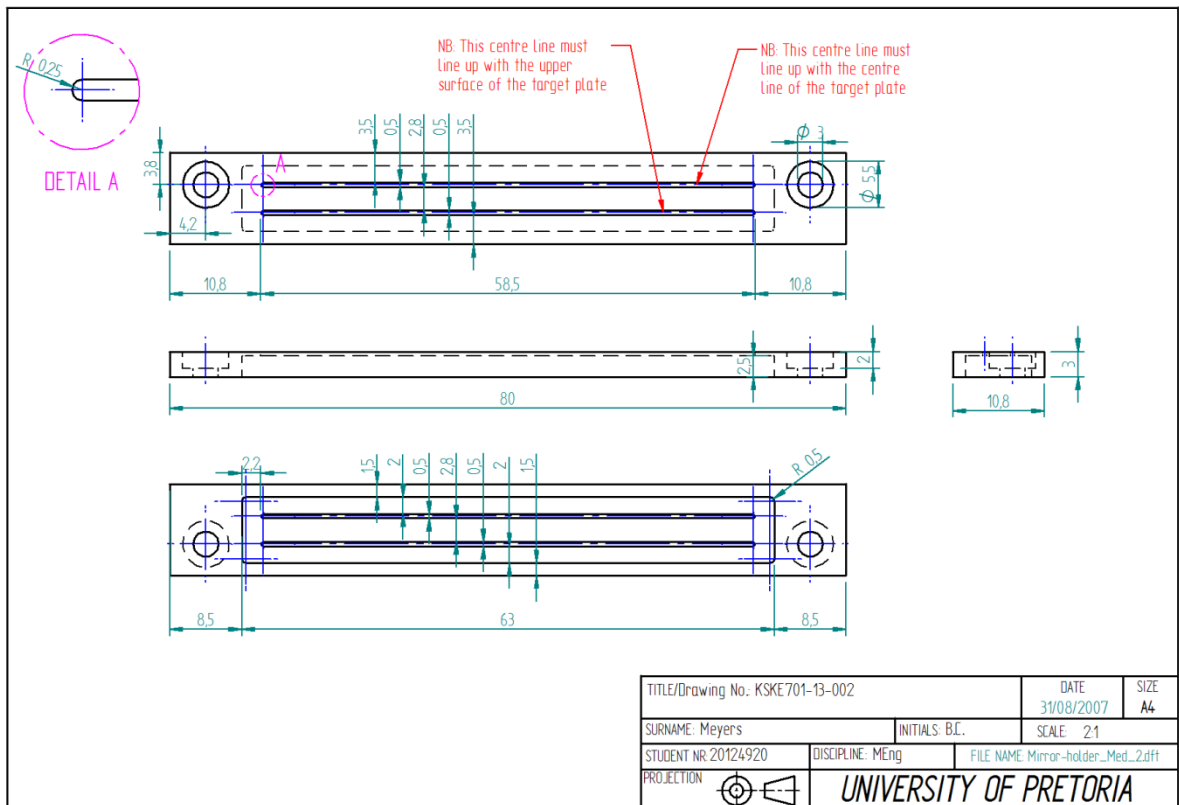


Figure C.21: Manufacturing drawing of the mirror holder

## C.2 Wedge ring tests

### C.2.1 Reacting experiment

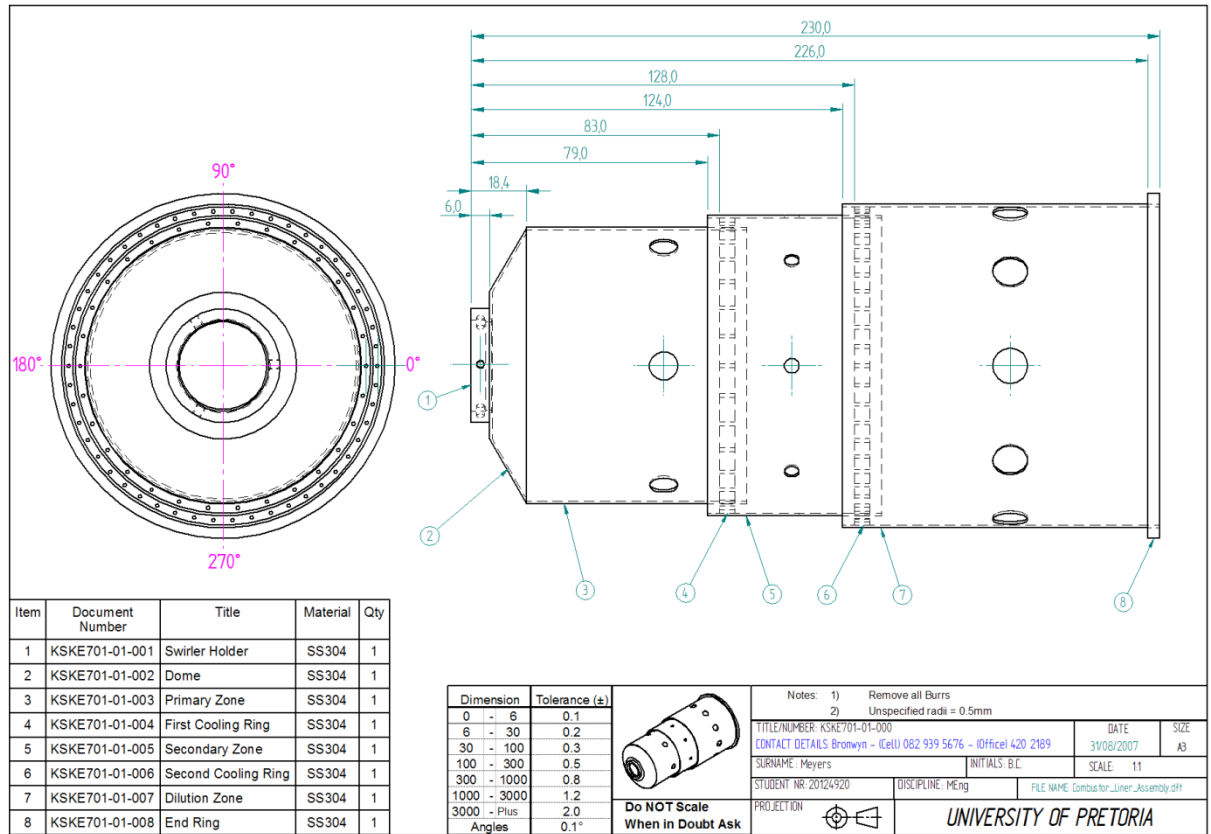


Figure C.22: Assembly drawing of the metal combustor liner

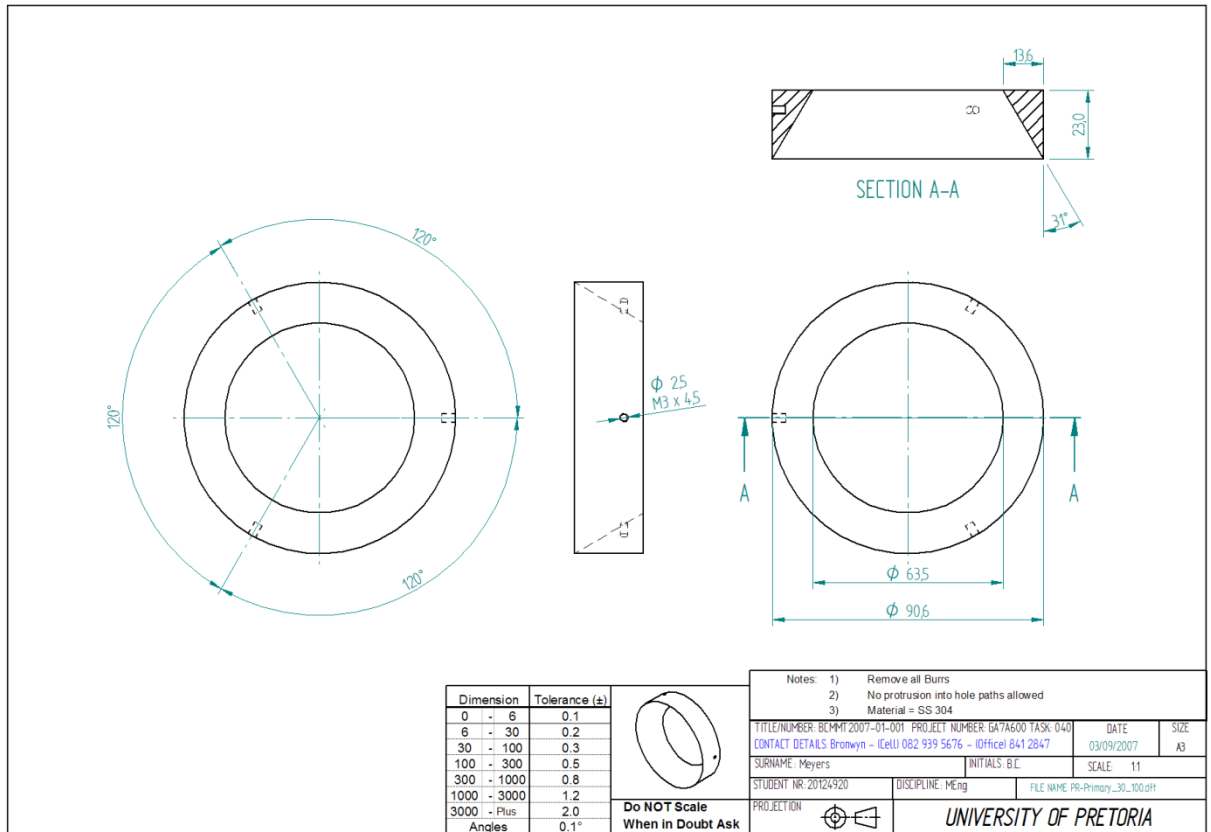


Figure C.23: The 30% primary wedge ring

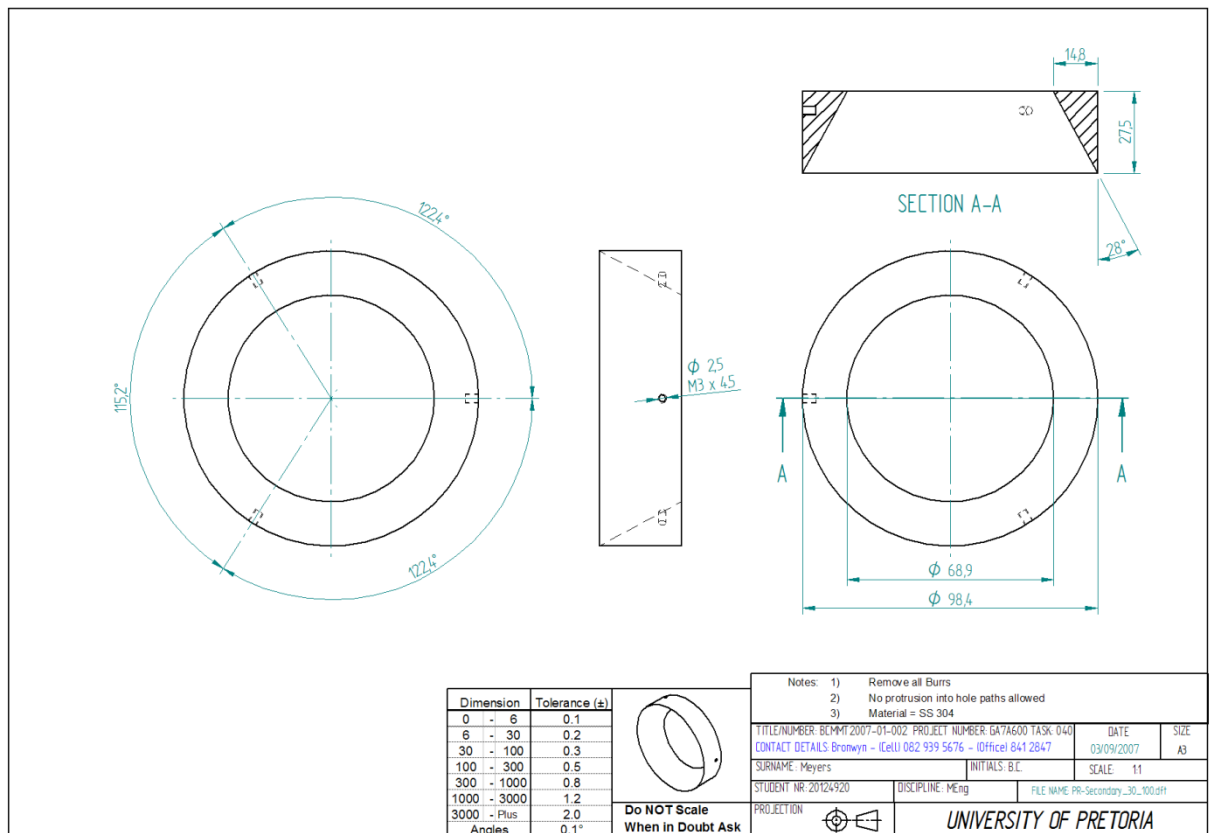


Figure C.24: The 30% secondary wedge ring

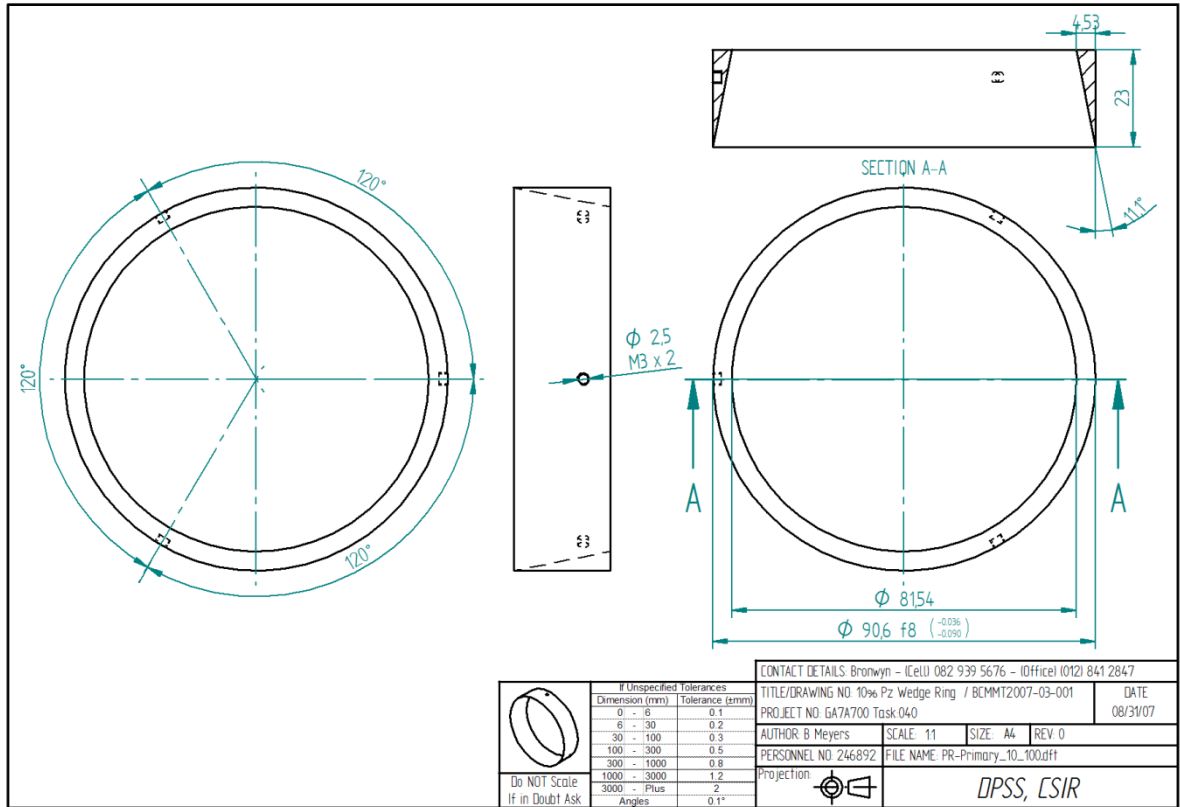


Figure C.25: The 10% primary wedge ring

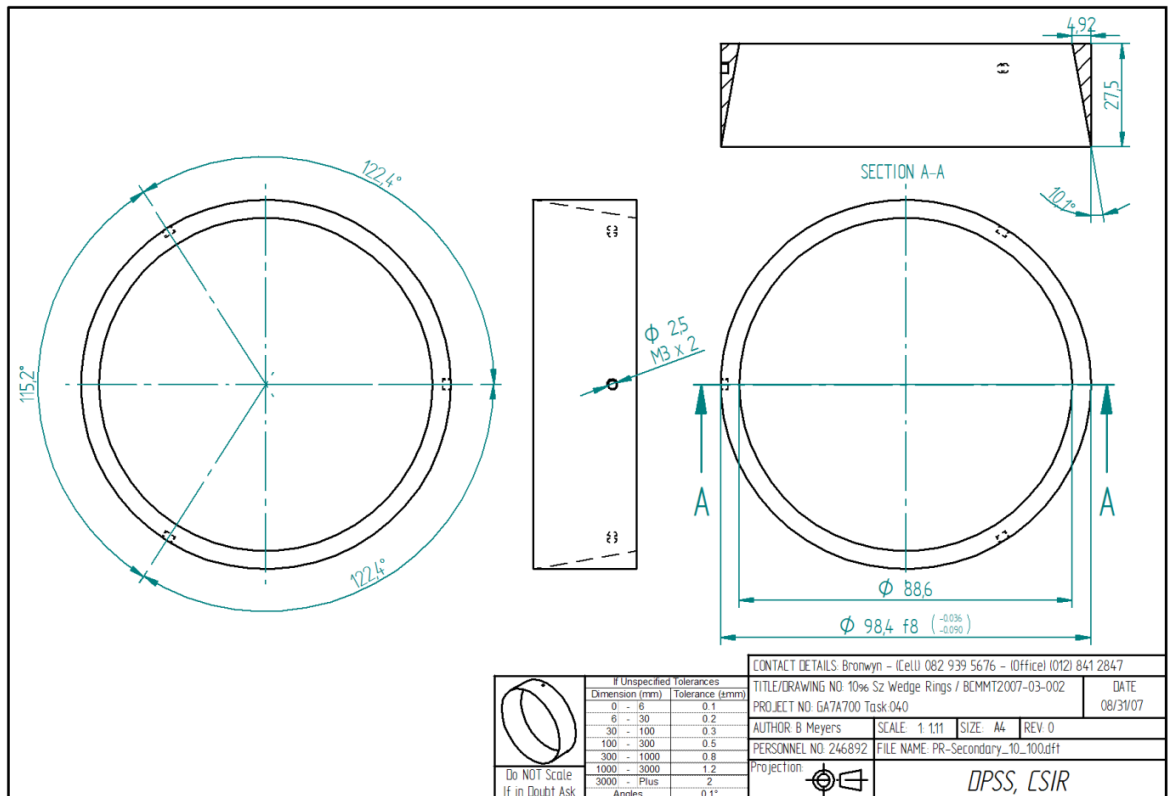


Figure C.26: The 10% secondary wedge ring



## APPENDIX D: UNCERTAINTY ANALYSIS

### NOMENCLATURE

Technical characters:

$\infty$  Infinite

Greek characters:

$\beta$  Bias error

$\delta$  Uncertainty

$\delta_{jk}$  Kronecker delta

$\varepsilon$  Random error or final error

$\sigma$  Standard deviation

Latin characters:

m Sample size

n Number of variables

R Result value

r Remainder term

v Variable

w General uncertainty interval

X Value placeholder

x Value placeholder in %

Subscripts:

1 Index number

2 Index number

3 Index number

A Referring to the average

i Indices

j Indices

k Indices

n Last index number

R Referring to a result

true Referring to the true value

v Referring to a variable



## ABBREVIATIONS

SEE Standard error of estimate

### D.1 Theory

In order to convey the uncertainty of experimental results, certain analyses can be done to determine a best estimate of the errors involved. For this dissertation, the following definitions from Moffat [D.1] were used.

*True value:* The objective of the measurement. There are two aspects of this definition: (1) the conceptual definition - the name of the thing one is trying to measure and, (2) the value itself.

*Corrected value:* The best estimate of the numerical value of the true value, after one has applied all corrections that one knows about.

*Error:* The difference between the true value and the indicated value.

*Fixed error:* An error that does not change on repeated readings at the same set point, over the entire period of the experiment. Fixed error can be detected only by calibration against a reference value.

*Residual fixed error:* An estimate of the possible range of the remaining fixed error after one has corrected the indicated value by one's best estimate of its "average fixed error", determined by calibration.

*Random error:* An error which changes randomly on repeated observations

*Uncertainty:* A possible value that the total error may have, including the effects of fixed and random error.

*Absolute uncertainty:* The uncertainty expressed in measured units, i.e.,  $\delta R = X \text{ kg/m}^3$ .

*Relative uncertainty:* The uncertainty expressed as a fraction of the measured value, i.e.  $\frac{\delta R}{R} = x \%$ .

*Uncertainty interval:* The interval around the measured value within which the true value is believed to lie.

*Uncertainty analysis:* The process of estimating how much effect the uncertainties in the individual measurements have on the calculated results.

*Single-sample experiments:* Experiments in which each variable is measured once per data set.

*Multiple-sample experiments:* Experiments in which each variable is measured many times and averaged before the results are processed.

*Accuracy:* The extent to which the system output is correct.

The choice as to whether an experiment is a single-sample or multiple-sample is, however, no longer confined to the rigid definitions provided above due to the use of electronic data acquisition equipment. The sample rates and required result are also used to determine which type of experiment is being done. If the sample rate of the data acquisition system is orders greater than the frequency of the changes in the variable

being measured, then this could be regarded as a single-sample experiment. The spectra of significant frequencies in the measured variable also contribute to the determination of the type of experiment. If the measured values are averaged, e.g. the fluctuations in the variable are not relevant, then this too can be regarded as a single-sample experiment. In the case where many data points are measured but the experiment is deemed a single-sample experiment, the uncertainty would include the high frequency random errors present in the measuring system [D.1].

Kline and McClintock [D.2] proposed a method for describing the uncertainties in a single-sample experiment result through the application of certain statistical theorems. This method is described below.

Let the result,  $R$ , be a function of  $n$  independent variables,  $v_1, v_2, v_3, \dots, v_n$  where  $v_i$  is the arithmetic mean of the experiment sample.

$$R = R(v_1, v_2, v_3, \dots, v_n) \quad \text{D-1}$$

To determine the effect of random errors,  $\varepsilon$ , in the variables on the random error in the result [D.3], equation [D-1] is approximated with a Taylor series expansion centred at  $v_i$  rather than  $v_{jitrue}$  since the interest lies in the random error. Thus assuming a small variation in the variables and referring to Figure D.1.

$$R_i = R(v_{1i}, v_{2i}, v_{3i}, \dots, v_{ni}) = R(v_1, v_2, v_3, \dots, v_n) + \frac{\partial R}{\partial v_1}(v_{1i} - v_1) + \frac{\partial R}{\partial v_2}(v_{2i} - v_2) + \frac{\partial R}{\partial v_3}(v_{3i} - v_3) + \dots + \frac{\partial R}{\partial v_n}(v_{ni} - v_n) + r \quad \text{D-2}$$

where the partial derivatives are evaluated at  $(v_1, v_2, v_3, \dots, v_n)$ . The remainder,  $r$  is given by

$$r = \frac{1}{2!} \left[ \frac{\partial^2 R}{\partial v_1^2}(v_{1i} - v_1)^2 + \frac{\partial^2 R}{\partial v_2^2}(v_{2i} - v_2)^2 + \frac{\partial^2 R}{\partial v_3^2}(v_{3i} - v_3)^2 + \dots + \frac{\partial^2 R}{\partial v_n^2}(v_{ni} - v_n)^2 \right] + \left[ \frac{\partial^2 R}{\partial v_1 \partial v_2}(v_{1i} - v_1)(v_{2i} - v_2) + \frac{\partial^2 R}{\partial v_1 \partial v_3}(v_{1i} - v_1)(v_{3i} - v_3) + \frac{\partial^2 R}{\partial v_1 \partial v_4}(v_{1i} - v_1)(v_{4i} - v_4) + \dots + \frac{\partial^2 R}{\partial v_1 \partial v_n}(v_{1i} - v_1)(v_{ni} - v_n) \right] + \dots \quad \text{D-3}$$

where partial derivatives are evaluated somewhere between  $(v_{1i}, v_{2i}, v_{3i}, \dots, v_{ni})$  and  $(v_1, v_2, v_3, \dots, v_n)$ . Using the linear approach to error propagation,  $r$  is assumed to be negligible, thus only the first-order, or linear, terms are retained giving

$$R(v_{1i}, v_{2i}, v_{3i}, \dots, v_{ni}) = R(v_1, v_2, v_3, \dots, v_n) + \frac{\partial R}{\partial v_1}(v_{1i} - v_1) + \frac{\partial R}{\partial v_2}(v_{2i} - v_2) + \frac{\partial R}{\partial v_3}(v_{3i} - v_3) + \dots + \frac{\partial R}{\partial v_n}(v_{ni} - v_n) \quad \text{D-4}$$

This is a reasonable assumption if  $(v_{ji} - v_j)$  are sufficiently small and/or if the partial derivatives in [D-3] are small.

Rearranging equation [D-4] gives

$$R(v_{1i}, v_{2i}, v_{3i}, \dots, v_{ni}) - R(v_1, v_2, v_3, \dots, v_n) = \frac{\partial R}{\partial v_1}(v_{1i} - v_1) + \frac{\partial R}{\partial v_2}(v_{2i} - v_2) + \frac{\partial R}{\partial v_3}(v_{3i} - v_3) + \dots + \frac{\partial R}{\partial v_n}(v_{ni} - v_n) \quad \text{D-5}$$

And using Figure D.1, it is evident that

$$\varepsilon_{Ri} = R(v_{1i}, v_{2i}, v_{3i}, \dots, v_{ni}) - R(v_1, v_2, v_3, \dots, v_n) \quad \text{D-6}$$

$$\varepsilon_{vji} = (v_{ji} - v_j) \quad \text{D-7}$$

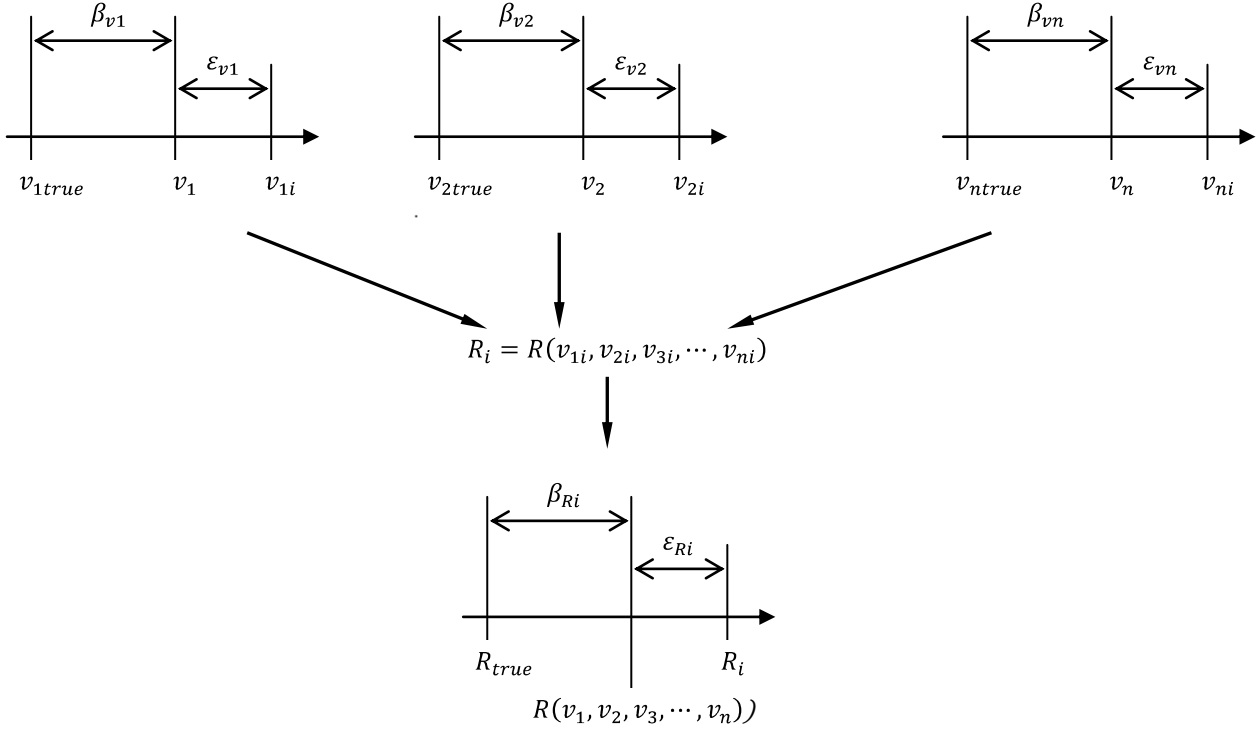


**Figure D.1: The propagation of errors into an experimental result (adapted from [D.3])**

Thus equation [D-5](#) can be rewritten as:

$$\varepsilon_{Ri} = \frac{\partial R}{\partial v_1} \varepsilon_{v1i} + \frac{\partial R}{\partial v_2} \varepsilon_{v2i} + \frac{\partial R}{\partial v_3} \varepsilon_{v3i} + \dots + \frac{\partial R}{\partial v_n} \varepsilon_{vni} \quad \text{D-8}$$

Squaring each side ensures positive values thus use

$$(\varepsilon_{Ri})^2 = \left[ \frac{\partial R}{\partial v_1} \varepsilon_{v1i} + \frac{\partial R}{\partial v_2} \varepsilon_{v2i} + \frac{\partial R}{\partial v_3} \varepsilon_{v3i} + \dots + \frac{\partial R}{\partial v_n} \varepsilon_{vni} \right]^2 \quad \text{D-9}$$

which when multiplied out is of the form

$$(\varepsilon_{Ri})^2 = \sum_{j=1}^n \left( \frac{\partial R}{\partial v_j} \varepsilon_{vji} \right)^2 + 2 \sum_{j=1}^n \sum_{k=1}^n \left[ \left( \frac{\partial R}{\partial v_j} \varepsilon_{vji} \right) \left( \frac{\partial R}{\partial v_k} \varepsilon_{vki} \right) (1 - \delta_{jk}) \right] \quad \text{D-10}$$

where the Kronecker delta is  $\delta_{jk} = \begin{cases} 1 \rightarrow j = k \\ 0 \rightarrow j \neq k \end{cases}$

To find the final error,  $\varepsilon_R$ , in the final result, which is calculated from the averages of the measured variables  $(v_1, v_2, v_3, \dots, v_n)$ , the errors,  $\varepsilon_{Ri}$ , need to be summed and divided by the number of measurements in a sample,  $m$ , thus

$$\frac{1}{m} \sum_{i=1}^m (\varepsilon_{Ri})^2 = \frac{1}{m} \sum_{i=1}^m \left[ \sum_{j=1}^n \left( \frac{\partial R}{\partial v_j} \varepsilon_{vji} \right)^2 + 2 \sum_{j=1}^n \sum_{k=1}^n \left[ \left( \frac{\partial R}{\partial v_j} \varepsilon_{vji} \right) \left( \frac{\partial R}{\partial v_k} \varepsilon_{vki} \right) (1 - \delta_{jk}) \right] \right] \quad \text{D-11}$$

which can be rewritten as

$$\frac{1}{m} \sum_{i=1}^m (\varepsilon_{Ri})^2 = \sum_{j=1}^n \left[ \left( \frac{\partial R}{\partial v_j} \right)^2 \frac{1}{m} \sum_{i=1}^m (\varepsilon_{vji})^2 \right] + 2 \sum_{j=1}^n \sum_{k=1}^n \left[ \left( \frac{\partial R}{\partial v_j} \right) \left( \frac{\partial R}{\partial v_k} \right) (1 - \delta_{jk}) \left( \frac{1}{m} \sum_{i=1}^m (\varepsilon_{vji})(\varepsilon_{vki}) \right) \right] \quad \text{D-12}$$

From the statistical definition for the variance, which is the standard deviation squared, of the sample sized,  $m$ , the following equation is used:

$$\sigma_{vj}^2 = \lim_{m \rightarrow \infty} \frac{1}{m} \sum_{i=1}^m (\varepsilon_{vji})^2 \quad \text{D-13}$$

And the covariance is given by

$$\sigma_{vjvk}^2 = \lim_{m \rightarrow \infty} \frac{1}{m} \sum_{i=1}^m (\varepsilon_{vji})(\varepsilon_{vki}) = 0 \quad \text{D-14}$$

Assuming a large number of data points, thus having enough points so as to approximate  $m \rightarrow \infty$ , and substituting equations [D-13](#) and [D-14](#) into equation [D-12](#), one gets

$$\frac{1}{m} \sum_{i=1}^m (\varepsilon_{Ri})^2 = \sum_{j=1}^n \left[ \left( \frac{\partial R}{\partial v_j} \right)^2 \sigma_{vj}^2 \right] + 2 \sum_{j=1}^n \sum_{k=1}^n \left[ \left( \frac{\partial R}{\partial v_j} \right) \left( \frac{\partial R}{\partial v_k} \right) (1 - \delta_{jk}) \sigma_{vjvk}^2 \right] \quad \text{D-15}$$

Independent variables would have  $\sigma_{vjvk}^2 = 0$ , so for  $m$  large we can assume

$$\frac{1}{m} \sum_{i=1}^m (\varepsilon_{Ri})^2 = \sum_{j=1}^n \left[ \left( \frac{\partial R}{\partial v_j} \right)^2 \sigma_{vj}^2 \right] \quad \text{D-16}$$

Thus the variance of the result,  $\sigma_R^2$ , is

$$\sigma_R^2 = \sum_{j=1}^n \left[ \left( \frac{\partial R}{\partial v_j} \right)^2 \sigma_{vj}^2 \right] \quad \text{D-17}$$

Thus the standard deviation of the result is

$$\sigma_R = \sqrt{\sum_{j=1}^n \left[ \left( \frac{\partial R}{\partial v_j} \right)^2 \sigma_{vj}^2 \right]} \quad \text{D-18}$$

which when expanded is given as

$$\sigma_R = \left[ \left( \frac{\partial R}{\partial v_1} \right)^2 \sigma_{v_1}^2 + \left( \frac{\partial R}{\partial v_2} \right)^2 \sigma_{v_2}^2 + \left( \frac{\partial R}{\partial v_3} \right)^2 \sigma_{v_3}^2 + \dots + \left( \frac{\partial R}{\partial v_n} \right)^2 \sigma_{v_n}^2 \right]^{\frac{1}{2}} \quad \text{D-19}$$

The standard deviation is a possible estimate of the uncertainty interval of the result,  $R$ , however, it is not the best estimate because it only encloses 68% of the measured data. The maximum deviation is also not a good estimate of the uncertainty interval because it is unlikely that all the variables will be at their maximum deviation at the same time [D.1]. Thus the best estimate is some general uncertainty interval,  $w_j$ , which is somewhere less than the maximum interval and more than the standard deviation. Thus substituting the standard deviation interval in equation [D-18] for the general uncertainty interval, an estimate for the uncertainty interval for the result,  $w_R$ , is given below [D.2].

$$w_R = \left[ \sum_{j=1}^n \left( \frac{\partial R}{\partial v_j} w_j \right)^2 \right]^{\frac{1}{2}} \quad \text{D-20}$$

The new challenge once this is known is to find the uncertainty of each variable used. There are various methods of estimating these uncertainties such as:

- Calibrate equipment and obtain uncertainty of measured variable
- Calculate twice the standard error of estimate of the regression curve obtained from a calibration
- Calculate variable uncertainty using the Kline-McClintock method [D.2]
- Use the accuracy quoted from the manufacturer
- Use scale accuracy, i.e. analogue scale -  $\frac{1}{2}$  the smallest scale reading, digital readout - smallest scale reading
- Estimate a value

If a linear least-squares regression (curve fit) has been applied to a set of data for adjustment, then twice the standard error of estimate can be used as a reasonable estimate of the uncertainty interval [D.3]. The standard error of estimate is given by the following equation:

$$SEE_{v_j} = \left\{ \frac{\sum_{i=1}^m (v_{ji} - v_{jiA})^2}{m - 2} \right\}^{\frac{1}{2}} \quad \text{D-21}$$

The above techniques are applied to calculate the errors in Section 3.4.3.

## REFERENCES

- [D.1] Moffat, R.J., "Experimental Methods in Heat Transfer," *ASME Continuing Education Course Notes*, Moffat Thermosciences, Inc., 2000.
- [D.2] Kline, S.J., McClintock, F.A., "Describing Uncertainties in Single-Sample Experiments," *Mechanical Engineering*, vol. 75, pp. 3-8, January 1953.
- [D.3] Coleman, H.W., Steele, W.G., *Experimentation and Uncertainty Analysis for Engineers*, 1st ed., John Wiley & Sons, Inc., United States of America, 1989.

## APPENDIX E: EXTENDED RESULTS

### NOMENCLATURE

Latin characters:

t Time

#### E.1 Non-reacting experiment

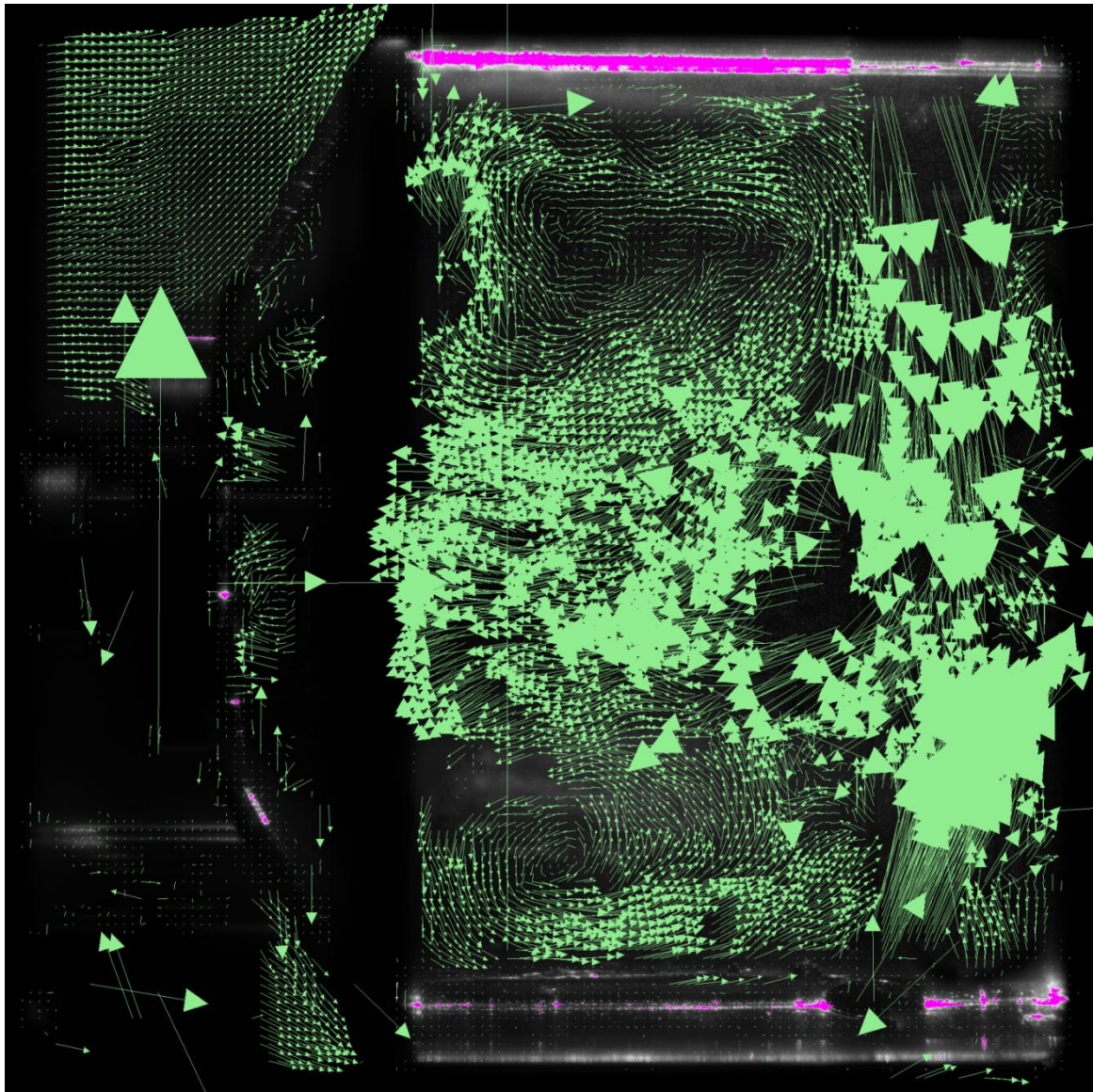


Figure E.1: The top primary zone vector field at  $t = 1\,188\,625\,000\ \mu\text{s}$

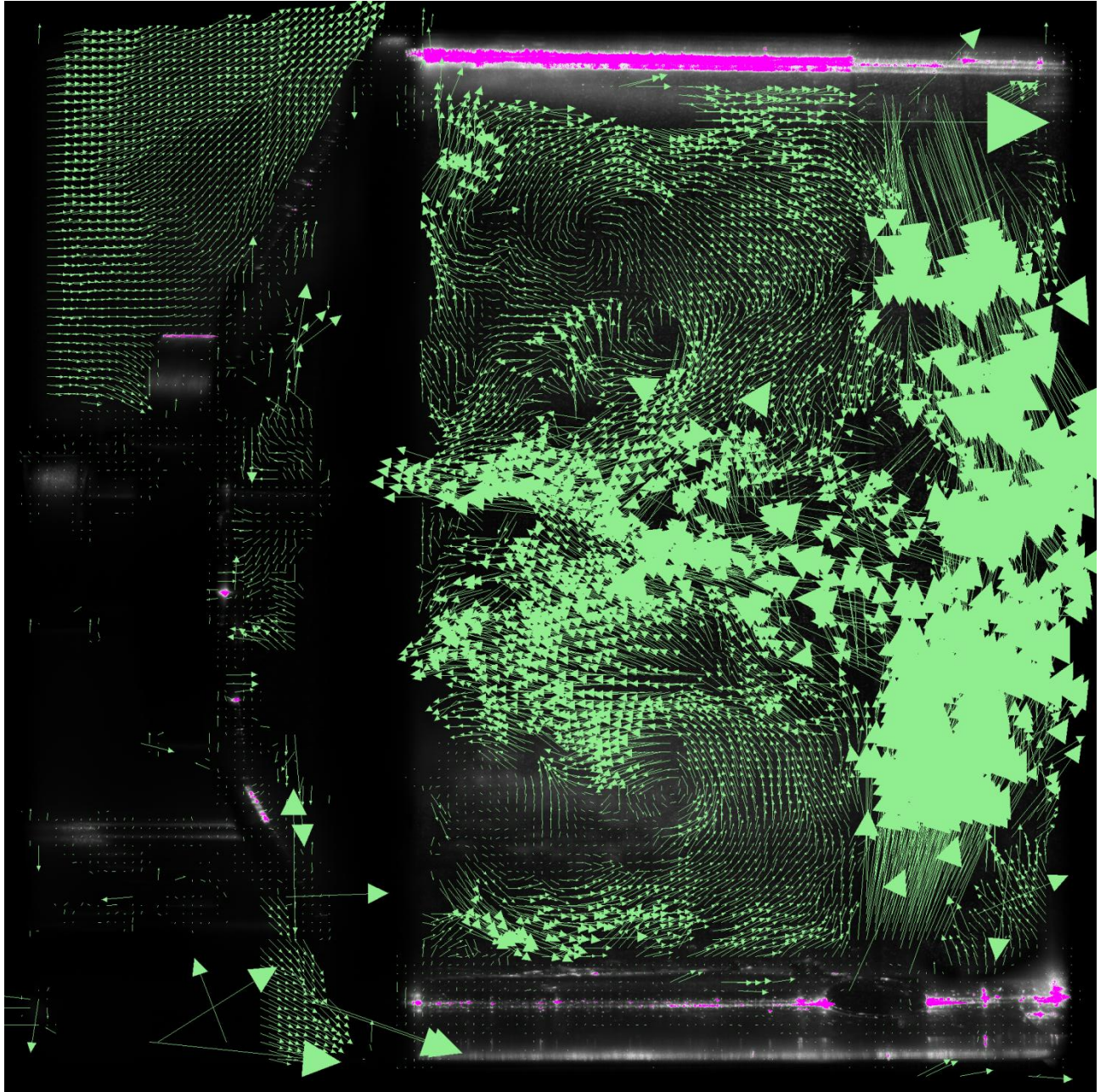


Figure E.2: The top primary zone vector field at  $t = 1\,190\,125\,000\ \mu\text{s}$  (+  $1\,500\,000\ \mu\text{s}$  from Figure E.1)

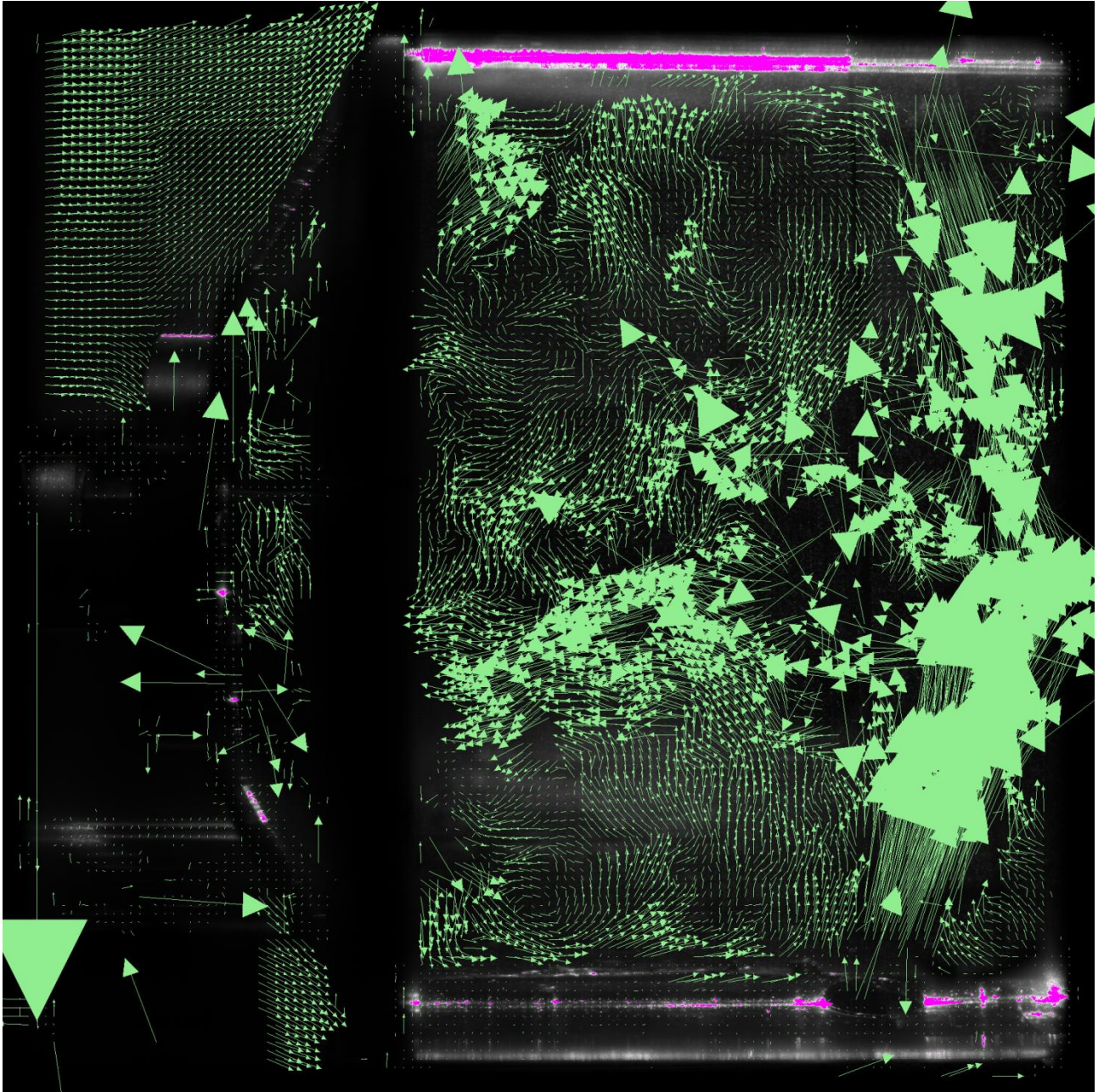


Figure E.3: The top primary zone vector field at  $t = 1\,191\,625\,000\ \mu\text{s}$  (+  $1\,500\,000\ \mu\text{s}$  from Figure E.2)

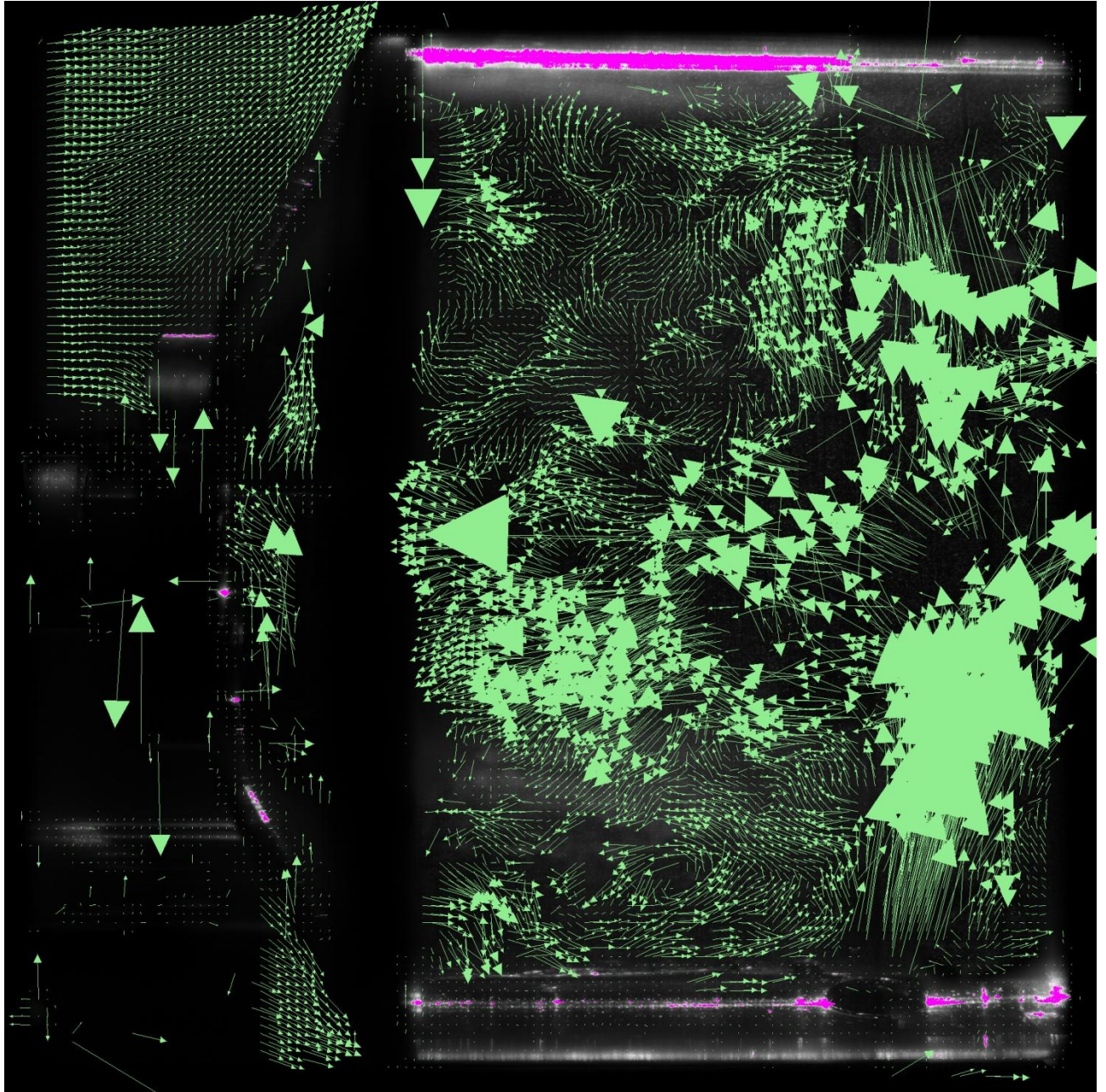


Figure E.4: The top primary zone vector field at  $t = 1\,193\,328\,125\ \mu\text{s}$  (+  $1\,703\,125\ \mu\text{s}$  from Figure E.3)

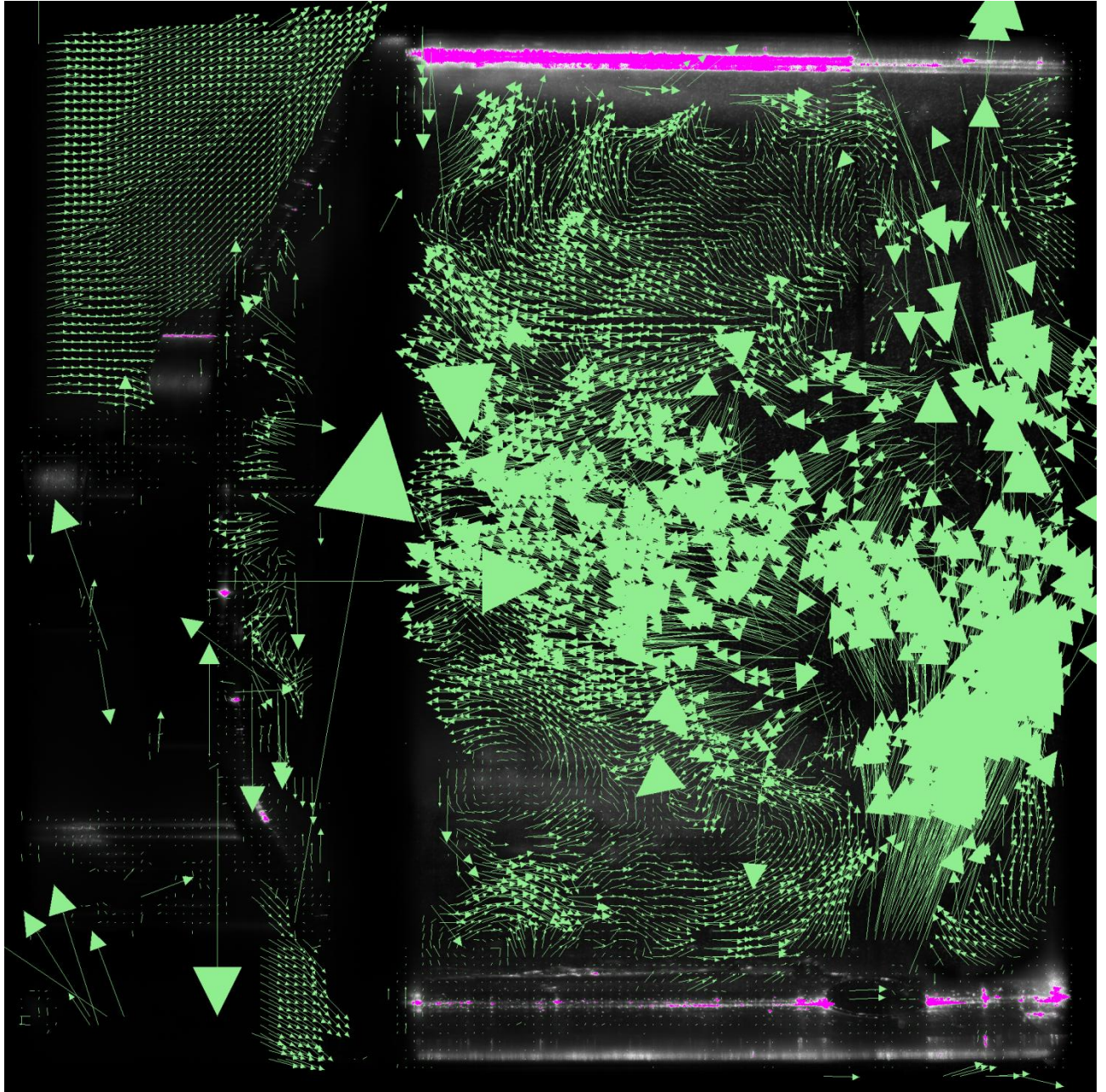


Figure E.5: The top primary zone vector field at  $t = 1\,195\,031\,250\ \mu\text{s}$  (+  $1\,703\,125\ \mu\text{s}$  from Figure E.4)

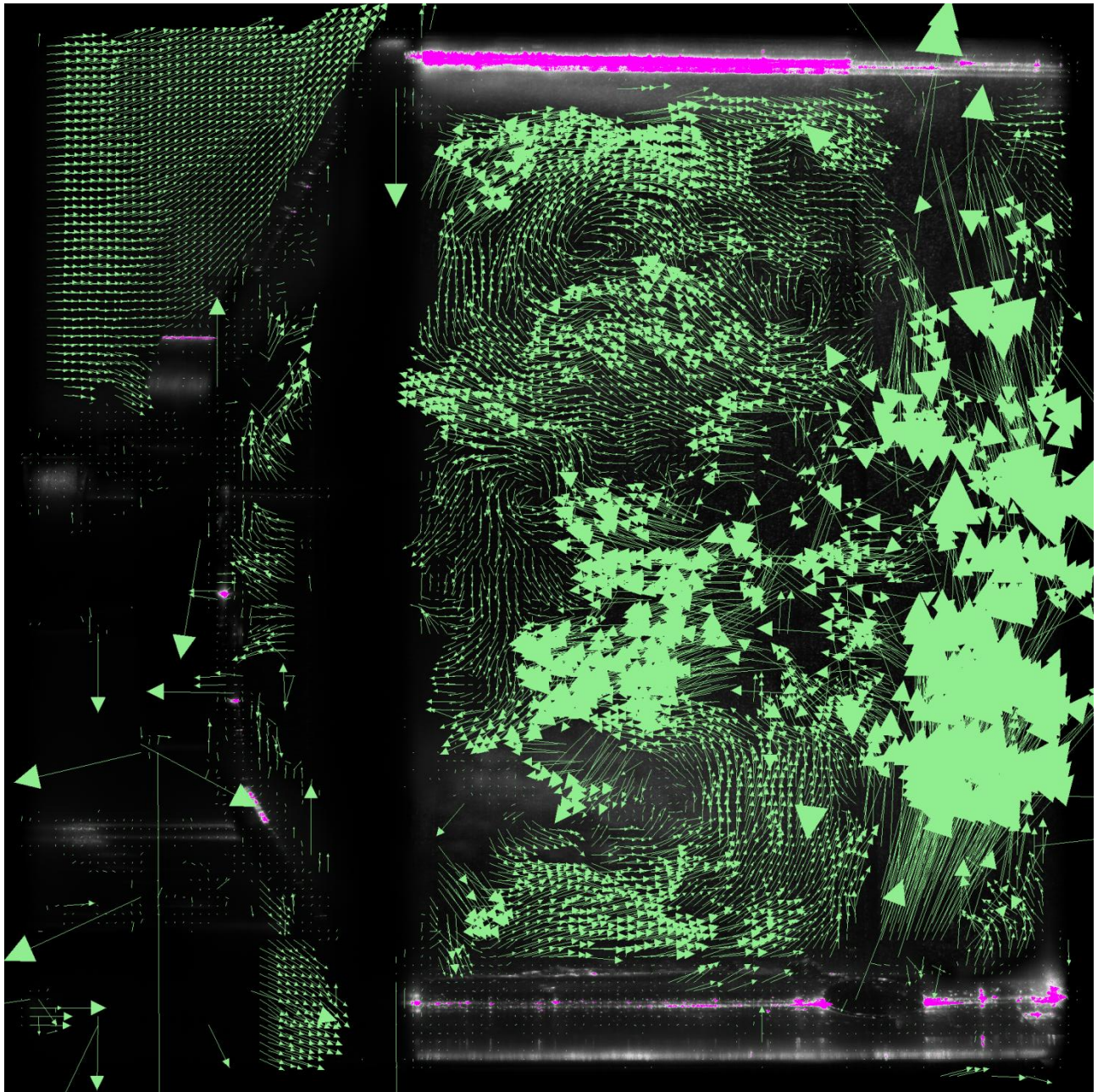


Figure E.6: The top primary zone vector field at  $t = 1\,196\,531\,250\ \mu\text{s}$  (+  $1\,500\,000\ \mu\text{s}$  from Figure E.5)

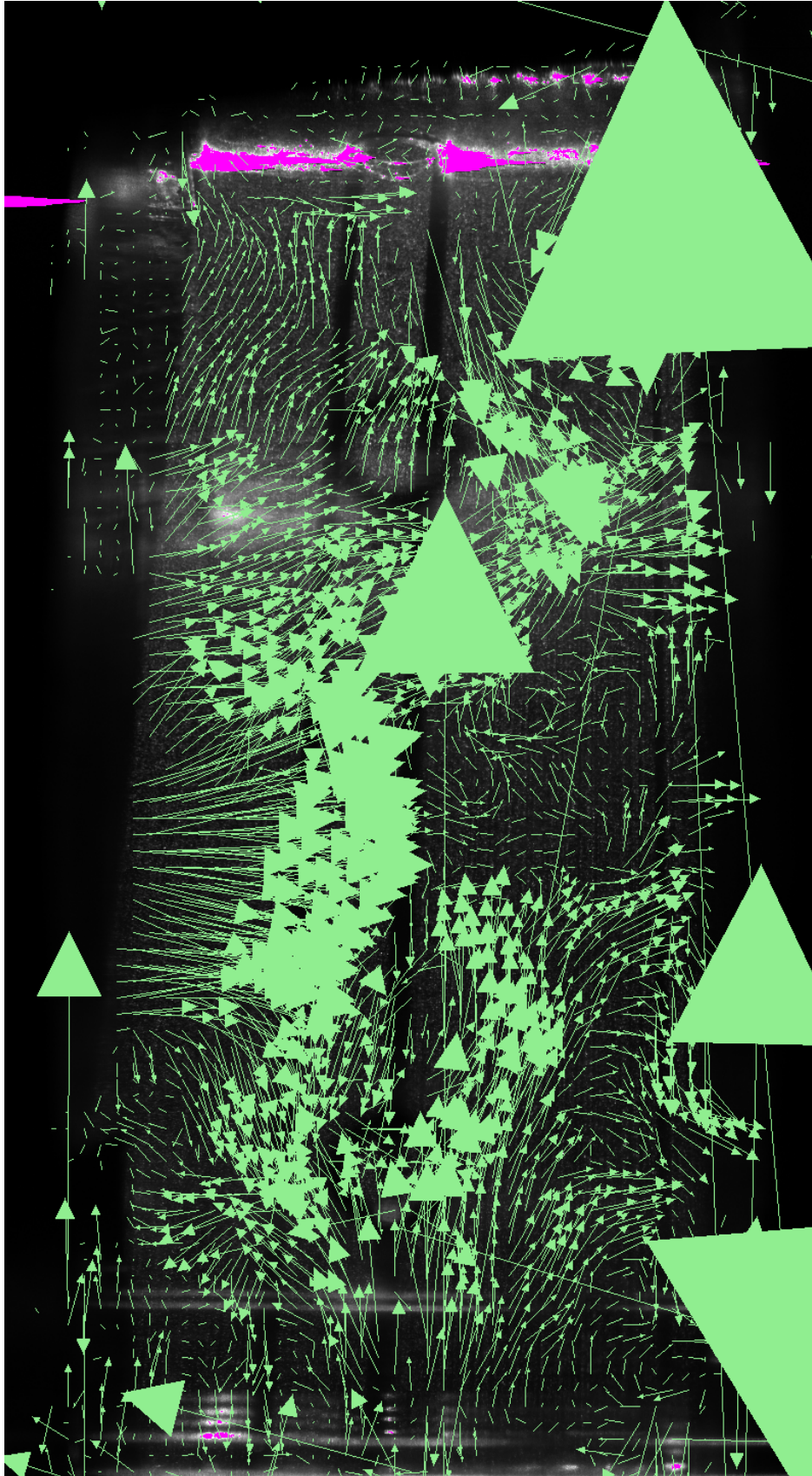


Figure E.7: The bottom secondary zone vector field at  $t = 1\,088\,437\,500\ \mu\text{s}$

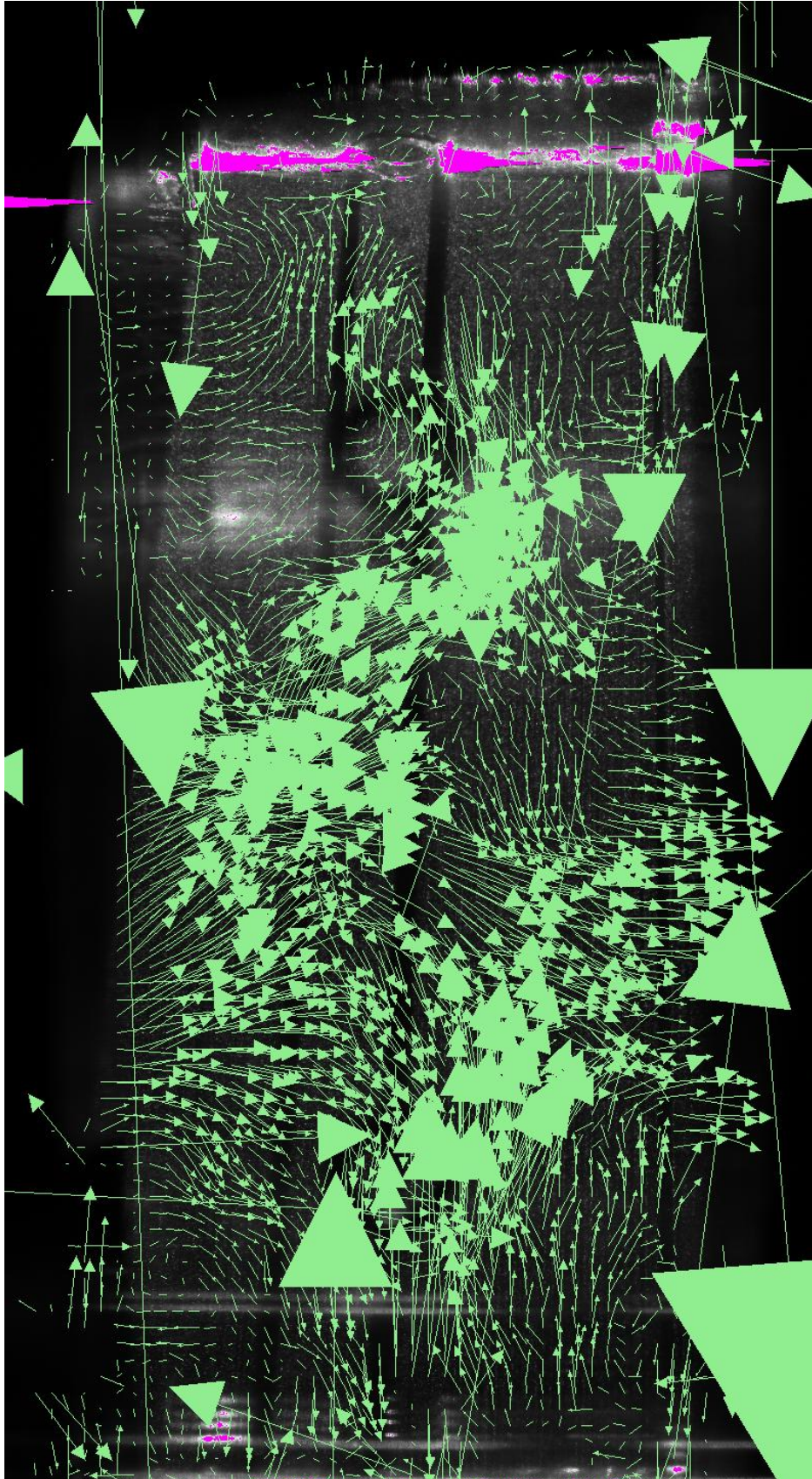


Figure E.8: The bottom secondary zone vector field at  $t = 1\,089\,937\,500\ \mu\text{s}$  (+  $1\,500\,000\ \mu\text{s}$  from Figure E.7)



Figure E.9: The bottom secondary zone vector field at  $t = 1\,091\,437\,500\ \mu\text{s}$  (+  $1\,500\,000\ \mu\text{s}$  from Figure E.8)

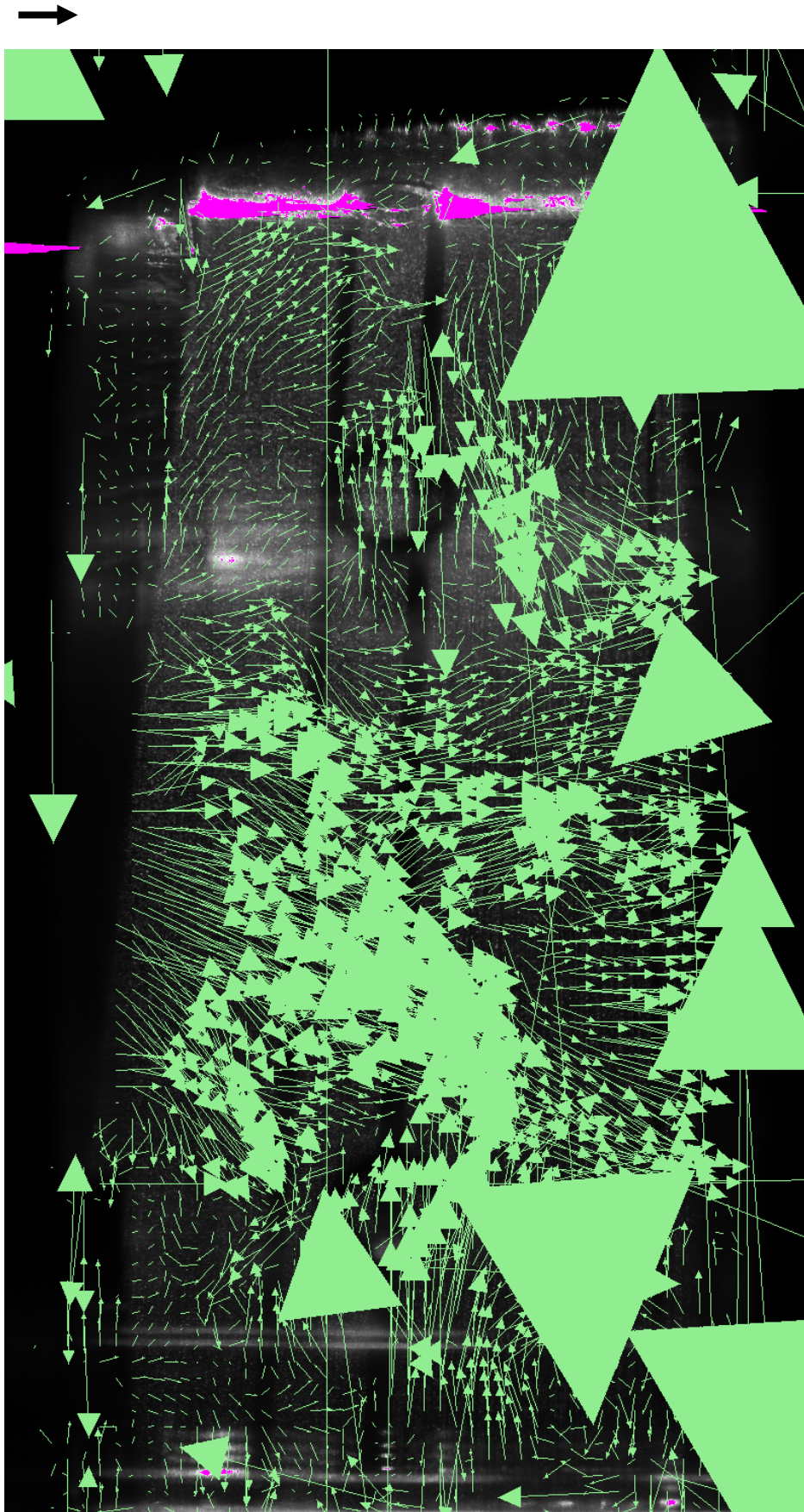


Figure E.10: The bottom secondary zone vector field at  $t = 1\,092\,937\,500\ \mu\text{s}$  (+  $1\,500\,000\ \mu\text{s}$  from Figure E.9)

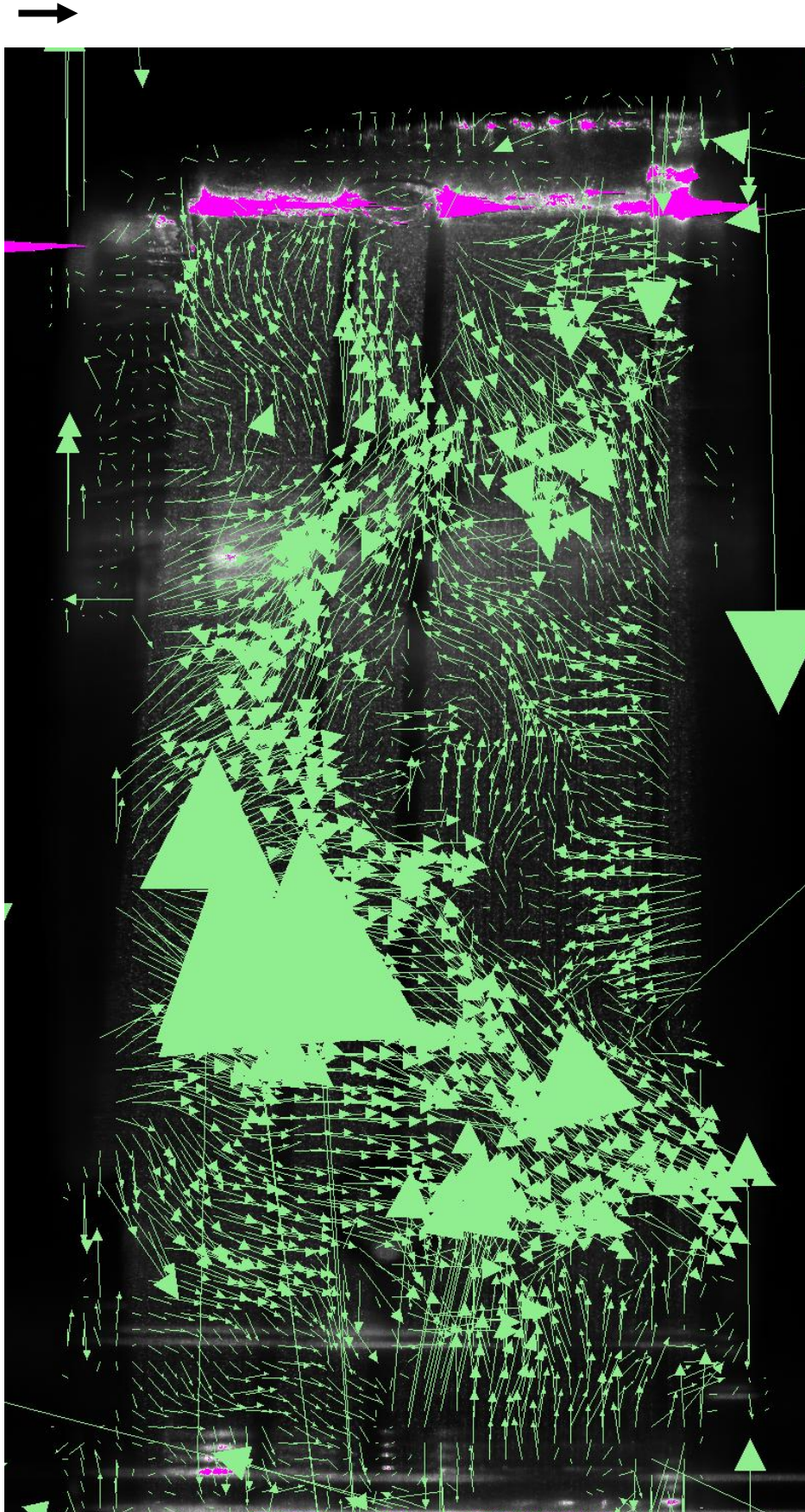


Figure E.11: The bottom secondary zone vector field at  $t = 1\,094\,640\,625\ \mu\text{s}$  (+  $1\,703\,125\ \mu\text{s}$  from Figure E.10)

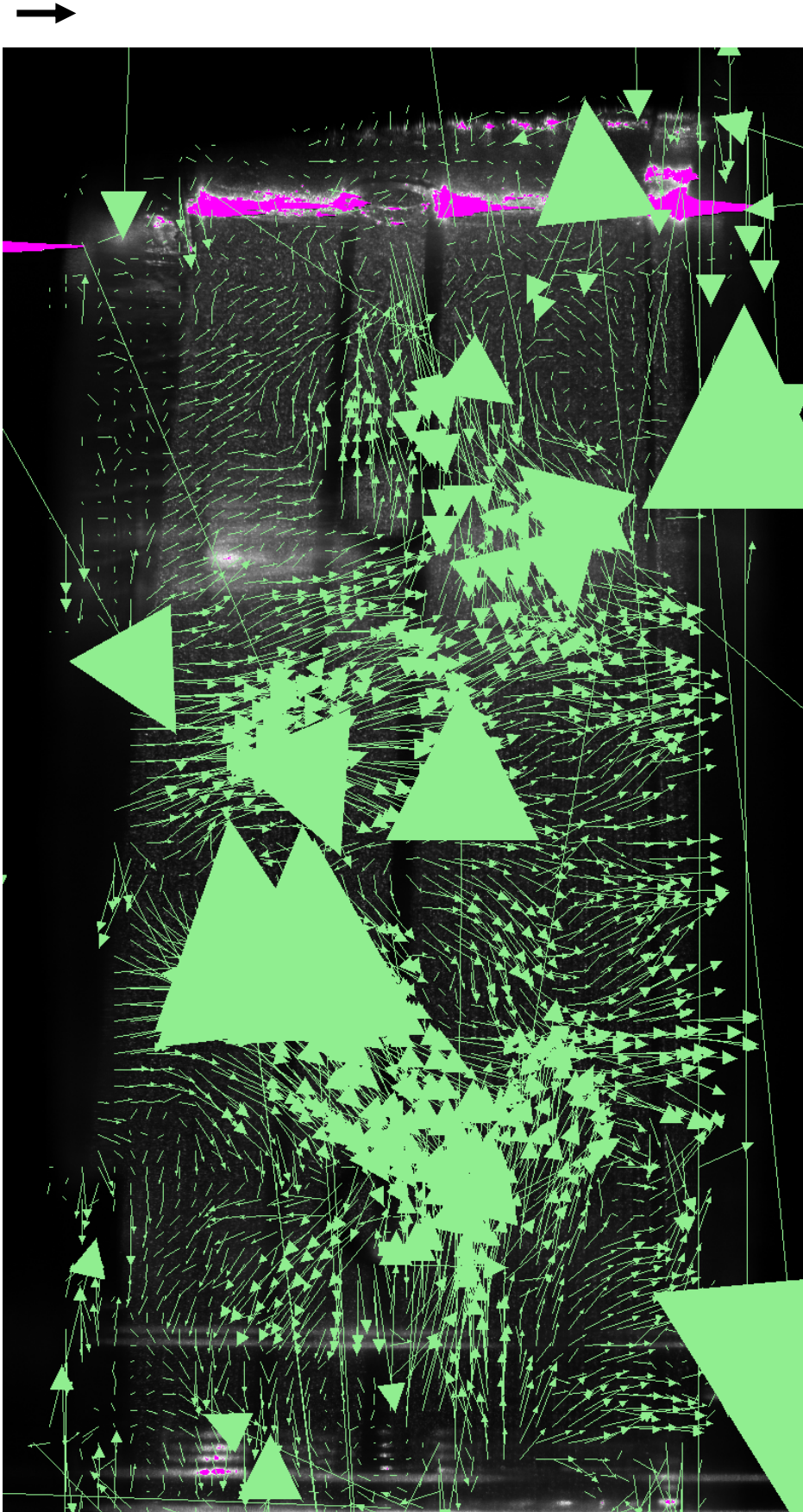


Figure E.12: The bottom secondary zone vector field at  $t = 1\,096\,046\,875\ \mu\text{s}$  (+  $1\,406\,250\ \mu\text{s}$  from Figure E.11)

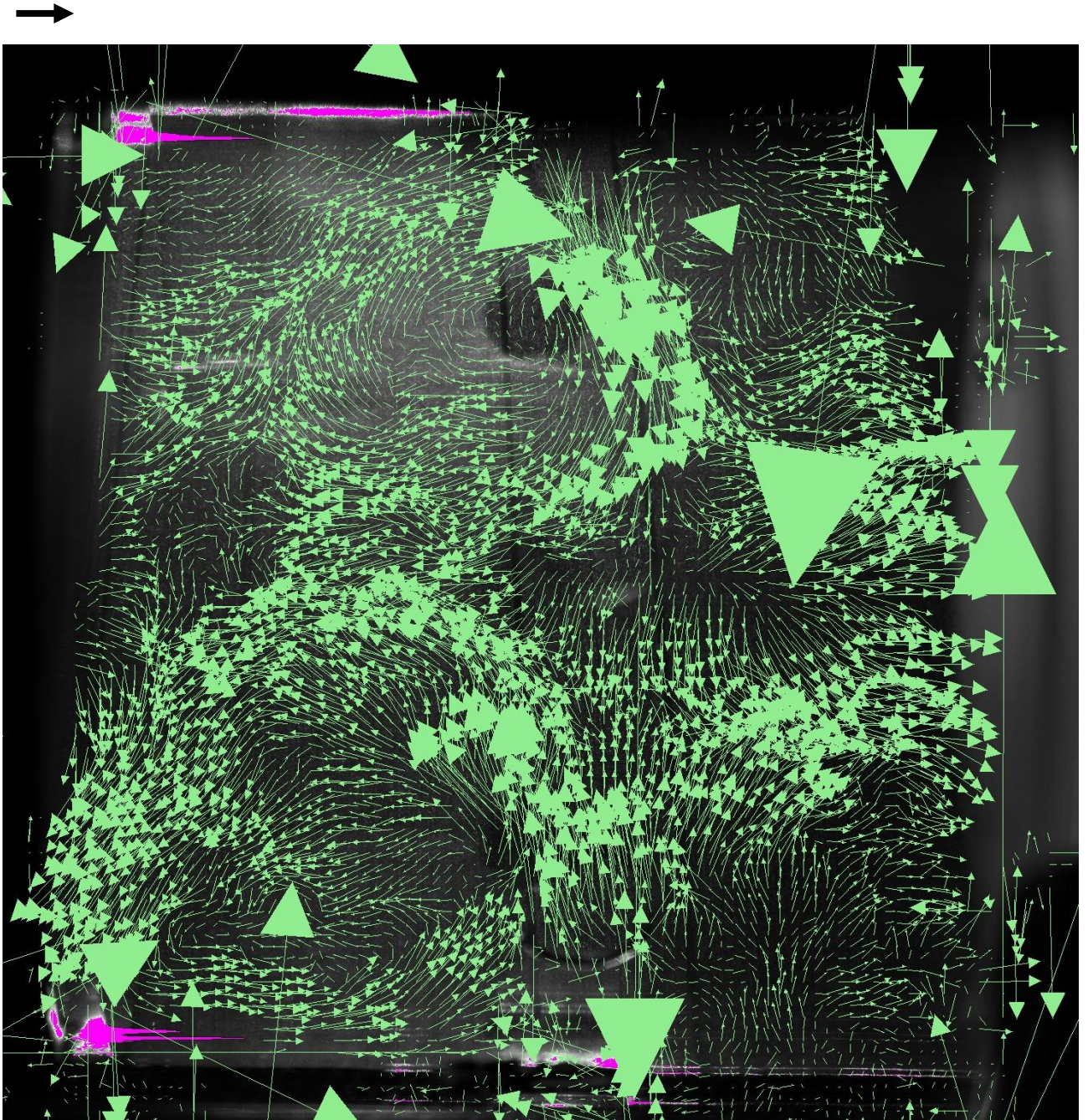


Figure E.13: The bottom dilution zone vector field at  $t = 1\ 105\ 406\ 250\ \mu\text{s}$

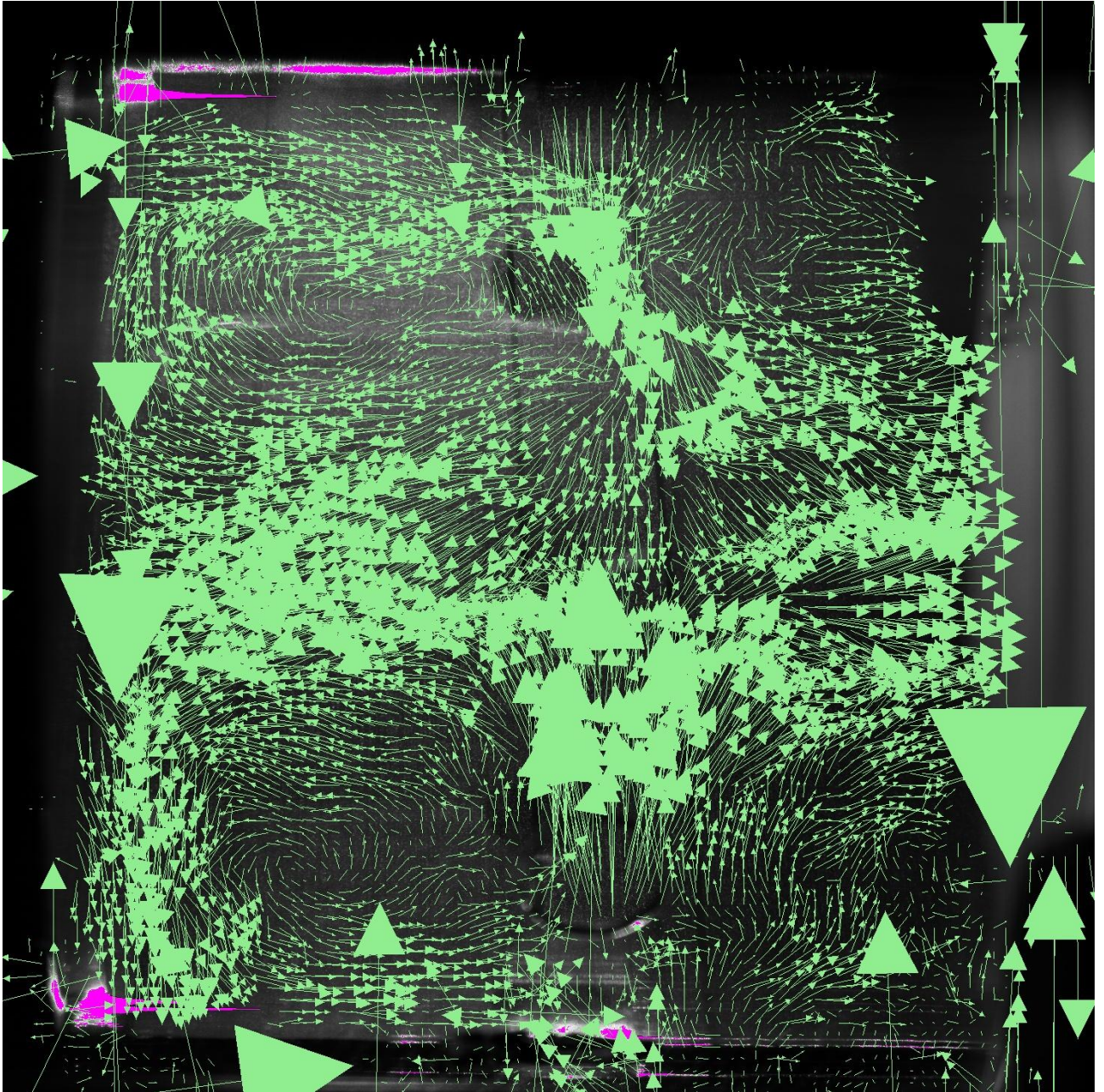


Figure E.14: The bottom dilution zone vector field at  $t = 1\,106\,703\,125\ \mu\text{s}$  (+  $1\,296\,875\ \mu\text{s}$  from Figure E.13)

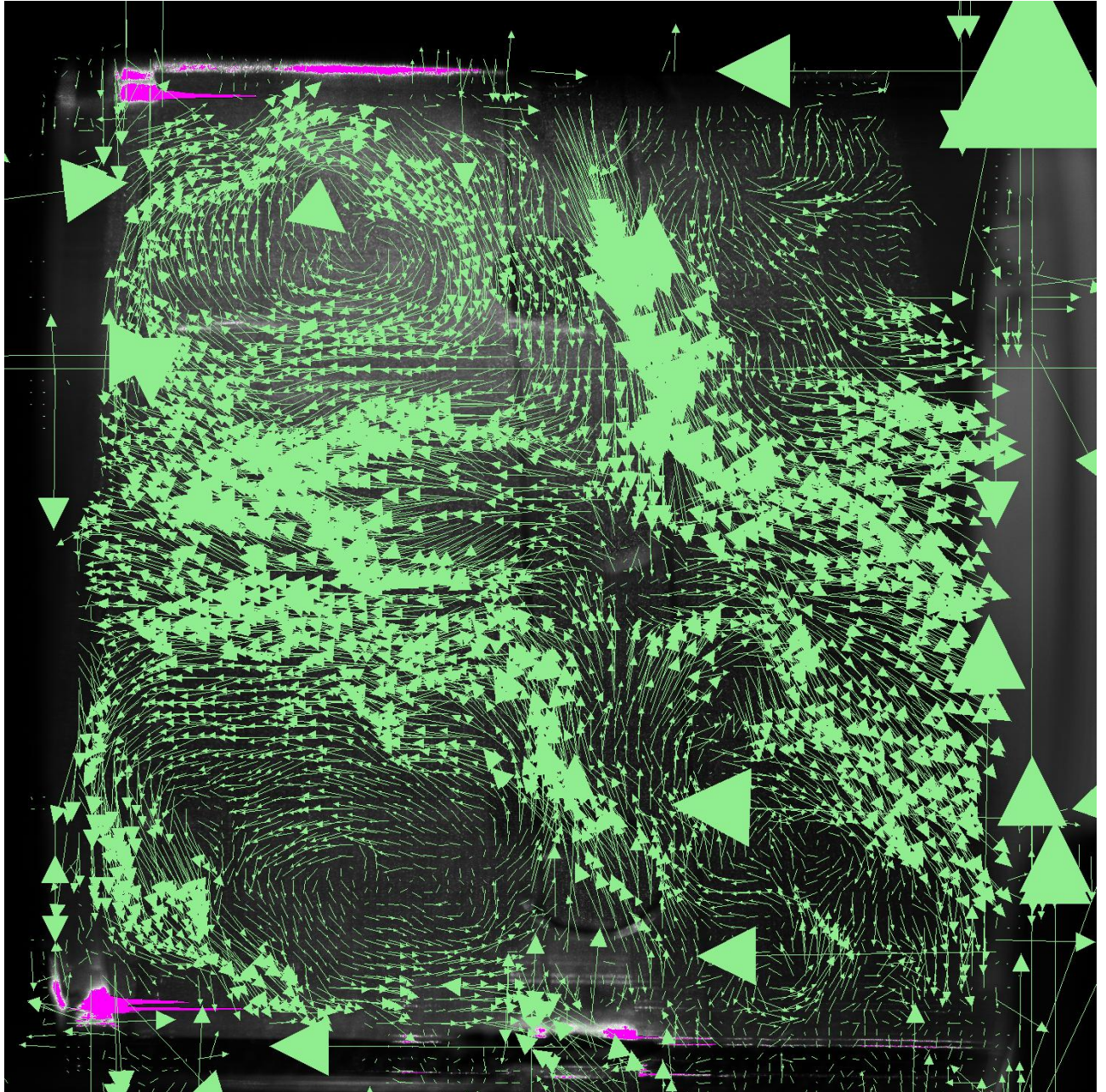


Figure E.15: The bottom dilution zone vector field at  $t = 1\,108\,203\,125\ \mu\text{s}$  (+  $1\,500\,000\ \mu\text{s}$  from Figure E.14)

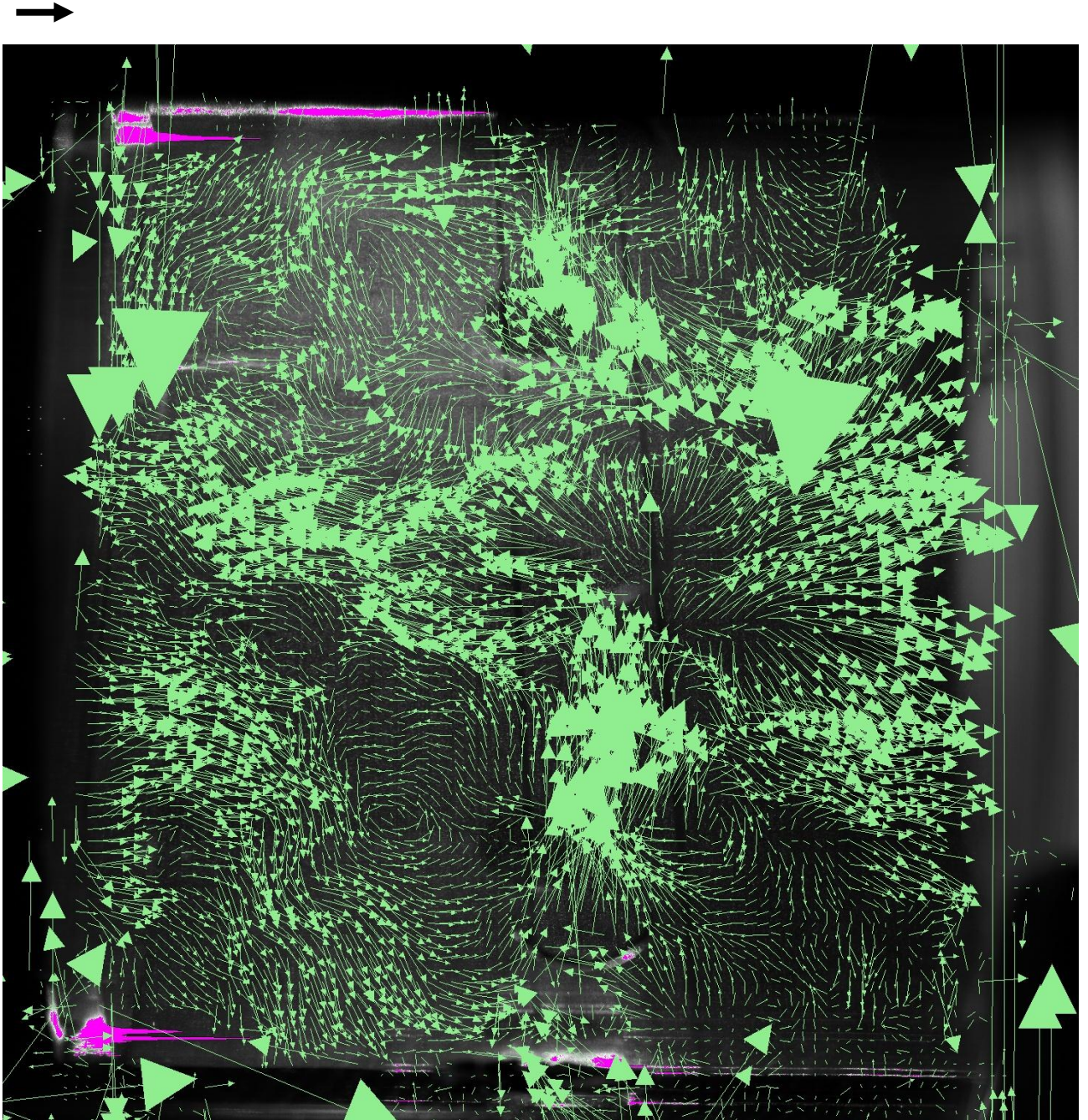


Figure E.16: The bottom dilution zone vector field at  $t = 1\,109\,906\,250\ \mu\text{s}$  (+  $1\,703\,125\ \mu\text{s}$  from Figure E.15)

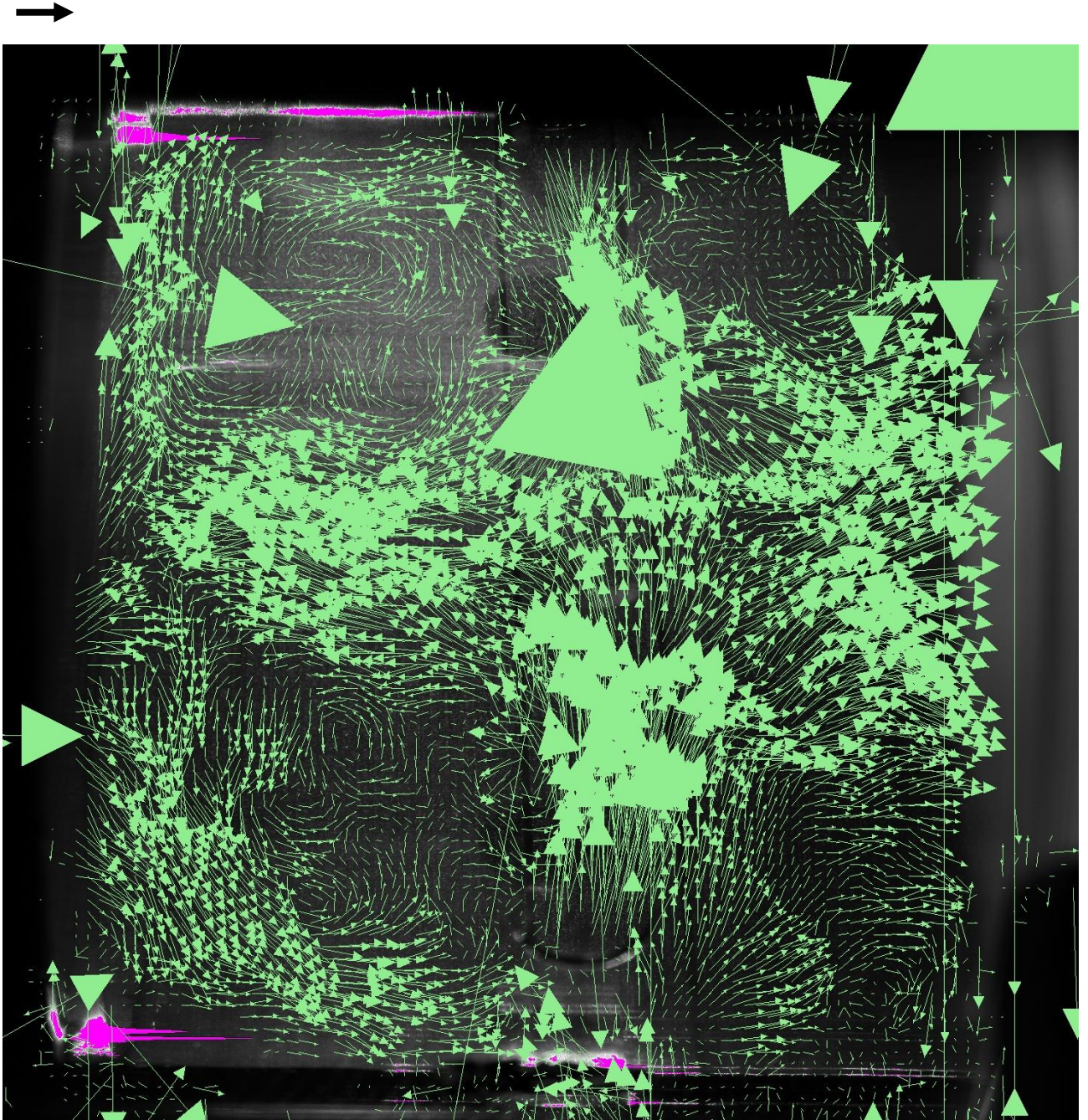


Figure E.17: The bottom dilution zone vector field at  $t = 1\,111\,406\,250\ \mu\text{s}$  (+  $1\,500\,000\ \mu\text{s}$  from Figure E.16)

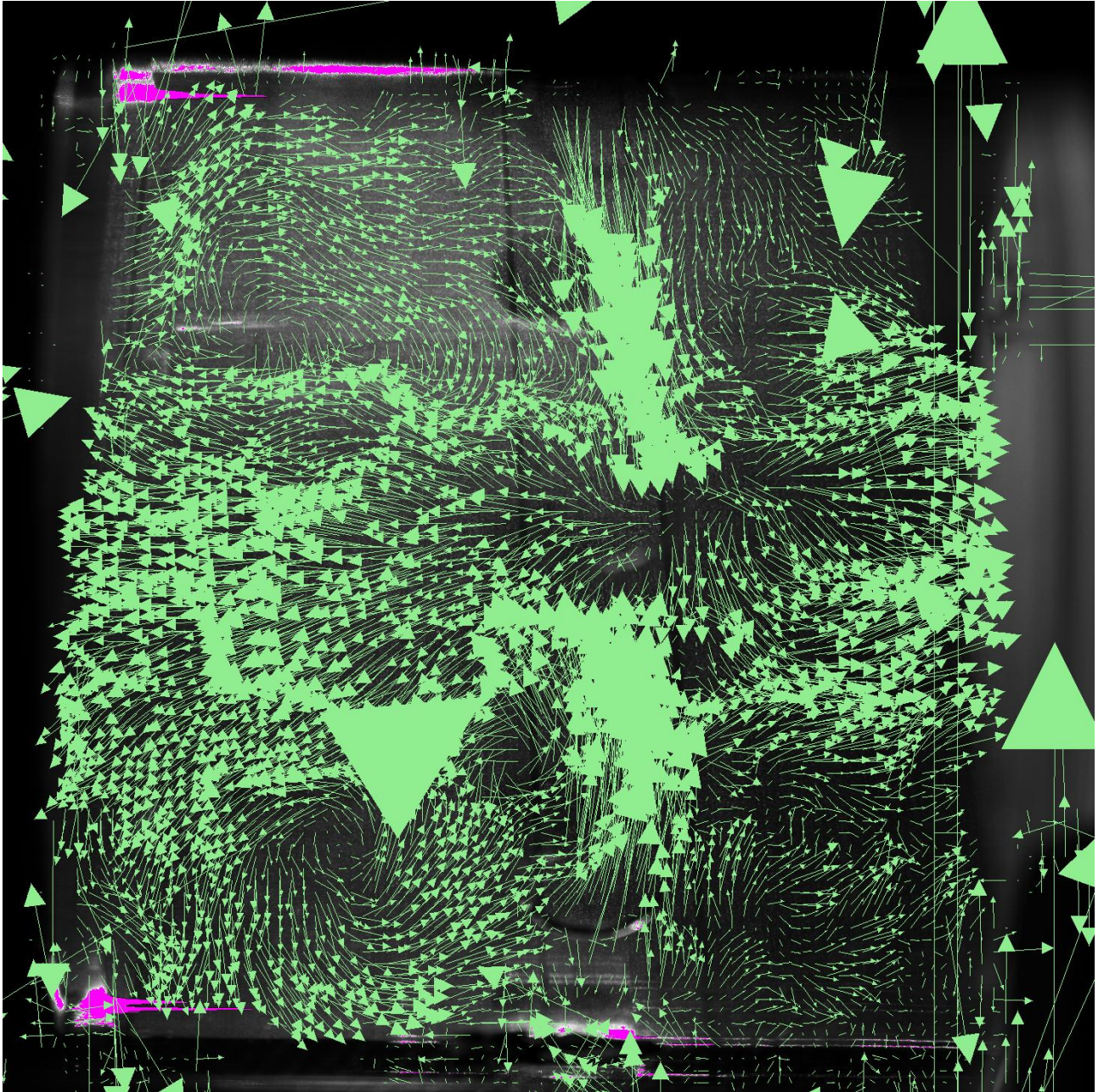


Figure E.18: The bottom dilution zone vector field at  $t = 1\,112\,906\,250\ \mu\text{s}$  (+  $1\,500\,000\ \mu\text{s}$  from Figure E.17)